ABSTRACT

Title of Dissertation: Submillimeter Test of the Gravitational Inverse-Square Law Using a Superconducting Differential Accelerometer

Violeta Amanda Prieto, Doctor of Philosophy, 2007

Dissertation directed by: Professor Ho Jung Paik
Department of Physics

The inverse-square law of gravitation is tested at submillimeter distances. To minimize Newtonian errors, the experiment employs a near null source, a circular disk of large diameter-to-thickness ratio. Two test masses, also disk-shaped, are suspended on the two sides of the source mass at a nominal distance of 180 μm. The source mass amplitude of motion is 16.1 μm. The signal is detected by a superconducting differential accelerometer. Careful matching and alignment makes the detector highly immune to platform vibrations. To reduce the thermal Brownian motion noise as well as the temperature noise of the instrument, the experiment is cooled to 1.7 K by pumping on liquid helium.

In this dissertation, I discuss the assembly, design, and design improvements of the inverse square law experiment. I perform a comprehensive analysis of the errors, identify the problems with the apparatus, and show ways to improve the design of the experiment. With the improved design, it will be possible to achieve a sensitivity of $|\alpha| = 2 \times 10^{-3}$ at $\lambda = 150$ μm, which will improve the current experimental limits by one order of magnitude at 150 μm and by over two orders of magnitude at shorter distances.

Submillimeter Test of the Gravitational Inverse-Square Law Using a Superconducting Differential Accelerometer

by

Violeta Amanda Prieto

Dissertation submitted to the Faculty of the Graduate School of the
University of Maryland, College Park in partial fulfillment
of the requirements for the degree of
Doctor of Philosophy
2007

Advisory Committee:

Professor Ho Jung Paik, Chairman/Advisor
Professor Theodore Allan Jacobson
Professor M. Coleman Miller
Dr. M. Vol Moody
Professor Peter S. Shawhan

© Copyright by
Violeta Amanda Prieto
2007

DEDICATION

To my parents.

To David.

To Krasi.

ACKNOWLEDGEMENTS

My career in physics has been a complex journey of search and exploration. I moved from theory to experiment, back and forth, again and again, and worked in areas from nanomaterials to general relativity and particle physics, acquiring a variety of skills and a range of knowledge I would have not acquired in just one of these.

The last (almost) five years of my life I spent in the gravitation experiment lab. I am very grateful to my advisor Prof. Ho Jung Paik. With his enthusiasm and stamina, he convinced me to join the gravitation experiment group and directed me through the completion of my project. With his help, I discovered how much I enjoy building things with my own hands and seeing them work. I am especially grateful to Dr. Vol Moody for his exceptional help, support, and technical assistance in the lab. He answered questions and was good humored and willing to help at any time.

Working in a small lab has been an incomparable experience. Krishna Venkateswara was always willing to help and has given me incomparable assistance since he joined our group. Ronald Norton provided most valuable hardware and software support. Dr. Yuqing Cao performed the finite element analysis and guided me through my first superconducting

joints. Ruozeng Liu taught me the secrets on how to wind pancake coils and Mark McMurray taught me how to wind transformers and make heat-switches.

Outside the lab, Russell Wood provided invaluable assistance and helpful suggestions during the machining of the experiment and supplementary parts.

Before joining the gravitation experiment group, I spent most of my time on the fourth floor of the department, interacting with the gravity and elementary particles theory groups. I initially worked with Prof. Markus Luty. I am grateful for his guidance and contagious passion for physics as well as for his great classes. I value the discussions with Profs. Bei Lok Hu and Jodesh Pati, the sincere concern in my success of Prof. Charles Misner, and more recent interaction with Profs. Alessandra Buonanno and Peter Shawhan. I am very grateful to Prof. Ted Jacobson who did a terrific job teaching our beginning quantum mechanics classes. He has followed the development of my career in physics with great interest and is serving as a committee member in my dissertation.

The outcome of my graduate work would not have been possible without all the help and support of my family. My parents, Juan Prieto and Elena Gortcheva, gave me the education, motivation, desire, and laid out the ground for me to reach this point in life. My grandmothers, Violeta Gorcheva and Amanda Valdés have been a great emotional support. The desire to see my aunt Krasimira Gorcheva has kept me going when there has not been anything else to justify it. I am also thankful to Martha Prieto, Amanda Laura Prieto, and Juan Manuel Prieto for their good thoughts and wishes.

I do not have words to describe everything I want to thank my husband, David Fiske, for. He has been a great friend, a loving companion, and an intellectually supporting partner. I would not have made it without his

encouragements and strength (and this thesis would probably not be in English either). Thank you!

I am grateful to Nushi Ademova, Sarah Donnelly, Matt Ferguson, Ramón Guevara, Liz Hays, Breno Imbiriba, Chen Ling, Debbie Pederson, Dan Sisan, Heather Sisan, Tim Stasevich, Neli Tomanova, Leora Vegosen, and Ayumi Yamada for their friendship.

This work has been supported by the National Science Foundation grant PHY-0244966 and NASA grant NAG-32874. During my initial graduate work I was a University of Maryland graduate teaching assistant and had the opportunity to teach a wide variety of classes. During 2002-2003 I received the GK-12 fellowship from the National Science Foundation. In addition, I was a teaching assistant and co-head teacher of Summer Girls Outreach Program at the University of Maryland for three years. I was very fortunate to be a coach of US Physics Team for the years 2001-2004. I received the Ilene H. Nagel travel grant to attend the Summer School on Astroparticle Physics and Cosmology, at the ICTP, Trieste (June 17 - July 5, 2002). I am grateful to Profs. James Gates and Jordan Goodman who provided matching funds for the travel.

TABLE OF CONTENTS

LIST OF TABLES

LIST OF FIGURES

Chapter 1

Introduction

Gravitation was the first of the four known fundamental interactions to be understood quantitatively in physics. The Newtonian inverse-square law (ISL) connected terrestrial phenomena such as free fall with astronomical observations and provided physical explanation of the planets' behavior such as Kepler's laws.

The ISL is a cornerstone of General Relativity (GR). Its validity has been impressively demonstrated by astronomical observations in the solar system, exceeding a level of one part in 10^8 at 10^7-10^9 km. The experimental limit at 1 cm-10 km stands at one part in 10^4. However, due to difficulties associated with designing sensitive short-range experiments, the range below 1 mm was mostly unexplored until a few years ago. In the wake of interests in searching for "extra-dimensions," the past two decades have seen increased activities in testing the ISL on the laboratory and geological scales.

In this chapter, I provide a review some of the theoretical motivations that inspired the short distance ISL test. Then I explain the measurements in broad terms, classify the types of experiments, and briefly describe our experiment. Finally, I review the current status of the experimental tests in the range between a few micrometers and a millimeter.

1.1 Theoretical motivation

The existence of a short-range mass-mass interaction implies a violation of the ISL, a cornerstone of GR. In an attempt to solve some of the greatest puzzles in physics, namely, the hierarchy problem, the cosmological constant problem, and the presence of dark matter and dark energy, a wide variety of theories have appeared recently, suggesting the possibility that new, interesting phenomena may occur at length scales below 1 mm. These theories include the presence of extra dimensions with size comparable to the range of our experiment, new particles such as the axion, radion, dilaton, and moduli, as well as the presence of a fundamental length scale of gravity, the "dark energy scale". This new physics is in the sensitive range of our experiment and can be probed directly by our ISL test.

In this section, I give a brief overview of the greatest puzzles in physics with the possible theories and predictions that attempt to solve them.

1.1.1 The hierarchy problem

There are two different fundamental energy scales observed in nature: the electroweak scale $E_{EW} \sim 1$ TeV and the gravitational scale $E_G \sim 10^{16}$ TeV. The fact that the ratio between the two scales is so large is known as the "hierarchy problem." Extra dimensions have been proposed as a very tempting solution to the hierarchy problem. By making use of them and implementing them in the theory, gravity is modified at distances smaller than the size of those extra dimensions. This means that we can expect modification in the behavior of objects smaller than those extra dimensions.

There are several reasons for speculating about extra dimensions. On one hand, here is no known reason for which those dimensions cannot exist. Extra dimensions were first proposed by Kaluza [30] and Klein [32] in order to unify general relativity and electrodynamics. Subsequently the weak and strong interactions were also unified with gravity in models with extra dimensions. String theory (M theory), a candidate theory for quantum gravity, can be formulated consistently only in a space

with six or seven extra dimensions. In addition, theories with infinite volume extra dimensions, the only theories that are not four dimensional at very low energies, have been proposed as candidates for solving the cosmological constant problem. Finally, Arkani-Hammed, Dimopoulus, and Dvali (ADD) [2, 3, 4] proposed a new solution to the hierarchy problem by bringing the fundamental Planck scale down to the weak scale by using *large extra dimensions*. Subsequently, Randal and Sundrum proposed a model with wrapped extra dimensions [67] to address the mass hierarchy problem as well.

I will focus here on the ADD formalism because the extra dimensions in it are large and thus potentially observable in laboratory-scale experiments. The ADD theory explained the weakness of gravity at long distances as due to the presence of n new spatial extra dimensions, called *large extra dimensions*, large compared to the Planck scale. In this framework, the Standard Model fields cannot feel the extra dimensions and are confined to a wall, a "3-brane," in the higher dimensional space. In principle, there can exist more than one compactification scale; namely, the different extra dimensions could be of different sizes. For simplicity, it is assumed here that all the large extra dimensions are of the same size, differing in size from the extra dimensions that are not large compared to the fundamental scale.

In 4 dimensions, the gravitational potential of a massive object with mass M at a distance r is

$$V(r) = -G_4 \frac{M}{r}, \tag{1.1}$$

where G_4 is the 4-dimensional gravitational constant (Newton's constant), related to the Planck mass M_{pl} by $G_4 \sim 1/M_{pl}^2$.

For n extra dimensions, the gravitational potential of a mass M in $(n+4)$-dimensions is then modified to

$$V(r) = -G_{4+n} \frac{M}{r^{n+1}}, \tag{1.2}$$

where G_{n+4} is the $(4+n)$-dimensional gravitational constant, and it is related to the $(4+n)$ dimensional Planck mass M_* by $G_{4+n} \sim 1/M_*^{n+2}$.

If we are interested in distances smaller than the size of the extra dimensions,

then the gravitational potential is independent of the size of the extra dimensions and is given by Eq. (1.2). The situation changes if the size R of the extra dimension is smaller than the distances we are interested in. Using Gauss' law, for $r > R$, we obtain

$$V(r) \sim -\frac{G_{4+n}}{R^n}\frac{M}{r}. \tag{1.3}$$

By comparing these last two equations, it is possible to relate the 4-dimensional Planck scale M_{pl}^2 to the fundamental, $(4+n)$-dimensional Planck scale M_*. The exact dependence is determined by the compactification method of the extra dimensions. For example, if all the extra dimensions have been compactified on a n-torus of radius R, the volume of the n-torus is $(2\pi R)^n$, and the relation between the two scales is given by

$$M_{pl}^2 = \left(\frac{2\pi cR}{\hbar}\right)^n M_*^{n+2}, \tag{1.4}$$

where $\hbar$ is Planck constant and c is the speed of light in vacuum. Taking $M_* \sim 1$ TeV/c^2 and assuming all n extra dimensions to be of the same size leaves

$$R \approx \frac{1}{\pi} 10^{-17+30/n}\,\text{cm} \tag{1.5}$$

for the possible sizes of the extra dimensions.

The non-observation of deviations from the 4-dimensional Newton's law constrains the size of the extra dimension. The $n = 1$ case gives $R \approx 10^{13}$ m, so this case is completely excluded since it would modify Newton's gravity at solar-system distances. The $n = 2$ case, which gives $R \approx 0.1$ mm, was the limit hoped for when this theory was first proposed, since gravity had never been tested at these distances, and has been the focus of many experiments during the last few years [27, 31, 38, 76, 81]. This case also seems to be excluded by those experiments. For larger n, the value of R decreases, but even for $n = 6$, R is large compared to $1/M_{pl}$.

According to string theories, in an effective low-energy theory, the volume of the extra dimensions must be stabilized by radions. The radion is a hypothetical particle that emerges as an excitation of the metric tensor but whose physical properties are virtually indistinguishable from a scalar in four dimensions, as shown in Kaluza-Klein

theory. The radion interaction is described by a Yukawa potential

$$V(r) = -G\frac{m_1 m_2}{r}[1 + \alpha e^{-r/\lambda}], \tag{1.6}$$

where λ is a length scale, also known as the range of the new interaction, and α is a dimensionless parameter, usually referred to as strength, since it compares the new interaction to gravity. It has gravitational strength couplings that determine the radius of the new dimensions. According to [1, 27], radion exchange will have a strength

$$\alpha = \frac{n}{n+2} \tag{1.7}$$

and a range of

$$\lambda \approx 2.4 \left(\frac{1\text{TeV}}{M_* c^2}\right) \text{mm}. \tag{1.8}$$

This is within the range of our designed experiment.

Another theory proposed to solve the hierarchy problem is supersymmetry (SUSY). SUSY is a symmetry between fermions and bosons that transforms the fundamental particles into superpartners. The superpartners differ from the original particles by half a unit of spin. Since the particles of the Standard Model do not have this property, supersymmetry must be a broken symmetry allowing the superparticles to acquire mass. SUSY solves the hierarchy problem by removing the power-law divergences of the radiative corrections to the Higgs mass by having automatic cancelations between fermionic and bosonic Higgs interactions.

Interesting predictions come from superstring theories in which SUSY is broken at low energies. Superstring theories generally contain gravitationally coupled scalar fields called moduli, which are massless at the string scale but can acquire mass from SUSY breaking. The expectation values of the moduli fields set the parameters of the effective theory. The most popular and best understood of these predicted scalar particles is the dilaton which determines the strength of gauge couplings.

1.1.2 Dark matter and the strong *CP* problem

The universe is held together by a form of matter different from ordinary matter and that cannot be detected by electromagnetic radiation; it therefore gives off no light

and is called dark.

The first evidence that much more than the visible matter should fill the universe dates back to 1933 when Zwicky [87, 88] measured the dispersion velocity in the Coma galaxies. Using the virial theorem, he was able to estimate the cluster's total mass based on "the internal rotation of the nebulae." When he compared this mass estimate to one based on the number of galaxies and total brightness of the cluster, he found a large discrepancy, predicting about 400 times more mass according to the motion of the galaxy near its edge than expected based on the luminosity. From his calculations, Zwicky inferred that there must be some non-visible form of matter which would provide enough of the mass and gravity to hold the cluster together. This was soon confirmed by Smith studying the Virgo cluster [75].

In the 70s, a much more systematic analysis was done. Rubin and Ford [74] analyzed the rotation of the Andromeda galaxy; later, Roberts and Roots [69] compared the rotation curves of the M31, M81, and M101 galaxies to ours, and again Rubin and collaborators analyzed 21 galaxies in a large range of luminosities and sizes [73]. They plotted the velocities of the galaxy rotation as a function of the distance to the galactic center and found that the velocity curves stay flat even outside the luminous disk, which implied that their mass densities were uniform well beyond the locations with most of the stars and subsequently cannot be explained by only the visible matter.

The most plausible explanation assumes that the visible material makes up only a small part of the clusters. Galaxies appear to be composed mostly of a roughly spherically symmetric, centrally concentrated halo of dark matter with the visible matter concentrated in a disc at the center. The dark matter halo measured by lensing agrees with the galaxy rotation curves. In addition, the dark matter affects galaxy clusters as well. X-ray measurements of hot intra-cluster gas correspond to observations of large mass-to-light ratios for galaxy clusters.

The dark matter candidates are classified into *baryonic* and *non-baryonic*. The *baryonic* dark matter comprises a very small fraction of all the dark matter and its most likely candidates are non-luminous gas, MACHOs (Massive Compact Halo Ob-

jects), brown dwarfs, and small, dense chunks of heavy elements. The *non-baryonic* dark matter is subclassified into *hot*, *warm* and *cold*. The *hot* dark matter consists of particles that travel with ultra-relativistic velocities, and neutrinos are the leading candidates. The *warm* dark matter is comprised by non-baryonic particles that move relativistically; common candidates are sterile neutrinos. The *cold* dark matter particles became non-relativistic very early and consequently were able to diffuse a negligible distance. Candidates are WIMPs (Weakly Interacting Massive Particles) and axions. None of these are part of the Standard Model, but they can arise in extensions to the Standard Model. For instance, many supersymmetric models naturally give rise to stable WIMPs generated by symmetry breaking during the primordial universe. The axion is one of the strongest candidates for the cold dark matter [82].

The Standard Model of particle physics successfully accounts for all existing particle data; however, according to it, the strong interactions have a non-trivial vacuum structure that in principle permits the violation of the combined symmetries of charge conjugation (C) and parity (P), collectively known as CP. The effects are parameterized by a dimensionless angle Θ_{QCD}. However, large CP violating interactions originating from QCD would induce a large electric dipole moment for the neutron. Experimental constraints on the neutron's electric dipole moment (currently unobserved) imply that CP violation arising from QCD must be extremely small or absent. This parameter is periodic, therefore, it could have any value between 0 and 2π. This presents a naturalness problem for the Standard Model: Why should this parameter be so small? This question constitutes what is known as the "strong CP problem."

In 1977, Peccei and Quinn [63, 64] developed an attractive resolution of this problem. They postulated the Peccei-Quinn mechanism in which Θ_{QCD} is promoted to a field/particle by adding a new global symmetry, the Peccei-Quinn symmetry, to the Standard Model. In one ramification of their theory, this symmetry becomes spontaneously broken resulting in a new light-mass boson (a pseudo-scalar particle), the axion [85, 86]. This particle fills the role of naturally relaxing the CP violation

parameter to zero. The name was first introduced by Wilczek, after a brand of detergent, because the problem with QCD had been finally "cleaned up." For a review of the strong *CP* problem, see [19].

The axion explains the very small limit of Θ_{QCD} by mediating a short-range spin-independent, mass-mass interaction between nucleons with a Yukawa-type potential, given by Eq. (1.6), with strength [41]

$$\begin{aligned} \alpha &= \left[\Theta_{QCD}\frac{m_a}{m_\pi}\frac{120\,\mathrm{MeV}}{f_\pi}\right]^2 \frac{m_u m_d}{(m_u+m_d)^2}\frac{\hbar c}{4\pi u^2 G} \\ &\approx \left[\left(\frac{\Theta_{QCD}}{10^{-10}}\right)\left(\frac{m_a c^2}{1\,\mathrm{meV}}\right)\right]^2 1.3\times 10^{-6}, \end{aligned} \tag{1.9}$$

and range

$$\lambda = \frac{\hbar c}{m_a c^2} \approx \left(\frac{1\,\mathrm{meV}}{m_a c^2}\right) 0.2\,\mathrm{mm}, \tag{1.10}$$

where $m_a \in [1\mu\mathrm{eV/c^2}, 10\,\mathrm{meV/c^2}]$ is the mass of the axion already constrained by astrophysical and laboratory bounds [25], m_π and f_π are the pion mass and decay constant, m_u and m_d are the masses of the up and down quarks, and u the atomic mass unit, respectively. It is also assumed that $m_u/m_d = 0.5$. The experimental limits on the neutron and mercury-atom electric dipole moment imply that $\Theta_{QCD} \leq 6\times 10^{-10}$ [66] and $\Theta_{QCD} \leq 1.5\times 10^{-10}$ [71], respectively.

1.1.3 Dark energy and the cosmological constant problem

The existence of the dark universe is also supported by standard inflation theory. Recent measurements indicate that the expansion of the universe is speeding up, rather than slowing down. This calls for the presence of a form of energy, "dark energy," whose gravity is repulsive and whose nature determines the destiny of our universe. The cosmological observations have shown that the universe is composed of 72% of dark energy, 24% of dark matter, and only 4% of regular matter [79]. The dark energy has a density of $\rho_d \approx 3.8\,\mathrm{keVcm^{-3}}$. This dark energy density corresponds to a distance $\lambda_d = (\hbar c/\rho_d)^{1/4} \approx 85\,\mu\mathrm{m}$ that may represent a fundamental length scale of gravity, and is so called the "dark energy scale". The discrepancy of 10^{60} between the predicted vacuum energy density and the observed gravitating vacuum

energy density is known as "the cosmological problem" and can be visualized as the discrepancy between the extreme flatness of the universe when compared to the extreme curvature expected from vacuum energy.

There have been extensive efforts to solve this problem, either by finding a mechanism that drastically reduces the quantum mechanical prediction for the vacuum energy density, or that reduce the gravitational coupling to the standard vacuum energy. Beane [5] pointed out that in any local effective quantum field theory, naturalness implies that new gravitational physics at length scales of about 1 mm would cutoff shorter distance contributions to the vacuum energy. In [80], Sundrum suggested that the cosmological constant problem can be solved if the graviton were a "fat" object with a size comparable to λ_d that would prevent it from seeing the short distance physics that dominates the vacuum energy. This would imply that the gravitational force would shut off for distances smaller than λ_d.

1.2 Measurements

The measurement of the ISL is performed by looking for violations of it. Depending on the theoretical model to be tested, different parameterizations are used to describe the exact dependence of the violation.

The main problem in testing the ISL at short length scales is the extreme weakness of gravity. This calls for designs that maximize the signal and minimize backgrounds and noise. To measure the ISL, it is necessary to have a source that provides the gravitational signal and a detector that detects the gravitational signal. Depending on the experiment components or the mode of operation, the experiments are classified into low frequency and high frequency. On the other hand, they group into resonance or off-resonance experiments. Finally, they can be divided into room-temperature or cryogenic experiments. The various designs have different advantages with respect to each other.

In this section I first describe several parameterizations used to test the ISL, then analyze the detector noise (present in all experiments) for the different types of

experiment, and end with a brief description of our experiment.

1.2.1 Parameterizations

Historically, the experimental tests used to set limits for the ISL were parameterized by

$$F(r) = G\frac{m_1 m_2}{r^{2+\epsilon}}. \tag{1.11}$$

This is not very well motivated since the exponent 2 reflects the fact that we live in a 3-dimensional world.

It is currently a much more common technique, to search for violations of the ISL by setting limits on an additional Yukawa term, as given by Eq. (1.6). The Yukawa potential comes from the interaction due to the exchange of a virtual boson with strength proportional to the coupling constant squared, and range $\lambda = \hbar/(m_b c)$ equal to the Compton wavelength of the exchange boson, where m_b is the boson mass. Eq. (1.6) is then a good description for boson mediated forces such as the ones described in Section 1.1. It also represents a good approximation to the expected effects of extra dimensions until the separation between the interacting masses becomes comparable to or smaller than the extra dimension.

A third parameterization includes power law modifications of the ISL in the form

$$V(r) = -G\frac{m_1 m_2}{r}\left[1 + \alpha_k \left(\frac{r_0}{r}\right)^{k-1}\right], \tag{1.12}$$

where r_0 is the scale associated with the new process and the α_k's are dimensionless constants. This type of potential can occur when two massless particles are exchanged. The type of particle depends on the order k. For example, $k = 2$ corresponds to the simultaneous exchange of two massless scalars, while $k = 5$ may be generated by the exchange of two massless axions or a massless neutrino-antineutrino pair. Depending on the theoretical model, different parameterizations are used.

1.2.2 Intrinsic noise of the detector

Independent of the type of detector, there will be two fundamental noise sources: the Brownian motion, or thermal noise and the amplifier noise. For a detailed discussion

of the intrinsic noise of our experiment, see Section 4.4. In addition, we can identify three modes of operation [55]:

- Below the resonance frequency f_0 of the detector, usually used with stiff spring experiments ($f \ll f_0$).
- At resonance ($f = f_0$).
- Above resonance, usually used for soft spring experiments ($f \gg f_0$).

The thermal motion noise in all three cases is, according to the Nyquist theorem,

$$S_T(f) \approx 4k_B T \frac{m\omega_0}{Q}, \tag{1.13}$$

where k_B is Boltzman's constant, T is the temperature, m is the mass of the detector, $\omega_0 = 2\pi f_0$ its (angular) resonance frequency, and Q is its mechanical quality factor. To reduce $S_T(f)$, we need a high quality factor, low resonance frequency, and low temperature.

The noise due to the amplifier is

- $(m\omega_0^2)^2(E_A(f)/\beta)$ for $f \ll f_0$
- $(m\omega_0^2/Q)^2(E_A(f)/\beta)$ for $f = f_0$
- $(m\omega^2)^2(E_A(f)/\beta)$ for $f \gg f_0$

where $E_A(f)$ is the equivalent noise energy of the amplifier, and β the energy coupling parameter. In this case, the best way of reducing the noise is to have a low-frequency resonance experiment with very high quality factors. Alternatively, if this is not possible, it is good to choose a low-frequency detector or perform the experiment at very low frequency.

1.2.3 Our experiment

At the University of Maryland, we perform a low frequency cryogenic experiment. To minimize the Newtonian error and maximize any potential mass-mass interaction, a

flat disk geometry is used for both the source and for the test masses. We use a near null source, a circular disk of large diameter-to-thickness ratio. Two test masses, also disk-shaped, are suspended on the two sides of the source mass. The source mass will be driven along the symmetry axis using superconducting coils. The violation signal will be measured by observing the differential displacement of the two test masses.

To reduce the thermal Brownian motion noise as well as the temperature noise of the instrument, the experiment is cooled to 1.7 K by pumping on liquid helium (LHe).

Our experiment is designed to use a nominal source-test mass spacing of 150 μm and a source drive amplitude of 87.5 μm. We look for Yukawa type violations of the ISL. The potential sensitivity of this experiment is $|\alpha| = 2 \times 10^{-3}$ at $\lambda = 150$ μm.

1.3 Current relevant ISL tests

Motivated largely by the possibility of observing compact extra dimensions, experimental searches for deviations from Newtonian gravity have improved in sensitivity by several orders of magnitude in the last few years. There have been a few review articles [1, 39], but they do not include the most recent and most sensitive tests.

In this section I will review the basic features of the experiments that impose the current limits on new physics between a few micrometers and a centimeter. For two centuries almost all the sensitive gravity experiments have been performed with torsion balances. This method is largely employed now as well. Depending on the parameterization, the experimental results are interpreted as exclusion plots in the $\alpha - \lambda$ parameter space for Eq. (1.6), or as constraints on the power law parameters α_k for $k = 2, 3, 4, 5$ for Eq. (1.12).

Figure 1.1 shows the existing limit of $|\alpha|$ for tests of the ISL at ranges below 1 cm, plotted as a function of the range λ. The lines represent violations predicted by the higher-dimensional string theory and the axion theory, respectively and the and the shaded part correspond to the region excluded by experiment.

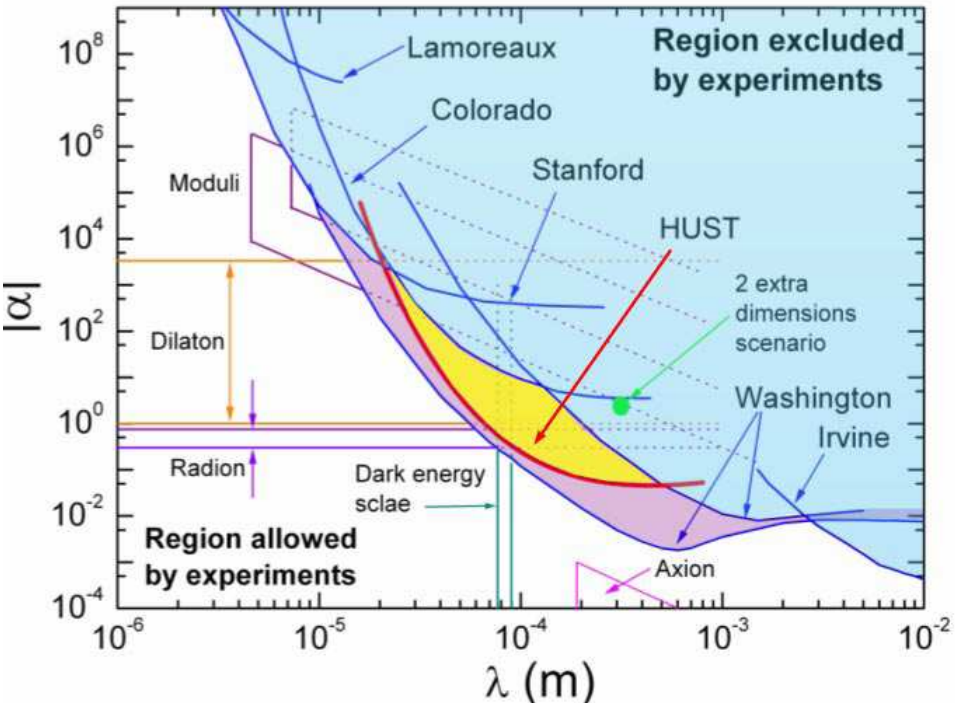

Figure 1.1: Constraints on Yukawa violations of the gravitational ISL. The lines labeled Lamoreaux [34], Washington [28, 27], Colorado [38], HUST [81], Washington [76], and Irvine [46] represent the limits by those respective groups. The shaded region is excluded by experiment. Reprinted figure with permission from L.-C. Tu, S.-G. Guan, J. Luo, C.-G. Shao, and L.-X. Liu, Phys. Rev. Lett. 98, 201101, 2007. Copyright 2007 by the American Physical Society.

1.3.1 The Washington experiment I

The University of Washington Eöt-Wash group developed a low-frequency torsion balance [28, 27] based on the "missing-mass" principle. Figure 1.2 shows the experiment. It consists of two principal parts, a torsion pendulum containing a detector made out of an aluminum (Al) ring with 10 equally spaced cylindrical holes and a copper (Cu) source with 10 similar holes that rotated uniformly by a geared-down motor about the vertical axis of the pendulum. In the absence of the holes, the disk would pull down on the ring, but the gravitational interaction between the holes of

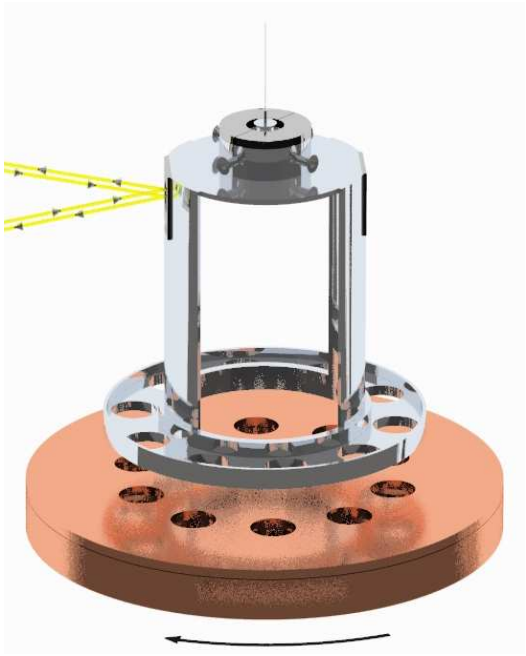

Figure 1.2: The University of Washington Eöt-Wash torsion pendulum and rotating source [28]. The vertical separation between source and the detector is not to scale and the shield is not shown. Reprinted figure with permission from E. G. Adelberger.

the detector and the source applied a torque

$$N(\phi) = -\frac{\partial V(\phi)}{\partial \phi}, \tag{1.14}$$

on the detectory, where $V(\phi)$ is the potential energy of the ring in the field of the disk when the holes from the disk are rotated by an angle ϕ with respect to the ones in the ring. $N(\phi)$ oscillated 10 times for each revolution of the source, giving torques at $10f$, $20f$, $30f$, etc., where f was the rotational frequency of the source. This torque twisted the pendulum and was measured by an autocollimator that reflected a laser beam twice from either of two plane mirrors mounted on the pendulum.

In order to cancel the gravitational interaction between the source and the detector, the authors used a second, thicker source disk, also made out of high-purity Cu, concentric and positioned below the first one. This disk also had 10 holes but was offset relative to the upper one by an angle equal to $\pi/10$. This second disk was designed so it would nearly cancel the torque, assuming that the ISL holds. It

would, however, allow the experiment to be sensitive to a violating interaction, parameterized by a Yukawa-type potential given by Eq. (1.6), as long as the range λ of the new force was less than the thickness of the upper disk. The cancelation was exact for a 2-mm separation between the lower surface of the pendulum and the top surface of the source disk. For smaller separations, the contribution of the lower disk was too small, while at larger separations, the lower disk contribution was too large.

The suspension system had several stages. The pendulum was suspended with a gold-coated 82 cm long and 20 μm in diameter tungsten (W) torsion fiber. Depending on the pendulum mass, its resonance frequency was 2.50 or 2.14 mHz. The torsion fiber hung from a passive damper, designed to minimize any damping of the torsional motion, while eliminating the swing, wobble, and guitar-string modes and was further attached to a computer controlled x-y-z-θ stage that allowed re-centering of the pendulum with respect to the source.

The electrostatic torques were minimized by using a very stiff, tightly stretched, 20-μm thick beryllium-cooper (Be-Cu) shield (not shown in the figure) between the source and the detector. In addition, the pendulum, mirrors, shield, and the top surface of the source were coated with gold (Au). The pendulum and shield were surrounded by a Au-plated Cu enclosure.

The Eöt-Wash group performed two separate experiments using source and detector thicknesses of approximately 2 and 3 mm, as well as different (missing) masses, and hole positions and sizes, but driving the source in both cases at approximately $f = f_0/17$, where f_0 was the resonance frequency of the torsion fiber. They calibrated the torque gravitationally by measuring the quadrupole moment between two small Al spheres inserted in opposite holes on the detector ring, and two larger bronze spheres rotated on a turntable outside the experiment. Over the two setups, they used vertical separations ranging between 137 μm and 10.77 mm. Since the test bodies were holes in a disk, however, the nominal distance between the test bodies was significantly larger. Their best sensitivity was achieved for $\lambda \approx 1.5$ mm, constraining $|\alpha| < 0.0079$ with a 95% confidence. They also constrained the maximum size of an extra dimension to $R < 160$ μm, and for the case of two extra dimensions,

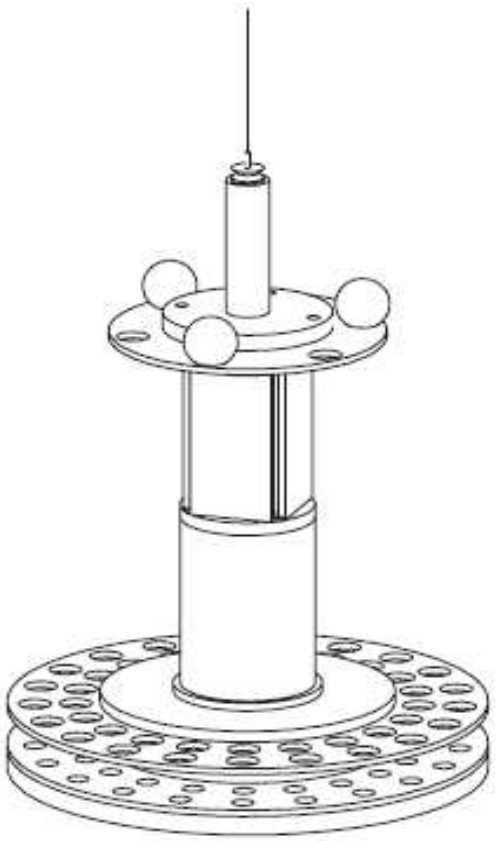

Figure 1.3: The second experiment of the Eöt-Wash group [31]. The purpose of the three spheres near the top of the detector was for continuous gravitational calibration. The four rectangular plane mirrors below the spheres are used to determine the torque twist. The electrical shield is not shown. Reprinted figure with permission from D. J. Kapner, T. S. Cook, E. G. Adelberger, J. H. Gundlach, B. R. Heckel, C. D. Hoyle, and H. E. Swanson, Phys. Rev. Lett. 98, 021101, 2007. Copyright 2007 by the American Physical Society.

imposed a lower bound on the unification mass $M_* \geq 1.7\,\mathrm{TeV/c^2}$.

1.3.2 The Washington experiment II

Using a second-generation low-frequency "missing-mass" torsion balance, Kapner *et al.* [31] of the Eöt-Wash group imposed the most sensitive limit between 10 μm and 4 mm. The principle is very much the same as the Washington Experiment I, except

for several improvements. Figure 1.3 shows a schematic view of the experiment. A torsion pendulum, suspended by a thin, 80-cm long W fiber contained the detector, a 0.997-mm thick molybdenum (Mo) ring, while the source mass, a 0.997-mm thick Mo disc, rotated uniformly by a geared-down motor. Note that the thickness of the source and detector were significantly reduced to half or a third as compared to the previous experiments. This allowed, using the same nominal separation between surfaces, the achievement of a shorter range experiment. On the other hand, in order not to reduce the magnitude of the signal, the product of the densities was increased by a factor of 4.5.

The test bodies were 42 holes machined in the detector and the source. The hole centers were arranged in two circles with 21-fold azimuthal symmetry. The relative size of the source and detector holes was optimized to increase the torque from a short-range interaction while reducing the Newtonian torque significantly. In this case, the detector oscillated 21 times for each revolution of the source, giving torques at $21f$, $42f$, $63f$, etc., where f was the rotational frequency of the source. This torque twisted the pendulum and was measured by an autocollimator that reflected a laser beam from either of four plane mirrors mounted on the pendulum. The performance of the autocollimator was improved as well.

To cancel the gravitational interaction between the source and the detector, a second, compensating thicker tantalum (Ta) disk with 21 holes was positioned below the source, such that the center of the holes were displaced by an angle equal to 360/42 degrees with respect to the ones on the source. Just like before, this second disk would nearly cancel the torque if the ISL holds. It would, however, be sensitive to a violating interaction, parameterized by a Yukawa-type potential given by Eq. (1.6), as long as λ was less than the thickness of the source. By having thinner active components and more holes, the cancelation of the Newtonian signal in this experiment was achieved to a higher degree.

The electromagnetic torques were minimized by coating the detector with Au and surrounding it by a Cu housing with small holes for the suspension fiber and the autocollimator beam and a tightly stretched 10-μm thick Be-Cu shield with

fundamental frequency of 1.6 kHz. Note that the shield was thinner than before. This contributed to reducing the source-detector spacing.

The suspension system was similar to that of Experiment I, but in this case, the authors added a more sophisticated 5-point torsion filter that removed effects of slow drifts in the equilibrium twist of the torsion pendulum. For calibration, they continuously measured the gravitational octupole interaction between three small spheres, mounted on the detector, and three larger spheres, mounted outside the vacuum on a turntable that rotated at a steady rate f_c. The entire system was held under a 10^{-6} torr vacuum in a temperature controlled and magnetically shielded environment.

The Eöt-Wash group performed three separate experiments using different thicknesses for the Ta compensating disc in order to discriminate against systematic errors. In addition, they used different suspension fibers and rotation frequencies. In the first experiment, they used a source frequency $f = f_0/28$ and a calibration frequency $f_c = 49f/3$, where $f_0/2\pi \approx 2$ mHz was the resonance frequency of the 20-μm in diameter torsion fiber. In the second experiment, they replaced the torsion fiber with one of 17-μm diameter with $f_0/2\pi \approx 1.54$ mHz and used $f = f_0/7.5$ and $f_c = 6f$. In their final experiment, they returned to the first fiber and used $f = f_0/7.5$, and $f_c = 3f$. In the three experiments the authors used vertical separations ranging between 55 μm and 9.53 mm. Their best sensitivity was achieved for $\lambda \approx 600$ μm, constraining $|\alpha| < 0.0037$ at the 95 % confidence level. They further constrained the gravitational-strength ($|\alpha| = 1$) Yukawa interaction to $\lambda < 56$ μm. They also constrained the maximum size of an extra dimension to $R < 44$ μm; in the case of two extra dimensions of the same size, they imposed a lower bound on the unification mass $M_* \geq 3.2\,\mathrm{TeV/c^2}$.

1.3.3 The HUST experiment

The Huazhong University of Science and Technology (HUST) group [81] also used a low-frequency torsion pendulum. Figure 1.4 represents a schematic top view of the experimental setup. It can be seen that their experiment was not symmetric. On

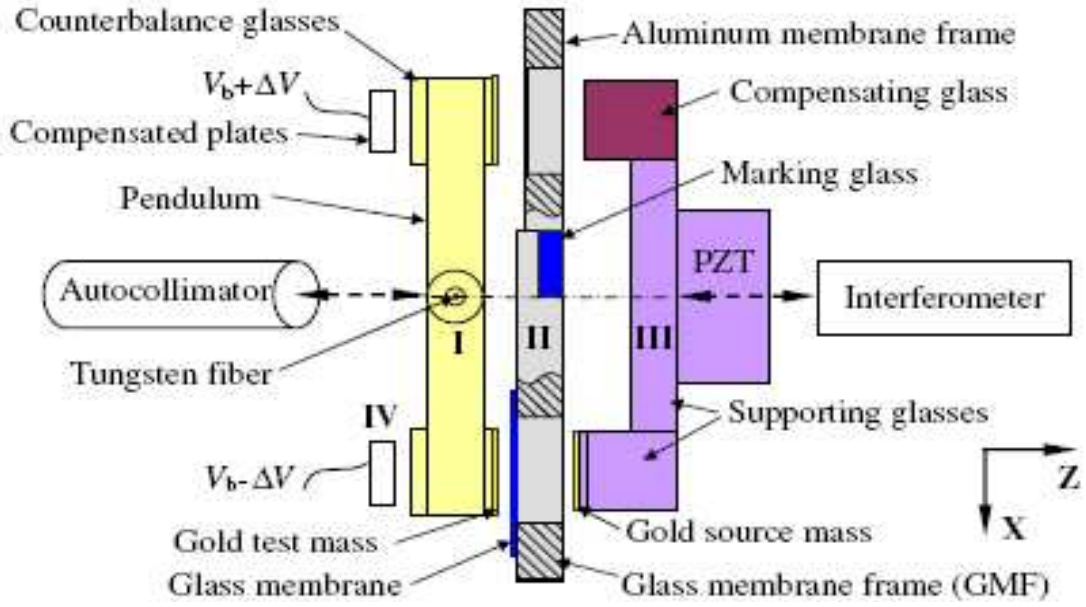

Figure 1.4: Schematic top view of the HUST experiment [81]. The four separate parts are labeled as follows: I is the pendulum, II is the membrane frames, III is the source mass platform, and IV the electrostatic compensating plates. III was fixed on an x-z translation stage (not shown) and then on a PZT. The pendulum twist and source mass movement were monitored by a two-axis autocollimator and a Michelson interferometer, respectively. Source mass motion was in the z direction. Reprinted figure with permission from L.-C. Tu, S.-G. Guan, J. Luo, C.-G. Shao, and L.-X. Liu, Phys. Rev. Lett. 98, 201101, 2007. Copyright 2007 by the American Physical Society.

one side (bottom of the page), it had the test mass and source mass, while on the other (top of the page), it had compensating masses. The full structure contained four separate parts: (I) the pendulum, (II) the membrane frame, (III) the source mass platform, and (IV) the electrostatic compensating plates.

The pendulum (I) consisted of five rectangular glass blocks: the main block, body of the pendulum, and four smaller blocks that protruded from the main block, two facing the inside of the experiment and two facing the outside. The test mass, machined out of Au, was attached to one of the inner blocks. The other inner block had an attached weight as a counterbalance, while the two outer blocks were made

the appropriate size to restore the pendulum symmetry about the suspension point. All the pendulum parts were connected with optical adhesive that solidified under ultraviolet light. To minimize variations in the electrostatic potential, the surface of the pendulum was coated with Au. The pendulum was suspended by an annealed W fiber that had a resonance frequency of 1.81 mHz. The upper end of the fiber was attached to the Cu disk of a magnetic damper system, used to suppress the simple pendulum motion. The Cu disk was then suspended by an annealed W pre-hanger fiber attached to a x-y-z stage on the top of the vacuum. The pendulum twist was monitored by a two-axis autocollimator.

The source mass platform (III), also Au-coated, was made out of three main parts: the source mass, a gravitationally compensating glass block, and supporting glass. The source mass block was made out of pure Au and was attached to a protruding glass block of the same surface area. The compensating glass was designed to null the Newtonian gravitational torque from the source platform for a nominal gap of 250 μm between the source and the test masses. Since the compensating block was at a much larger separation as compared to the source mass, the non-Newtonian gravitational effects could not be reduced with this block. The supporting glass block connected these two parts together and to a piezoelectric translator (PZT) that moved the platform in the z direction. The movement of the source mass was monitored by an interferometer.

The two Au-coated membrane frames (II) were used to further reduce the electrostatic interaction between the source and the test mass. On the source-test mass side, there was a glass membrane frame (GMF) with a hole covered by a 56-μm thick Au-plated membrane used to encase the source mass. On the other side, an Al membrane frame encased the compensating glass mass and receded from the pendulum as compared to the GMF. The source mass platform and PZT were attached to an x-z translation stage. The x-y translation stage of the source platform, and the membrane frames, were fixed on an Al base and mounted to a six degrees of freedom stage.

The compensating plates (IV) were used to keep the W fiber untwisted by apply-

ing different voltages $V_- = V_b - \Delta V$ and $V_+ = V_b + \Delta V$, where V_b was a bias voltage. Then, ΔV was a measure of the torques generated by the masses interactions.

The experiment was inside a vacuum of 10^{-5} Pa. For calibration purposes, a Cu cylinder, mounted on a turntable outside the vacuum, was continuously rotated with a frequency of $f_c = 0.556$ mHz. The PZT was driven continuously by applying a trapezoidal wave voltage, at a frequency of 0.463 Hz with a total displacement of the source of (165 ± 3) μm.

The HUST group probed the ISL for source to test mass separations between 176 and 341 μm and obtained their best sensitivity $|\alpha| < 0.047$ for $\lambda \approx 260$ μm at the 95 % confidence level. They also constrained the maximum size of an extra dimension to $R < 53$ μm, and for the case of two extra dimensions, imposed a lower bound on the unification mass of $M_* \geq 2.8\,\mathrm{TeV/c^2}$.

1.3.4 The Colorado experiment

Long *et al.* at the University of Colorado [38] performed a high-frequency, resonance, torsion balance experiment. Their experiment, shown in Figure 1.5, used a planar geometry for the source and detector in order to concentrate as much mass as possible on the length scale of interest. In addition, the planar geometry was approximately null with respect to inverse-square forces, a key feature in the search for new forces. The source mass was a small, 305-μm thick W cantilever, or "diving board." It was driven vertically at 1 kHz, its second cantilever mode by a PZT. This frequency was carefully matched to the frequency of a normal mode of the detector. The detector was a 195-μm W double torsional oscillator made out of two coplanar rectangles joined by a short segment along their central axis. In the resonant mode of interest, the fifth mode, the two rectangles counter-rotated about the torsional axis, with the smaller rectangle having a larger amplitude.

Electrostatic and acoustic backgrounds were suppressed with a stiff conducting shield between the source and the detector. The shield was a 60-μm thick sapphire plate coated with 100 nm of Au. The shield, source, and detector were mounted on separate vibration isolation stacks to minimize any mechanical coupling. The

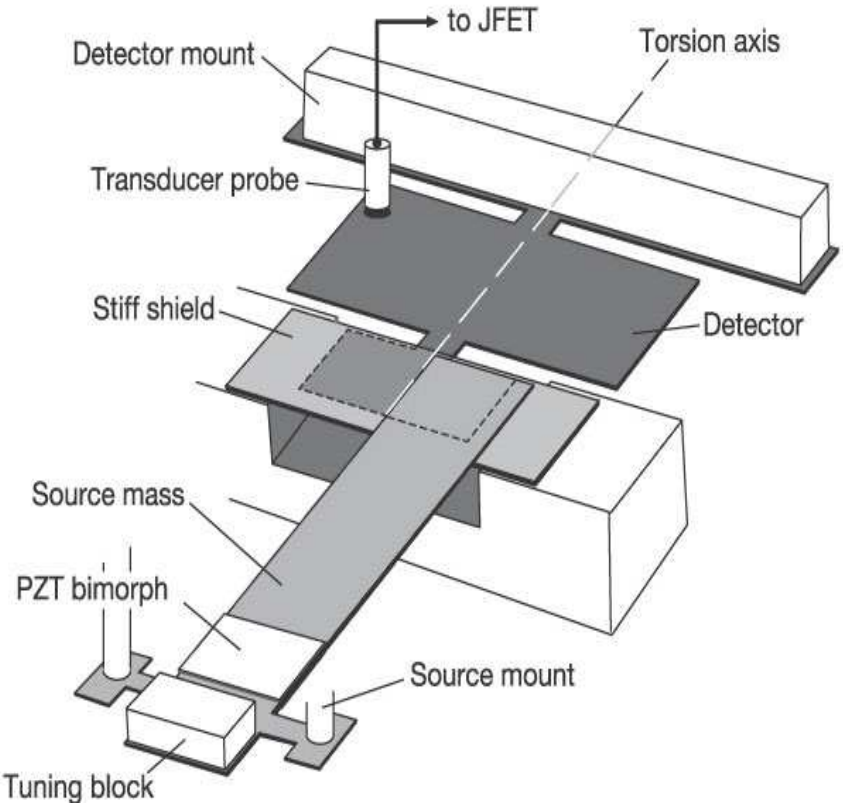

Figure 1.5: Schematic diagram of the instrument used by the University of Colorado group showing the source, detector, and stiff conducting shield positioned in between them. A transducer probe was used to measure the oscillations of the detector. Reprinted by permission from Macmillan Publishers Ltd: [Nature] (J. C. Long, H. W. Chan, A. B. Churnside, E. A. Gulibs, M. C. Varney, and J. C. Price reference citation, Nature 421, 2003, 922 [38]), copyright (2003).

alignment and relative position was achieved by displacing the different parts and measuring the points of mechanical contact.

The source was positioned, above and parallel to the detector plane, so that the front edge of the source mass was aligned with the back edge of the smaller rectangle, and the side edge was aligned with the detector's torsion axis. The source was driven to an amplitude of 19 μm with a PZT bimorph. The oscillations of the detector were read out with a capacitive transducer, a brass cylinder positioned 0.1 mm above the rear corner of the large rectangle of the detector.

The whole assembly was placed inside a 75-liter vacuum bell jar and pumped continuously to 2×10^{-7} torr. The temperature was maintained at (305.0 ± 0.1) K using a silicon (Si) diode sensor and a resistive heating element. The experiment was limited by thermal noise due to dissipation in the detector mass. In order to reduce this dissipation, the Colorado team annealed the detector mass at 1300°C, achieving $Q = 2.55 \times 10^4$.

In order to know the precise form of the signal, the authors provisionally removed the electrostatic shield and applied a 1.5-V bias to the detector. This provided a large attractive electrostatic force. Measuring that force and its phase gave a prediction of what to expect from new physics signals.

Long *et al.* tested the ISL at a source-to-test-mass separation of 108 μm and obtained $|\alpha| < 5.6 \times 10^3$ for $\lambda \approx 20$ μm at the 95% confidence level. They also excluded most of the gluon and strange moduli forces and constrained the limit on the dilaton range, for $\alpha = 2 \times 10^3$ to $\lambda = 23$ μm, which corresponds to a dilaton mass $m_d \geq 8.6\,\mathrm{meV/c^2}$.

1.3.5 The Stanford experiment

The Stanford University group developed a micro-cantilever resonance experiment to probe the 10-μm range using scanning force microscopy and micro-fabrication techniques [16, 76]. Figure 1.6 shows a schematic view of their apparatus. The test mass, a Au prism $50 \times 50 \times 30$ μm in size and 1.4 μg in mass, was attached to a micro-cantilever with a thin layer of epoxy. The micro-cantilever was a 0.335-μm

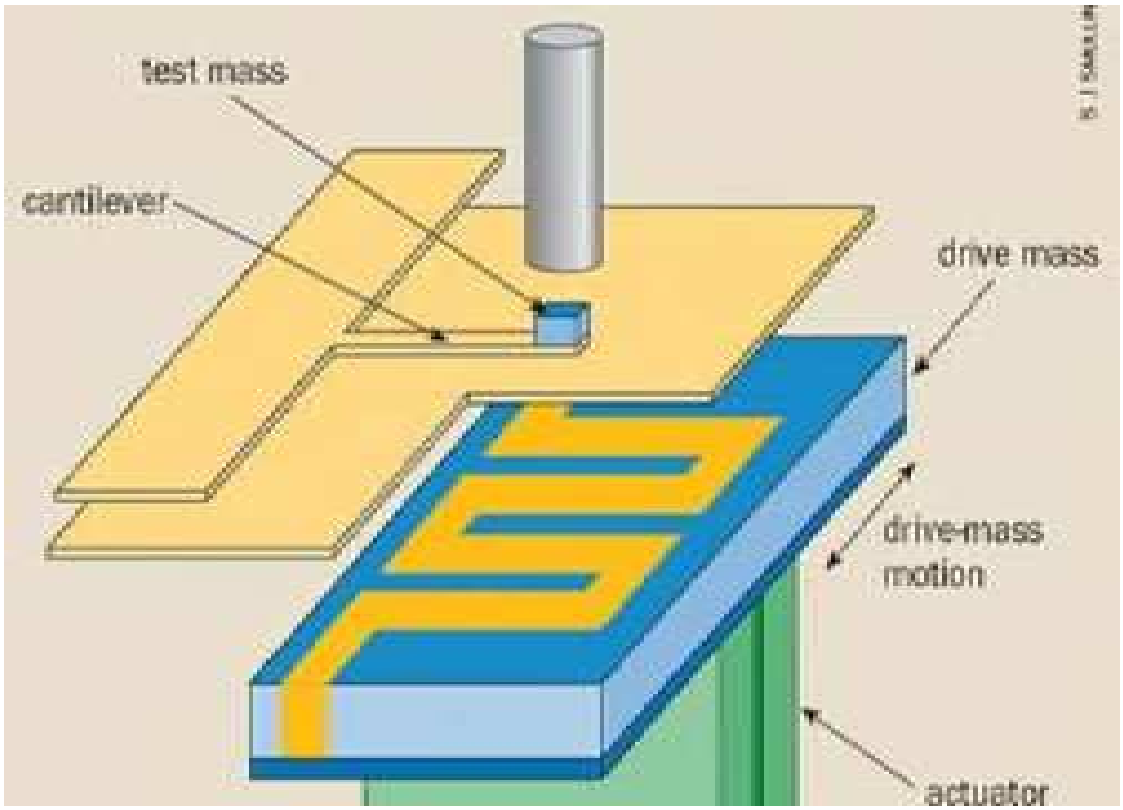

Figure 1.6: Schematic diagram of the Stanford University group experiment [76] showing the source mass, the cantilever that holds the Ag test mass, and a gold-coated silicon nitride (Si_3N_4) shield membrane that separates the masses. Reprinted figure with permission from S. J. Smullin, A. A. Geraci, D. M. Weld, J. Chiaverini, S. Holmes, and A. Kapitulnik, Phys. Rev. D 72, 122001, 2005. Copyright 2005 by the American Physical Society.

thick, single-crystal, Si diving-board-shaped oscillator with a quality factor in the $10^3 - 10^5$ range and the resonance frequency of its lowest mode of the cantilever at about 7000 Hz. This frequency was shifted to about 300 Hz once the test mass was attached. The source mass consisted of five pairs of alternating strips of Au and Si, each 100 μm wide. In the first experiment, the authors had the surface of the Au and Si exposed, but, as an improvement, in their second-generation experiment, they had the source covered with a 2-μm thick Si layer, followed by an aluminium oxide (Al_2O_3)(for electrical insulation), and finalized with a 100-nm layer of Au.

The source mass was driven horizontally, below the plane of the detector, in

the direction perpendicular to the alternating strips. This drive was performed by attaching the source to a piezoelectric bimorph actuator. The actuator motion was measured capacitively. The actuator drive frequency was tuned to one third of the cantilever resonance frequency, and its amplitude of motion was (98 ± 7) μm. The particular frequency was chosen so that it would be below the resonance of the bimorph. Because of the geometry of the source mass and the amplitude of the oscillation, any gravitational coupling between the masses would create a force on the cantilever at harmonics of the drive frequency including the cantilever resonance frequency. The relative position between the test mass and the source mass was determined using a capacitive positioning sensor. The motion of the cantilever on resonance was measured using an optical-fiber interferometer.

By having the source oscillate perpendicular to the strips, the vibration coupling was minimized. In addition, two mass-spring vibration isolation stages with resonant frequencies of $\sim$ 2 Hz separated the cantilever mount from the actuator mount, achieving an attenuation of about eight orders of magnitude at 300 Hz.

An electrostatic shield, fabricated from a 3-μm thick Si_3N_4 membrane covered with a 100-nm Au plating on both sides, was placed between the source and the detector. The shield was attached to the base of the cantilever mount, 15 μm below the detector mass.

To test the system, in the first experiment, the test mass had a 100-nm layer of nickel (Ni). By sending current through the Au of the source, the two masses were coupled magnetically. This technique was used for alignment as well. In the second experiment, there were two sets of test masses, pure Au, non-magnetic ones, and magnetic, like the one in the first experiment.

With a quality factor of about 1200, the limiting background for this experiment was expected to be the thermal noise of the cantilever. To reduce this noise, the experiment was inserted in a LHe dewar and operated at temperatures in the 9-11 K range and pressures of 10^{-4} torr. Nevertheless, in the first experiment, the limiting background was about 10 times larger than the expected thermal noise for an integration time of a few thousand seconds. The phase and magnitude of the

observed signal as a function of the source-to-test-mass separation were not consistent with a mass-coupled force generated by the source mass. The most likely source of this deceptive force was identified as electrostatic. A difference in potential of about 0.3 V between the shield and the detector were sufficient to produce the observed force.

As mentioned above, the second experiment had significant design improvements. To facilitate the data-acquisition process while maintaining the low thermal noise of the high quality factor cantilever, Smullin *et al.* [76] used feedback cooling. In addition, they performed a much more detailed data analysis. With all this, the second-generation experiment showed significantly improved results, especially at the largest separation.

The Stanford University team tested the ISL for source-to-test-mass separations as small as 25 μm, obtaining the most stringent test in the range 6-20 μm at the time of the experiment. They obtained their shortest distance limit of $|\alpha| \approx 10^8$ for $\lambda \approx 4$ μm at the 95 % confidence level and excluded most of the parameter space expected from moduli exchange.

1.4 Summary and organization

In this chapter, I reviewed the theoretical motivations that inspired the short distance ISL test focusing on some of the greatest puzzles in physics, namely, dark matter and energy, the hierarchy problem, and the cosmological constant problem. I included a wide range of theoretical developments suggesting that new phenomena may occur in a region accessible by our experiment and would allow us to test some of these puzzles. In addition, I gave an overview of the current status of the experimental tests in the range between a few micrometers and a millimeter.

This thesis is organized as follows: In Chapter 2, I provide an in-depth overview of the design of the ISL experiment, focusing first on the principle of the experiment and following with a description of the experimental hardware, the building process, and the circuitry. In Chapter 3, I study the dynamics of the ISL experiment. I

include a Lagrangian formulation of the system and follow with a detailed analysis of the circuits and a description of the motion of the different components of the experiment. Then, in Chapter 4, I provide a detailed error model in which I discuss the metrology errors, random errors, and possible systematic error. In Chapter 5, I illustrate the cool-down and calibration procedure of the experiment, including all the necessary tests to verify the experiment is operational. Chapter 6 contains the actual data of the experiment and the data analysis. I perform a comprehensive analysis of the error and identify the experimental challenges. Finally, Chapter 7 is dedicated to a detailed examination of the problems and a solution of how to improve the design of the experiment, as well as the conclusions.

Three appendixes are also included. They contain, in Appendix A, much more detailed calculations on the superconducting coils and, in Appendix B, the source metrology. Appendix C gives a history of all the cool-downs, tests, problems, and improvements.

Chapter 2

Design and Construction of the Inverse-Square Law Experiment

2.1 Principle of the experiment

The ISL experiment employs a Newtonian null source and a superconducting differential accelerometer as the detector. In this section, I will start by discussing null sources and null detectors and identify the choice for the experiment, then delve into the principle of a superconducting accelerometer and a differential superconducting accelerometer. Next, I will proceed with second-harmonic detection and finish with the expected signal.

2.1.1 Newtonian null source

An experiment designed to test the ISL usually has a source mass and a detector. It is advantageous to place precision requirements either on the source mass or on the detector, as opposed to both. If an experiment uses a source that produces a constant or null gravitational field, such a source is a null source and the requirement for metrological precision falls on the source. Examples of null sources include but are not limited to the infinite plane, the spherical shell, and the infinite cylindrical shell.

If, on the other hand, an experiment is performed using a null detector, one that is insensitive to a Newtonian gravitational field, the requirement for metrological

precision falls on the detector. As pointed out in [52], an example of a null detector is a Laplacian detector, one that measures the Laplacian of the Newtonian potential. The Laplacian of the Newtonian potential ϕ is calculated from the sum of the three diagonal components of the gravity gradient tensor Γ_{ii}

$$\nabla^2\phi = -\sum_i \Gamma_{ii} = 4\pi\rho, \tag{2.1}$$

where ρ is the local mass density. The output of the Laplacian detector depends only on the local mass density and is independent of the mass distribution in the rest of the universe. In [44, 58], a three-axis gravity gradiometer was used as a null detector to measure the three diagonal components of the gravity gradient tensor simultaneously. Choosing a source mass located on the outside, the output sum of the three axes must remain constant as a source mass is moved.

In the present experiment, in order to minimize the Newtonian error and maximize any potential mass-mass interaction, a flat disk geometry is used for both the source and for the test masses. Figure 2.1 illustrates the configuration of the source and test masses with their associated coils (the axial dimensions are not to scale). The unlabeled coils are the returns of the labeled ones. The source mass, located in the middle, is a circular disk of large diameter-to-thickness ratio and it approximates an infinite plane slab, a Newtonian null source. Two disk-shaped test masses are suspended on the two sides of the source mass at a distance of 150 μm and are coupled magnetically to form a differential accelerometer.

2.1.2 Superconducting differential accelerometer

A local gravity measurement is unable to distinguish between gravitational acceleration and the acceleration of the reference frame due to the Equivalence Principle. A non-local measurement can be made using a superconducting differential accelerometer, also known as a gravity gradiometer. The differential accelerometer measures gravitational force gradients. It is made by combining two accelerometers sensitive to acceleration along the same axis, but displaced with respect to each other along

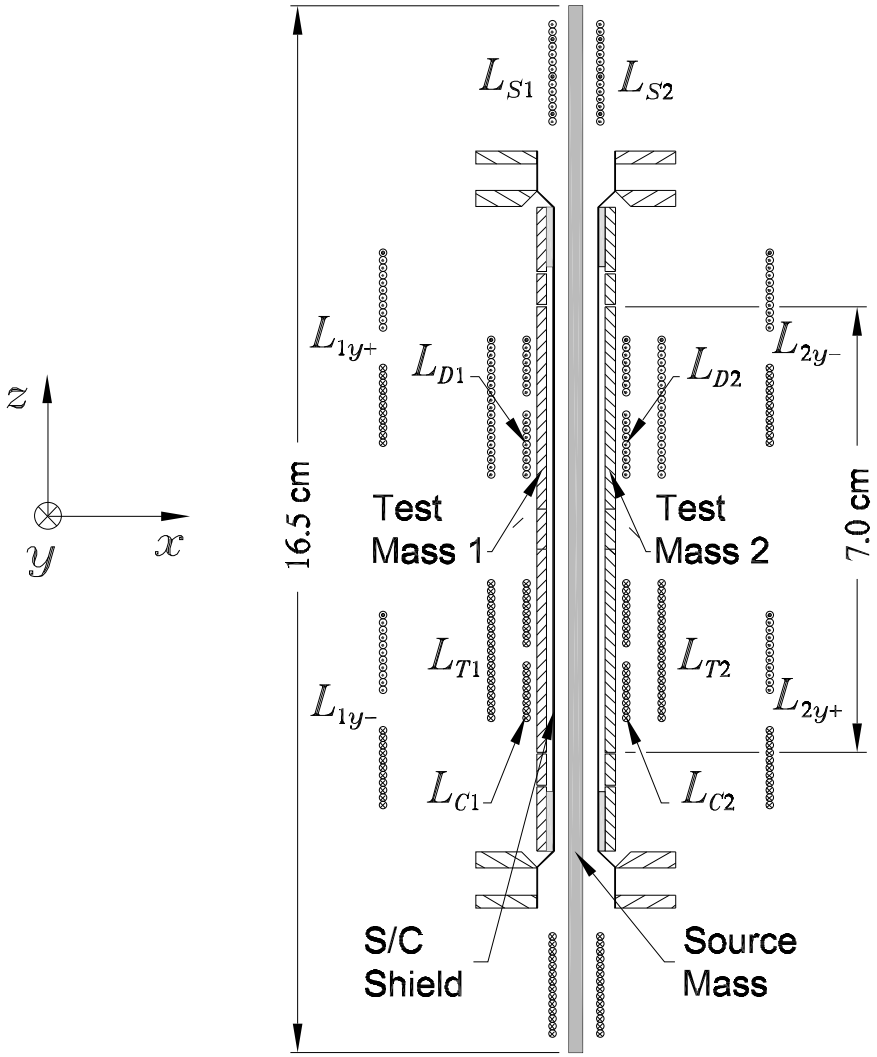

Figure 2.1: Configuration of the source and test masses with associated coils.

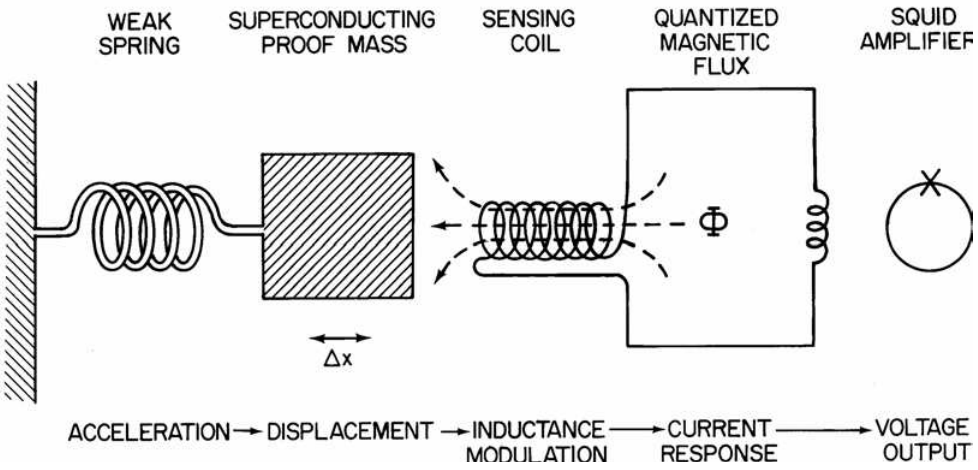

Figure 2.2: Principle of a superconducting linear accelerometer. Reprinted figure with permission from H. A. Chan, M. V. Moody, and H. J. Paik, Phys. Rev. D 35, 3551, 1987. Copyright 1987 by the American Physical Society.

that axis.

The principle of the superconducting accelerometer is illustrated in Figure 2.2. For a detailed review, see [53, 54]. A test mass is suspended by a spring in close proximity to a superconducting sensing coil. The sensing coil is connected to an output coil in a superconducting loop. Both coils are mounted rigidly. A persistent current is stored in the loop. The test mass is also made out of a superconducting material and excludes any magnetic field through the Meissner effect [49]. As the mass moves, the inductance of the sensing coil is modulated. Due to flux quantization, the total flux through a complete superconducting loop is conserved. Therefore, the change of the magnetic flux through the sensing coil is always complemented by an equal and opposite change in magnetic flux through the output coil in the superconducting loop. By coupling the output coil to a SQUID (Superconducting Quantum Interference Device), the change in current is amplified and converted to an output voltage, which is proportional to the test mass displacement.

The superconducting differential accelerometer is made by connecting the sensing coils of two superconducting accelerometers that share the same SQUID input coil. Proper polarity is chosen in the stored currents of the various loops so that a common acceleration applied to the two accelerometer test masses produces no net effect on

the current in the output inductor.

2.1.3 Second-harmonic detection

As the source mass is driven at frequency f_S along the symmetry axis, the first-order Newtonian fields arising from the finite diameter of the source mass are canceled upon differential measurement, leaving only a second-order error at $2f_S$. This can be understood by visualizing the differential signal. For instance, let the coordinate axis $\vec{x}$ be the symmetry axis of the source mass. As the source moves in the $-\hat{x}$ direction, the force felt by the test mass located on the left will be larger and positive. As the source moves to the right, the force felt by the test mass on the right will be dominant and negative. The difference between those will then be maximum when the source mass is at its peak positions, which produces a second-harmonic response of the source motion. For the same reason, the Yukawa signal also appears at $2f_S$. The second-harmonic detection, combined with the common mode rejection ratio (CMRR) of the detector, reduces the source-detector vibration coupling by over 200 dB.

2.1.4 Expected signal

The differential acceleration signals expected from the Yukawa force, Eq. (1.6) with $|\alpha| = 10^{-3}$ and $\lambda = 150\,\mu$m, are plotted in Figure 2.3 as a function of the source mass position. Note that the source mass is not infinite. Consequently, there will be a small nonzero correction due to the finite diameter of the source mass. This effect is very small due to the proximity between the source mass and the detector. The small Newtonian term arising from the finite source mass diameter is also shown; the source mass really looks like an infinite plane slab to the test mass due to its proximity. The Yukawa signal is almost purely second harmonic to the source motion. Its rms amplitude, corresponding to a $\pm 87\,\mu$m displacement, is 2.6×10^{-14} m s^{-2}.

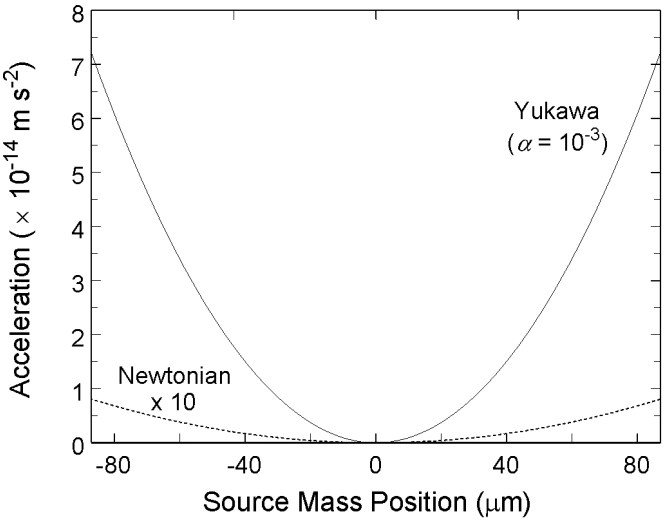

Figure 2.3: Newtonian and Yukawa signals versus source position.

2.2 Experimental hardware

Most of the time of my dissertation work I spent building, testing, and fixing the current experiment, originally designed by Paik and Moody [59, 60] with the help of Cao. In this section, I will describe the building stage of the experimental hardware and include the improvements and modifications to make it operational. I begin with a brief overview of the apparatus and then follow with details on each part. I also include an overview of the modifications to the heat-treatment system, which was necessary to accommodate the significantly larger parts of the current experiment.

2.2.1 Overview of the apparatus

Figure 2.4 shows an expanded view of the whole assembly, which consists of two housings, a source mass, two test masses, two superconducting shields, and superconducting coils and transformers. To eliminate differential contraction and provide a good electromagnetic shielding, the entire housing is fabricated from niobium (Nb). The source mass is made out of Ta, which closely matches Nb in thermal contraction. It is suspended by cantilever springs and driven magnetically with two source coils. The rim of the source mass is bolted inside the two housings using titanium (Ti) screws. Ti also has a closely matched thermal expansion coefficient to that of Nb.

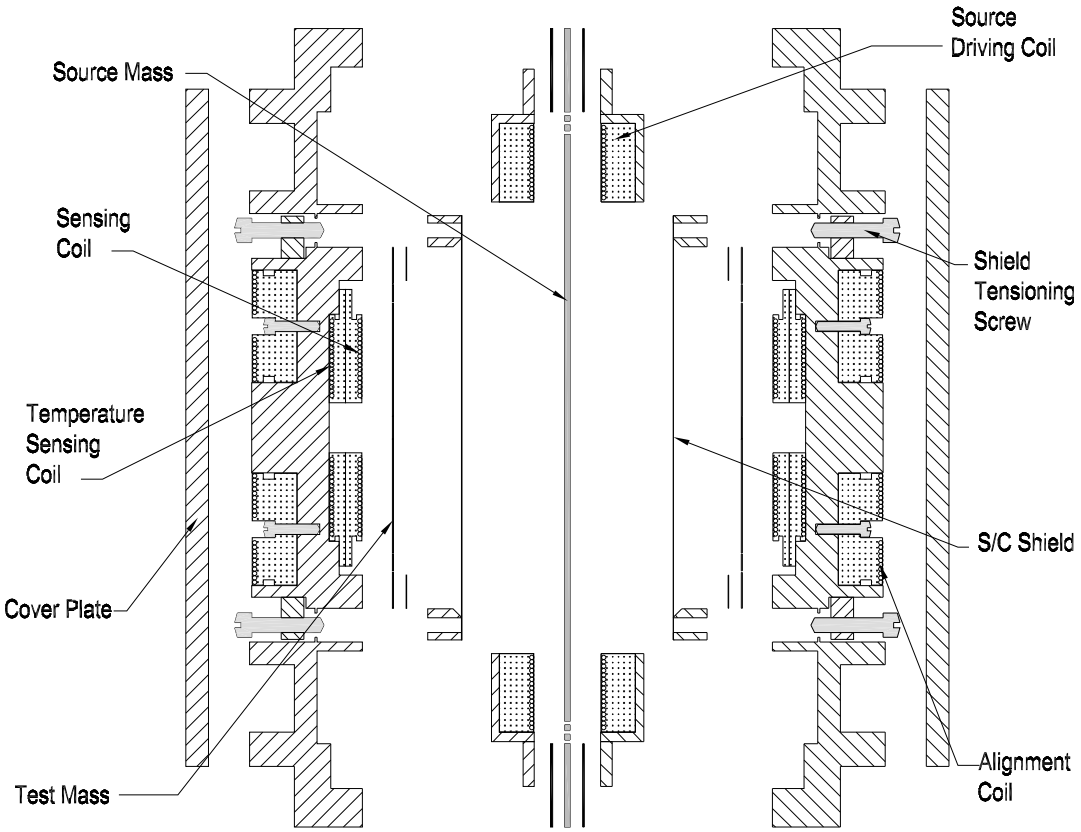

Figure 2.4: Expanded cross-section of the experiment.

The spacing between the source and the housings is adjusted by adding precision machined spacers between them.

The inside of the center block of each housing has a cavity containing two Nb coils, a temperature sensing coil that faces the Nb housing and a sensing coil that faces one of the test masses. The coils are positioned back-to-back and separated from each other with a Nb foil in order to reduce magnetic cross-coupling. They are attached to the housing with Nb screws. The test masses are also made out of Ta and suspended by cantilever springs. They are attached to the housing using GE varnish. On top of the test masses are test mass spacers, GE varnished to the test masses. A thin Nb sheet, made by diffusion-bonding a 12.5-μm thick Nb foil to a Nb rim, separates the test masses from the source, providing electrostatic and magnetic shielding between them. The shield is stretched tight by pulling its rim

with tensioning screws.

The outer side of each housing has four cavities in its center part containing Nb alignment coils, additional cavities for transformers and four pockets for the superconducting joints, and heat-switches. The alignment coils face the Nb housing cover.

Finally, on the outside of the cover, Nb shaker coils are mounted. Since the experimental assembly has finite mass, as the source mass is driven, there will be a reaction force on the assembly, displacing it in the opposite direction. By sending the appropriate currents through the shaker coils, it will be possible to cancel the recoil of the platform in response to source mass motion, as well as to shake the experiment for calibration purposes. Figure 2.5 shows the assembled experiment, integrated to the cryostat.

The orientation of the experiment can be visualized in Figure 2.1. The sensitive axis $\hat{n}$, the axis along which the source and test masses displace, is aligned with the $\hat{x}$ axis. Calling the housings housing 1 and housing 2, $\hat{x}$ points from 1 to 2. The $\hat{z}$ axis lies along the vertical, pointing up, so that when the experiment is not being tilted, $\vec{g} = -g\hat{z}$. The source and test masses are located in the y-z plane. For calibration purposes, the experiment can be tilted about the $\hat{y}$ axis. In this case, a component of gravity will be along $\hat{x}$. Alternatively, if the two test masses are not concentric, or parallel to each other, this tilt, as well as the tilt about the $\hat{x}$ axis will induce a response in the accelerometer that will alow a direct measure of those quantities.

2.2.2 Heat-treatment system

The heat-treatment system was initially constructed to improve the electrical and mechanical properties of Nb pieces and achieve high quality factors [22]. It uses a resistive heating element made out of two vertical Nb rods connected to each other with six horizontal strips of Nb foil bent in a hexagonal shape, held together with six thin Nb vertical slabs at the vertices. A current is sent from one Nb rod, flows through the six foils, and then returns through the other rod. The heating element has a room-temperature resistance of $0.017\,\Omega$, which becomes $0.07\,\Omega$ at 1600°C and is

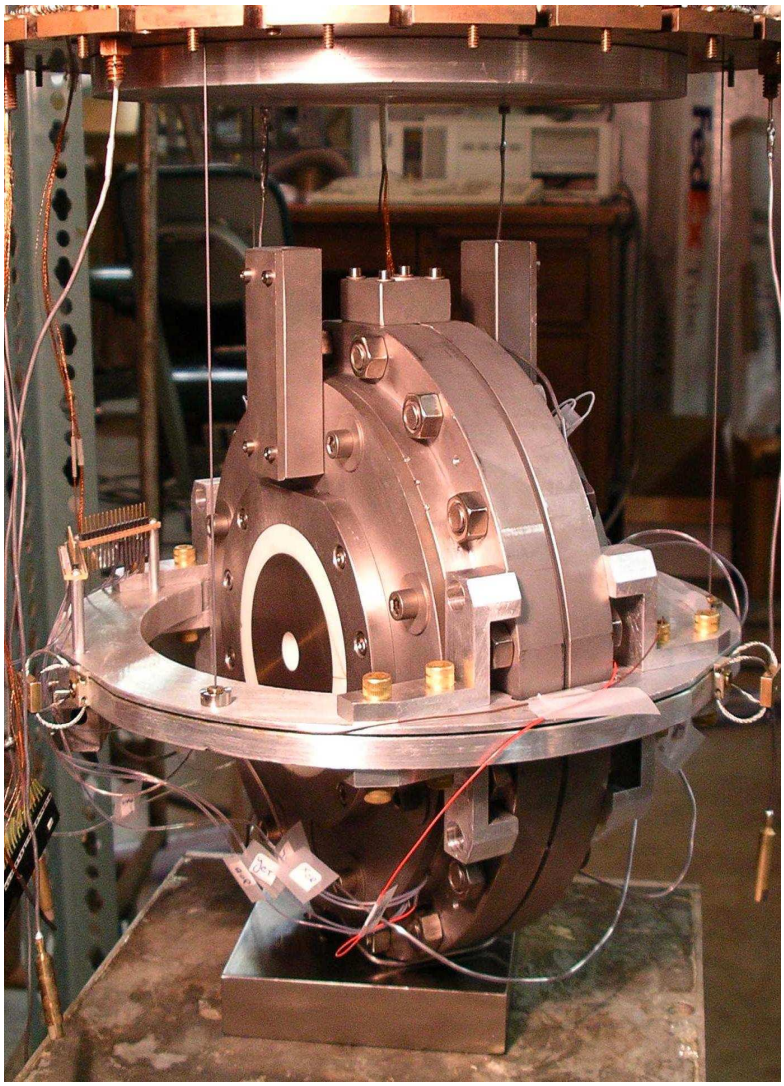

Figure 2.5: Assembled experiment.

designed to approach the impedance of the power supply used for the heat-treatment (maximum output of 40 V and 400 A). It encloses a heating space of cylindrical shape with a base diameter of about 17 cm and is surrounded by five radiation shields. All the components are placed inside an Al vacuum chamber with double walls that allow sending cold water through its bell jar jacket.

A new Nb hot zone with larger inner dimensions had to be constructed for the oven to accommodate the 22.9-cm diameter housings and source mass. The new heating element has a different design to accommodate the new heating volume and has a room-temperature resistance of $0.025\,\Omega$. A horizontal semicircular piece of Nb is attached to the top of each of the vertical Nb rods and holds five equidistant vertical Nb foils. The ten foils are connected at the bottom to a circular Nb slab that does not touch the rods. The slabs are held to the rods using Nb screws, while the foils are spot-welded to the slabs. A current is sent from one Nb rod, flows down through five of the foils, then up through the other five, and returns through the second rod.

Unfortunately, since we wanted to keep the same vacuum can, the new heating element can be used only by reducing the number of radiation shields, in this case to three. This limits the maximum operational temperature as follows: At the highest temperatures, the heat is transferred mostly by radiation. The radiation power is calculated from the Stefan-Boltzmann law

$$\mathcal{P} = \sigma A e (T^4 - T_0^4), \tag{2.2}$$

where $\sigma = 5.68^{-8}\,\mathrm{W/(m^2K^4)}$ is the Stefan-Boltzmann constant, A is the surface area of the hot zone, T is the temperature of the hot zone, T_0 the temperature of the surroundings, and e the emissivity. Note that the emissivity depends on the number of shields N_{sh} according to

$$e(N_{sh}) = \left[\frac{1}{e_{Nb}} + \frac{1}{e_{Al}} + 2N_{sh}\left(\frac{1}{e_{Nb}} - 1\right)\right]^{-1}, \tag{2.3}$$

so decreasing the number of shields increases the emissivity from 0.042 to 0.06. In addition, the new area is also larger, so for the same amount of power, the maximum

temperature is decreased. It will then be necessary to alternate between the two designs, depending on whether the maximum size or maximum temperature is the limiting factor.

2.2.3 The housings

Each housing is machined out of a single block of Nb. Nb becomes a superconductor at 9.26 K (well above our operating temperature), so it excludes the magnetic field and provides a good electromagnetic shielding. The machining was done using electric discharge machining (EDM). The electric discharge from an electrode provides gentle cutting without putting undesirable stress on the thin diaphragms.

Since the source mass shares the same housing as the test masses, special provisions must be made to prevent the reaction forces from distorting the detector. To this end, the center parts of the housing containing the detector are decoupled from the outer rim by inserting a mechanical weak link, a cantilever spring, between them. This soft suspension also permits the alignment of the test masses using the alignment coils. The cantilever springs are highly linear, weak springs that provide motion along the symmetry axis. In the initial design, the cantilever springs were 1.27 mm thick, having an axial mode of 74.6 Hz, a rocking mode of 116.2 Hz, and a lateral mode of 971.7 Hz. To achieve the required alignment, they were thinned to 0.635 mm, obtaining the following theoretically predicted modes:

- an axial mode of 27.3 Hz,
- a rocking mode of 42.7 Hz,
- a lateral mode of 694 Hz.

Thinning the cantilever afterwards was done by using punch EDM. The spring on the first housing was machined badly, thinning it too much at some parts and making the spring weaker. The second one was machined properly. At room temperature, its transverse mode was measured to be 35.5 Hz and there were two identifiable rocking modes at 49.0 and 51.5 Hz, respectively.

The cantilever springs in one of the housings was found to be bent. This made the center part of the housing stick in and was corrected by heat-treating it in high vacuum. The housing was placed with its inner part down on a flat ceramic plate made out of 95% Al_2O_3 (alumina). A second smaller ceramic plate was placed over its center part with a heavy Nb weight on top. The stack was heat-treated at 1100°C. The yield strength of Nb at that temperature decreases enough, so the chosen Nb weight was sufficient. The other housing was heat-treated at 1100°C as well to relieve stress.

2.2.4 Source and test masses

Figure 2.6 shows the source and a test mass located above it.

The source is a disk 1.65 mm thick by 165 mm in diameter, with a dynamic mass of 565 g. The source mass, cantilever springs, and rim are machined out of a single Ta plate. Ta is chosen for its high density (16.6 g cm^{-3} compared to 8.57 g cm^{-3} for Nb), which increases the signal. Unfortunately, the critical temperature of Ta (theoretically predicted as 4.48 K but actually measured in the experiment as 4.3 K) is not as high as Nb (9.26 K), so we are obliged to cool the experiment below LHe temperature. At 1.7 K, Ta has a relatively high critical field, $H_c = 0.070$ T. The source mass suspension should be soft enough to reduce the required driving field, thus minimizing the reaction force and magnetic cross-talk. On the other hand, if it is too soft, the source mass will sag too much laterally. We chose a cantilever design that gives an axial frequency of 11.5 Hz and a lateral frequency of 75 Hz.

To machine the source mass to the required precision, two 1.75-mm thick Ta sheets were "double face ground" by a commercial vendor to improve the surface flatness. A measurement with dial indicators showed the surface to be flat to within 10 μm, an acceptable tolerance for the experiment. The source mass was produced from one of these sheets by using wire EDM and then heat-treated to relieve stress and prevent bowing.

The test masses are identical Ta disks 250 mm thick by 70 mm in diameter. Their dynamic mass is 18.8 g. At 4.2 K, the mechanical resonance frequency of a test mass

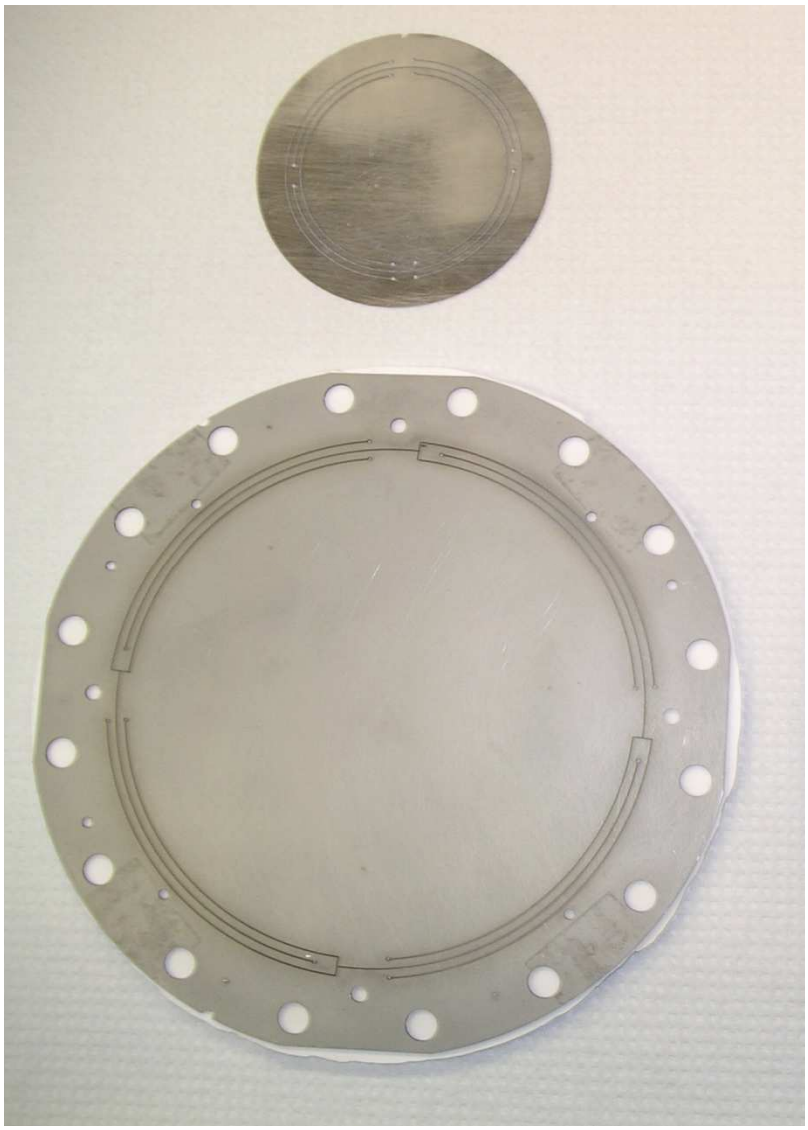

Figure 2.6: Source and test masses.

is 11.35 Hz while its lateral frequency is 350 Hz. Four test masses were machined, also with wire EDM, from a 0.25-mm thick Ta sheet. The equilibrium spacing between the source and each test mass is 150 μm. The test masses are separated by a baseline of 2.65 mm.

The experiment has been designed to be compatible with existing Nb cantilever springs and sensing coils, spare parts from the Superconducting Gravity Gradiometer (SGG) project. The Ta test mass has identical dimensions to the old Nb one, except that the bolt holes were omitted. The Nb spring structure can be used as a substitute test mass to investigate the systematics of the experiment.

2.2.5 Superconducting shields

It is necessary to provide good electrostatic and magnetic shielding between the source mass and each test mass. A superconducting shield is constructed by diffusion-bonding a 12.5-μm thick Nb foil to a Nb ring. The diffusion-bonding is performed at our heat-treatment facility, using a procedure developed after an extensive research of the existing literature [7, 20, 21, 29] and numerous tests to achieve the desired result. The suggested conditions for best diffusion-bonding are:

- Heat-treat to $0.5 - 0.75\,T_m$; achieving $0.75\,T_m$ recommended.
- The surfaces must be oxide free.
- The two surfaces must be in contact.

Here T_m is the melting temperature of the material to be diffusion-bonded.

There are five interrelated variables that can be controlled and modified in order to achieve the best diffusion-bonding: temperature, vacuum pressure, surface finish, applied pressure, and time at the maximum temperature. Our heat-treatment system is made out of Nb, which constrains our maximum achievable temperature. In addition, ceramic plates are used as support and to separate the parts to be heat-treated from the oven and from the weight applied. The melting temperature of Nb is 2467°C, while the melting temperature for alumina, the ceramic used, is 2050°C.

Alternate materials were sought, but alumina was found to be the most desirable material due to its strength and stability at high temperatures. This gave an additional constraint for the maximum achievable temperature, making it impossible to reach $0.75\,T_m$ for Nb.

The vacuum pressure used was 10^{-7} torr. The Nb ring was lapped to a mirror finish using consecutively finer grade sandpaper, and finishing with 0.3-μm grade lapping fluid on a lapping pad. All surfaces were cleaned first with Alcanox using an ultrasonic cleaner, and then with toluene, followed by acetone, alcohol, and distilled water. For the applied pressure, uniaxial pressing was recommended to avoid macroscopic deformations. This can be done by one of three methods: applying a dead load, using jigs made from a low expansion material, or using hydraulically operated rams. Due to the characteristics of the heat-treatment system and the temperatures sought, the first method was employed with a 10-kg load of Nb. It was found that the optimum temperature and time to obtain a good diffusion-bonding between the Nb foil and the Nb rim, while having no bonding to the alumina, is 1500°C for four hours. After several successful tests, the diffusion-bonding method was perfected by using an alumina plate with a small taper, which made the bond stronger.

2.2.6 Capacitor plates

In the initial design, there was no possibility for direct monitoring of the source mass position or distance to each shield. After several cool-downs (for additional detail, refer to Appendix C) and successive increases in the spacing between the source mass and the shields and source coils, the source mass resonance frequency was still undetectable. To understand the source mass behavior, capacitive position sensors were installed on both sides of the source mass. Figure 2.7 shows the capacitor plates, mounted on the periphery of the Nb shield on each housing. I intended for the capacitor plates to stick out of the shield plane slightly, so that if the source touched something, it would be a capacitor plate, and not a shield.

Each capacitor plate is made with circuit board material, a 1-mm thick fiberglass part covered with a thin film of Cu serving as the electrode. The boards were

Figure 2.7: Capacitor plates mounted on the periphery of the Nb shield on each housing.

machined in a ring shape. The Cu film was machined off at four places in the radial direction, obtaining four electrodes for each side. When mounted, they were oriented so that top, bottom, left, and right sensing could be made for each side of the source. Cu wires were soldered to each of the electrodes. The capacitor plates were dipped in liquid nitrogen several times to make sure the solder joints were good and that the Cu would not separate from the fiberglass. Adding the capacitor plates was risky since it required further increase in the source-mass-to-shields spacing and the exact deformation and position of the capacitor plates would not be known, but it allowed monitoring of the source mass position and motion.

2.2.7 Superconducting coils

The superconducting coils in the experiment are either sensing coils that sense the test mass motion or temperature fluctuations, driving coils that are responsible for

Figure 2.8: Inner part of one housing, before mounting the test mass and shield. A sensing coil and a source driving coil are shown in their location.

the motion of the source, or alignment coils that permit the alignment of the center part of the housings. Figure 2.8 shows the sensing coils and the source driving coils inside a housing before mounting the test mass and the shield, while Figure 2.9 shows the alignment coils before placing the outer cover.

All the coil-forms are made out of machinable glass ceramic, Macor, whose thermal expansion coefficient matches closely that of Nb at cryogenic temperatures. All the coils use a continuous length of insulated Nb wire of thickness ranging between 0.114 mm and 0.152 mm. The sensing, temperature, and alignment coils are wound

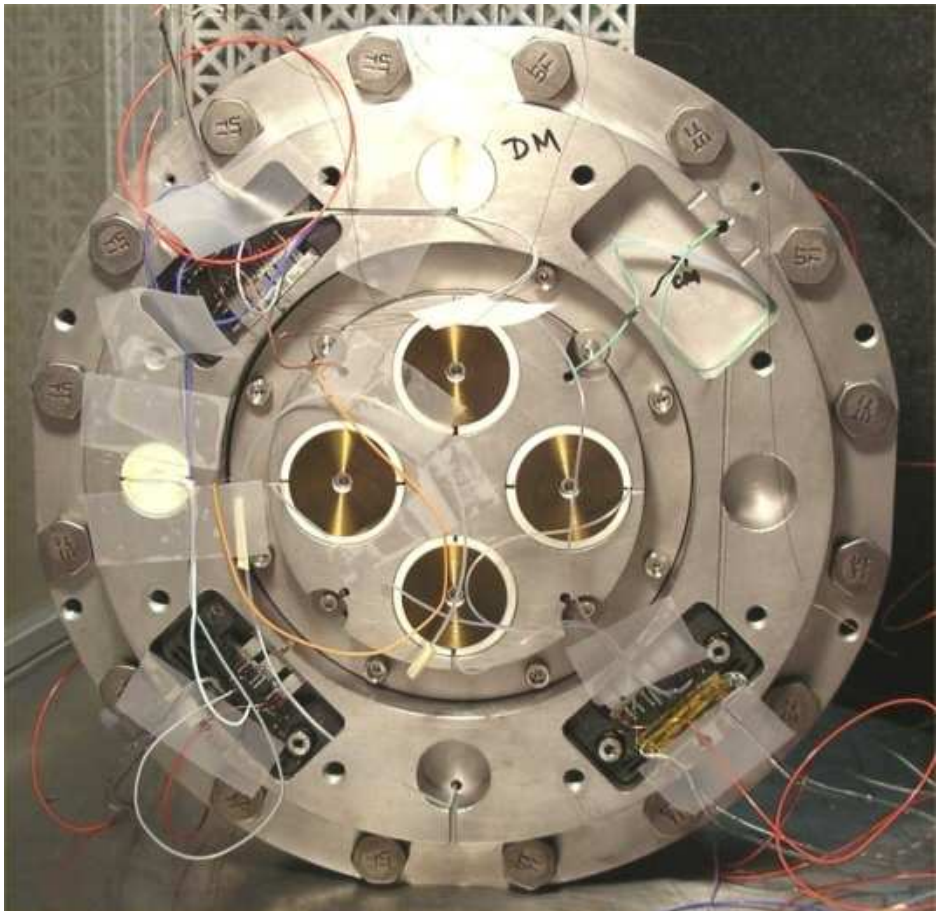

Figure 2.9: Outer part of one housing. The alignment coils and superconducting circuits are placed inside their cavities.

on the coil-form in a single layer and are usually referred to as pancake coils due to their shape. For a detailed derivation of the inductance of pancake-shaped coils, see Appendix A.

The sensing coils use a 0.102-mm thick Nb wire covered with insulation to 0.132 mm. In order to have multiple circuits that sense exactly the same motion, the sensing coils actually consist of three coils with approximately equal areas. The innermost coils has 90 turns and is used in one of the sensing circuits, the next one has 50 turns and acts as a separation, and the final has 40 turns and is used in the

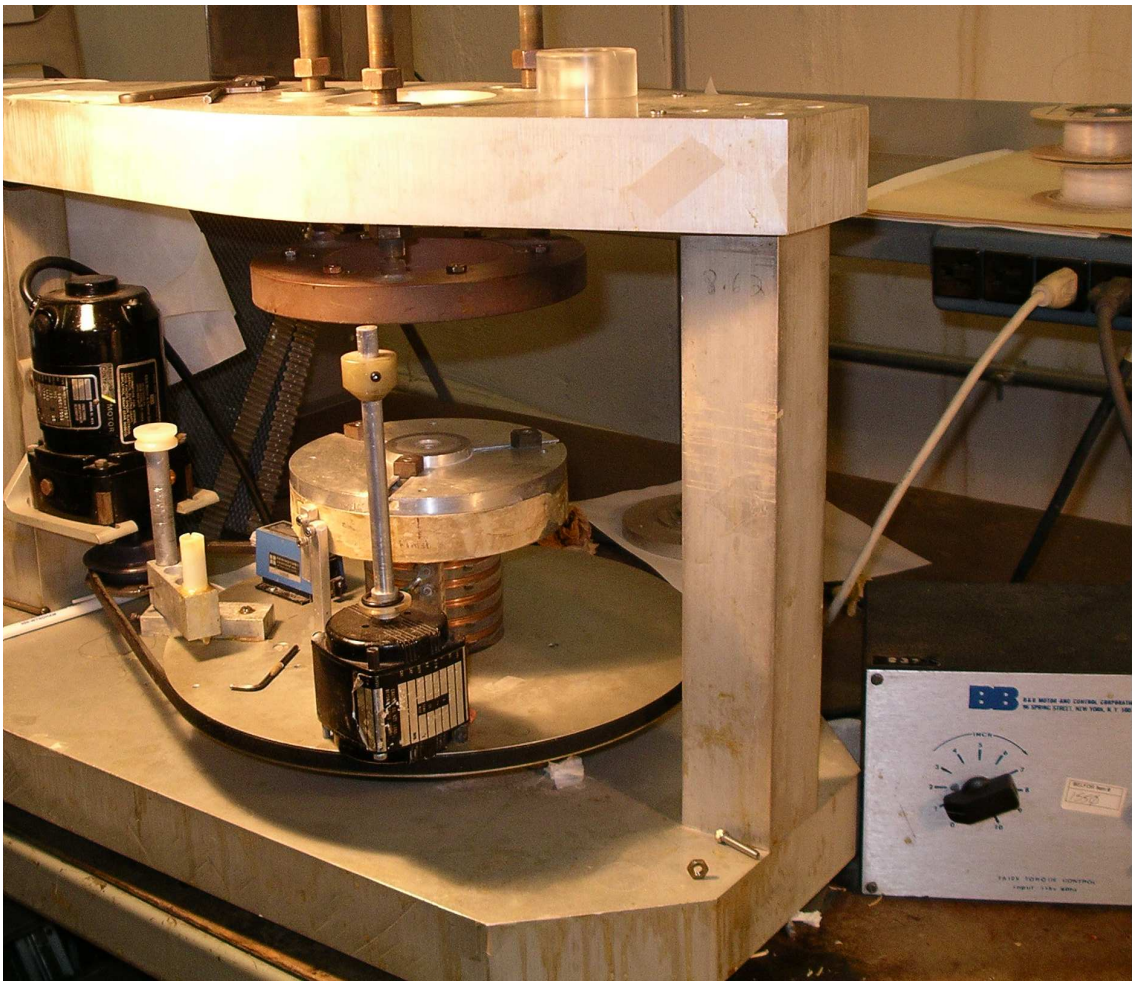

Figure 2.10: Coil winder.

other sensing circuit. The temperature coils use a 0.127-mm thick Nb wire covered with insulation to 0.152 mm and have 131 turns. The alignment coils use a 0.102-mm thick Nb-clad Nb-Ti wire covered with insulation to 0.127 mm and have 85 turns. The source driving coils are multilayered coils wound using the same wire as the sensing coils but with 425 turns.

Figure 2.10 shows the coil-winding machine, custom made for our laboratory to wind superconducting coils. It has three main parts: a rigid part, a rotating platform and a tension control. The coil is attached to the rotating platform. A motor with coarse and fine tuning capabilities controls the rotational speed and the direction of rotation. A rotation counter is used to keep track of the number of turns. The rigid part is used to attach a backing plate that controls the spacing to the coil (see

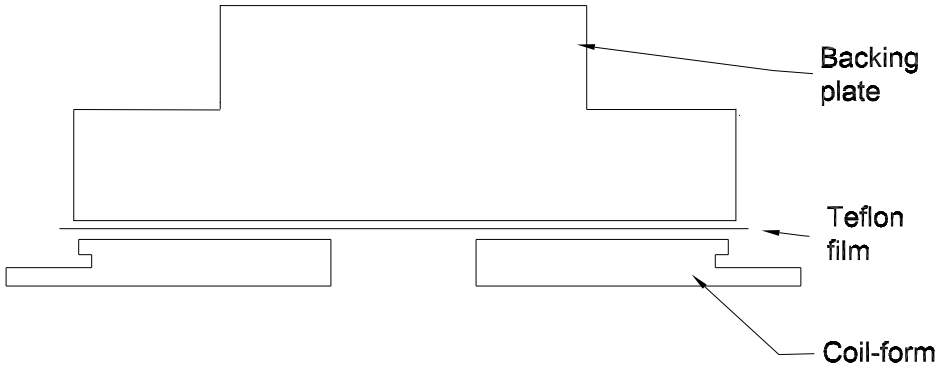

Figure 2.11: Coil winding diagram showing the coil-form, Teflon film, and backing plate.

coil-winding procedure below). There is a separate control for the wire tension.

The winding procedure used for the pancake-shaped coils is similar to that described in [12]. The Macor is machined in the desired shape and polished to a 5-μm flatness. After this flatness is achieved, a final roughing of the surface is done with a few strokes of 330-grade sandpaper. This roughing guarantees good bond to the wire. A radial groove tangential to the center of the hole, of the size of the diameter of the wire to be used, is made on the coil-form. The coil-form is then cleaned using Alcanox in an ultrasonic cleaner, followed by acetone, alcohol, and distilled water.

Figure 2.11 shows a diagram of the parts used in the coil winding process. A transparent Plexiglas backing plate of a slightly larger diameter than the coil-form is machined and lapped flat to a surface finish of 0.3 μm that keeps it very transparent. An 0.152-mm thick Teflon film is cut slightly larger than the Plexiglas. The backing plate and Teflon are cleaned and attached to each other by using a few drops of water between them and pressing them together with a heavy weight on top. The surface tension of the water is enough to keep them attached for the current purpose.

A Teflon spacer is inserted in the center hole of the coil-form so that it sticks out of it by more than the diameter of the wire. The coil-form is held rigidly in the coil-winding machine. The backing plate (with the Teflon facing the coil-form) is

placed on top of it, leaving a spacing equal to the Nb wire diameter and adjusted with three screws until he mating surfaces of the coil-form and the backing plate become parallel. By spreading epoxy on the coil-form, one should be able to push the epoxy in front of the wire and be able to move it without scratching the Teflon surface. The tension in the wire is selected so that the wire is straight, and the beginning of the wire is placed in the groove. Winding starts from the center of the coil using the Teflon spacer as a guide and ends after a fixed number of turns. A low viscosity transparent epoxy (BIPAX TRA-BOND, produced by TRA-CON) is used to bond the Nb wire to the coil-form, so the whole process is monitored through the transparent Plexiglas. After curing overnight, the backing plate is separated and both the Teflon film and the Teflon spacer are removed.

To produce a large enough force to drive the source mass with a modest current, the source coils had to be wound in multiple layers. The coil winding procedure was further modified for this purpose. Due to the large diameter, achieving a high parallelism between the spacer and the coil-form was not possible and a Teflon spacer could not be used. Instead, a Plexiglas ring was machined leaving an oversized, 0.254-mm thick lip so that when pushed inside the coil, the ring would stick above the coil-form by 0.343 mm. This is equivalent to 2.75 layers of 0.132-mm Nb wire. After winding the coil, the Plexiglas is machined off. The lip is made small enough so that it can just be peeled off of the coil.

2.2.8 Transformers

Some of the circuits need transformers to provide impedance matching and limit the DC current flowing through the SQUID input coil. They are wound on spool coil-forms, also machined out of Macor. Figure 2.12 shows a transformer next to an alignment coil. In order to restrain the magnetic field in the spool and achieve high coupling, we use a field guide made out of a thin Nb foil. It wraps the coil-form but with a small spacing between the layers where the two ends overlap so the superconductor does not form a closed surface and the magnetic field can penetrate inside the spool.

Figure 2.12: Transformer (top) and alignment coil (bottom).

The number of turns in the transformer coils are chosen so that the coupling to the SQUID is optimum and the amplifier noise is minimum. A comprehensive derivation of the optimization is provided in Section 4.4.2, while Appendix A has a detailed calculation of the inductances. The primary of the transformer usually needs more than one layer of winding, in which case the secondary of the transformer is sandwiched between primary layers. The wire is attached to the coil-form using GE-varnish. After winding the transformer, the outer surface of the spool is wrapped with a second Nb foil, without a spacing so it does form a closed surface and does not let the magnetic field escape.

2.2.9 Heat-switches

The heat-switches are one of the most fascinating components in the superconducting world. They are used to store currents in the superconducting circuits. Once the currents are stored, they circulate forever due to the zero resistance of the superconducting wires. A Nb wire that is part of a superconducting circuit is wound non-inductively around a shielded resistor. As a current pulse is sent through the resistor, it warms up, driving the superconducting wire above its critical temperature, making it a normal resistive wire. The Nb wire goes from the heat-switch to a heat-sink. This allows only a small section of the wire to warm up, as opposed to having a large part of the circuit become non-superconducting. The desired current is sent while the Nb wire is normal. The heat is then dissipated into the body of the experiment, making the Nb wire superconducting again and the current is stored!

The heat-switches are made using Xicon 1/10 W chip resistors that are 2.2 kΩ at room temperature. Their resistance becomes 3.2 kΩ at 4.23 K and 4.3 kΩ at 1.7 K. Two manganin wires are soldered to the resistor, which is then wrapped with a layer of cigarette paper and dipped in GE-varnish to provide an insulating layer. The wires are then passed through a Teflon tubing. In order to shield the heat-switches, a piece of lead (Pb) tubing is prepared and one of its ends is opened enough to fit the resistor. The resistor with the manganin wires is then placed inside the Pb tubing and the end containing the resistor is soldered, forming a small cup. A piece of Nb wire is then wound non-inductively around the outside surface of this cup and held with TRA-BOND epoxy. The Nb leads coming from the heat-switch are then wound around a heat-sink using Stycast 2850FT black epoxy, a thermally conductive epoxy produced by Emerson & Cuming.

This design is a modification of a previous model with Pb foil instead of Pb tubing. The new model provides the needed strength and durability to be reused in several cool-downs. It, however, has a higher heat capacity, which slows down the response time of the heat-switches.

2.2.10 Superconducting joints

The procedure of making superconducting joints was modified from an existing procedure as well. In order to make superconducting joints, it was necessary to perform a violent chemical cleaning, first using nitric acid to remove the wire insulation, and then using Nb polishing acid made out of equal parts of nitric, phosphoric, and hydrofluoric acids. Then, the wire had to be squished to about half its original diameter and laid along a piece of cleaned Nb foil (previously attached to a fixture) of 0.076 mm, chosen to be approximately the thickness of the Nb wire after it was squished (we use Nb wires ranging from 0.114 to 0.152 mm in diameter). The wire is then spot-welded to the foil by applying pressure and sending a large voltage through two electrodes. This is repeated for all the wires going into the joint.

In some cases, if one of the wires has a faulty joint, it is possible to remake it, but in others it is not and the whole procedure must be repeated. Since the foil was previously attached to a fixture, this means that all the foils with all their joints had to be replaced. The lengthly repairs of faulty joints, and above all the danger of the acids made modification a must.

After speaking to the JPL group [65], I experimented with several Nb wires and Nb foils and ended up with a new procedure, that works no worse than the previous, but does not have the associated risks. The end of the wires to be spot-welded are cleaned using an Eraser, model AR0221 wire stripper. This removed the insulation and left the wire clean and polished. Next, a small piece of Nb foil is cut and the end of it is folded so the Nb wire fits inside; the wire is spot-welded to the foil in at least three places. This is repeated for all the wires going to the joint by folding the Nb foil successively. Then, the foil is taped to the fixture. In addition to eliminating the use of dangerous acids, this procedure allows remaking only the faulty joints. The new joints were tested by dipping them in LHe and were found to be able to carry up to 40 A, as much as the previous ones.

2.2.11 Thermometers

To continuously monitor the temperature of the experiment, a germanium (Ge) thermometer is mounted directly on the outside of the housing. Its surface is cleaned thoroughly and it is screwed onto the housing with a thin layer of vacuum grease in between. The temperature of the cold plate is monitored separately with a second such thermometer, mounted directly on the cold plate, outside the experiment, but still in the vacuum space. The thermometers are model GR-200A-500-CD-1.4D from Lake Shore Cryotronics, Inc. (Serial Number 29607 for the experiment and Serial Number 29148 for the cold plate). For a detailed description of the cryostat, vacuum can, and Cu plate, refer to Section 5.1. The resolution of both thermometers at 1.7 K is 13 μK.

2.2.12 Heater

The experiment was designed with two thermometers and a temperature sensing circuit. In addition, a heater was integrated by making a groove in the support flange and winding 30 turns of manganin wire inside the groove. This heater allows warming the experiment slightly, as for example to make the Ta masses non-superconducting, while keeping the Nb ones superconducting. It also facilitates the quick warm-up of the experiment.

2.3 Superconducting circuits

2.3.1 Sensing circuits

There are two sensing circuits in the experiment, designed to be physically identical but with a different current configuration. This way, the better performing circuit can always be chosen to measure the differential mode (DM). The sensing mode of the circuit is controlled by the relative polarity of the two sensing currents. For the common mode (CM), the polarity is chosen so that CM responses from the test mass add at the input of the SQUID, while for the DM, the polarity is chosen so that the

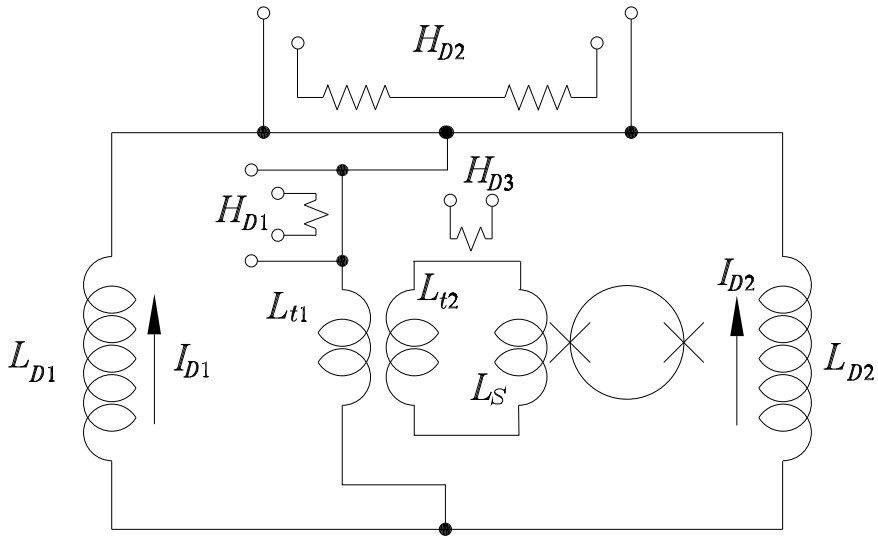

Figure 2.13: Circuit I: DM sensing circuit

CM responses subtract at the input of the SQUID.

The DM sensing circuit is shown in Figure 2.13. L_{D1} and L_{D2} are pancake coil inductors for the two test masses. The transformer has a primary L_{t1} and a secondary L_{t2} and is used to connect the parallel combination of L_{D1} and L_{D2} to a SQUID to form a sensing circuit. The transformer provides impedance matching and limits the DC current flowing through the SQUID input coil L_s. H_{D1} and H_{D2} are shielded heat-switches. H_{D2} is used to store a series current in the loop comprised by L_{D1} and L_{D2}, while H_{D1} is used to store a persistent current $I_{D1} + I_{D2}$ through the loop comprising the parallel combination of L_{D1} and L_{D2} and the transformer primary. A small series current is usually needed to tune the ratio I_{D2}/I_{D1} without modifying the value of $I_{D1} + I_{D2}$. This matches the scale factors of the component accelerometers and achieve CM rejection. In addition, there is a third heat-switch H_{D3} between L_{t2} and L_s that is turned on every time there is a current change. It protects the SQUID by preventing a large current from being induced in L_s.

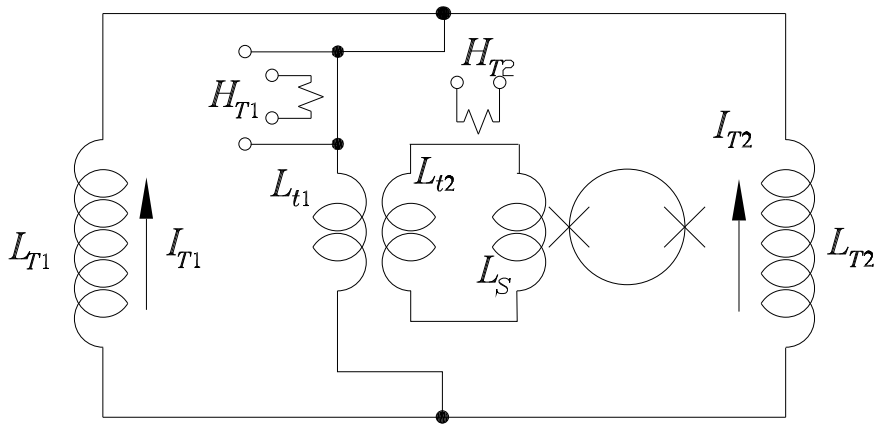

Figure 2.14: Temperature sensing circuit

2.3.2 Temperature circuit

The inductance of a superconducting coil varies with temperature through a temperature dependence of the penetration depth. This property can be used to sense temperature variation with a superconducting circuit [43].

Figure 2.14 shows the temperature sensing circuit. L_{T1} and L_{T2} are pancake coils mounted directly on the Nb housing (Figure 2.4), making them sensitive only to temperature variation. Just like in the sensing circuits, there is a transformer with a primary L_{t1} and a secondary L_{t2} that connects the parallel combination of L_{T1} and L_{T2} to the SQUID, provides impedance matching, and limits the DC current flowing through the SQUID. The resistive heat-switch H_{T1} is used to store a persistent current $I_{D1} + I_{D2}$. The heat-switch H_{T2} is turned on every time H_{T1} is on to protect the SQUID. In this circuit, the currents are stored in DM, so that only relative changes in temperature between the two sides of the housing are important. By comparing the spectra of the DM and the temperature circuits, the output of the

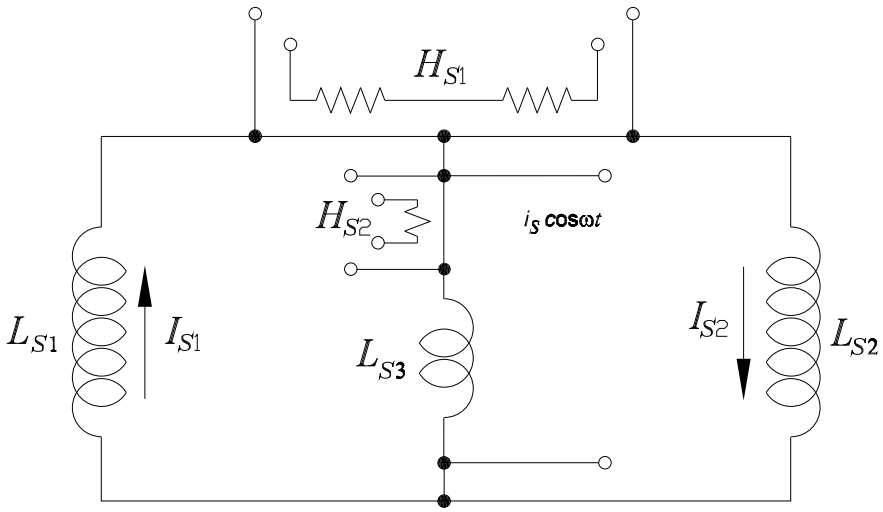

Figure 2.15: Source driving circuit

temperature circuit can be used to compensate the temperature sensitivity of the differential accelerometer by a factor of 10.

2.3.3 Source driving circuit

The source driving circuit is shown in Figure 2.15. L_{S1} and L_{S2} are the source driving coils. L_{S3} is a supplementary shunt inductor. The source driving circuit was modified several times. The last modification was adding L_{S3} to be able to center the source mass. Using the heat-switch H_{S1}, a large persistent current I_S is stored in the loop comprising L_{S1} and L_{S2}. Another persistent current I_P is stored in the loop comprising the parallel combination of L_{S1} and L_{S2} and the shunt inductor L_{S3} to center the source mass with respect to the shields. This modifies the currents stored in L_{S1} and L_{S2}. The source is then driven by sending a small current $i_S \cos\omega t$ across the AC leads. In order to reduce the magnetic cross-talk the smallest effective AC current is used. L_{S3} is chosen to be much larger than L_{S1} and L_{S2}, so that the

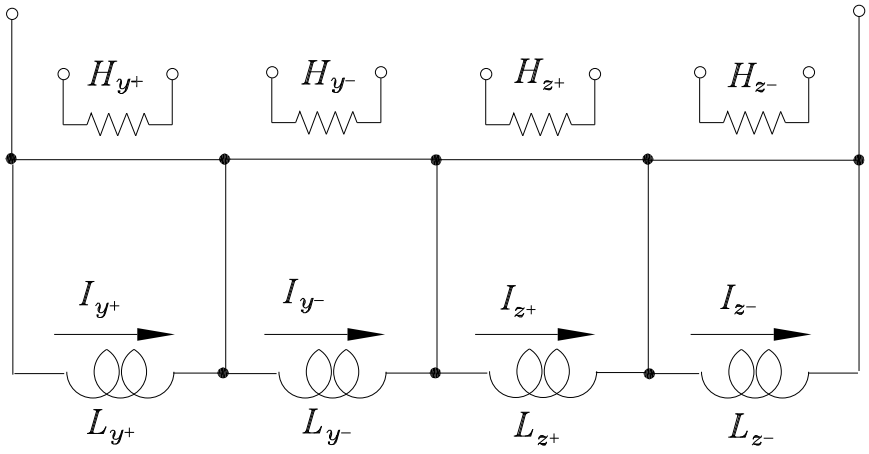

Figure 2.16: Alignment circuit for one of the housings; the second housing circuit is identical.

AC current flowing through it is very small. For a detailed discussion of the source circuit operation, see Section 3.5.

2.3.4 Alignment circuits

To align the sensitive axes of the test masses, four alignment coils are provided for each housing, two per degree of freedom. Figure 2.16 shows the circuit configuration for one side. Each alignment coil is connected with a heat-switch. One set of charging leads is used for storing current in all of the coils on each side, by choosing the heat-switch corresponding to the coil. Figure 2.4 shows the physical location of the y axis coils. By storing current in one of these two coils, a torque is exerted on the cover plate. This aligns the axis in the xz plane. The notation for the alignment coils is chosen, so that when storing current in the $y+$ coil, the center part of the housing rotates clockwise about the y axis, while current in the $y-$ coil gives a counterclockwise rotation about y. By storing current in all the coils, the center part of the housing can be moved inward.

Chapter 3

Dynamics of the Inverse-Square Law Experiment

The analysis of the basic accelerometer was first made by Paik [50, 51] for a gravitational wave transducer in which the mass was suspended between two superconducting pancake coils connected in parallel. This analysis was extended for a current-differencing gravity gradiometer in [57] and [84]. It was shown that by adjusting the ratio between currents in the sensing loops, it was possible to balance an applied common acceleration to high precision in a restricted bandwidth, the width of which depends on how well the mechanical parameters are matched.

Due to the high quality factors Q of the superconducting masses in the experiment, it is desirable and often necessary to have wide-band balance (balance for all frequencies). Mapoles [40] achieved wide-band balance in a displacement-differencing gravity gradiometer by using one common sensing coil and two additional tuning coils. It is possible to obtain the wide-balance by using more current components instead of additional coils, as shown by Chan [12].

In this chapter, I will study the dynamics of the ISL experiment, starting with a Lagrangian formulation of the system, followed by a detailed analysis of the sensing and source circuits. I will use a Mathcad model to justify the use of analytical approximations, in particular, the use of a source model and a reduced accelerometer model. Using those simpler models, I will describe the motion of the source mass and of the test masses. Finally, I will perform an in-depth study of the CM and DM response of the detector, including resonance frequencies and transfer functions.

3.1 Lagrangian formulation of the superconducting accelerometer

The standard classical Lagrangian is modified to include superconducting inductors. The Lagrangian for the system including the source mass, the housings, the shields, and the test masses can be written as the sum:

$$\mathcal{L} = \mathcal{L}_M + \mathcal{L}_s + \sum_{i=1}^{2} [\mathcal{L}_{hi} + \mathcal{L}_{shi} + \mathcal{L}_i] - \frac{1}{2} \sum_j I_j^2 L_j, \tag{3.1}$$

where

$$\mathcal{L}_M = \frac{1}{2} M \dot{x}_M^2 - \frac{1}{2} M \omega_M^2 x_M^2, \tag{3.2}$$

$$\mathcal{L}_s = \frac{1}{2} m_s (\dot{x}_s + \dot{x}_M)^2 - \frac{1}{2} m_s \omega_s^2 (x_s + x_{s0})^2, \tag{3.3}$$

$$\mathcal{L}_{hi} = \frac{1}{2} m_{hi} (\dot{x}_{hi} + \dot{x}_M)^2 - \frac{1}{2} m_{hi} \omega_{hi}^2 (x_{hi} + x_{hi0})^2, \tag{3.4}$$

$$\mathcal{L}_{shi} = \frac{1}{2} m_{shi} (\dot{x}_{shi} + \dot{x}_{hi} + \dot{x}_M)^2 - \frac{1}{2} m_{shi} \omega_{shi}^2 (x_{shi} + x_{shi0})^2, \tag{3.5}$$

and

$$\mathcal{L}_i = \frac{1}{2} m_i (\dot{x}_i + \dot{x}_{hi} + \dot{x}_M)^2 - \frac{1}{2} m_i \omega_{mi}^2 (x_i + x_{i0})^2. \tag{3.6}$$

Here $\mathcal{L}_M$, $\mathcal{L}_s$, $\mathcal{L}_{hi}$, $\mathcal{L}_{shi}$, and $\mathcal{L}_i$ represent the Lagrangians for the platform, the source, the housings, the shields, and the test masses, respectively, when no currents are stored in the superconducting circuits, L_j and I_j are the circuit inductances and the stored persistent currents, and the sum on j is over all the inductances. The index i runs from 1 to 2; M is the mass of the platform excluding the source, test masses, and shields, as well as the center of the housings; m_s, m_{h1}, m_{h2}, m_{sh1}, m_{sh2}, m_1, and m_2 are the active masses of the source mass, the center part of each housing, the shields, and the two test masses, respectively, and x_M, x_s, x_{h1}, x_{h2}, x_{sh1}, x_{sh2}, x_1, and x_2 are their positions. The equilibrium position of the platform is assumed to be the origin of the coordinate system, while x_{s0}, x_{h10}, x_{h20}, x_{sh10}, x_{sh20}, x_{10}, and x_{20} are the equilibrium positions of the other parts. Also, ω_M, ω_s, ω_{h1}, ω_{h2}, ω_{sh1}, ω_{sh2}, ω_{m1}, and ω_{m2}, are the mechanical (angular) resonance frequencies of the respective masses.

Since only the sensing circuits and the source circuit need to have stored currents in order to operate as desired and expected, and all other parts either do not have a coupled circuit or usually operate without current in it, I will ignore all currents, except for the ones in the source and sensing circuits in the following treatment. Adding external forces, the equations of motion are

$$\begin{aligned}
\frac{d}{dt}\left(\frac{\partial \mathcal{L}}{\partial \dot{x}_M}\right) - \frac{\partial \mathcal{L}}{\partial x_M} &= M_{\rm tot}\ddot{x}_M + m_s\ddot{x}_s + \sum_{i=1}^{2}\left(m_{{\rm tot}hi}\ddot{x}_{hi} + m_{shi}\ddot{x}_{shi} + m_i\ddot{x}_i\right) \\
&+ M\omega_M^2 x_M = F_M, \qquad (3.7) \\
\frac{d}{dt}\left(\frac{\partial \mathcal{L}}{\partial \dot{x}_s}\right) - \frac{\partial \mathcal{L}}{\partial x_s} &= m_s(\ddot{x}_M + \ddot{x}_s) + m_s\omega_s^2(x_s + x_{s0}) - \frac{1}{2}\sum_j I_j^2\frac{\partial L_j}{\partial x_s} \\
&= F_s, \qquad (3.8) \\
\frac{d}{dt}\left(\frac{\partial \mathcal{L}}{\partial \dot{x}_{hi}}\right) - \frac{\partial \mathcal{L}}{\partial x_{hi}} &= m_{{\rm tot}hi}(\ddot{x}_M + \ddot{x}_{hi}) + m_{shi}\ddot{x}_{shi} + m_i\ddot{x}_i \\
&+ m_{hi}\omega_{hi}^2(x_{hi} + x_{hi0}) = F_{hi}, \qquad (3.9) \\
\frac{d}{dt}\left(\frac{\partial \mathcal{L}}{\partial \dot{x}_{shi}}\right) - \frac{\partial \mathcal{L}}{\partial x_{shi}} &= m_{shi}(\ddot{x}_M + \ddot{x}_{hi} + \ddot{x}_{shi}) + m_{shi}\omega_{shi}^2(x_{shi} + x_{shi0}) \\
&= F_{shi}, \qquad (3.10) \\
\frac{d}{dt}\left(\frac{\partial \mathcal{L}}{\partial \dot{x}_i}\right) - \frac{\partial \mathcal{L}}{\partial x_i} &= m_i(\ddot{x}_M + \ddot{x}_{hi} + \ddot{x}_i) + m_i\omega_{mi}^2(x_i + x_{i0}) \\
&- \frac{1}{2}\sum_j I_j^2\frac{\partial L_j}{\partial x_i} = F_i, \qquad (3.11)
\end{aligned}$$

where F_M, F_s, F_{h1}, F_{h2}, F_{sh1}, F_{sh2}, F_1, and F_2, are the external forces acting on M, m_s, m_{h1}, m_{h1}, m_{h1}, m_{h1}, m_1, and m_2, respectively. The total mass for the assembly is

$$M_{\rm tot} = M + m_s + m_{h1} + m_{h2} + m_{sh1} + m_{sh2} + m_1 + m_2,$$

while the total mass enclosed in the center part of the housings is

$$m_{{\rm tot}hi} = m_{hi} + m_{shi} + m_i.$$

The equations of motion (3.7)-(3.11) can be simplified by using

$$\mu_M = \frac{M}{M_{\rm tot}}, \;\; \mu_s = \frac{m_s}{M_{\rm tot}}, \;\; \mu_{{\rm tot}hi} = \frac{m_{{\rm tot}hi}}{M_{\rm tot}}, \qquad (3.12)$$

$$\mu_{hi} = \frac{m_{hi}}{M_{\rm tot}}, \;\; \mu_{shi} = \frac{m_{shi}}{M_{\rm tot}}, \;\; \mu_i = \frac{m_i}{M_{\rm tot}}. \qquad (3.13)$$

We obtain

$$\ddot{x}_M + \mu_s \ddot{x}_s + \sum_{i=1}^{2} (\mu_{\mathrm{tot}hi} \ddot{x}_{hi} + \mu_{shi} \ddot{x}_{shi} + \mu_i \ddot{x}_i) + \mu_M \omega_M^2 x_M = \frac{F_M}{M_{\mathrm{tot}}}, \quad (3.14)$$

$$\ddot{x}_M + \ddot{x}_s + \omega_s^2 (x_s + x_{s0}) - \frac{1}{2m_s} \sum_j I_j^2 \frac{\partial L_j}{\partial x_s} = \frac{F_s}{m_s}, \quad (3.15)$$

$$\ddot{x}_M + \ddot{x}_{hi} + \frac{\mu_{shi}}{\mu_{\mathrm{tot}hi}} \ddot{x}_{shi} + \frac{\mu_i}{\mu_{\mathrm{tot}hi}} \ddot{x}_i + \frac{\mu_{hi}}{\mu_{\mathrm{tot}hi}} \omega_{hi}^2 (x_{hi} + x_{hi0}) = \frac{F_{hi}}{m_{\mathrm{tot}hi}}, \quad (3.16)$$

$$\ddot{x}_M + \ddot{x}_{hi} + \ddot{x}_{shi} + \omega_{shi}^2 (x_{shi} + x_{shi0}) = \frac{F_{shi}}{m_{shi}}, \quad (3.17)$$

$$\ddot{x}_M + \ddot{x}_{hi} + \ddot{x}_i + \omega_{mi}^2 (x_i + x_{i0}) - \frac{1}{2} \sum_j I_j^2 \frac{\partial L_j}{\partial x_i} = \frac{F_i}{m_i}. \quad (3.18)$$

In order to further describe the system, it is necessary to analyze the circuits and obtain the current dependent terms in the equations of motion.

3.2 Circuit analysis

By storing currents in the superconducting coils that are facing the active masses of the experiment, the resonance frequencies of those masses are modified. This can be seen from Eqs. (3.15) and (3.18). In order to know the exact frequency modification, it is necessary to analyze each circuit involved. In this section, I will study the sensing and source circuits and obtain all the necessary parameters to analyze the equations of motion of the full system.

3.2.1 Sensing circuits

The sensing circuit shown in Figure 2.13, Circuit I, has five inductances, which makes it difficult to analyze. It can be shown that it is equivalent to a simpler circuit, Circuit II, shown in Figure 3.1 for a specific value of the inductance L_e. In order to show this equivalence and find the value of L_e, I will analyze the magnetic flux conservation equations for both circuits. Due to flux quantization, the total flux through a complete superconducting loop is conserved. Therefore, as the inductances are modulated by the motion of the test masses, the currents will be modulated as

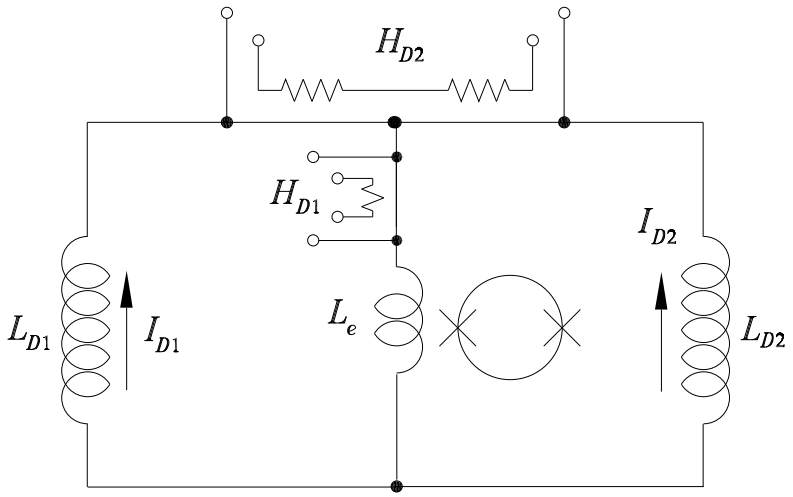

Figure 3.1: Circuit II: equivalent DM circuit

well, in such a way as to keep the initial magnetic flux through the superconducting loop (before the masses move) invariant.

In Circuit II, there are two independent magnetic flux conservation equations:

$$\Phi_1 = L_1 I_1 + L_e(I_1 + I_2) = \Phi_{10} \tag{3.19}$$

and

$$\Phi_2 = L_2 I_2 + L_e(I_1 + I_2) = \Phi_{20}, \tag{3.20}$$

where Φ_1 and Φ_2 are the magnetic fluxes of the two circuit loops at an arbitrary moment of time, and Φ_{10} and Φ_{20} are the initial magnetic fluxes in those circuits.

In Circuit I, there are three magnetic flux conservation equations. The magnetic flux conservation in the loop directly coupled to the SQUID and consisting of the transformer secondary L_{t2}, and the SQUID input coil L_s is

$$\Phi_s = (L_{t2} + L_s) I_s - M_t(I_{D1} + I_{D2}) = \Phi_{s0}, \tag{3.21}$$

where $M_t = \kappa_t \sqrt{L_{t1} L_{t2}}$ is the mutual inductance between the transformer primary and secondary L_{t1} and L_{t2}, Φ_s is the magnetic flux at an arbitrary moment of time, and Φ_{s0} is the initial magnetic flux in that circuit. Solving for the current in that loop,

$$I_s = \frac{\Phi_{s0} + M_t(I_{D1} + I_{D2})}{L_{t2} + L_s}. \tag{3.22}$$

The conservation of the magnetic flux in the other two loops of the DM sensing circuit gives two equations:

$$\Phi_{D1} = L_{D1}I_{D1} + L_{t1}(I_{D1} + I_{D2}) - M_t I_s = \Phi_{D10} \tag{3.23}$$

and

$$\Phi_{D2} = L_{D2}I_{D2} + L_{t1}(I_{D1} + I_{D2}) - M_t I_s = \Phi_{D20}, \tag{3.24}$$

where Φ_{D1} and Φ_{D2} are the magnetic fluxes of the two circuit loops at an arbitrary moment of time, and Φ_{D10} and Φ_{D20} are the initial magnetic fluxes in those circuits.

Substituting I_s in Eqs. (3.23) and (3.24),

$$\Phi_{D1} - \frac{M_t\Phi_{s0}}{L_{t2}+L_s} = L_{D1}I_{D1} + \left[L_{t1} - \frac{M_t^2}{L_{t2}+L_s}\right](I_{D1} + I_{D2}) \tag{3.25}$$

and

$$\Phi_{D2} - \frac{M_t\Phi_{s0}}{L_{t2}+L_s} = L_{D2}I_{D2} + \left[L_{t1} - \frac{M_t^2}{L_{t2}+L_s}\right](I_{D1} + I_{D2}). \tag{3.26}$$

It is possible to rewrite Eqs. (3.25) and (3.26) in the same form as Eqs. (3.19) and (3.20) by redefining

$$\Phi_1 = \Phi_{D1} - \frac{M_t\Phi_{s0}}{L_{t2}+L_s} \tag{3.27}$$

and

$$\Phi_2 = \Phi_{D2} - \frac{M_t\Phi_{s0}}{L_{t2}+L_s}, \tag{3.28}$$

and identifying

$$L_e = L_{t1} - \frac{M_t^2}{L_{t2}+L_s}, \tag{3.29}$$

$I_{D1} = I_1$, and $I_{D2} = I_2$. Note that the subindex "D" was kept to indicate that the currents were stored in the DM configuration. From now on, I will omit this subindex, but keep in mind that the currents are stored in DM. For CM circuit configuration, the polarity of one of the currents needs to be reversed.

By replacing Circuit I with Circuit II, I will work with the simplest possible equations. At the end of all the calculations, I will recover the original circuits. The initial conditions for the two new superconducting loops are

$$\Phi_{10} = L_{10}I_{10} + L_e(I_{10} + I_{20}) \tag{3.30}$$

and

$$\Phi_{20} = L_{20} I_{20} + L_e (I_{10} + I_{20}), \tag{3.31}$$

where L_{10} and L_{20} are the initial inductances, and I_{10} and L_{20} the initial currents. The problem is then reduced to finding I_1 and I_2 by solving Eqs. (3.19) and (3.20) simultaneously, obtaining

$$I_1 = I_{10} + \frac{I_{20}(L_2 - L_{20})L_e - I_{10}(L_1 - L_{10})(L_2 + L_e)}{(L_1 + L_2)L_e + L_1 L_2} \tag{3.32}$$

and

$$I_2 = I_{20} + \frac{I_{10}(L_1 - L_{10})L_e - I_{20}(L_2 - L_{20})(L_1 + L_e)}{(L_1 + L_2)L_e + L_1 L_2}. \tag{3.33}$$

The inductance of a spiral coil is approximated by (for a detailed discussion and derivation, see Appendix A)

$$L(x) = L_0 + \lambda x + \gamma x^2, \tag{3.34}$$

where x is the distance the test mass is displaced from the coil, $L_0 = \mu_0 n^2 A\, d_0 D/(d_0 + D)$, $\lambda = \mu_0 n^2 AD/(d_0+D)^2$, and $\gamma = -\mu_0 n^2 AD^2(d_0+D)^3$, with d_0 the initial position of the coil with respect to the front superconducting plane, and D the distance to the back plane (see Figure A.1). In this case, there are two test masses, which gives two equations. Because of the geometry of the experiment, in one case, for x_1, a positive x corresponds to moving away from the coils while for the other, for x_2, a negative x has the same effect. The equations of the inductances are then, respectively,

$$L_1(x_1) = L_{10} + \lambda_1 x_1 + \gamma_1 x_1^2 \tag{3.35}$$

and

$$L_2(x_2) = L_{20} - \lambda_2 x_2 + \gamma_2 x_2^2. \tag{3.36}$$

By using the explicit form of the inductance and expanding Eqs. (3.32) and (3.33) to first order in x_1 and x_2,

$$I_i = I_{i0} + (-1)^i \, \frac{I_{i0}(L_{j0} + L_e)\lambda_i x_i + I_{j0} L_e \lambda_j x_j}{L_{\rm tot}^2}, \tag{3.37}$$

where $i = 1, 2;\ j \neq i$; and

$$L_{\rm tot}^2 = (L_{10} + L_{20})L_e + L_{10} L_{20}.$$

The square of the currents is then, to first order in x_1 and x_2,

$$I_i^2 = I_{i0}^2 + 2(-1)^i I_{i0} \frac{I_{i0}(L_{j0} + L_e)\lambda_i x_i + I_{j0} L_e \lambda_j x_j}{L_{\text{tot}}^2}. \tag{3.38}$$

According to Eq. (3.18), in order to solve the equations of motion, it is necessary to find $I_j^2\ \partial L_j/\partial x_1$ and $I_j^2\ \partial L_j/\partial x_2$. From Eqs. (3.35), (3.36) and (3.38),

$$\frac{1}{2}\sum_j I_j^2 \frac{\partial L_j}{\partial x_i} = \frac{1}{2} I_i^2 \frac{\partial L_i}{\partial x_i} = \frac{1}{2} I_i^2 [(-1)^{i+1}\lambda_i + 2\gamma_i x_i] = F_{Di} - k_i x_i - k_{12} x_j, \tag{3.39}$$

where

$$F_{Di} = \frac{\lambda_1}{2} I_{i0}^2, \tag{3.40}$$

$$k_{12} = \frac{I_{10} I_{20} L_e \lambda_1 \lambda_2}{L_{\text{tot}}^2}, \tag{3.41}$$

and

$$k_i = \left[\frac{(L_{j0} + L_e)\lambda_i^2}{L_{\text{tot}}^2} - \gamma_i \right] I_{i0}^2. \tag{3.42}$$

Using Eq. (3.42), it is possible to define a new resonance frequency:

$$\omega_{i0}^2 = \frac{k_{mi} + k_i}{m_i} = \omega_{mi}^2 + \frac{k_i}{m_i}. \tag{3.43}$$

3.2.2 Source driving circuit

As described in Section 2.3.3, the source circuit consist of three coils: two driving coils, L_{S1} and L_{S2}, positioned on each side of the source mass used to drive the source, and a shunt inductor L_{S3} used to center it with respect to the other two coils (see Figure 2.15). In this section, I will analyze the motion of the source mass when storing currents in the different loops. The procedure for storing the currents is the following:

- A large persistent series current I_S is stored in the loop comprising L_{S1} and L_{S2}. The currents passing through L_{S1} and L_{S2} are equal: $I_{S1} = I_{S2} = I_S$, with no current passing through L_{S3}.

- A small persistent current I_P is stored in the loop comprising the parallel combination of L_{S1} and L_{S2} and the shunt inductor L_{S3} in order to center the source mass with respect to the shields. This modifies the currents passing through each L_{S1} and L_{S2} as

$$I_{S1} = I_S - I_P \frac{L_{S2}}{L_{S1} + L_{S2}} \tag{3.44}$$

and

$$I_{S2} = I_S + I_P \frac{L_{S1}}{L_{S1} + L_{S2}}. \tag{3.45}$$

Identifying the initial currents as

$$I_{S10} = I_S - I_P \frac{L_{S20}}{L_{S10} + L_{S20}} \tag{3.46}$$

and

$$I_{S20} = I_S + I_P \frac{L_{S10}}{L_{S10} + L_{S20}}, \tag{3.47}$$

the circuit analysis is similar to the simplified analysis for the sensing circuits, replacing L_1, L_2, and L_e, by L_{S1}, L_{S2}, and L_{S3}. From the flux conservation equations, the currents passing through these coils can be described by Eqs. (3.32) and (3.33). The inductances of both circuits are, in analogy to Eqs. (3.35) and (3.36),

$$L_{S1}(x_s) = L_{S10} + \lambda_{S1} x_s + \gamma_{S1} x_s^2 \tag{3.48}$$

and

$$L_{S2}(x_s) = L_{S20} - \lambda_{S2} x_s + \gamma_{S2} x_s^2, \tag{3.49}$$

with the difference that now there is only one mass even though its motion has the opposite effect on both inductors. A peculiar characteristic is that the circuits are described identically, even though in the case of the sensing circuits, the coils are used for sensing the masses, while in the case of the source, the circuits are used for driving it.

By using the explicit form of the inductance and expanding Eqs. (3.32) and (3.33) to first order in x_s,

$$I_{Si} = I_{Si0} + (-1)^i \, \frac{I_{Si0}(L_{Sj0} + L_{S3})\lambda_{Si} + I_{Sj0} L_{S3} \lambda_{Sj}}{L_{S\text{tot}}^2} \, x_s, \tag{3.50}$$

where again $i = 1, 2;\ j \neq i$; and

$$L_{S\text{tot}}^2 = (L_{S10} + L_{S20}) L_{S3} + L_{S10} L_{S20}.$$

The square of the currents is then, to first order in x_s,

$$I_{Si}^2 = I_{Si0}^2 + 2(-1)^i I_{Si0} \frac{I_{Si0}(L_{Sj0} + L_{S3})\lambda_{Si} + I_{Sj0} L_{S3} \lambda_{Sj}}{L_{S\text{tot}}^2} \, x_s. \tag{3.51}$$

Using Eqs. (3.48), (3.49), and (3.51), the current term in Eq. (3.15) can be rewritten as

$$\frac{1}{2}\sum_j I_j^2 \frac{\partial L_j}{\partial x_s} = \frac{1}{2}\sum_{i=1}^{2}\left[I_{Si}^2[(-1)^{i+1}\lambda_{Si} + 2\gamma_{Si}x_s]\right] = F_S - k_S x_s, \tag{3.52}$$

where

$$F_S = \frac{1}{2}(\lambda_{S1}I_{S10}^2 - \lambda_{S2}I_{S20}^2) \tag{3.53}$$

and

$$k_S = \frac{2I_{S10}I_{S20}\lambda_{S1}\lambda_{S2}L_{S3}}{L_{S\mathrm{tot}}^2} + \sum_{i=1}^{2}\left[I_{Si0}^2\left(\frac{\lambda_{Si}^2(L_{Sj0}+L_{S3})}{L_{S\mathrm{tot}}^2} - \gamma_{Si}\right)\right]. \tag{3.54}$$

Note that F_S represents the force that pushes the source mass and centers it. In addition, with Eq. (3.54), it is possible to define the modified resonance frequency of the source mass:

$$\omega_S^2 = \frac{k_s + k_S}{m_s} = \omega_s^2 + \frac{k_S}{m_s}. \tag{3.55}$$

3.3 The eight mass model

Now that the shift in frequency and additional forces on the masses due to the stored persistent currents have been found, the equations of motion for the full system (3.14)-(3.18) can be reexamined. Introducing damping terms, taking the Fourier transform, and making use of Eqs. (3.39)-(3.43) and (3.52)-(3.55), the equations of motion can be rewritten as

$$\begin{aligned} -\omega^2 x_M(f) - \omega^2\mu_s\, x_s(f) - \omega^2\sum_{i=1}^{2}\left[\,\mu_{\mathrm{tot}hi}\, x_{hi}(f) + \mu_{shi}\, x_{shi}(f) + \mu_i\, x_i(f)\,\right] \\ +\mu_M\left[\omega_M^2 + \frac{i\omega\omega_M}{Q_M}\right] x_M(f) = \frac{F_M(f)}{M_{\mathrm{tot}}}, \end{aligned} \tag{3.56}$$

$$-\omega^2[x_M(f) + x_s(f)] + \left[\omega_S^2 + \frac{i\omega\omega_s}{Q_s}\right] x_s(f) + \omega_s^2\, x_{s0} = \frac{F_s(f) + F_S}{m_s}, \tag{3.57}$$

$$\begin{aligned} -\omega^2\left[x_M(f) + x_{hi}(f)\right] - \omega^2\frac{\mu_{shi}}{\mu_{\mathrm{tot}hi}}x_{shi}(f) - \omega^2\frac{\mu_i}{\mu_{\mathrm{tot}hi}}x_i(f) + \omega_{hi}^2\, x_{hi0} \\ +\frac{\mu_{hi}}{\mu_{\mathrm{tot}hi}}\left[\omega_{hi}^2 + \frac{i\omega\omega_{hi}}{Q_{hi}}\right] x_{hi}(f) = \frac{F_{hi}(f)}{m_{\mathrm{tot}hi}}, \end{aligned} \tag{3.58}$$

$$-\omega^2\left[x_M(f)+x_{hi}(f)+x_{shi}(f)\right]+\left[\omega_{shi}^2+\frac{i\omega\omega_{shi}}{Q_{shi}}\right]x_{shi}(f)+\omega_{shi}^2\,x_{shi0} = \frac{F_{shi}(f)}{m_{shi}}, \quad (3.59)$$

and

$$-\omega^2\left[x_M(f)+x_{hi}(f)+x_i(f)\right]+\left[\omega_i^2+\frac{i\omega\omega_{mi}}{Q_i}\right]x_i(f)+\frac{k_{12}}{m_i}x_j(f)+\omega_{mi}^2x_{i0} = \frac{F_i(f)+F_{Di}}{m_i}, \quad (3.60)$$

where Q_M, Q_s, Q_{h1}, Q_{h2}, Q_{sh1}, Q_{sh2}, Q_1, and Q_2 are the quality factors of the involved masses, and the additional forces and new (angular) resonance frequencies ω_1, ω_2, and ω_S are introduced.

This group of equations can only be solved numerically. The coupling between the different masses and the effect that the displacement of some will have on the others is calculated using a Mathcad model containing all eight masses in addition to external ground noise. The parameters in the Mathcad program can be changed, and by doing so, different situations containing real, possible, or fictitious forces can be studied. The Mathcad program will be used to calculate all the conceivable sources of error we thought about. It is, however, convenient to have an algebraic solution.

In order to solve the problem algebraically, many approximations are needed. Some of these approximations are justified by construction, while others do not affect the full description of the system significantly and can be made. A justification for each assumption is given. I will start with the mechanical approximations.

The experiment was designed to have two symmetrical sides, each containing a housing and a test mass. By design, their masses and resonance frequencies were identical, limited by the machining precision. Four test masses were made out of a 250-mm thick Ta plate. They were weighed and their resonance frequencies were measured. The two test masses with closest properties were chosen for the experiment (0.02% error in their mass). The two housings were analyzed, weighed (0.08% error) and their resonance frequencies were measured (2.5% error). For this reason:

- Assume the masses of both test masses are equal. They will both be denoted by m.

- Assume the masses of both housings are equal, so m_h will be used for the masses and μ_h for the reduced masses.

- Assume the two housing resonance frequencies are the same.

Unfortunately, even though the housing resonance frequencies were closely matched initially, in reality, since one of the housings was damaged, its resonance frequency ended up being about 37% lower. This is a serious problem to be addressed; for a detailed discussion, see Section 7.1.

The quality factors of the test masses, source mass and shields have been measured, see Section 5.4, and are much bigger than unity. For this reason:

- Ignore the damping terms for the source mass and test masses.

The shields are much lighter than anything else (1% of the test masses, 0.01% of the housings), and since their behavior is not the main concern of the experiment:

- Ignore the equations of motion of the shields from the problem and in the case of coupling to the other masses, μ_{shi} is approximated to zero.

The test masses are much lighter than the housing (about 1%) and than the whole assembly (about .1%) so:

- Approximate μ_i to zero.

- A consequence of the previous two items is that $m_{\mathrm{tot}hi} = m_{hi}$.

All the above considerations and approximations give some errors in the final normal frequencies of the system. When the resonance frequencies obtained using the Mathcad model are compared with the ones using the approximations, there is a less than 2% discrepancy.

The following approximations on the other hand contributes for up to 6% error. The Q's for the housings and the suspension are bigger than unity:

- Ignore the damping terms for the housings and the suspension.

The source masses is much lighter than the experiment (about 3.5%). For this reason:

- Ignore the mass of the source.

With these, the equations can be written in matrix form:

$$\Omega(f)X(f) = A(f), \tag{3.61}$$

where $\Omega(f)$ is given by

$$\begin{pmatrix} \omega_M^2\mu_M - \omega^2 & 0 & -\omega^2\mu_h & -\omega^2\mu_h & 0 & 0 \\ -\omega^2 & \omega_S^2 - \omega^2 & 0 & 0 & 0 & 0 \\ -\omega^2 & 0 & \omega_{h1}^2 - \omega^2 & 0 & 0 & 0 \\ -\omega^2 & 0 & 0 & \omega_{h2}^2 - \omega^2 & 0 & 0 \\ -\omega^2 & 0 & -\omega^2 & 0 & \omega_{10}^2 - \omega^2 & k_{12}/m \\ -\omega^2 & 0 & 0 & -\omega^2 & k_{12}/m & \omega_{20}^2 - \omega^2 \end{pmatrix}, \tag{3.62}$$

and the displacement and acceleration are

$$X(f) = (x_M(f),\ x_s(f),\ x_{h1}(f),\ x_{h2}(f),\ x_1(f),\ x_2(f))^T \tag{3.63}$$

and

$$A(f) = (a_M(f),\ a_s(f),\ a_{h1}(f),\ a_{h2}(f),\ a_1(f),\ a_2(f))^T . \tag{3.64}$$

The eigenfrequencies of the matrix given by Eq. (3.62) are

$$\omega_1^2 = \frac{M_{\rm tot}\omega_h^2 + M\omega_M^2}{2M} - \frac{[(M_{\rm tot}\omega_h^2 + M\omega_M^2)^2 - 4M^2\omega_h^2\omega_M^2]^{1/2}}{2M}, \quad (3.65)$$

$$\omega_2^2 = \omega_S^2, \quad (3.66)$$

$$\omega_3^2 = \omega_h^2, \quad (3.67)$$

$$\omega_4^2 = \frac{M_{\rm tot}\omega_h^2 + M\omega_M^2}{2M} + \frac{[(M_{\rm tot}\omega_h^2 + M\omega_M^2)^2 - 4M^2\omega_h^2\omega_M^2]^{1/2}}{2M}, \quad (3.68)$$

$$\omega_5^2 = \frac{1}{2}(\omega_{10}^2 + \omega_{20}^2) - \frac{1}{2}\left[(\omega_{10}^2 - \omega_{20}^2)^2 + 4\frac{k_{12}^2}{m_1 m_2}\right]^{1/2}, \quad (3.69)$$

$$\omega_6^2 = \frac{1}{2}(\omega_{10}^2 + \omega_{20}^2) + \frac{1}{2}\left[(\omega_{10}^2 - \omega_{20}^2)^2 + 4\frac{k_{12}^2}{m_1 m_2}\right]^{1/2}. \quad (3.70)$$

Note that for this approximation, the source mass frequency is completely decoupled from the rest of the masses. According to the numerical Mathcad model, in the exact solution, this is modified by about 3.5%. In addition, the two test masses are completely decoupled from the rest of the masses. In the exact solution, this is modified by about .001%, making it a really good approximation. These result justify independently separating the source and the two test masses from the rest in order to obtain an in-depth model of the detector. I will use this fact in the reduced accelerometer model in the next section, as well as in the source mass model, in Section 3.5.

3.4 Reduced accelerometer model

In order to understand the detector, it is necessary to analyze the dynamics of the two test masses. Since to first approximation they decouple from the rest of the system, in this section, I will focus on the reduced accelerometer model consisting of the two test masses.

3.4.1 CM and DM resonance frequencies

Using Eqs. (3.39) and (3.43) in Eq. (3.11), and taking the Fourier transform gives

$$-\omega^2 x_1(f) + \left(\omega_{10}^2 + \frac{i\omega\omega_{m1}}{Q_1}\right)x_1(f) + \frac{k_{12}}{m_1}x_2(f) + \omega_{m1}^2 x_{10} = \frac{F_1(f) + F_{D1}}{m_1} \quad (3.71)$$

and

$$-\omega^2 x_2(f) + \left(\omega_{20}^2 + \frac{i\omega\omega_{m2}}{Q_2}\right) x_2(f) + \frac{k_{12}}{m_2} x_1(f) + \omega_{m2}^2 x_{20} = \frac{F_2(f) + F_{D2}}{m_2}. \quad (3.72)$$

For very high quality factors, the dynamic terms can be written in matrix form:

$$\begin{pmatrix} -\omega^2 + \omega_{10}^2 & k_{12}/m_1 \\ k_{12}/m_2 & -\omega^2 + \omega_{20}^2 \end{pmatrix} \begin{pmatrix} x_1(f) \\ x_2(f) \end{pmatrix} = \begin{pmatrix} a_1(f) \\ a_2(f) \end{pmatrix}, \quad (3.73)$$

where

$$a_i(f) = \frac{F_i(f) + F_{Di}}{m_i}. \quad (3.74)$$

The solutions are

$$x_1(f) = \frac{a_1(f)(\omega^2 - \omega_{20}^2) + a_2 k_{12}/m_1}{k_{12}^2/(m_1 m_2) - (\omega^2 - \omega_{10}^2)(\omega^2 - \omega_{20}^2)} \quad (3.75)$$

and

$$x_2(f) = -\frac{a_2(f)(\omega^2 - \omega_{10}^2) + a_1 k_{12}/m_2}{k_{12}^2/(m_1 m_2) - (\omega^2 - \omega_{10}^2)(\omega^2 - \omega_{20}^2)}. \quad (3.76)$$

The (angular) resonance frequencies can be identified as CM and DM

$$\omega_d^2 = \frac{1}{2}(\omega_{10}^2 + \omega_{20}^2) - \frac{1}{2}\left[(\omega_{10}^2 - \omega_{20}^2)^2 + 4\frac{k_{12}^2}{m_1 m_2}\right]^{1/2} \quad (3.77)$$

and

$$\omega_c^2 = \frac{1}{2}(\omega_{10}^2 + \omega_{20}^2) + \frac{1}{2}\left[(\omega_{10}^2 - \omega_{20}^2)^2 + 4\frac{k_{12}^2}{m_1 m_2}\right]^{1/2}. \quad (3.78)$$

They correspond to in-phase and out-of-phase motion of the two test masses, described by the CM and DM accelerations:

$$a_c(f) = \frac{1}{2}(a_1(f) + a_2(f)) \quad (3.79)$$

and

$$a_d(f) = a_1(f) - a_2(f). \quad (3.80)$$

3.4.2 DM and CM transfer functions

To derive the first-order acceleration-to-current transfer functions, it is necessary to determine the current through the SQUID. Using the conservation of flux in the loop containing L_{t2} and L_S,

$$I_s = I_{s0} + \frac{M_t}{L_{t2} + L_s}\left[I_1 + I_2 - I_{10} - I_{20}\right], \quad (3.81)$$

and with Eq. (3.37), the varying part of it is

$$I_s = \frac{M_t}{L_{t2}+L_s}\,\frac{-I_{20}L_{10}\lambda_2 x_2 - I_{10}L_{20}\lambda_1 x_1}{L_{\rm tot}^2}. \tag{3.82}$$

By using Eqs. (3.75) and (3.76) and expressing the answer in terms of the CM and DM accelerations, the time varying term from Eq. (3.82) can be written as

$$I_s(f) = H_{aI}^d(f)a_d(f) + H_{aI}^c(f)a_c(f), \tag{3.83}$$

where

$$\begin{aligned} H_{aI}^d(f) &= -\frac{M_t I_{10} m_2 L_{20}\lambda_1[k_{12}-m_1(\omega^2-\omega_{20}^2)]}{2(L_{t2}+L_s)L_{\rm tot}^2[k_{12}^2-m_1m_2(\omega^2-\omega_{10}^2)(\omega^2-\omega_{20}^2)]} \\ &- \frac{M_t I_{20} m_1 L_{10}\lambda_2[k_{12}-m_2(\omega^2-\omega_{10}^2)]}{2(L_{t2}+L_s)L_{\rm tot}^2[k_{12}^2-m_1m_2(\omega^2-\omega_{10}^2)(\omega^2-\omega_{20}^2)]} \end{aligned} \tag{3.84}$$

and

$$\begin{aligned} H_{aI}^c(f) &= \frac{M_t I_{20} m_1 L_{10}\lambda_2[k_{12}+m_2(\omega^2-\omega_{10}^2)]}{(L_{t2}+L_s)L_{\rm tot}^2[k_{12}^2-m_1m_2(\omega^2-\omega_{10}^2)(\omega^2-\omega_{20}^2)]} \\ &- \frac{M_t I_{10} m_2 L_{20}\lambda_1[k_{12}+m_1(\omega^2-\omega_{20}^2)]}{(L_{t2}+L_s)L_{\rm tot}^2[k_{12}^2-m_1m_2(\omega^2-\omega_{10}^2)(\omega^2-\omega_{20}^2)]}, \end{aligned} \tag{3.85}$$

$H_{aI}^d(f)$ and $H_{aI}^c(f)$ represent the acceleration-to-current transfer functions for the DM and CM, respectively.

3.4.3 CM balance

The circuit will operate purely in DM if the CM balance condition, $H_{aI}^c = 0$, is satisfied. Explicitly, this gives

$$\frac{I_{20}}{I_{10}} = \frac{m_2 L_{20}\lambda_1[k_{12}+m_1(\omega^2-\omega_{20}^2)]}{m_1 L_{10}\lambda_2[k_{12}+m_2(\omega^2-\omega_{10}^2)]} \tag{3.86}$$

for the ratio between the two sensing currents. This can be rewritten as

$$\frac{I_{10}\lambda_1/L_{10}}{-\omega^2+\omega_{1c}^2} = \frac{I_{20}\lambda_2/L_{20}}{-\omega^2+\omega_{2c}^2}, \tag{3.87}$$

where

$$\omega_{ic}^2 = \omega_{i0}^2 + \frac{k_{12}}{m_j} = \omega_{mi}^2 + \frac{k_i}{m_i} + \frac{k_{12}}{m_j} \tag{3.88}$$

are the equivalent frequencies of the two test masses with $i = 1, 2;\ j \neq i$. The CM balance condition is in general a frequency-dependent condition. Since our experiment is conducted at low frequency ($f \ll f_{1c}, f_{2c}$), it is possible to operate it with a balance in the neighborhood of f. However, due to the ground noise, the resonance frequencies of the two test masses are excited, overloading the SQUIDs. It is then desirable to obtain a frequency independent, or wide-band, balance. In order for Eq. (3.87) to be frequency independent, it is required that both

$$\omega_{1c}^2 = \omega_{2c}^2 \tag{3.89}$$

and

$$\frac{I_{10}\lambda_1}{L_{10}} = \frac{I_{20}\lambda_2}{L_{20}} \tag{3.90}$$

are simultaneously satisfied. Note that for high frequencies ($f \gg f_{1c}, f_{2c}$), Eq. (3.90) is satisfied. For very low frequencies, $f \ll f_{1c}, f_{2c}$, the CM balance condition becomes

$$\frac{1}{\omega_{1c}^2}\frac{I_{10}\lambda_1}{L_{10}} = \frac{1}{\omega_{2c}^2}\frac{I_{20}\lambda_2}{L_{20}}. \tag{3.91}$$

The actual achievement of the CM balance will be discussed in detail in Section 5.7.3.

3.4.4 Fully matched accelerometer approximation

For fully matched accelerometers, $m_1 = m_2 \equiv m$, $\omega_{m1} = \omega_{m2} \equiv \omega_m$, $\omega_{10} = \omega_{20} \equiv \omega_0$, $L_{10} = L_{20} \equiv L_{D0}$, $\lambda_1 = \lambda_2 \equiv \lambda$, $\gamma_1 = \gamma_2 \equiv \gamma$, and $k_1 = k_2 \equiv k$. In addition, the DM balance condition is satisfied if $I_{20} = I_{10}$, which I will call I_0. Under these conditions, and using Eqs. (3.42), (3.41), and (3.43), the CM and DM resonance frequencies become

$$\omega_c^2 = \omega_0^2 + \frac{k_{12}}{m} = \omega_m^2 + \frac{k}{m} + \frac{k_{12}}{m} = \omega_m^2 + \frac{I_0^2}{2m}\left[\frac{\lambda^2}{L_0} - \gamma\right] \tag{3.92}$$

and

$$\omega_d^2 = \omega_0^2 - \frac{k_{12}}{m} = \omega_m^2 + \frac{k}{m} - \frac{k_{12}}{m} = \omega_m^2 - \frac{I_0^2}{2m}\left[\frac{\lambda^2}{L_0 + 2L_e} + \gamma\right]. \tag{3.93}$$

From Eq. (3.84), using Eqs. (3.77) and (3.29)

$$H_{aI}^d(f) = \frac{M_t I_0 \lambda/2}{(L_{t2} + L_s)(L_{t1} + L_0/2) - M_t}\frac{1}{(\omega_d^2 - \omega^2)}. \tag{3.94}$$

Although not realistic, the fully matched accelerometer approximation is very useful for the estimation of the intrinsic noise of the detector as discussed in Section 4.4.2.

3.5 The source mass model

In order to understand the the actual motion of the source, it is necessary to analyze its dynamics when driven with an AC current. Since to first approximation the source decouples from the rest of the system, in this section, I will focus on the uncoupled source model. Eq. (3.57) can be rewritten as

$$-\omega^2 x_s(f) + \left[\omega_s^2 + \frac{i\omega\omega_s}{Q_s}\right] x_s(f) + \omega_s^2\, x_{s0} = \frac{F_s(f) + F_S}{m_s}, \tag{3.95}$$

where ω_S is given by Eq. (3.55) and F_S by (3.53). In Section 3.2.2, only DC currents were passing through L_{S1} and L_{S2}. Since the external force $F_s(\omega)$ comes from applied currents as well, in this section, I will generalize the treatment developed before to obtain the total external force acting on the source mass $F_s(\omega) + F_S$.

In order to drive the source sinusoidally, in addition to the previously defined steps:

- The source is driven by sending a small AC current i_S through the parallel combination of L_{S1}, L_{S2}, and L_{S3}. The AC current divides and the new currents are

$$I_{S1} = I_{S1\text{old}} - i_S\, \frac{L_{S2}L_{S3}}{(L_{S1}+L_{S2})L_{S3} + L_{S1}L_{S2}}, \tag{3.96}$$

$$I_{S2} = I_{S2\text{old}} + i_S\, \frac{L_{S1}L_{S3}}{(L_{S1}+L_{S2})L_{S3} + L_{S1}L_{S2}}, \tag{3.97}$$

$$I_{S3} = I_P - i_S\, \frac{L_{S1}L_{S2}}{(L_{S1}+L_{S2})L_{S3} + L_{S1}L_{S2}}. \tag{3.98}$$

Since L_{S3} does not depend on x_s, I expand only the currents through the two source coils. By using the explicit form of the inductance, the currents, to first order in x_s, are

$$I_{Si} = I_{Si0} + (-1)^i\, \frac{i_S L_{Sj0} L_{S3}}{L_{S\text{tot}}^2} + (-1)^i\, \frac{I_{Si0}(L_{Sj0}+L_{S3})\lambda_{Si} + I_{Sj0}L_{S3}\lambda_{Sj}}{L_{S\text{tot}}^2}\, x_s + i_S L_{S3}\, \frac{L_{Sj0}(L_{Sj0}+L_{S3})\lambda_{Si} + L_{Si0}L_{S3}\lambda_{Sj}}{L_{S\text{tot}}^4}\, x_s, \tag{3.99}$$

where again $i = 1, 2;\ j \neq i$; and

$$L^2_{S\text{tot}} = (L_{S10} + L_{S20})L_{S3} + L_{S10}L_{S20}.$$

The square of the currents is then, to first order in x_s,

$$\begin{aligned} I^2_{Si} &= I^2_{Si0} + 2(-1)^i I_{Si0}\ \frac{i_S L_{Sj0} L_{S3}}{L^2_{S\text{tot}}} + \frac{i_S^2 L^2_{Sj0} L^2_{S3}}{L^4_{S\text{tot}}} \\ &+ 2(-1)^i I_{Si0} \frac{I_{Si0}(L_{Sj0} + L_{S3})\lambda_{Si} + I_{Sj0} L_{S3}\lambda_{Sj}}{L^2_{S\text{tot}}}\, x_s \\ &+ 2 i_S L_{Sj0} L_{S3} \frac{I_{Si0}(L_{Sj0} + L_{S3})\lambda_{Si} + I_{Sj0} L_{S3}\lambda_{Sj}}{L^4_{S\text{tot}}}\, x_s \\ &+ 2 i_S I_{Si0} L_{S3}\ \frac{L_{Sj0}(L_{Sj0} + L_{S3})\lambda_{Si} + L_{Si0} L_{S3}\lambda_{Sj}}{L^4_{S\text{tot}}}\, x_s \\ &+ 2(-1)^i i_S^2 L_{Sj0} L^2_{S3}\ \frac{L_{Sj0}(L_{Sj0} + L_{S3})\lambda_{Si} + L_{Si0} L_{S3}\lambda_{Sj}}{L^4_{S\text{tot}}}\, x_s. \end{aligned} \tag{3.100}$$

Assuming matched coils: $L_{S1} = L_{S2} \equiv L_S$, $\lambda_{S1} = \lambda_{S2} \equiv \lambda_S$, $\gamma_{S1} = \gamma_{S2} \equiv \gamma_S$, using Eqs. (3.48), (3.49), and (3.101), and keeping only up to first-order terms in x_s and i_S, the current term in (3.15) can be rewritten as

$$\frac{1}{2}\sum_j I_j^2 \frac{\partial L_j}{\partial x_s} = \frac{1}{2}\sum_{i=1}^{2} \left[I^2_{Si}[(-1)^{i+1}\lambda + 2\gamma x_s] \right] = F_{S\text{tot}} - k_{S\text{tot}} x_s, \tag{3.101}$$

where

$$k_{S\text{tot}} = \frac{(I^2_{S10} + I^2_{S20})(L_{S0} + L_{S3}) + 2 + I_{S10} I_{S20} L_{S3}}{L_{S0}(L_{S0} + 2L_{S3})}\lambda^2 - (I^2_{S10} + I^2_{S20})\gamma \tag{3.102}$$

and

$$F_{S\text{tot}} = F_{\text{push}} + F_{\text{AC}}, \tag{3.103}$$

with

$$F_{\text{push}} = \frac{\lambda}{2}(I^2_{S10} - I^2_{S20}) \tag{3.104}$$

and

$$F_{\text{AC}} = -i_S \lambda \frac{(I_{S10} + I_{S20})L_{S3}}{L_{S0} + 2L_{S3}}. \tag{3.105}$$

Note that in this case, the total force contains both the force that pushes the source mass and centers it and the force used to drive it sinusoidally. In addition, with

Eq. (3.102), it is possible to define the modified resonance frequency of the source mass:

$$\omega_{S_{\rm tot}}^2 = \frac{k_s + k_{S\rm tot}}{m_s} = \omega_s^2 + \frac{k_{S\rm tot}}{m_s}. \tag{3.106}$$

With these, for very high quality factors, the dynamic terms of Eq. (3.95) can be written as:

$$\left[-\omega^2 + \omega_{S_{\rm tot}}^2\right] x_s(f) = -\frac{i_S(f)\lambda(I_{S10} + I_{S20})L_{S3}}{m_s(L_{S0} + 2L_{S3})}, \tag{3.107}$$

which has a solution

$$x_s(f) = -\frac{i_S(f)\lambda(I_{S10} + I_{S20})L_{S3}}{m_s(L_{S0} + 2L_{S3})\left[\omega_{S_{\rm tot}}^2 - \omega^2\right]}. \tag{3.108}$$

3.6 Summary

In this chapter, I obtained the equations of motion describing the full dynamic system of the ISL experiment. These equations were used to build a numerical Mathcad model containing all eight masses in addition to external ground noise. This model will be used to predict the coupling between the different masses and the effect that the displacement of some will have on the others. The parameters in the Mathcad program can be changed, and by doing so, different situations containing real, possible, or fictitious forces can be studied.

In addition, I justified the use of an uncoupled source model and a reduced accelerometer model. Using those simpler models, I described the motion of the source mass and of the test masses. I also performed an in-depth study of the CM and DM response of the detector.

The detailed analysis of the sensing and source circuits leads to obtaining the shift in resonance frequencies as a result of stored current in the source and sensing circuits and will be used later to determine the circuit parameters.

Chapter 4

Error Model

The success of a high-precision experiment depends on a large scale on the ability to identify, isolate, and distinguish the signal from the noise. For this reason, a good understanding of all the possible error sources is very important. In this chapter, I perform a detailed analysis of all the possible sources of error in the experiment and estimate their contributions.

The chapter is organized as follows: First, I analyze the metrology errors. Since the source is a null source, the requirements for metrological precision fall on the source. I follow with the circuit nonlinearities for both the sensing and the source circuits. Then, I discuss the errors in the superconducting accelerometer such as the centrifugal acceleration errors, the finite baseline error, the misalignment errors, and the CM balance error. Later, I consider the intrinsic noise of the detector, including the Brownian motion noise and the amplifier noise. Then I investigate the temperature noise and vibration noise. Finally, I estimate the errors due to magnetic cross-talk between the source and the detector, residual gas pressure, magnetic pressure, and electrostatic backgrounds that could be present in the ISL experiment.

4.1 Source mass metrology

The source mass is a disk of given diameter and thickness machined out of Ta. In this section, I will review some of the possible source mass metrology errors and estimate their value and importance. Originally, a Ta plate of a preselected thickness

was ordered. The thickness was not as uniform as expected. The analysis of the source metrology was performed in order to decide the tolerance requirements in the machining.

In this section, I will start by analyzing the ideal source situation, follow with the errors due to the radial and thickness tolerance, then compute the density fluctuation and the thickness variation errors as first-order corrections. Later I will calculate the radial taper and bowing errors. For the complete analysis with detailed derivations, see Appendix B. Note that I am not considering the errors in the detectors. In reality, the test masses do not have exact cylindrical symmetry. This asymmetry can be averaged out by repeating the experiment with the source mass rotated with respect to the test masses.

4.1.1 Calculation procedure

Consider one source mass and two test masses, both with density ρ. The source mass has a radius a and a thickness T. At an arbitrary instant, its center is located at $z = \delta z$, while its equilibrium position is $z = 0$ and is at a distance d from the center of each test mass. The test masses have a radius b and a thickness t and are positioned symmetrically with respect to $z = 0$. One of them is centered at $z = d$, and the other at $z = -d$. All the masses are concentric.

Following Appendix B, the source mass can be represented as a density distribution ρ that leads to a gravitational potential Φ at any point. From the potential, the force on each test mass is calculated. Once those forces are known, the differential and common forces are defined, respectively, as the difference and the half-sum of the forces on each test mass. From those forces, the differential and common acceleration of the two-test-mass system are calculated. For reference, the following constants are

used

$$\begin{aligned} G &= 6.673 \times 10^{-11}\ \mathrm{m}^3/\mathrm{kg.s}^2, \\ \rho_0 &= \rho_{Ta} = 1.66 \times 10^4\ \mathrm{kg/m}^3, \\ T &= 1.65 \times 10^{-3}\ \mathrm{m}, \\ t &= 2.50 \times 10^{-4}\ \mathrm{m}, \\ a &= 8.25 \times 10^{-2}\ \mathrm{m}, \\ b &= 3.50 \times 10^{-2}\ \mathrm{m}, \\ d &= T/2 + t/2 + 1.50 \times 10^{-4}\ \mathrm{m}, \\ \delta z &\in [-87.5, 87.5]\ \mu\mathrm{m}. \end{aligned} \tag{4.1}$$

4.1.2 Newtonian error: ideal source case

Even if the source was perfect, it would produce a signal due to its finite diameter. In the ideal case of an infinite source, this result would be zero.

As the source mass is driven at a frequency f along the symmetry axis, the amplitude of the differential acceleration corresponding to the source displacement δz_{max}, according to Eq. (B.17) from Appendix B, is

$$\Delta a_d(2f) = 2.23 \times 10^{-16}\ \mathrm{m/s}^2, \tag{4.2}$$

rms. The CM acceleration, given by Eq. (B.20), on the other hand, is

$$\Delta a_c(f) = 7.49 \times 10^{-12}\ \mathrm{m/s}^2, \tag{4.3}$$

rms. For simplicity, all accelerations values in this chapter will be rms.

The differential acceleration, Δa_d, represents the Newtonian error due to the finite diameter of the source and appears at $2f$, which is the signal frequency. This error could be corrected to one part in 100 to 1000, if necessary. Note that the CM acceleration is much larger than the DM. Even though a CM rejection of 10^4 will be applied, this signal will still be larger than the Newtonian signal. Nevertheless, this will not be a problem, since it appears at the fundamental frequency f.

4.1.3 Radius and absolute thickness errors

For the radius error, in addition to the values (4.1), I consider the case where the radius of the source has an error of up to 10 μm with respect to the previously specified value. This gives a differential acceleration that differs from the ideal case by

$$\Delta a_d(2f) = 1.28 \times 10^{-19} \text{ m/s}^2. \tag{4.4}$$

I assume now that the thickness of the source differs by up to 10 μm from the previously specified value. I still assume that the mass is centered (the case of thickness error on only one side will be analyzed later). This gives a differential acceleration that differs from the ideal case by

$$\Delta a_d(2f) = 2.47 \times 10^{-18} \text{ m/s}^2. \tag{4.5}$$

4.1.4 Density fluctuation

The variations of the density lead to modifications in the detectable gravitational field. Those modifications will depend on the amount of impurities present in the sample. The density is expressed as a constant plus an error term, according to Eq. (B.21):

$$\rho(r') = \rho_0 + \Delta_\rho \rho(r'). \tag{4.6}$$

Due to the cylindrical symmetry of the problem, the density fluctuations $\Delta_\rho \rho(r')$ are expanded in terms of the Fourier-Bessel series. By using the Bessel expansion of the Greens function, the force on the test mass is further expanded. Each term of the expansion can be numerically integrated and in this way, the Newtonian error for each order is computed. The rms value of these terms is used to calculate the average sensitivity of the experiment to the density fluctuations.

There are two advantages to this method of calculation. On one hand, it allows comparison of the results with its limit of constant density, verification of the validity of the expansion and determination of the minimum number of terms necessary to get the required accuracy. On the other hand, it would give an estimate of the

variation of the potential corresponding to a given variation of the density. This can be used to determine the specification on the density in order to obtain a result with a desired precision.

If the results are to be compared with those of constant density from the previous subsection, the following modifications need to be made:

- Eq. (B.21) is to be taken as $\rho(r') = \Delta_\rho \rho(r')$.
- Since we are trying to reproduce the case of constant density ρ_0, $\Delta_\rho \rho(r')$ needs to be taken as constant equal to ρ_0.
- All results are total potentials, forces, and accelerations, and not small variations on them. It is concluded that 1500 terms from the Bessel expansion are probably the optimum number, since adding subsequent terms gives a variation of less than 1% from the value. The terms decrease rapidly.

This procedure gives

$$\Delta a_d(2f) = (2.217 \pm 0.014) \times 10^{-16} \text{ m/s}^2, \tag{4.7}$$

which reproduces the result from Eq. (4.2).

If the result is to be used to estimate the actual value of the error introduced by certain density fluctuation, the following procedure is used. Each term of the expansion can be numerically integrated to obtain the Newtonian error for each order. Recall that the density error $\Delta_\rho \rho(r')$ is not known *a priori*. It can only be estimated or some specific dependence can be assumed.

I represent $\Delta_\rho \rho(r')$ as a random number times the initial constant density of the sample ρ_0. Since the error coefficients A_{0n}, given by Eq. (B.23), are assumed to be independent of one another, I apply a different random number α_n for each coefficient:

$$A_{0n} = \frac{2\alpha_n \rho_0}{a^2 J_1^2(x_{0n})} \int_0^a dr' r' J_0\left(\frac{x_{0n} r'}{a}\right) = \frac{2\alpha_n \rho_0}{J_1(x_{0n}) x_{0n}}. \tag{4.8}$$

By choosing a random set of coefficients in the range of the density variation limits, it is possible to estimate the total density fluctuation error. Note that the total

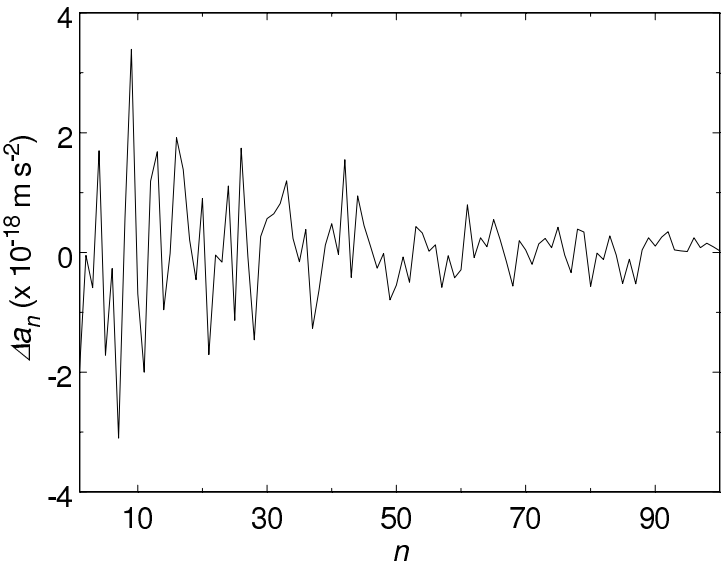

Figure 4.1: Acceleration error due to density fluctuations of 10^{-4}.

density fluctuation error will correspond to this particular set of coefficients. (In practice, those coefficients may not be totally random, but have a certain pattern, depending on the machining and lapping method.) For one set of random coefficients, see Figure 4.1.

By repeating this calculation a large number of times and averaging the result, we can estimate the actual error in the experiment. Taking 100 different sets of random numbers α_n in the range $[-10^{-4}, 10^{-4}]$ and repeating this several times to get a reasonable estimate, the rms error in the amplitude of the differential acceleration corresponding to the source displacement δz_{max} is

$$\Delta_\rho \Delta a_d(2f) = 1.6 \times 10^{-18} \text{ m/s}^2. \tag{4.9}$$

As expected, this is a very small error.

4.1.5 Thickness variation

The thickness variation can be modeled as surface density fluctuations of the source mass. The size of these fluctuations can be adjusted to match the mass errors due

to the thickness variation. To accommodate the mass error due to the thickness variation, the density is expressed as a constant plus an error term, according to Eq. (B.38):

$$\rho(r', z') = \rho_0 + \Delta_T \rho(r', z'). \tag{4.10}$$

In order to estimate the actual value of the error introduced by a thickness fluctuation of a given maximum magnitude, the following procedure is used. Each term of the expansion can be numerically integrated to find the Newtonian error for each order. It is concluded that 1200 terms are probably the optimum number, since subsequent terms give a variation of less than 1% from the value. The terms decrease rapidly.

I will use the same density fluctuation procedure to estimate the actual value of the error introduced by certain thickness fluctuations. I represent $\Delta Z_+(r')$ and $\Delta Z_-(r')$ in Eq. (B.41) as independent sets of random numbers ΔZ_{n+} and ΔZ_{n-} of magnitude in the range of the thickness variations. Then the coefficients become

$$B_{0n\pm} = \frac{2\Delta Z_{n\pm}}{a^2 J_1^2(x_{0n})} \int_0^a dr' r' J_0\left(\frac{x_{0n} r'}{a}\right) = \frac{2\Delta Z_{n\pm}}{J_1(x_{0n}) x_{0n}}. \tag{4.11}$$

Note that the resulting total thickness fluctuation error corresponding to each set of random coefficients will also be random. For one set of random coefficients, see Figure 4.2.

By repeating this calculation a large number of times and averaging the result, the actual error in the experiment can be estimated. The error is calculated for 100 different sets of random numbers with $\Delta Z_{n\pm}$ in the range $[-10^{-5}, 10^{-5}]$ and an average is estimated. This corresponds to a thickness error of 10 μm rms. According to Eq. (B.51) or thickness fluctuations in the range of 87.5 μm, the rms error is found to be

$$\Delta_T \Delta a_{d\text{thick}}(2f) = 2.02 \times 10^{-15} \text{ m/s}^2. \tag{4.12}$$

4.1.6 Radial taper

It is assumed that there is radial taper only on one side of the source mass. I consider a taper of 10 μm, which corresponds to a taper-to-radius ratio error of $\sigma = 0.0001212$. The radial taper will produce an error mainly at the source driving

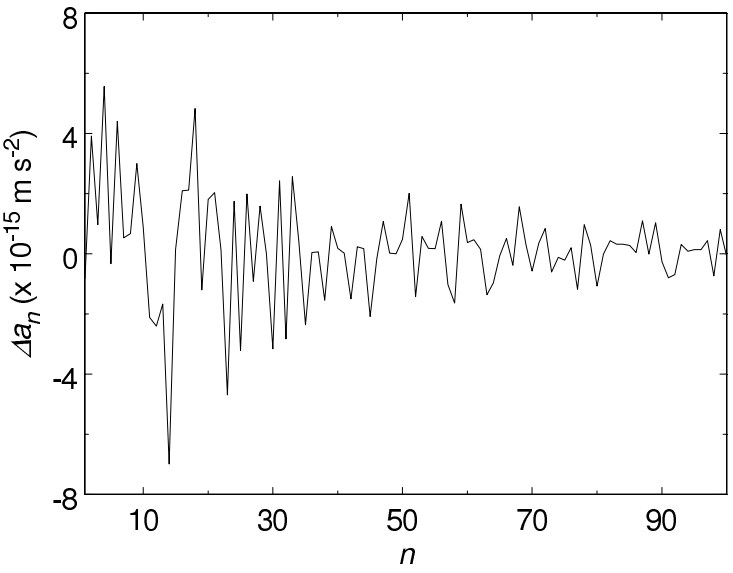

Figure 4.2: Acceleration error due to thickness fluctuations of 10 μm.

frequency f. The signals at $2f$ are calculated using the nonlinearity coupling, as explained in Section 4.2.

The signals at f are, from Eqs. (B.62) and (B.65):

$$\Delta a_d(f) = 2.61 \times 10^{-15} \text{ m/s}^2 \tag{4.13}$$

and

$$\Delta a_c(f) = 1.72 \times 10^{-14} \text{ m/s}^2. \tag{4.14}$$

4.1.7 Static and dynamic bowing

A static bowing (independent on the source mass motion) of 10 μm in magnitude corresponds to a bowing coefficient of $\xi = 0.00147$ m^{-1}. The signals at f from Eqs. (B.73) and (B.76) are

$$\Delta a_d(f) = 4.391 \times 10^{-14} \text{ m/s}^2 \tag{4.15}$$

and

$$\Delta a_c(f) = 1.150 \times 10^{-15} \text{ m/s}^2. \tag{4.16}$$

The static bowing produces a much smaller error at $2f$. The signals at $2f$ are

$$\Delta a_d(2f) = 6.500 \times 10^{-19}\ \mathrm{m/s^2} \tag{4.17}$$

and

$$\Delta a_c(2f) = 1.728 \times 10^{-17}\ \mathrm{m/s^2}. \tag{4.18}$$

According to our finite element analysis (FEA), the amplitude of the dynamic bowing is 0.07 μm for a source of thickness $T = 1.65\,\mathrm{mm}$. A dynamic bowing (proportional to the source mass motion) of 0.07 μm in magnitude corresponds to a dynamic bowing coefficient of $\varepsilon = 0.2057\ \mathrm{m^{-2}}$. The signals at f from Eqs. (B.84) and (B.87) are

$$\Delta a_d(f) = 1.25 \times 10^{-14}\ \mathrm{m/s^2} \tag{4.19}$$

and

$$\Delta a_c(f) = 1.52 \times 10^{-13}\ \mathrm{m/s^2}, \tag{4.20}$$

while the signals at $2f$ are

$$\Delta a_d(2f) = 3.78 \times 10^{-16}\ \mathrm{m/s^2} \tag{4.21}$$

and

$$\Delta a_c(2f) = 4.08 \times 10^{-18}\ \mathrm{m/s^2}. \tag{4.22}$$

4.1.8 Total source metrology

The estimated errors can be summarized in Table 4.1. The radius and absolute thickness are very small errors. They appear as a deviation from the Newtonian error and would become important only if we were to compensate for it. Note that the largest error comes from the thickness fluctuations. This means that if the source metrology was the limiting error in the experiment, a new more precisely machined source would be a must.

Error Source	Allowance	Error ($\times 10^{-16}$ m/s^2)
Radius	10 μm	0.001
Absolute thickness	10 μm	0.024
Density fluctuations	10^{-4}	0.02
Radial thickness fluctuations	10 μm	20.2
Radial taper	10 μm	0.41
Bowing (static)	10 μm	0.006
Bowing (dynamic)	0.07 μm	3.8
Total error		20.6

Table 4.1: Source mass metrology errors.

4.2 Circuit nonlinearities

The superconducting coils are nonlinear. Part of their nonlinearity comes from the superconducting plane (see Appendix A), but there is also the edge effect, as well as the curvature of the wire. In addition, in superconducting circuits, nonlinearity comes from the flux quantization condition. Additional nonlinearities come from the fact that the involved inductances are not identical. The nonlinearity of single superconducting coils can be determined by measuring the displacement of a known superconducting mass as a function of the stored current. The total nonlinearity found this way is usually about 3 times the nonlinearity coming from the back plane, but the actual number varies with the coil geometry and spacings. In this section, I will analyze the nonlinearities of the sensing circuits and the source circuit.

4.2.1 Sensing circuits

In Section 3.4.2, the first-order acceleration-to-current transfer functions were found by determining the current through the SQUID, expanding it to first order in x_1 and x_2, and expressing it in terms of a_c and a_d, respectively. If instead of expanding to first order in x_1 and x_2, we keep the second-order terms as well, and substitute the

corresponding common and differential accelerations, Eq. (3.83) is replaced by

$$I_s = H_d a_d + H_c a_c + H_{dd} a_d^2 + H_{cc} a_c^2 + H_{cd} a_c a_d, \tag{4.23}$$

where H_d and H_c correspond to

$$\begin{aligned} H_{aI}^d &= -\frac{M_t I_{10} m_2 L_{20} \lambda_1 (k_{12} - m_1(\omega^2 - \omega_{20}^2))}{2(L_{t2}+L_s)L_{tot}^2[k_{12}^2 - m_1 m_2(\omega^2-\omega_{10}^2)(\omega^2-\omega_{20}^2)]} \\ &- \frac{M_t I_{20} m_1 L_{10} \lambda_2 (k_{12} - m_2(\omega^2 - \omega_{10}^2))}{2(L_{t2}+L_s)L_{tot}^2[k_{12}^2 - m_1 m_2(\omega^2-\omega_{10}^2)(\omega^2-\omega_{20}^2)]} \end{aligned} \tag{4.24}$$

and

$$\begin{aligned} H_{aI}^c &= \frac{M_t I_{20} m_1 L_{10} \lambda_2 (k_{12} + m_2(\omega^2 - \omega_{10}^2))}{(L_{t2}+L_s)L_{tot}^2[k_{12}^2 - m_1 m_2(\omega^2-\omega_{10}^2)(\omega^2-\omega_{20}^2)]} \\ &- \frac{M_t I_{10} m_2 L_{20} \lambda_1 (k_{12} + m_1(\omega^2 - \omega_{20}^2))}{(L_{t2}+L_s)L_{tot}^2[k_{12}^2 - m_1 m_2(\omega^2-\omega_{10}^2)(\omega^2-\omega_{20}^2)]}, \end{aligned} \tag{4.25}$$

as was given by Eqs. (3.84) and (3.85), while H_{dd}, H_{cc}, and H_{cd} become

$$\begin{aligned} H_{dd} &= -\frac{M_t I_{10} L_{20} m_2^2 (L_{tot}^2 \gamma_2 - (L_{20}+L_e)\lambda_1^2)(k_{12} - m_1(\omega^2-\omega_{20}^2))^2}{(L_{t2}+L_s)(2L_{tot})^4[k_{12}^2 - m_1 m_2(\omega^2-\omega_{10}^2)(\omega^2-\omega_{20}^2)]} \\ &- \frac{M_t (I_{10}L_{10} + I_{20}L_{20}) L_e m_1 m_2 \lambda_1 \lambda_2 (k_{12} - m_1(\omega^2-\omega_{20}^2))(k_{12} - m_2(\omega^2-\omega_{10}^2))}{(L_{t2}+L_s)(2L_{tot})^4[k_{12}^2 - m_1 m_2(\omega^2-\omega_{10}^2)(\omega^2-\omega_{20}^2)]^2} \\ &- \frac{M_t I_{20} L_{10} m_1^2 (L_{tot}^2 \gamma_1 - (L_{10}+L_e)\lambda_2^2)(k_{12} - m_2(\omega^2-\omega_{10}^2))^2}{(L_{t2}+L_s)(2L_{tot})^4[k_{12}^2 - m_1 m_2(\omega^2-\omega_{10}^2)(\omega^2-\omega_{20}^2)]^2}, \end{aligned} \tag{4.26}$$

$$\begin{aligned} H_{cc} &= -\frac{M_t I_{10} L_{20} m_2^2 (L_{tot}^2 \gamma_2 - (L_{20}+L_e)\lambda_1^2)(k_{12} + m_1(\omega^2-\omega_{20}^2))^2}{(L_{t2}+L_s)(2L_{tot})^4[k_{12}^2 - m_1 m_2(\omega^2-\omega_{10}^2)(\omega^2-\omega_{20}^2)]} \\ &- \frac{M_t (I_{10}L_{10} + I_{20}L_{20}) L_e m_1 m_2 \lambda_1 \lambda_2 (k_{12} + m_1(\omega^2-\omega_{20}^2))(k_{12} + m_2(\omega^2-\omega_{10}^2))}{(L_{t2}+L_s)(2L_{tot})^4[k_{12}^2 - m_1 m_2(\omega^2-\omega_{10}^2)(\omega^2-\omega_{20}^2)]^2} \\ &- \frac{M_t I_{20} L_{10} m_1^2 (L_{tot}^2 \gamma_1 - (L_{10}+L_e)\lambda_2^2)(k_{12} + m_2(\omega^2-\omega_{10}^2))^2}{(L_{t2}+L_s)(2L_{tot})^4[k_{12}^2 - m_1 m_2(\omega^2-\omega_{10}^2)(\omega^2-\omega_{20}^2)]^2}, \end{aligned} \tag{4.27}$$

and

$$\begin{aligned} H_{cd} &= \frac{M_t I_{10} L_{20} m_2^2 (L_{tot}^2 \gamma_2 - (L_{20}+L_e)\lambda_1^2)(k_{12}^2 - m_1^2(\omega^2-\omega_{20}^2)^2)}{(L_{t2}+L_s)(2L_{tot})^4[k_{12}^2 - m_1 m_2(\omega^2-\omega_{10}^2)(\omega^2-\omega_{20}^2)]} \\ &+ \frac{M_t k_{12} (I_{10}L_{10} + I_{20}L_{20}) L_e m_1 m_2 \lambda_1 \lambda_2 (m_2(\omega^2-\omega_{10}^2) + m_1(\omega^2-\omega_{20}^2))}{(L_{t2}+L_s)(2L_{tot})^4[k_{12}^2 - m_1 m_2(\omega^2-\omega_{10}^2)(\omega^2-\omega_{20}^2)]^2} \\ &+ \frac{M_t I_{20} L_{10} m_1^2 (L_{tot}^2 \gamma_1 - (L_{10}+L_e)\lambda_2^2)(k_{12}^2 - m_2^2(\omega^2-\omega_{10}^2)^2)}{(L_{t2}+L_s)(2L_{tot})^4[k_{12}^2 - m_1 m_2(\omega^2-\omega_{10}^2)(\omega^2-\omega_{20}^2)]^2}, \end{aligned} \tag{4.28}$$

with

$$L_{tot}^2 = (L_{10}+L_{20})L_e + L_{10}L_{20}.$$

H_d	H_c	H_{cc}	H_{dd}	H_{cd}
0.1890	4.71×10^{-6}	0.1565	0.0285	-0.0159

Table 4.2: Transfer function contributions assuming wide-band balance; H_d is in A/(m/s^2), while H_{cc}, H_{dd}, and H_{cd} are in A/(m/s^2)^2.

The ISL experiment is designed so that when driving the source mass at f, any violation signal would appear at $2f$ in the DM output. The CM output appears at f. Consequently, a piece of the $H_{cc}a_c^2$ term will also appear at $2f$. An important exercise is to estimate the maximum amount of CM acceleration (due to tilt of the whole assembly as well as to other forces) that we will be able to tolerate before seeing a signal.

The acceleration-to-current transfer functions were calculated using a numerical model. The numerical model was used to predict the coil parameters, spacings, measured resonance frequencies, and measured inductances (reported in Chapter 5), as well as the currents necessary for a wide-band balance of the present experiment. We assume that the CM balance is good to one part in 4×10^4, which corresponds to $H_c/H_d = 2.5 \times 10^{-5}$. The actual CM balance is discussed in Section 5.8. Table 4.2 summarizes the transfer functions obtained from the numerical model. Note that the the CM misbalance is represented by $\delta h^c = H_c/H_d$, while the second-order contribution comes from H_{cc}, so the circuit nonlinearity is defined as $\delta\epsilon_{nl} = H_{cc}/H_d$. Assuming that the CM and DM contribute only the fundamental frequency, Table 4.3 shows the fundamental and second harmonic contributions to the transfer functions for various CM and DM accelerations.

4.2.2 Source driving circuit

In Section 3.5, I assumed matched source driving coils and kept only up to first-order terms in x_s and i_S. However, the two source driving coils are not identical. If we take this into consideration and keep up to second-order terms in i_S, even for a purely sinusoidal current drive i_S, there will be second harmonic contribution in the motion of the source. All of these are second-order effects, but it is still useful to estimate

a_c (m/s^2)	a_d (m/s^2)	Contribution at f (A)	Contribution at $2f$ (A)
10^{-5}	0	4.71×10^{-11}	7.82×10^{-12}
0	10^{-5}	1.89×10^{-11}	1.43×10^{-22}
10^{-5}	10^{-5}	6.60×10^{-11}	7.82×10^{-12}
10^{-10}	0	4.71×10^{-16}	7.82×10^{-22}
0	10^{-10}	1.89×10^{-16}	1.43×10^{-32}
10^{-10}	10^{-10}	6.60×10^{-16}	7.82×10^{-22}

Table 4.3: Transfer function contributions corresponding to wide-band balance.

them since they add up with other errors.

By considering the general case of unmatched inductances and keeping all terms up to second-order in i_S , the total force $F_{S\text{tot}}$ given by Eq. (3.103) can be rewritten as

$$F_{S\text{tot}} = F_{\text{DC}} + F_{\text{AC}}(f) + F_{\text{AC}}(2f), \tag{4.29}$$

where f is the driving frequency and the three force terms are

$$F_{\text{DC}} = \frac{\lambda_1 I_{S10}^2 - \lambda_2 I_{S20}^2}{2}, \tag{4.30}$$

$$F_{\text{AC}}(f) = -i_S(f) L_{S3} \frac{\lambda_1 I_{S10} L_{S20} + \lambda_2 I_{S20} L_{S10}}{L_{S\text{tot}}^2}, \tag{4.31}$$

and

$$F_{\text{AC}}(2f) = -i_S^2(f) L_{S3}^2 \frac{\lambda_1 L_{S20}^2 - \lambda_2 L_{S10}^2}{2 L_{S\text{tot}}^4}. \tag{4.32}$$

The first term represents the DC force used to center the source mass. The second term is the source drive and is proportional to the driving AC current. Since the last term is proportional to the driving AC current squared, it gives a second harmonic contribution. In order to estimate how large this contribution is, I take the ratio between the second harmonic and the fundamental contributions:

$$\frac{F_{\text{AC}}(2f)}{F_{\text{AC}}(f)} = \frac{i_S(f) L_{S3}}{2 L_{S\text{tot}}^2} \frac{\lambda_2 L_{S10}^2 - \lambda_1 L_{S20}^2}{\lambda_1 I_{S10} L_{S20} + \lambda_2 I_{S20} L_{S10}}. \tag{4.33}$$

The two main contributing factors on how large that ratio is are:

- The ratio between the AC and the DC currents.

- How mismatched the two coils/inductaces are.

For the second factor, I use the values measured in the experiment. For the last cool-down, the measured inductances were $L_{S10} = 6.76\,\mathrm{mH}$, $L_{S20} = 6.49\,\mathrm{mH}$, and the calculated coil parameters $\lambda_1 = 2.39\,\mathrm{H/m}$, $\lambda_2 = 3.66\,\mathrm{H/m}$. The initial values for the DC current passing through the source coils can be described by Eqs. (3.46) and (3.47).

The estimate of the ratio between the AC and the DC currents can be obtained as follows: As $F_{\mathrm{AC}}(2f)$ is increased, so is the amplitude of the source displacement. Increasing I_{S10} and I_{S20} will increase that force, but it will also stiffen the source mass, making it harder to move, according to Eq. (3.106).

In the actual experiment, the source had a DC current in series ranging between 0.5 A and 1 A. An additional DC current in parallel of up to 30 mA was used to push the source. From Eq. (4.33), and using the AC currents needed to displace the source by 15 μm, the nonlinearity ratio was determined to be up to 5×10^{-3}.

4.3 Differential accelerometer error model

As the source mass is driven inside the housing, there is a reaction force on the entire platform that makes it recoil, and since it is suspended on three points, it makes it rotate as well. Consequently, the platform is a rotating and linearly accelerating reference frame. The experiment is designed so the tilt can be reduced by a factor of 100 by doing tilt control. The displacement can be reduced as well with the shaker coils. However, if the differential accelerometer is not perfectly aligned and balanced, the residual tilt and displacement of the platform brings additional errors. Each accelerometer is located in a rotating and linearly accelerating reference frame. The linear acceleration of the main body of the experiment was considered in Chapter 3. The rotation of it, however, was ignored. In this section, I will analyze the error model of the accelerometer starting with a discussion of a non-inertial frame of reference, including the rotation and linear acceleration. I will then focus on the centrifugal acceleration error, obtain the gravity noise error, and finally introduce misalignment

and misbalance errors.

4.3.1 Non-inertial frame of reference

If $\vec{r}$ is the position of the test mass of one accelerometer with respect to the platform, and $\vec{r}_M$ and $\vec{\Omega}$ the position and angular velocity of the platform with respect to the inertial reference frame, the acceleration of the test mass is calculated as

$$\vec{a} = -\ddot{\vec{r}}_M - \nabla\phi - 2\vec{\Omega} \times \dot{\vec{r}} - \vec{\Omega} \times (\vec{\Omega} \times \vec{r}) - \dot{\vec{\Omega}} \times \vec{r}, \tag{4.34}$$

the acceleration of a body in a non-inertial frame of reference (For a detailed derivation, see [23, 35]). Here the first term on the righthand side is the acceleration of the platform, the second term is the gravitational acceleration, the third term is the Coriolis acceleration, the fourth term the centrifugal acceleration, and the last term is related to the non-uniformity of the rotation and couples the angular acceleration to the linear acceleration in proportion to the displacement of the test mass with respect to the platform. Since there are two test masses, Eq. (4.34) has to be written for each one of them. I will assume that both accelerometers are sensitive along the same axis $\hat{n}$ and are located at

$$\vec{r}_i(t) = (-1)^i \, \vec{l}/2 + \vec{x}_i(t), \tag{4.35}$$

where $i = 1, 2$ labels the test mass, $-\vec{l}/2$ and $\vec{l}/2$ represent their equilibrium positions, and $\vec{x}_1(t)$ and $\vec{x}_2(t)$ the respective displacements away from equilibrium. Substituting Eq. (4.35) into (4.34), the accelerations are

$$\begin{aligned} \vec{a}_i = &-\ddot{\vec{r}}_M - \nabla\phi(\vec{x}_i + (-1)^i \, \vec{l}/2) - 2\vec{\Omega} \times \dot{\vec{x}}_i - \vec{\Omega} \times (\vec{\Omega} \times \vec{x}_i) \\ &+(-1)^{i-1} \, \frac{1}{2}\vec{\Omega} \times (\vec{\Omega} \times \vec{l}) - \dot{\vec{\Omega}} \times \vec{x}_i + (-1)^{i-1} \, \frac{1}{2}\dot{\vec{\Omega}} \times \vec{l}. \end{aligned} \tag{4.36}$$

Taking the component along the sensitive axis,

$$\begin{aligned} a_i = &-\hat{n} \cdot \ddot{\vec{r}}_M - \hat{n} \cdot \nabla\phi(\vec{x}_i + (-1)^i \, \vec{l}/2) - 2\hat{n} \cdot (\vec{\Omega} \times \dot{\vec{x}}_i) - \hat{n} \cdot [\vec{\Omega} \times (\vec{\Omega} \times \vec{x}_i)] \\ &+(-1)^{i-1} \, \frac{\hat{n}}{2} \cdot [\vec{\Omega} \times (\vec{\Omega} \times \vec{l})] - \hat{n} \cdot (\dot{\vec{\Omega}} \times \vec{x}_i) + (-1)^{i-1} \, \frac{\hat{n}}{2} \cdot (\dot{\vec{\Omega}} \times \vec{l}). \end{aligned} \tag{4.37}$$

In addition to both accelerometers having identical sensitive axis, $\hat{n}$, I will further assume that $\hat{n}$ is collinear with their separation. Then,

$$\vec{x}_i = x_i \hat{n} \tag{4.38}$$

and

$$\vec{l} = l\hat{n}. \tag{4.39}$$

With this, Eq. (4.37) becomes

$$a_i = -\hat{n} \cdot \ddot{\vec{r}}_M - \hat{n} \cdot \nabla\phi(\vec{x}_i + (-1)^i \vec{l}/2) + [\Omega^2 - (\Omega \cdot \hat{n})^2](\vec{x}_i + (-1)^i \vec{l}/2). \tag{4.40}$$

Note that $\vec{x_1}$ and $\vec{x_2}$ are infinitesimal and will be dropped in comparison to $\vec{l}$.

Since the CM and DM accelerations are given by

$$a_c = \frac{a_1 + a_2}{2} \tag{4.41}$$

and

$$a_d = a_1 - a_2 = \Gamma l, \tag{4.42}$$

where Γ is the DM signal (different from the gravity gradient tensor Γ_{ij}) and l is the baseline between the two accelerometers. Simplifying Eq. (4.37) and substituting Eqs. (4.41) and (4.41),

$$a_c = -\hat{n} \cdot \ddot{\vec{r}}_M - \frac{\hat{n}}{2} \cdot [\nabla\phi(-\vec{l}/2) + \nabla\phi(\vec{l}/2)] \tag{4.43}$$

and

$$a_d = -\hat{n} \cdot [\nabla\phi(\vec{l}/2) - \nabla\phi(-\vec{l}/2)] + l\Omega^2 - l(\Omega \cdot \hat{n})^2. \tag{4.44}$$

In the limit when l approaches zero,

$$a_c = -\hat{n} \cdot \ddot{\vec{r}}_M + \hat{n} \cdot \vec{g} \tag{4.45}$$

and

$$a_d = \Gamma_{ij} n^i n^j l + l\Omega^2 - l(\vec{\Omega} \cdot \hat{n})^2, \tag{4.46}$$

where $g = -\nabla\phi$ and $\Gamma_{ij} = -\partial_i \partial_j \phi$.

Note that I have assumed first that both accelerometers have the same sensitive axis $\hat{n}$, second, that it is aligned with their axis of separation, and third, that the

baseline approaches zero. Under these assumptions, the CM output is sensitive to platform motion and gravity signal along the sensitive axis, while the DM output is sensitive to gravity gradients as well as centrifugal acceleration. We want to measure pure gravity gradients and minimize any other detected signals. Eq. (4.46) can be rewritten as

$$a_d = \Gamma_{ij} n^i n^j \, l + \delta a_d, \tag{4.47}$$

where δa_d represents those additional signals. In the remainder of this section, I will be analyzing all the terms included in δa_d.

4.3.2 Centrifugal acceleration error

The sensitivity of the differential accelerometer to rotational motion comes from the fact that any rotational motion tends to pull both test masses outward. The differential acceleration due to this rotation is given by

$$\delta a_{d_{rot}} = l\Omega^2 - l(\vec{\Omega} \cdot \hat{n})^2, \tag{4.48}$$

and is an effective tidal gravitational acceleration given by the centrifugal acceleration. As mentioned previously, this error is minimized by using tilt compensation. Alternatively, due to its specific form, when not compensated, this signal is used to calibrate the sensitivity of the differential accelerometer.

4.3.3 Gravity gradient noise

In Section 4.3.1, I assumed that the baseline is zero. However, the differential accelerometer comprises two test masses, so there is a finite baseline between them. This baseline introduces an additional error in the measurement of the gravitational gradient and can be calculated by subtracting the differential signal of an ideal differential accelerometer from the signal of one with a finite baseline

$$a_d = -\hat{n} \cdot [\nabla\phi(\vec{l}/2) - \nabla\phi(-\vec{l}/2)] - \Gamma_{ij} n^i n^j \, l. \tag{4.49}$$

Expanding $\nabla\phi$ in a Taylor series, the lowest order term is

$$\delta a_{d_{grav}} = -\frac{l^3}{24}(\hat{n} \cdot \nabla)^4 \phi. \tag{4.50}$$

With a baseline of only 2.41 mm, the experiment has only a very small coupling to the gravity noise of the environment.

4.3.4 Misalignment error

In Section 4.3.1, I assumed that both accelerometers have the same sensitive axis $\hat{n}$, and that this axis is aligned with their baseline $\vec{l} = l\hat{n}$. The real life situation is much different. Each accelerometer is sensitive along an individual axis, and neither of those axis are along their baseline. In this case, Eq. (4.37) is modified to

$$a_i = -\hat{n}_i \cdot \ddot{\vec{r}}_M - \hat{n}_i \cdot \nabla\phi(\vec{x}_i + (-1)^i\,\vec{l}/2) - 2\hat{n}_i \cdot (\vec{\Omega} \times \dot{\vec{x}}_i) - \hat{n}_i \cdot [\vec{\Omega} \times (\vec{\Omega} \times \vec{x}_i)] \\ +(-1)^{i-1}\,\frac{\hat{n}_i}{2} \cdot [\vec{\Omega} \times (\vec{\Omega} \times \vec{l})] - \hat{n}_i \cdot (\dot{\vec{\Omega}} \times \vec{x}_i) + (-1)^{i-1}\,\frac{\hat{n}_i}{2} \cdot (\dot{\vec{\Omega}} \times \vec{l}). \quad (4.51)$$

Identifying the displacements as $\vec{x}_1 = x_1\hat{n}_1$ and $\vec{x}_2 = x_2\hat{n}_2$ and ignoring them again with respect to $\vec{l}$, the accelerations are

$$a_i = -\hat{n}_i \cdot \ddot{\vec{r}}_M - \hat{n}_i \cdot \nabla\phi((-1)^i\,\vec{l}/2) + (-1)^{i-1}\,\frac{\hat{n}_i}{2} \cdot [\vec{\Omega} \times (\vec{\Omega} \times \vec{l})] + (-1)^{i-1}\,\frac{\hat{n}_i}{2} \cdot (\dot{\vec{\Omega}} \times \vec{l}). \quad (4.52)$$

Defining the new sensitive axis as the average between the two accelerometer sensitive axis,

$$\hat{n} = \frac{\hat{n}_1 + \hat{n}_2}{2}, \quad (4.53)$$

the differential acceleration is

$$a_d = -\hat{n} \cdot [\nabla\phi(\vec{l}/2) - \nabla\phi(-\vec{l}/2)] - \hat{n} \cdot [\vec{\Omega} \times (\vec{\Omega} \times \vec{l})] - \hat{n} \cdot (\dot{\vec{\Omega}} \times \vec{l}) \\ -\frac{\hat{n}_2 - \hat{n}_1}{2} \cdot [2\ddot{\vec{r}}_M + \nabla\phi(-\vec{l}/2) + \nabla\phi(\vec{l}/2)]. \quad (4.54)$$

Defining two misalignment errors,

$$\delta\hat{n} = \hat{n}_2 - \hat{n}_1, \quad (4.55)$$

the misalignment between the two sensitive axis, and

$$\delta\hat{l} = \frac{\vec{l}}{l} - \hat{n}, \quad (4.56)$$

the misalignment between the baseline axis and the mean sensitive axis, the differential acceleration becomes

$$a_d = \Gamma_{ij} n^i n^j\, l + l\Omega^2 - l(\vec{\Omega} \cdot \hat{n})^2 - \delta a_{d_{ma}}, \quad (4.57)$$

where

$$\delta a_{d_{ma}} = l(\hat{n}\cdot\delta\hat{l})\Omega^2 - l(\vec{\Omega}\cdot\hat{n})(\vec{\Omega}\cdot\delta\hat{l}) - l\hat{n}\cdot(\dot{\vec{\Omega}}\times\delta\hat{l}) + \delta\hat{n}\cdot(-\ddot{\vec{r}}_M + \vec{g}). \tag{4.58}$$

Note that

$$\delta\hat{n}\cdot\hat{n} = 0 \tag{4.59}$$

and

$$\delta\hat{l}\cdot\hat{n} = -(\delta\hat{l})^2/2. \tag{4.60}$$

Consequently, the first term of the righthand side of Eq. (4.58) is second order and can be ignored, leaving for the differential acceleration due to misalignment:

$$\delta a_{d_{ma}} = -l(\vec{\Omega}\cdot\hat{n})(\vec{\Omega}\cdot\delta\hat{l}) - l\hat{n}\cdot(\dot{\vec{\Omega}}\times\delta\hat{l}) + \delta\hat{n}\cdot(-\ddot{\vec{r}}_M + \vec{g}). \tag{4.61}$$

The two types of misalignment make the differential accelerometer sensitive to different effects. The misalignment between the two sensitive axes $\delta\hat{n}$ generates DM sensitivity to vibration and to the local gravity acceleration. On the other hand, the misalignment between the baseline axis and the sensitive axis $\delta\hat{l}$ causes the differential accelerometer to be sensitive to angular acceleration. In addition, $\delta\hat{l}$ can be visualized as misconcentricity between the two test masses. The additional sensitivity to centrifugal acceleration is small compared to the already large dynamical error analyzed in Section 4.3.2. We initially assumed a radial misalignment of $l\,\delta\hat{l} = 50\ \mu$m and a misalignment in the sensitive axes of $\delta\hat{n} = 10^{-5}$. The actual measurement of $\delta\hat{l}$ and $\delta\hat{n}$ is discussed in Section 5.8.

4.3.5 CM balance error

Eq. (3.83) gives the current amplified by the DM SQUID as a function of the common and differential acceleration experienced by the two test masses. The CM or DM operation of the circuits is decided by changing the value and polarity of the currents in those circuits. In order for the accelerometer to operate in DM, the CM balance condition given by Eq. (3.86) is required. If the CM balance is not perfect, H^c_{aI} will not vanish and the differential accelerometer will be sensitive to the CM acceleration.

This error can be represented as additional CM signal

$$\delta a_{d_{mb}} = \delta h^c \hat{n} \cdot (-\ddot{\vec{r}}_M + \vec{g}), \tag{4.62}$$

where

$$\delta h^c = \frac{H^c_{aI}}{H^d_{aI}}. \tag{4.63}$$

Note that this error is equivalent to the axis misalignment error, except that they couple to different components of external acceleration. We initially assumed a misbalance of $\delta h^c = 10^{-6}$. The actual measurement of δh^c is discussed in Section 5.8.

4.4 Intrinsic noise of the detector

In this section, I use the equivalent, matched accelerometer model to compute the fundamental noise of the experiment. The intrinsic instrument noise has two contributions: the Nyquist or Brownian motion noise and the amplifier noise.

4.4.1 Brownian motion noise

The effective noise due to the Brownian motion that each mass experiences can be calculated from the force noise power spectral density given by the Nyquist theorem:

$$F_T(f) = \frac{4k_B T}{\tau_d(f)}, \tag{4.64}$$

where k_B is Boltzman's constant, T is the temperature, and $\tau_d(f)^{-1}$ is the general damping coefficient of the DM at f. In particular, $\tau_d(f)^{-1}$ becomes ω_d/Q, where Q is the mechanical quality factor of differential resonance mode of the accelerometer. Assuming matched accelerometers, the gradient noise is

$$S_T(f) = \frac{8}{m}\frac{k_B T}{\tau_d(f)}. \tag{4.65}$$

4.4.2 Amplifier noise

The SQUID amplifier noise is specified as the equivalent noise energy per bandwidth

$$E_{SQ}(f) = \frac{1}{2} L_S I_{n,S}^2(f) \tag{4.66}$$

at the SQUID input coil, where $I_{n,S}(f)$ is the equivalent current noise through the SQUID input coil. The gradient noise spectral density due to the amplifier is

$$S_{SQ}(f) = \left[\frac{I_{n,S}^2(f)}{H_{aI}^d(f)} \right]^2, \tag{4.67}$$

where $H_{aI}^d(f)$ is the acceleration-to-current transfer function at f. Using Eq. (4.66) in (4.67),

$$S_{SQ}(f) = \left[\frac{1}{H_{aI}^d(f)} \right]^2 \frac{2E_{SQ}(f)}{L_S}. \tag{4.68}$$

It is now convenient to define the electromechanical coupling parameter β and the circuit coupling efficiency η. The electromechanical coupling parameter

$$\beta = \frac{m\omega_d^2 - m\omega_m^2}{m\omega_d^2}, \tag{4.69}$$

is defined as the fraction of the mechanical energy that enters the sensing circuit. For matched accelerometers,

$$\beta = \frac{I_0^2}{m\omega_d^2} \left[\frac{\lambda^2 (L_t + L_s)/2}{(L_{t2} + L_s)(L_{t1} + L_0/2) - M_t^2} - \gamma \right]. \tag{4.70}$$

The second coupling constant

$$\eta = \frac{L_s I_s^2}{(m/2)(\omega_d^2 - \omega_m^2) x_d^2}, \tag{4.71}$$

is the fraction of the energy in the sensing circuit that enters the SQUID input coil, where

$$x_d = x_2 - x_1 = \frac{(L_{t2} + L_s)(L_{t1} + L_0/2) - M_t^2}{M_t I_0 L_0 \lambda/2} I_s \tag{4.72}$$

is the differential displacement of the test masses, obtained by solving Eq. (3.82). Substituting Eq. (4.72) into (4.71), we find

$$\eta = \frac{\lambda^2 M_t^2 L_s/2}{\left[\frac{\lambda^2 (L_t + L_s)/2}{(L_{t2} + L_s)(L_{t1} + L_0/2) - M_t^2} - \gamma \right] \left[(L_{t2} + L_s)(L_{t1} + L_0/2) - M_t^2 \right]^2}, \tag{4.73}$$

so that the product of coupling constants is

$$\beta\eta = \frac{I_0^2}{m\omega_d^2} \frac{M_t^2 \lambda^2 L_s}{\left[(L_{t2} + L_s)(L_{t1} + L_0/2) - M_t \right]^2}. \tag{4.74}$$

Comparing Eq. (4.74) with (3.94),

$$\frac{1}{H_{aI}^{d}(\omega)^2}\frac{1}{L_s} = \frac{2}{\beta\eta\omega_d^2 m}(\omega_d^2 - \omega^2)^2. \tag{4.75}$$

Substituting this into Eq. (4.68), the amplifier noise contribution to the accelerometer becomes

$$S_{SQ}(f) = \frac{4\omega_d^2}{m}\frac{E_{SQ}(f)}{\beta\eta},\ \omega \ll \omega_d. \tag{4.76}$$

To minimize this noise, $\beta\eta$ needs to be maximized by simultaneously maximizing the DM acceleration-to-current transfer function with respect to L_{t1}, L_{t2}, and I_0^2. The solutions to this optimization are

$$L_{t1,opt} = \frac{[L(-L\gamma + \lambda^2)]^{1/2}}{2(1-\kappa_t^2)^{1/2}(-\gamma)^{1/2}}, \tag{4.77}$$

$$L_{t2,opt} = \frac{L_s}{(1-\kappa_t^2)^{1/2}}, \tag{4.78}$$

and

$$I_{0,opt}^2 = \frac{m\ (\omega_m^2 - \omega^2)L}{[-L\gamma(-L\gamma + \lambda^2)]^{1/2}}. \tag{4.79}$$

With these results,

$$\beta = 1/2, \tag{4.80}$$

$$\eta = \frac{k^2\ [\sqrt{-L\gamma + \lambda^2} - \sqrt{-L\gamma}]^2}{[1 + \sqrt{1-\kappa_t^2}]^2\ \lambda^2}, \tag{4.81}$$

and

$$H_{aI}^{d} = \frac{k\sqrt{m}\ [\sqrt{-L\gamma + \lambda^2} - \sqrt{-L\gamma}]}{2\ \sqrt{2\ L_s}\ [1 + \sqrt{1-\kappa_t^2}]\ \lambda\ (\omega^2 - \omega_m^2)^{1/2}}. \tag{4.82}$$

4.4.3 Total intrinsic noise

Combining the Brownian noise with the amplifier noise gives the intrinsic power spectral density of the gradient noise:

$$S_a(f) = S_T(f) + S_{SQ}(f) = \frac{8}{m}\left[\frac{k_B T}{\tau_d(f)} + \frac{\omega_d^2}{\beta\eta}E_{SQ}(f)\right], \tag{4.83}$$

which agrees with the expression derived in [13] and [45]. The intrinsic noise of the detector is usually a large source of error in an experiment. Low temperature and high quality factors are essential to reduce the Brownian motion noise. Low

DM resonance frequency, as well as high couplings, on the other hand, is a key to reducing the amplifier noise. For our experiment, we assume $T = 1.5\,\mathrm{K}$, $Q = 10^5$, $m = 18.8\,\mathrm{g}$, $f_d = \sqrt{2} \times 11.35\,\mathrm{Hz}$, $\eta = 0.25$, and $\beta = 0.5$. In addition, $E_{SQ}(f) = 1 \times 10^{-30}(1 + 0.1\,\mathrm{Hz}/f)\,\mathrm{J/Hz}$, and $f = 0.1\,\mathrm{Hz}$. With these, $S_T^{1/2}(0.1\,\mathrm{Hz}) = 3.16 \times 10^{-12}\,\mathrm{m\,s^{-2}\,Hz^{-1/2}}$, $S_{SQ}^{1/2}(0.1\,\mathrm{Hz}) = 5.85 \times 10^{-12}\,\mathrm{m\,s^{-2}\,Hz^{-1/2}}$. Consequently, the total intrinsic noise of the detector is $S_\Gamma^{1/2}(0.1\,\mathrm{Hz}) = 6.65 \times 10^{-12}\,\mathrm{m\,s^{-2}\,Hz^{-1/2}}$. Assuming an integration time of $10^6\,\mathrm{s}$, the error associated to the intrinsic noise of the detector at $0.1\,\mathrm{Hz}$ is $6.65 \times 10^{-15}\,\mathrm{m\,s^{-2}}$.

4.5 Temperature noise

The modulation of the penetration depth of a superconductor with temperature gives rise to temperature sensitivity [13, 14]. In our experiment, the sensing coils are configured such that the temperature sensitivity competes directly with the differential acceleration, making it a very serious source of error. A temperature circuit with coils positioned back to back to the sensing coils is designed to directly measure the temperature fluctuations to allow for compensation by a factor of 100.

A preliminary analysis to estimate the temperature noise was done using the noise spectrum of the SGG obtained right after helium (He) transfer, as shown in Figure 4.3. The spectral density obtained by extrapolating the low-frequency noise for $f = 0.1\,\mathrm{Hz}$ is $S_T^{1/2}(0.1) = 1.0 \times 10^{-6}\,\mathrm{K\,Hz^{-1/2}}$. Multiplying this by the measured temperature coefficient of superconducting coils, $1.5 \times 10^{-8}\,\mathrm{m\,K^{-1}}$ [45], and by the optimum resonance frequency of the detector, $\omega_d^2 = 2\,\omega_{d0}^2$, the temperature-induced noise is $1.57 \times 10^{-10}\,\mathrm{m\,s^{-2}\,Hz^{-1/2}}$ at $f = 0.1\,\mathrm{Hz}$. Taking into account the compensation and assuming an integration time of 10^6, we obtain a noise of $\delta a_{d_T} = 1.57 \times 10^{-15}\,\mathrm{m\,s^{-2}}$.

During the He transfer, the cryostat gets supercooled and He boiling stops until thermal equilibrium is reestablished. This produces the period of lowest temperature noise. Since the ISL experiment is cooled below the lambda point of He (2.17 K), boiling will be minimized and the above situation would be reproduced. The $1/f^2$

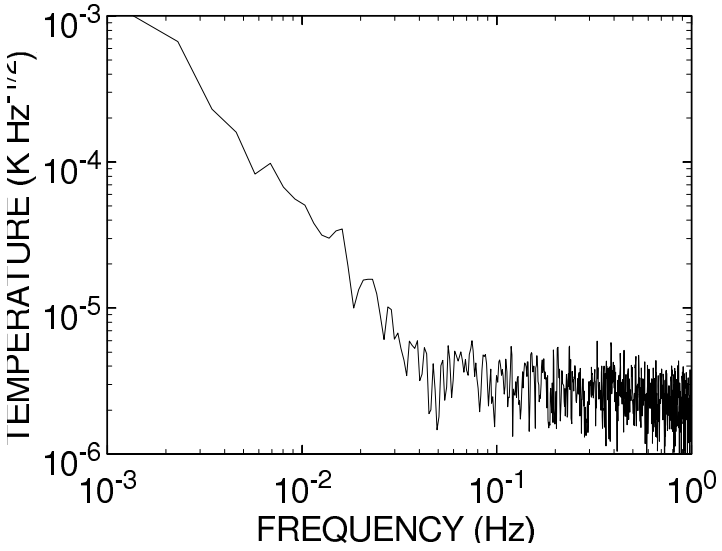

Figure 4.3: Temperature noise of the SGG at 4.2 K.

characteristic at low frequencies is due to the two-stage low-pass thermal filter used. The white noise above 0.05 Hz corresponds to the noise floor of the Ge thermometer bridge circuit.

The detailed measurement of the temperature noise and calculation of the actual temperature coefficient of superconducting coils in the ISL experiment is discussed in Section 4.5.

4.6 Vibration noise

4.6.1 Seismic noise

The Gravitation Experiment Laboratory is located in the basement of the Physics Building. It was previously a Nuclear Physics Laboratory with reinforced 2-m thick concrete ceiling and walls. The vibration noise is expected to be less than that on other floors of the building. The linear and angular acceleration noise measured in the laboratory at 0.1 Hz are $1.0 \times 10^{-7}\,\mathrm{m\,s^{-2}\,Hz^{-1/2}}$ and $7.9 \times 10^{-9}\,\mathrm{rad\,s^{-2}\,Hz^{-1/2}}$. We initially assume that the linear acceleration is rejected by 10^6. The angular

Seismic noise (10^6 s averaging)	$a_d(2f)$ ($\times 10^{-16}$ m/s^2)
Linear acceleration	1.73
Angular acceleration	3.95
Centrifugal acceleration	2.41
Total seismic noise	4.94

Table 4.4: Seismic noise.

acceleration couples to the detector through misconcentricity between the two test masses, $\delta l \approx 50$ μm. The accelerometer also has a residual sensitivity to centrifugal acceleration through its nonzero baseline, $l = 2.41$ mm.

Assuming an integration time of 10^6 s, Table 4.4 summarizes the residual seismic driven noise experienced by the detector.

4.6.2 Source-driven noise

With the source and the detector suspended from the same platform, mechanical cross coupling through either a source driven distortion or motion of the detector is a critical error source. FEA of various designs of the housing were performed and indicated necessity to insert a weak mechanical link between the outer rim, which supports the source mass, and the inner test mass blocks. Figure 4.4 is an exaggerated view of the source-driven distortion of the housing. Notice that the test mass blocks are isolated from this distortion through cantilevers.

According to the FEA, with a 30-Hz suspension of the test mass blocks, the distortion of the detector is reduced by 10^5 to produce an error of $5.1 \times 10^{-17}\,\mathrm{m\,s^{-2}}$ at $2\,f$. We improve this by another factor of 10^2 by mounting the source driving coils at the four places where the source mass cantilever is attached to the rim. This balances the reaction forces to 1%. The test mass blocks have a 50-Hz rotational compliance with respect to the outer housing. This allows fine magnetic alignment of the blocks with a dynamic range of 10^{-3} rad.

The 87.5-μm displacement of the source induces a platform displacement of 1.95×10^{-9} m and a tilt of 8.15×10^{-6} rad about the y axis at the driving frequency. While

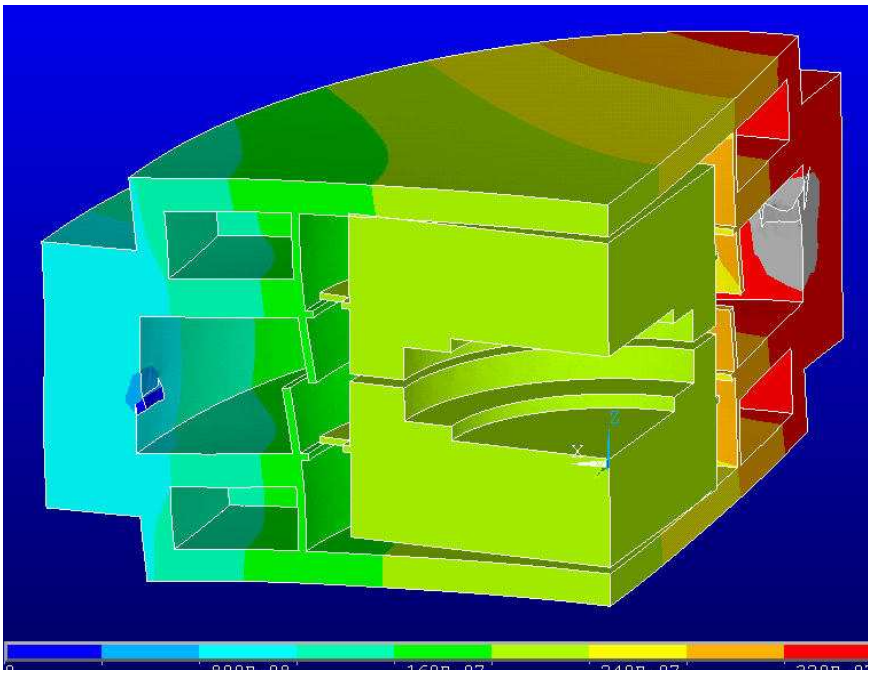

Figure 4.4: Exaggerated view of the source driven distortion of a housing.

the displacement has a negligible effect, the tilt modulates the Earth's gravity and produces a linear acceleration $a_x = 7.99 \times 10^{-8}\,\mathrm{m\,s^{-2}}$ at f. With a CMRR of 10^6 and a second harmonic rejection of 10^3, the acceleration noise becomes $7.99 \times 10^{-16}\,\mathrm{m\,s^{-2}}$. The tilt also generates an angular acceleration $y = 2.62 \times 10^{-6}\,\mathrm{rad\,s^{-2}}$ at f. This acceleration couples through δl. With the second harmonic rejection, the angular acceleration noise also becomes $2.62 \times 10^{-14}\,\mathrm{m\,s^{-2}}$. The nonlinearity of the detector couples to the signal at f squared and in this case is $1.28 \times 10^{-11}\,\mathrm{m\,s^{-2}}$. It is crucial to remove or reduce the tilt.

The source-driven tilt will be canceled by a factor of 10^2 with a feedback loop. The tilt is measured with the optical tilt sensor and the signal is fed back to the voice-coil actuators to null the tilt signal (see Figure 5.1). Taking into account the tilt cancelation, Table 4.5 summarizes the source-driven dynamic noise experienced by the detector.

Source driven noise	$a_d(2f)$ ($\times 10^{-15}\,\mathrm{m/s^2}$)
Linear acceleration	0.80
Angular acceleration	0.4
Nonlinear response	1.28
Total source driven noise	1.56

Table 4.5: Source driven dynamic noise.

4.7 Magnetic cross-talk

Magnetic cross-talk between the source and detector is an important source of error. The isolation requirement for the experiment is 200 dB. In order to achieve this, the entire housing is machined out of Nb and a Nb shield is positioned between the source and each test mass. The superconducting shield alone is expected to give over 200-dB isolation [68]. The frequency discrimination (second-harmonic detection) provides additional rejection.

Flux creep is minimized by cooling and performing the experiment in a low magnetic field. For this purpose, the cryostat is equipped with two layers of mu-metal shield that insures that any external magnetic field will be almost completely excluded from the cryogenic space. In addition, during the cool-down, this shield minimizes the trapped magnetic flux as the superconductors are slowly cooled through their transition temperature.

4.8 Residual gas pressure

During the present run, there was still a small pressure leak, so in order to keep the experiment in operation with a functioning refrigerator, it was necessary to continuously pump on it. The best stable pressure achieved during this run was $p_{exp} = 1 \times 10^{-5}$ torr, estimated to be about one order of magnitude larger than the pressure read out from the pressure gauge, located close to the pumping line. The residual gas pressure will affect several parts of the experiment. As the source

mass moves, the residual gas between it and each housing will be compressed. This produces the following serious effects:

- The force on the center part of each housing will be modulated, so will the acceleration of it. Since the test masses are located inside the center part of the housings, they will see this acceleration modulation as well.
- The force on the shields will be modulated, and they will vibrate as a function of the source modulation. The displacement of the shields can be calculated. The displacement of the shields will in turn compress the residual gas between itself and the test mass, exerting a modulated force on it too.

The force due to a residual pressure p_{exp} exerted over an area A_{tot} is

$$F_p = p_{exp} A_{tot}. \tag{4.84}$$

As the source mass moves, this force is modulated

$$\delta F_p = \frac{\delta p_{exp}}{p_{exp}} A_{tot} = \frac{p_{exp} A_{tot}}{d} \delta d. \tag{4.85}$$

The source mass is not perfectly centered. In order to estimate a worst case scenario, I assume that the effect on one side is negligible compared to the other. Table 4.6 gives the values of the exerted force, housing displacement, CM acceleration at f, and DM acceleration at $2f$ for different separations and modulation amplitudes between the source and the housings, using the values for the total exposed area $A_{tot} = 1.27 \times 10^{-2}\,\mathrm{m}^2$, the mass of the housing center block $m_h = 1.377$ kg, the resonance frequency of the housing $f_h = 30$ Hz, and the modulation frequency $f = 0.05$ Hz. The amplitude of the force on the housing is calculated using Eq. (4.85), while the housing displacement, CM, and DM output are calculated using the numerical model referred to in Section 3.3. The contribution at the second harmonic is coming from the nonlinearities in the source circuit.

The acceleration of the shields is calculated in a similar way and is two orders of magnitude smaller.

d (μm)	δd (μm)	Force magnitude (N)	Housing displacement (m)	$a_c(f)$ ($\times 10^{-11}\,\mathrm{m/s^2}$)	$a_d(2f)$ ($\times 10^{-13}\,\mathrm{m/s^2}$)
25	16.1	1.36×10^{-6}	5.07×10^{-10}	6.8	2.4
100	87.5	1.48×10^{-6}	5.51×10^{-10}	9.3	2.8

Table 4.6: CM acceleration at f and DM acceleration at $2f$ resulting from the residual gas pressure acting on the center part of the housings for different source modulation amplitudes and separation between the source and the shields.

4.9 Magnetic pressure

The superconducting coils with a current running through them produce a magnetic field. Since this field cannot penetrate a superconductor [49], it will produce a force on it. The superconducting coils face the surfaces they are designed to move, but a fraction of the magnetic field they produce can reach other superconducting surfaces. For instance, the source driving coils are shielded from the shields, but a part of the magnetic field they produce can still reach the shields. This field will exert a force on the shields and on the center part of the housings. In addition, the sensing coils are facing the test masses. However, each test mass's cantilever spring allows a fraction of the field from the sensing coil to leak to the other side, which is enclosed between the shield and the test mass. As the shield moves, there will be a force due to the magnetic pressure on the test mass.

As the current through the source coils varies, the source mass motion will induce the following:

- The forces on the center parts of the housings will vary, and so will their accelerations. The test masses, located inside the center parts of the housings, will see these acceleration changes as well.

- The forces on the shields will make them vibrate in response to the source motion. The shields are directly facing the test masses. Their motion couples to the test masses due to the magnetic pressure.

For the magnetic pressure due to the source driving coils, I assume that the area

of penetration of the magnetic field is modulated as

$$A_{frac} = 2\pi\ r\ d_0,$$

where r is the radius of the shields, and d_0 the distance between the source and the source driving coil. Assuming that about 1 % of the field produced by the source coils reaches the shields, the rms force produced by each coil will be

$$F_{MP}^{Source} = \frac{(B_S)^2 A_{fr}}{2\sqrt{2}\mu_0} \times 10^{-4}, \tag{4.86}$$

where $B_S = \mu_0 n I_i$ is the magnetic field produced by one of the source coils with current I_i and wire density n. As the source mass motion is modulated by δd, so is the force:

$$\delta F_{MP}^{Source} = \frac{B_S^2 A_{fr}}{2\sqrt{2}\mu_0 d_0} \delta d \times 10^{-4}. \tag{4.87}$$

For the magnetic pressure due to the sensing coils, I assume that 1 % of the magnetic field leaks through the test mass cantilever. The area of penetration of the magnetic field is just the area of the shields, $A_{sh} = 8.11 \times 10^{-3}\,\mathrm{m}^2$, and the rms force is

$$F_{MP}^{sens} = \frac{B_{sens}^2 A_{sh}}{2\sqrt{2}\mu_0} \times 10^{-4}, \tag{4.88}$$

where $B_{sens} = \mu_0 n I_{sens}$ is the magnetic field produced by one of the sensing coils with current I_{sens} and wire density n.

I assume again the worst case scenario in which the effect on one side is negligible compared to the other. In addition, I assume currents of 1 A in the source coils. This means that in the case of the source, the amplitude is varied by varying just the AC current. If the affected side corresponds to the housing, Table 4.7 gives the values of the exerted force, housing displacement, CM acceleration at f, and DM acceleration at $2f$ for different separations and modulation amplitudes between the source and the housings, using the values for the area of the housing, the mass of the housing center block, the resonance frequency of the bad housing, and the modulation frequency, defined above. The amplitude of the force on the housing is calculated using Eq. (4.86), while the housing displacement, CM, and DM outputs are calculated using the numerical model. The contribution at the second harmonic

d (μm)	δd (μm)	Force magnitude (N)	Housing displacement (m)	$a_c(f)$ ($\times 10^{-13}\,\mathrm{m/s^2}$)	$a_d(2f)$ ($\times 10^{-15}\,\mathrm{m/s^2}$)
25	16.1	5.67×10^{-8}	2.12×10^{-12}	2.8	0.84
100	87.5	3.08×10^{-7}	1.16×10^{-11}	19.4	5.8

Table 4.7: CM acceleration at f and DM acceleration at $2f$ resulting from the magnetic pressure from the source coils exerted on the shields that makes the center part of the housing displace for different source modulation amplitudes and separation between the source and the shields.

is coming from the nonlinearities in the source circuit. The CM and DM outputs are rms.

The acceleration of the shields is calculated in a similar way and is two orders of magnitude smaller.

4.10 Electrostatic coupling

At very small distances the electrostatic interactions between the test bodies may become much larger than the gravity signal. In this section, I will center on the dominant electrostatic background effects found in the experiment.

All of the following errors are significant due to the very small spacing between the source mass and the shields. They produce a force either on the center parts of the housings, on the shields, or on the capacitor plates.

The shields are directly facing the test masses. Their motion can couple to the test masses with several mechanisms, the most relevant of which are the above discussed residual gas pressure, and the magnetic pressure. In the case of the magnetic pressure, it is due to the small amount of magnetic field that can leak through the test mass cantilever, and in the case of the residual gas pressure, it is due to the gas enclosed in that volume.

The capacitor plates are connected to the rim of the shields, which is fixed to the housings, so a force on them translates directly into a force on the center part of

each housing.

4.10.1 Capacitor plate force

The capacitor plates were installed in the experiment to monitor the source mass position with respect to each shield. They stick out of the shield plane slightly and are closest to the source mass. Each housing contains four capacitor plates, witch form a ring, as shown in Figure 2.7. Each capacitor plate has a sensing span of close to 90 ° on the ring and is oriented to sense the top, bottom, or side separation to the source mass. Since the sensing is done only on one side, only one of the housings will experience the capacitor plate force. In addition, the force on only one capacitor plate can induce a rotation of the center part of that housing. This leads to asymmetry, which couples to the second harmonic.

The force between the capacitor plates and the source mass is

$$F_{cap} = \frac{C_d V_{cap}^2}{2d}, \tag{4.89}$$

where $C_d = \epsilon_0 A_c/d$ is the capacitance of the capacitor used to sense, A_c is its area, V_{cap} is the applied voltage, and d the distance to the source. As the source mass moves by δd, the force is modulated as

$$\delta F_{cap}(f) = \frac{\epsilon_0 A_c V_{cap}^2}{d^3} \delta d. \tag{4.90}$$

The displacement in the second harmonic is

$$\delta F_{cap}(2f) = \frac{3}{4}\frac{\delta d}{d}\, \delta F_{cap}(f). \tag{4.91}$$

The worst case scenario corresponds to having the capacitor plate on the housing with the broken cantilever. The displacement of the center part of the housing is approximately

$$\delta x_h = \frac{\delta F_{cap}}{m_h \omega_h^2}. \tag{4.92}$$

A more accurate value for the housing displacement is obtained using the numerical model referred to in Section 3.3. Table 4.8 gives the values of the exerted force, housing displacement, CM acceleration at f, and DM acceleration at $2f$ for different

d (μm)	δd (μm)	Force magnitude (N)	Housing displacement (m)	$a_c(f)$ ($\times 10^{-14}\,\mathrm{m/s^2}$)	$a_d(2f)$ ($\times 10^{-14}\,\mathrm{m/s^2}$)
25	16.1	6.8×10^{-9}	3.3×10^{-13}	2.7	1.3
100	87.5	1.55×10^{-9}	5.69×10^{-14}	0.62	0.41

Table 4.8: CM acceleration at f and DM acceleration at $2f$ resulting from the force exerted by the capacitor plate for different source modulation amplitudes and separations between the source and the capacitor plates.

separations and modulation amplitudes between the source and the capacitor plates, using the values for the area of the capacitor plate $A_c = 8 \times 10^{-4}\,\mathrm{m}^2$, the applied voltage $V_{cap} = 0.05\,\mathrm{V}$, the mass of the housing center block $m_h = 1.377$ kg, the resonance frequency of the housing $f_h = 30$ Hz, and the modulation frequency $f = 0.05$ Hz. The amplitude of the force on the capacitor plate is calculated by using Eq. (4.90), while the housing displacement, CM, and DM outputs are calculated using the numerical model.

4.10.2 Patch fields

In the case of the capacitor plates, a known potential was applied to give the corresponding force and displacement. Since the force is proportional to the applied voltage squared, reducing the applied voltage will reduce the error signal due to it. All other surfaces in the experiment are grounded. From an intuitive point of view, this should guarantee that the electrostatic forces between these surfaces are much smaller than the forces due to the charged capacitor plates.

However, a variety of effects can cause the metals to have different electrical potentials. If two metals are placed in contact with each other, a potential difference

$$V_1 - V_2 = -\frac{W_1 - W_2}{e} \tag{4.93}$$

can appear between them, where e is the electric charge, and W_1 and W_2 are the work functions of the two metals. The origin for the difference in work functions comes from the difference between the electrochemical potentials of the metals. The

electrochemical potential is the minimum energy needed to remove an electron from a metal surface.

The difference in the electrochemical potential can arise either due to difference in the energies of the electrons in the material for different metals (known as "contact potential"), or due to differences in the surface properties of the material, as for example, a difference in the dipole moment of the metal associated with different exposed crystallographic planes (within the same metal) [36]. This last case is also known as "patch effect," where the surface of a polycrystalline material is composed of patches with different crystallographic orientation.

In addition to the crystallographic orientation, factors such as oxide layers, adsorption layers, contaminant layers [8, 62, 72], or temperature differences (thermionic emission) [26] can affect the patch potential distribution and magnitude. When contaminations are present, there can be two kinds of patches, the ones due to the crystal size, and the ones produced due to non-uniform contamination by adsorbates.

The authors of [72] measured patch potentials on polycrystalline Cu and Au surfaces due to non-uniform contamination by adsorbates, which generally produce patches over length scales larger than the crystal size. According to them, the patch potentials drift at rates of up to 0.05 mV/min and given sufficient time, their variations are generally smoothed out, apparently due to preferential adsorption of background contaminants.

Camp *et al.* [8] reported that baking the surfaces in ultrahigh vacuum increased the patch variations (except for gold and graphite), while exposure to air decreased them. They explained the effect with preferential adsorption of background contaminants, or migration of existing adsorbates along the surface. They concluded that contaminants may adsorb onto the surface in such a way as to reduce potential fluctuations.

Nevertheless, the concentration of contaminants in any particular experiment is usually unknown and may be unstable. In addition, heat-treatment above the recrystallization temperature can produce crystal size substantially larger than the material thickness.

The patch effect can be quantified using a Kelvin probe [62], or the newest, non-invasive, Kelvin probe force microscope [47]. The Kelvin probe allows measurements of contact potential difference with high spatial resolution. For the LISA mission, the spatial and temporal variations in surface potential were quantified using this technique [70].

In [77], Speake analyzed some of the properties of surface potentials and used them to calculate the magnitudes of forces and force gradients between infinite parallel conductors in terms of the spatial distribution of the surface potentials. He assumed that the surface potentials are generated by a dipole layer of varying magnitude across the surface. He then calculated the correlation functions between the potential distributions of the two surfaces, and from it the potential energy stored in the electric field between the conductors. By differentiation with respect to specified directions, Speake found the forces and force gradients in those directions. By assuming different forms of the potential distribution, he estimated the force gradients as

$$\delta F_{Pa} = \alpha \epsilon_0 \frac{A_{tot} \nu^2}{d^3} \delta d, \tag{4.94}$$

where A_{tot} is the common area of the metals, ν is the standard deviation of the patch voltage, d the distance between the plates, and α is a dimensionless constant related to the assumed voltage distribution and direction of the force gradient. The worst case scenario corresponds to fluctuations with spatial frequencies of $k = 3/d$ or $k = 5/d$ and α ranges between 1.2 and 1.8.

In a later paper [78], Speake and Trenkel performed a more detailed analysis. They obtained

$$F_p(d) = -\frac{2\epsilon_0 A \sigma_v^2}{k_{max}^2 - k_{min}^2} \int_{k_{min}}^{k_{max}} \frac{k^3}{\sinh^2 kd} dk \tag{4.95}$$

for the force between two parallel plates, where A is the area of the plates, d the distance between the planes, σ_v is the variance between the work functions in the different crystallographic planes of the material. In our case, it is important to consider how $F_p(d)$ varies with d. The integration limits k_{min} and k_{max} correspond to the minimum and maximum frequencies of spatial fluctuations, which in turn correspond to the maximum and minimum crystal sizes. Taking the derivative, the

force gradient between the two planes is

$$\frac{\partial F_p(d)}{\partial d} = \frac{4\epsilon_0 A\sigma_v^2}{k_{max}^2 - k_{min}^2} \int_{k_{min}}^{k_{max}} \frac{k^4}{\sinh^3 kd} \cosh kd\, dk. \tag{4.96}$$

For a distance modulation δd, the force at f is

$$\delta F_p(f) = \frac{4\epsilon_0 A\sigma_v^2 \delta d}{k_{max}^2 - k_{min}^2} \int_{k_{min}}^{k_{max}} \frac{k^4}{\sinh^3 kd} \cosh kd\, dk, \tag{4.97}$$

and the force at $2f$ is

$$\delta F_p(2f) = \frac{2\epsilon_0 A\sigma_v^2 (\delta d)^2}{k_{max}^2 - k_{min}^2} \int_{k_{min}}^{k_{max}} \left[\frac{k^5}{\sinh^4 kd} \cosh^2 kd - \frac{k^5}{\sinh^2 kd}\right] dk. \tag{4.98}$$

The maximum magnitude of the patch potential in pure Nb corresponding to the contact of a (110) and a (116) plane is 0.92 V. The actual patch potential variation depends on the size of the crystals as well as the chemical contamination and the cleanliness of the surface. The standard deviation between the voltage in the different planes of Nb is 0.36 V.

The modulated force will affect the housings, but, in addition, it will affect the shields. The size of the crystallographic planes is one of the most important variables. Tables 4.9 and 4.10 give the values of the exerted force due to the patch field effect, the housing displacement, CM acceleration at f, and DM acceleration at $2f$ for different source modulation amplitudes, separations between the source and the shields, for crystal sizes in the range $[25\,\mu\text{m}, 70\,\mu\text{m}]$ and $[1\,\mu\text{m}, 10\,\mu\text{m}]$, respectively. The effect on the shields is at least two orders of magnitude smaller.

4.10.3 Casimir force

In 1948, Casimir predicted that two parallel, closely separated, conducting plates will be mutually attracted [11]. The attraction is the result of the exclusion of electromagnetic modes between the plates when compared to free space. The general idea is that the electromagnetic field must satisfy certain boundary conditions at the surfaces of the conducting plates, and these boundary conditions rule out some of the modes (oscillators) that would otherwise exist in unbounded space. This can be understood as follows: If a zero-point energy $\hbar\omega/2$ is assigned to each mode, only

d (μm)	δd (μm)	Patch field force (N)	Housing displacement (m)	$a_c(f)$ ($\times 10^{-10}\,\mathrm{m/s^2}$)	$a_d(2f)$ ($\times 10^{-10}\,\mathrm{m/s^2}$)
25	16.1	7.5×10^{-5}	3.6×10^{-9}	6.1	3.0
100	87.5	3.7×10^{-7}	1.7×10^{-11}	0.023	0.0147

Table 4.9: CM acceleration at f and DM acceleration at $2f$ resulting from the housings displacement due to the patch fields for different source modulation amplitudes, separations between the source and the shields, and crystal sizes in the range $[25\,\mu\mathrm{m}, 70\,\mu\mathrm{m}]$.

d (μm)	δd (μm)	Patch field force (N)	Housing displacement (m)	$a_c(f)$ ($\times 10^{-12}\,\mathrm{m/s^2}$)	$a_d(2f)$ ($\times 10^{-13}\,\mathrm{m/s^2}$)
25	16.1	2.4×10^{-7}	1.1×10^{-11}	1.5	9.6
100	87.5	8.3×10^{-14}	4.0×10^{-18}	0.0000051	0.0000033

Table 4.10: CM acceleration at f and DM acceleration at $2f$ resulting from the housings displacement due to the patch fields for different source modulation amplitudes, separations between the source and the shields, and crystal sizes in the range $[1\,\mu\mathrm{m}, 10\,\mu\mathrm{m}]$.

the modes whose wavelengths fit an integer number of times into the gap should be counted. Since there are fewer modes between the plates, there is a difference in the total energy between the plates as compared to free space. This results in an attractive force pressing the plates together.

The Casimir force between two grounded, perfectly conducting, smooth, infinite planes at zero temperature, separated by a distance d, has magnitude (per unit surface area A) of

$$\frac{F_C}{A} = \frac{\pi hc}{480 d^4}. \tag{4.99}$$

An alternative explanation for the Casimir force was obtained from the the van der Waals attraction between dielectric bodies in the Lifshitz theory [37]. Casimir result for two parallel plates was reproduced by letting the dielectric constant approach infinity, which is an appropriate description for a conducting material.

The Casimir force must be corrected for finite temperature, finite conductivity, and surface roughness. All these corrections vary with the separation d, making it difficult to distinguish a gravitational anomaly from an electrical effect. Direct measurements of the Casimir force were completed in [33, 34, 6, 15, 17, 18].

The Casimir force is inversely proportional to the distance to the fourth power, so it becomes large very quickly as the distance becomes small. In our experiment, the Casimir force between the source mass and the shields is

$$F_C = \frac{\pi hc}{480}\frac{A_{tot}}{d^4}, \tag{4.100}$$

where A_{tot} is the area of the shields and d the distance between the source and the shield. As the source moves by δd, the force is modulated as

$$\delta F_C = \frac{\pi hc}{120}\frac{A_{tot}}{d^5}\delta d. \tag{4.101}$$

This force, calculated for the area of the shields, will affect the shields, but it will affect the housings as well. Table 4.11 gives the values of the exerted force, housing displacement, CM acceleration at f, and DM acceleration at $2f$ for different separations, modulation amplitudes between the source and the capacitor plates. The effect on the shields is at least two orders of magnitude smaller.

The force on the housings and shields is calculated using Eq. (4.101), while housing displacements, shields displacement, CM and DM outputs are calculated using the numerical model, using the calculated force on the housings. The coupling between the shields and the test masses is calculated assuming that it is due to the residual gas pressure and magnetic pressure in the enclosed volume.

4.11 Summary of all contributing errors

All the errors are summarized in Table 4.12, where the worst case scenario is considered. It is assumed that the source-to-test-mass spacing is 150 μm, the source-to-shield spacing is 100 μm and the source is displacing by $\delta d = 87.5$ μm. Note that the dominant source of error comes from the patch field force.

d (μm)	δd (μm)	Casimir force (N)	Housing displacement (m)	$a_c(f)$ ($\times 10^{-17}\,\mathrm{m/s^2}$)	$a_d(2f)$ ($\times 10^{-17}\,\mathrm{m/s^2}$)
25	16.1	1.4×10^{-10}	6.5×10^{-15}	88.1	9.96
100	87.5	5.76×10^{-13}	2.15×10^{-17}	0.906	0.324

Table 4.11: CM acceleration at f and DM acceleration at $2f$ resulting from the housings displacement due to the Casimir force for different source modulation amplitudes and separations between the source and the shields.

Error source	$a_d(2f)$ ($\times 10^{-15}\,\mathrm{m/s^2}$)
Metrology	2.1
Intrinsic noise (10^6 s averaging)	6.65
Temperature noise (10^6 s averaging)	1.57
Seismic noise (10^6 s averaging)	0.49
Source dynamic	1.56
Residual gas pressure	280
Magnetic coupling	< 0.1
Electrostatic coupling	1470
Total	1500

Table 4.12: Total error budget for a source to test mass spacings of 150 μm, source to shields spacing of 100 μm and a source is displacement of $\delta d = 87.5\,\mu$m.

Chapter 5

Cool-down and Calibration of the Inverse-Square Law Experiment

5.1 The cryostat

The ISL experiment is operated in a very quiet, super-insulated cryostat, schematically shown in Figure 5.1. This cryostat was initially designed for the SGG and was extensively used to test it. It is a low boil-off LHe dewar (William G. Goree, Inc., Los Altos, CA) with an inner diameter of 0.378 m and an inner depth of 1.80 m. Figure 5.2 shows a picture of the experiment being pulled out of the cryostat after a cool-down.

In order to maximize the LHe hold-time and minimize the environmental noise, the dewar uses super-insulation instead of liquid nitrogen (LN_2) shields. The boil-off of LN_2 is a much noisier source of vibrations than the boil-off of LHe. In the traditional LN_2 jacketed dewar, the nitrogen (N_2) is the primary heat-sink for thermal radiation from the laboratory. Such a dewar uses a minimal amount of insulation and relies upon the large heat capacity of LN_2 to achieve a low LHe boil-off rate. As a consequence, the rate at which the LN_2 boils off is very high. On the other hand, a super-insulated dewar has many layers of insulation that shield the LHe from room-temperature thermal radiation. Therefore, the LHe boil-off rate is very low.

The dewar has double walls. The inner wall is a cylinder made of thin fiberglass, which has low thermal-conductivity-to-mechanical-strength ratio, and is wrapped

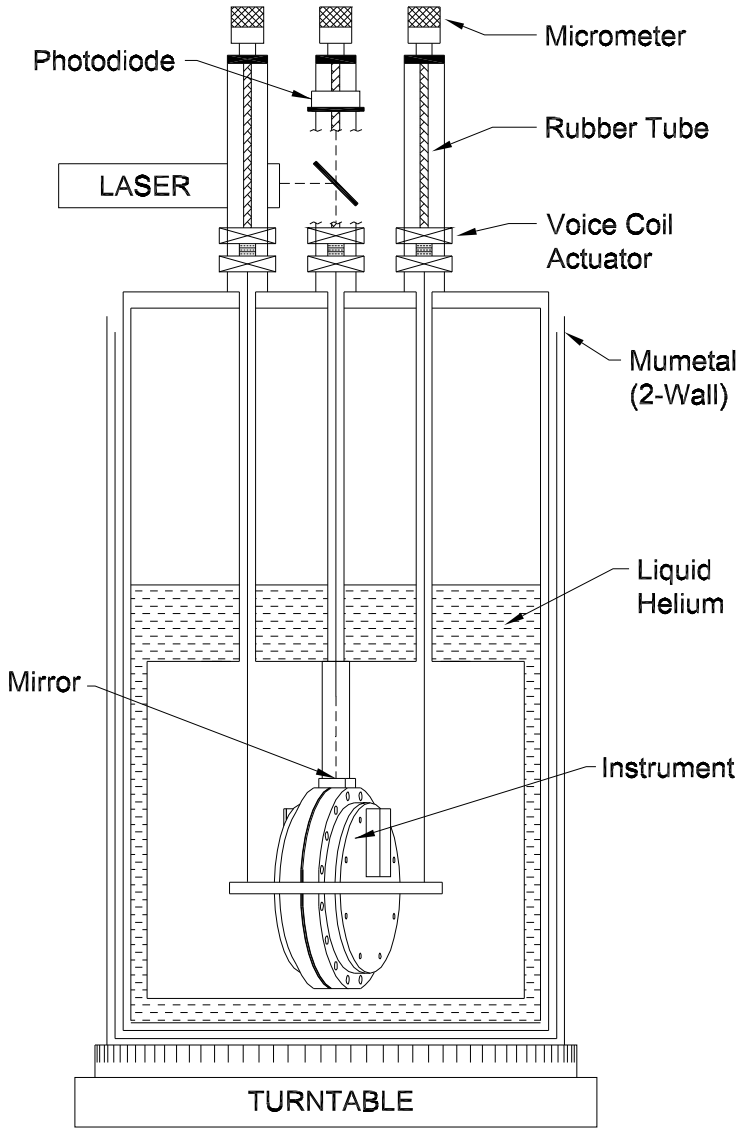

Figure 5.1: Schematic view of the cryostat, which shows the dewar, the double wall mu-metal, the instrument, and its suspension. The orientation is adjusted with the three micrometers and monitored with the photodiode that reads the laser reflection from a mirror positioned on the top of the experiment. The voice-coil actuators are used to shake the instrument for balance and calibration. The space around the experiment submerged in the He bath represents the vacuum can. The experiment is actually located in a Cu can (not shown), inside the vacuum can.

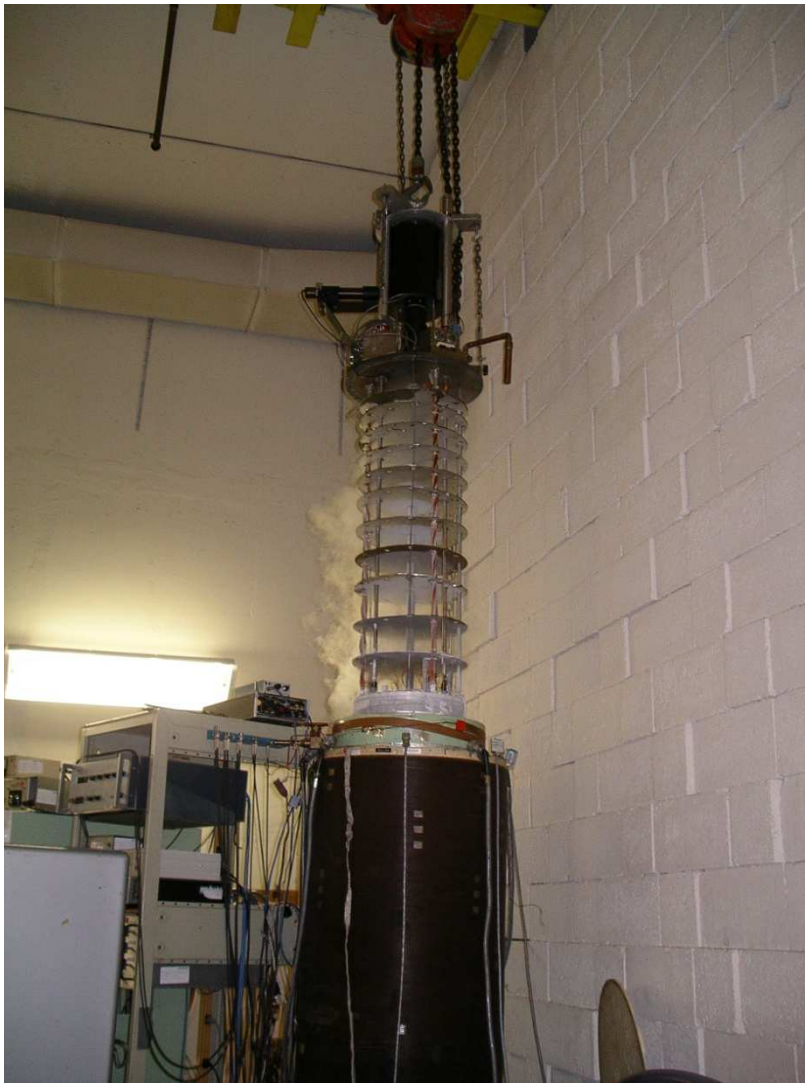

Figure 5.2: Picture of the experiment being pulled out of the cryostat after a cool-down.

with many layers of super-insulation. The outer wall is made out of Al. Pressure pads are sandwiched between the inner and the outer walls, near the bottom of the dewar, making the entire dewar significantly rigid, and preventing any possible swinging motion of the weak inner tube. In addition, the space between the walls is filled with charcoal. The charcoal acts as an absorption pump at low temperatures and helps maintain vacuum for extended periods of time. Before a cool-down, the getter power is regenerated by evacuation at room temperature and it again increases as the temperature decreases.

In order to isolate the dewar from electromagnetic disturbances, the cryostat sits inside a double-wall mu-metal shield. This shield insures that any external magnetic field will be almost completely excluded from the cryogenic space. This is important during the experiment, but also during the cool-down, since it minimizes the trapped magnetic flux as the superconductors are slowly cooled through their transition temperature.

A cryogenic insert fits tightly into the cryogenic space. The top plate of the insert bolts to the top of the cryostat and a large rubber O-ring seals the cryogenic space from the laboratory. An Al vacuum can is located at the bottom of the insert. The can was initially coated with a thin layer of lead, forming a type-I superconducting shield, but this coating has been scratched and is not effective anymore. To further reduce the level of the magnetic flux inside the experimental space, lead shielding was placed inside the vacuum jacket. The outer surface of the can has felt strips that push against the dewar wall, damping the insert from swinging motions. The can is supported by four fiberglass tubes, one at the center and the other three equally spaced on a ring near the edge of the vacuum can. Each end of the tubes is fitted to an Al fixture used to bolt the tubes in place, sealed with a thin layer of Armstrong A12 epoxy (Lunar Products, Inc., Fullerton, Ca), which matches the expansion between the fiberglass and the Al. The tubes support several radiation shields, made out of fiberglass and coated with reflecting foil. The shields provide thermal shielding and mechanically stiffen the insert. The shields are spaced close together near the top of the dewar, where the thermal gradient is greatest, and farther apart closer to the

vacuum can, where the gradient is reduced.

The top plate of the insert has three levels, placed on a 0.66-m diameter and spaced at 120 degrees. The cryostat, on the other hand, has three adjustment screws located at the bottom, nearly half way between those levels that allow raising a specific side of the dewar to level the cryostat. To further control the orientation, the experiment is clamped to a horizontal ring of Al, which is suspended from the top of the cryostat via three stainless steel wires connected to rubber tubes located inside three stainless steel tube structures. In addition to providing support, the rubber tubes provide vertical vibration isolation above its vertical resonance frequency. The three-point suspension provides horizontal vibration isolation above the pendulum frequency as well. The vertical and rocking frequencies of the platform are approximately 2.5 and 3.8 Hz, respectively. The horizontal and torsional frequencies are 0.5 and 0.95 Hz, clearly above the signal frequency. Since the Al ring clamped to the experiment lays in a plane that passes through the center of gravity of the experiment, the pendulum motion should be decoupled from the rocking motion. For a detailed calculation of all of the original pendulum modes and couplings, see Appendix C in [61]. The soft suspension isolates the detector from high-frequency vibrations, which can overload the SQUID amplifiers and increase the noise at the signal frequency by nonlinear down-conversion.

The vertical position of each rubber tube can be adjusted by a micrometer head, placed at the top of the each suspension point. These three adjustments allow us to set and to modify very precisely the orientation of the experiment with respect to the vertical.

The dewar is equipped with shakers and an optical tilt sensor. The shakers consist of voice-coil transducers incorporated into each vertical leg of the suspension by mounting strong magnets at the base of the rubber springs and along with matching coils on the outside of the stainless steel tubes. These non-contacting actuators are used to dynamically shake the instrument for balance and calibration purposes. A shaker interface with three inputs and three outputs is used to send current through each of the shaker coils. By adjusting the relative gains within the shaker interface,

the magnitude and phase of the current through the shaker coils are modified, and the instrument can be shaken, tilted, or vertically accelerated.

The tilt is sensed with a two-dimensional optical lever consisting of a laser, a chopper, a beam splitter, an x-y photodiode, the planar mirror mounted at the top of the instrument, and demodulating electronics. The x-y photodiode is mounted at the top of the cryostat and monitors the position of the beam in the x and y direction.

The dewar is equipped with a He level gauge (American Magnetics, Inc., Oak Ridge, TN) which monitors the He level above the top of the vacuum can. In addition, six matched, thermally sensitive carbon (C) resistors, are used to measure the temperature at various heights inside the cryogenic space. A large boil-off heater is attached at the bottom of the vacuum can to remove the excess LN_2 from the dewar. It is machined out of Al and has twelve 10-W, 1-Ω resistors connected in series.

All the leads that enter the vacuum can are vapor-cooled and heat-sunk to the LHe bath and then to the cold plate. The heat capacity of the experiment and the weak thermal coupling to the He bath forms a two-stage low-pass filter for temperature fluctuations. All the unshielded leads are spirally wound around the fiberglass support tubes in order to increase the surface area of the wire and allow for greater vapor-cooling.

In order to reduce the RF noise, the leads also pass through high quality pi-filters, preceding the room-temperature connector. There are two types of connectors. The unshielded leads go to six forty-one pin connectors, while the shielded ones are connected to two ten pin connectors. The shielded connectors and corresponding feed-through were specifically made for the ISL experiment. For a detailed explanation of the procedure for making feed-throughs, see the description in [12].

Inside the vacuum can, there is a Cu can. The experiment is contained in the Cu can. The cover of this can is also being referred to as the cold plate. On top of the cold plate sits the refrigerator reservoir or 1 K pot. It is connected to the LHe space through a tube, that runs to the top of the vacuum can and is covered with a porous

material that allows a small amount of LHe to flow to the reservoir. By pumping on the refrigerator, the pressure in it is reduced, and subsequently the temperature is reduced as well. Having the 1 K pot allowed a much more cost-effective operation of the experiment, as well as LHe transfers while the refrigerator was running.

The ISL experiment contains many current charging leads, heat-switches, and control leads, most of which are controlled automatically. The custom electronics interface can be controlled manually or with a computer. The amount of current used for the heat-switches is set manually, but the time the heat-switches will be on, the currents to be sent in the different circuits, as well as the boil-off of the LN_2, are all computer controlled, commanded, or automated.

5.2 Cool-down procedure

There are four places that can and need to be evacuated before and during a cool-down: the vacuum can, the space between the walls of the dewar, the inside of the dewar, and the refrigerator. Two of them need to be evacuated before starting the cool-down. The vacuum can is initially pumped and leak tested with a Leybold-Heraeus Ultratest-F He leak detector. Simultaneously, the space between the walls in the cryogenic dewar is evacuated in order to reactivate the getter power of the charcoal. Since the charcoal is in direct contact with the inner wall of the cryostat, this procedure must be performed before starting the cool-down. Usually pumping overnight is sufficient. The refrigerator should be pumped out and leak checked as well. Once we are ready to start the cool-down, the refrigerator is slightly over-pressured to 4-5 psi with He gas.

The insert is further transferred to the cryostat and sealed, isolating it from the laboratory atmosphere. During the transfer and at all the times when there is cold N_2 in the dewar, the refrigerator cavity is kept slightly over-pressured with He gas to prevent the N_2 from penetrating through the porous material and filling the refrigerator cavity, since this will subsequently cause it to freeze. The experiment is backfilled with a few torr of He gas so that the cooling process is sped up. Too

little exchange gas makes the cool-down extremely lengthly, but too much causes excessive use of cooling power. LN_2 is then transferred to pre-cool the insert. Carbon resistors are used to measure the level of LN_2 in the cryogenic space. The temperature of the cold plate and the experiment are separately monitored with the two Ge thermometers, already described in Section 2.2. After the experiment reaches LN_2 temperature, the inside of the dewar is pumped with a single-stage, rotary piston, Kinney vacuum pump model KD-50 to reach close to the triple point of N_2, 98 mm of Hg. The pressure is read out with a Wallace & Tiernan pressure gauge model 61B-1D-0800. The pressure is maintained for several hours, usually overnight, by adjusting a Lakeshore regulator model 329. After the experiment reaches equilibrium, the LN_2 is boiled off using the above described boil-off plate.

A quick boil-off is desired, so that the experiment does not warm up. It is sometimes a good idea to pump out the experimental space one more time before the He transfer. The temperature in the dewar is checked by monitoring the N_2 level resistors. After making sure all the LN_2 is completely boiled off, the dewar is backfilled with N_2 gas. The refrigerator valve, currently still slightly over-pressured, is closed. The experiment is backfilled with about two torr of He gas, just like before, in order to speed up the cool-down, and the transfer of LHe is started.

The cool-down is performed slowly and uniformly. In addition to preserving the equipment, this is important so that the magnetic field generated inside the dewar due to currents coming from thermal emf is small, minimizing the possibility of trapped magnetic flux in the superconductors as they are cooled through their transition temperatures.

During the last few cool-downs, there was a small leak. To counter this, we used a Pfeiffer turbo-pump model TSH 071 P to pump continuously on the experiment. The refrigerator was continuously operated as well using a Welch duo-seal vacuum pump model 1397 and a Honeywell (invensys) pressure gauge model 19C015PA4K, calibrated with the Wallace & Tiernan gauge.

5.3 Circuit verification and inductance measurements

In order to verify that all the parts of the experiment are functional, measurements are performed at each stage. For example, the capacitance of all the coils are measured during the assembly and before connecting the circuits. This gives a direct measure of the distance between the respective coils and the superconducting masses. Table 5.1 gives a summary of all the resistance and capacitance measured before the last assembly. Note that the alignment coils are named with a y or a z. This represents the axis about which the rotation is performed. The subindex 1 or 2 refers to the side of the housing, as defined in Section 2.2.1, and the $\pm$ subindex represents either a positive or a negative rotation about that axis.

After connecting the circuits, the current and heat-switch leads are checked for continuity (before and after transferring into the cryostat and during the cool-down). Once the LHe temperature is reached and the experiment is in equilibrium, the inductances are measured and crosschecked with their predicted values from the room-temperature capacitance measurements to make sure coils have not moved.

The inductances are determined by measuring the flux trapped in a circuit. After a known current is stored in the circuit, the flux is measured by the time integral of the voltage decay across the inductor with the heat-switch on [50]. Table 5.2 gives a summary of all the inductance measurements. Some circuits are composed of multiple coils connected in series and/or in parallel with other coils/transformers, so there is no direct way of measuring the inductances. In those cases, the inductances are determined by comparing the series and parallel inductances of the same circuit.

Since the source and shaker circuits have extra AC leads, the actual inductances of the source coils (and the shaker coils) can be measured by storing current in the loop containing both coils, pulsing the heat-switch, and looking at the output only across the coil to be measured (across the AC leads). Table 5.3 shows the measured inductances of each source and each shaker coil.

On the other hand, the inductance of the sensing circuits has to be calculated

Circuit	Measured capacitance (pF)	Measured resistance (Ω)
Source 1	140.5 ± 0.4	$(4.222 \pm 0.001) \times 10^3$
Source 2	161.4 ± 0.4	$(4.234 \pm 0.001) \times 10^3$
Coil 1 DM	40.4 ± 0.5	164.1 ± 0.1
Coil 1 CM	43.9 ± 0.7	163.2 ± 0.1
Coil 1 spare	45.2 ± 0.6	155.4 ± 0.1
Coil 2 DM	38.7 ± 0.5	166.0 ± 0.1
Coil 2 CM	41.2 ± 0.5	162.6 ± 0.1
Coil 2 spare	44.8 ± 0.4	161.9 ± 0.1
Temperature 1	572 ± 0.2	192.7 ± 0.1
Temperature 2	538 ± 0.2	192.5 ± 0.1
z_{1+} alignment	8.1 ± 0.4	211.7 ± 0.1
z_{1-} alignment	8.6 ± 0.8	204.0 ± 0.1
y_{1+} alignment	7.2 ± 0.8	203.8 ± 0.1
y_{1-} alignment	7.0 ± 0.9	201.1 ± 0.1
z_{2+} alignment	9.6 ± 0.6	211.1 ± 0.1
z_{2-} alignment	8.5 ± 0.4	204.8 ± 0.1
y_{2+} alignment	9.3 ± 0.7	206.9 ± 0.1
y_{2-} alignment	8.4 ± 0.7	207.4 ± 0.1

Table 5.1: Capacitance and resistance measurements for all the coils. The errors are instrumental errors associated with the measurement in addition to the standard deviation over several measurements.

Circuit	Measured inductance (μH)
Source series	13.1×10^3
Source parallel	16.1×10^3
Shaker	629
Sensing 1 parallel	50.5
Sensing 1 series	28.1
Sensing 2 parallel	45.6
Sensing 2 series	29.4
Temperature sensing	30.0
z_{1+} alignment	81.7
z_{1-} alignment	103.1
y_{1+} alignment	Open circuit
y_{1-} alignment	28.3
z_{2+} alignment	20.7
z_{2-} alignment	21.5
y_{2+} alignment	21.2
y_{2-} alignment	21.5

Table 5.2: Inductance measurements for all the circuits

Circuit	Measured inductance (mH)
Source coil 1	6.76
Source coil 2	6.49
Shaker coil 1	0.391
Shaker coil 2	0.226

Table 5.3: Inductance measurements for for the source and shaker coils

Circuit	Inductance (μH)
Inner coil side 1	17.1
Inner coil side 2	12.8
Outer coil side 1	17.4
Outer coil side 2	open

Table 5.4: Inductances of the sensing coils calculated from the parallel and series inductances in Table 5.2.

from the series and parallel combination of their respective circuits and by taking into account the inductance of the transformer. The transformers have inductances measured to be

$$L_{t1} = (33.5 \pm 0.7)\,\mu\text{H} \tag{5.1}$$

and

$$L_{t2} = (7.4 \pm 0.5)\,\mu\text{H} \tag{5.2}$$

for sensing circuit 1, and

$$L_{t1}(35.8 \pm 0.7)\,\mu\text{H} \tag{5.3}$$

and

$$L_{t2} = (7.5 \pm 0.5)\,\mu\text{H} \tag{5.4}$$

for sensing circuit 2, in agreement with the predicted ones from Eqs. (A.35)-(A.36). Table 5.4 shows the inductances of the sensing coils, calculated from the transformer values and the series and parallel inductances given in Table 5.2. From these, we calculate the distance to each test mass at 264 μm to mass 1 and 194 μm to mass 2.

The sensing coil inductance measurement was repeated at a temperature slightly above 4.5 K. This way the test masses were non-superconducting and the inductance represented the distance between the sensing coils and the shields. Performing the same measurements, we calculated that the distance to the shields is (276 ± 12) μm. Together with the measurement of the spacing between the sensing coils and the test masses, the actual distance between the test masses and the shields was calculated at (183 ± 12) μm for side 1 and (254 ± 12) μm for side 2.

Coil	Inductance (μH)	Predicted spacing (mm)	Average capacitance (pF)	Front plane capacitance (pF)	Predicted spacing (mm)
z_{1+}	81.7	.68	20.7 ± 0.2	8.1 ± 0.4	0.59 ± 0.09
z_{1-}	103.1	.66	23.7 ± 0.7	8.6 ± 0.8	0.66 ± 0.09
y_{1+}	open circuit	-	20.4 ± 0.6	7.2 ± 0.8	0.60 ± 0.08
y_{1-}	28.3	.80	19.4 ± 0.5	7.0 ± 0.9	0.62 ± 0.09
z_{2+}	20.7	.60	22.0 ± 0.4	9.6 ± 0.6	0.45 ± 0.03
z_{2-}	21.5	.60	22.0 ± 0.3	8.5 ± 0.4	0.51 ± 0.03
y_{2+}	21.2	.59	21.5 ± 0.5	9.3 ± 0.7	0.46 ± 0.04
y_{2-}	21.5	.60	21.0 ± 0.6	8.4 ± 0.7	0.51 ± 0.05

Table 5.5: Inductances, capacitances and respective predicted spacings for the alignment coils

Table 5.5 shows the predicted distances from inductance and capacitance measurements in the alignment coils. From that data, it can be seen that according to both capacitive and inductive measurements, the center part of housing 1 has moved towards the source mass. After opening the experiment, the displacement of the center part of the housing was also measured with a depth gauge. The results are consistent with the inductance measurements for that side.

5.4 Resonance frequencies and quality factors

The resonance frequencies are measured at several stages during the experiment. We first identify them at room temperature by using the capacitor plates and the sensing circuits connected to a capacitive bridge. During the cool-down, we monitor them through the SQUID outputs. We look for the resonance peaks by shaking the platform and looking for the excitable peaks. Later, we store current in the source and sensing circuits and modify the resonance frequencies of the source and test masses.

Part	Frequency (Hz)	Quality factor	Pressure (torr)	Temperature (K)
Source	11.540	4×10^4	2.2×10^{-5}	2.3
Test mass 1	11.359	8.2×10^4	2.5×10^{-5}	2.5
Test mass 2	11.304	2.5×10^5	2.5×10^{-5}	2.5
Shield 1	625	1.9×10^5	1.3×10^{-4}	4.2
Shield 2	1275	1.5×10^5	1.3×10^{-4}	4.2
Housing 1	22.87	4.9×10^2	1.5×10^{-5}	1.7
Housing 1	29.33	4.1×10^3	1.5×10^{-5}	1.7
Suspension	0.45	1.8×10^3	1.5×10^{-5}	1.7
Suspension	0.515	1.3×10^3	1.5×10^{-5}	1.7

Table 5.6: Resonance frequencies and quality factors for different parts of the experiment

The quality factors are measured by exciting a resonance and looking for the decay curve. We measured the quality factors of different masses at various pressures and temperatures. A high quality factor is usually an indication that the corresponding mass is free.

The resonance frequencies and best measured quality factors in the experiment are shown in Table 5.6. The pressure and temperature for the measurements are shown as well.

5.5 Calibration

5.5.1 External shaker characterization and angle calibration

The experiment has many leads that connect it to the cryostat. These leads have different stiffness, which varies over the cool-down process. During the assembly, I made an effort to position those leads as loosely and symmetrically as possible. Each lead nonetheless acts as a small spring that stiffens the suspension frequency

of the experiment and couples to the different suspension modes and mixes them. This coupling additionally complicates the motion of the experiment induced by the external shaker when shaken about the x or y axis, or driven vertically. For this reason, although the experiment axes are aligned with the actuators, the shaker gains have to be adjusted for different drive frequencies, to obtain the desired tilts.

The photodiode is rotated until its axes are collinear with those of the experiment. The first channel of the tilt sensor, T_j, measures the orientation of the experiment about the $-y$ axis, while the second one, T_i, measures the orientation of the experiment about the x axis. The outputs of T_j and T_i are given in volts. The tilt sensor is mounted on a movable micrometer table. Because the vertical distance between the micrometer table and the mirror that reflects the laser is known, the tilt angle corresponding to a displacement of the laser beam can be reproduced by moving the table. By measuring the actual displacement of the laser beam as a function of voltage, both tilt sensor channels are calibrated with calibration factors

$$\alpha_i = (1.30 \pm 0.04) \times 10^{-4}\,\mathrm{rad/V} \tag{5.5}$$

and

$$\alpha_j = (1.31 \pm 0.03) \times 10^{-4}\,\mathrm{rad/V}. \tag{5.6}$$

The real tilt angles are then calculated as

$$\theta_i = T_i\alpha_i, \;\; \theta_j = T_j\alpha_j. \tag{5.7}$$

In the future, I will be using the calibration factors given by Eqs. (5.5) and (5.6) to calculate the angles θ from the tilt outputs T.

5.5.2 CM calibration

The two sensing circuits are usually referred to as CM and DM, representing the fact that they were designed to operate in the respective mode. Nonetheless, they were built identical, and their functions can be exchanged. In the DM operation, the currents are stored in such a way that only the differential acceleration of the two test masses will produce signals. If the relative direction of the currents in the

Drive frequency (Hz)	T_j (V)	CM output Sensing circuit 1 (V)	CM output Sensing circuit 2 (V)
0.05	0.0913	1.18	4.91
0.075	0.0896	1.17	4.88
0.1	0.0897	1.17	4.85

Table 5.7: Output for both sensing circuits with 10-mA CM sensing current, a fixed driving amplitude of 0.125 V and various frequencies.

two sensing coils is reversed, then the same circuit operates purely in CM. Being an identical electromechanical system, the DM has the same characteristics towards differential accelerations (acceleration gradients) as the CM has towards common accelerations. In the experiment, applying pure acceleration is much easier than applying an acceleration gradient of sufficient magnitude. For this reason, the interchangeability between the roles of the two circuits and accelerations provides a useful tool to calibrate the differential accelerometer.

A CM calibration is obtained by storing series current in each of the circuits, tilting the experiment by a known amount, and measuring the resultant signal. A tilt with respect to the vertical of an angle $\vec{\theta}$ produces a CM signal of

$$\vec{a} = -\vec{\theta} \times \vec{g}. \tag{5.8}$$

Periodic tilt about the y axis by an angle $\theta_j \sin(2\pi f_j t)$ produces

$$a_i = \theta_j g \sin(2\pi f_j t). \tag{5.9}$$

Initially, CM currents of 10 mA are stored in both circuits. Driving the shaker with the same amplitude of 0.125 V at a few different frequencies (with adjusted shaker gains so that in each case only the tilt T_j is present) gives the results shown in Table 5.7.

The actual tilt angles are calculated, and with these angles, using Eq. (5.9), the acceleration is obtained. The calibration factor for each circuit is then found as

$$H_{aV}^{c} = \frac{\text{CM output}}{\text{CM acceleration}}. \tag{5.10}$$

Drive amplitude (V)	T_j (V)	CM output Sensing circuit 1 (V)	CM output Sensing circuit 2 (V)
0.125	0.0989	2.56	10.7
0.25	0.2012	5.12	21.4
0.5	0.401	9.81	42.34

Table 5.8: Output for both sensing circuits with 10-mA CM sensing current, a fixed frequency of 0.05 Hz and various driving amplitudes.

Using the SQUID parameters, this calibration factor can be related to the acceleration-to-current transfer functions for the CM, H^c_{aI}. For this reason, I am denoting it with H^c_{aV}. The resulting calibration factors for a current of 10 mA are

$$H^c_{aV1} = (9.4 \pm 0.5) \times 10^3\,\mathrm{V/(m/s^2)} \tag{5.11}$$

and

$$H^c_{aV2} = (3.9 \pm 0.3) \times 10^4\,\mathrm{V/(m/s^2)}. \tag{5.12}$$

For small currents, it is expected that the CM output is proportional to the stored current. In order to test this, a larger, 20-mA current is now stored in both sensing circuits. Since no significant frequency dependence was found for frequencies in the neighborhood of the driving frequency, it is useful to vary the driving amplitude instead of the driving frequency. Table 5.8 shows the output of both sensing circuits with 20 mA stored in CM when shaking the experiment at 0.05 Hz with various driving amplitudes.

As the driving amplitude increases, the CM output does not increase proportionally. For the smallest driving amplitude, the resulting calibration factors for a current of 20 mA are

$$H^c_{aV1} = 1.81 \times 10^4\,\mathrm{V/(m/s^2)} \tag{5.13}$$

and

$$H^c_{aV2} = 7.80 \times 10^4\,\mathrm{V/(m/s^2)}. \tag{5.14}$$

Using the calibration factors obtained for the different currents in Eqs. (5.11)-(5.14), the general, current-independent CM calibration factors for the two sensing circuits

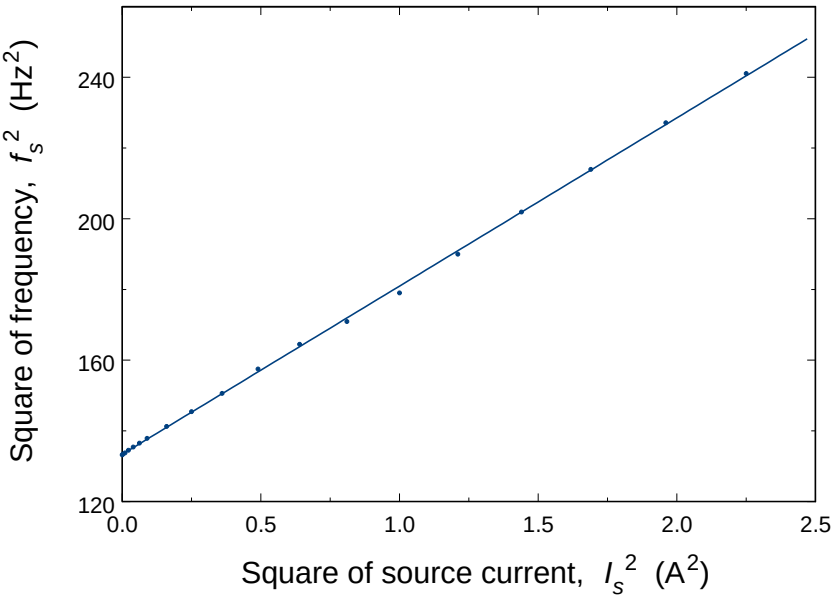

Figure 5.3: Source mass frequency as a function of the stored series current.

for small currents are

$$H_1^c = (9.4 \pm 0.8) \times 10^2 \, (I_0/\text{mA}) \times \text{V}/(\text{m/s}^2) \tag{5.15}$$

and

$$H_2^c = (3.9 \pm 0.3) \times 10^3 \, (I_0/\text{mA}) \times \text{V}/(\text{m/s}^2), \tag{5.16}$$

where I_0 denotes the current in the sensing circuit. When storing current in the CM, the current is directly stored in the series combination of the sensing coil. However, in the DM, the current is stored in the parallel combination of these same two coils, splitting between them. For this reason, the DM calibration factor is related to the CM calibration factor by

$$H^d = \frac{H^c}{2}. \tag{5.17}$$

For a detailed discussion, see [12].

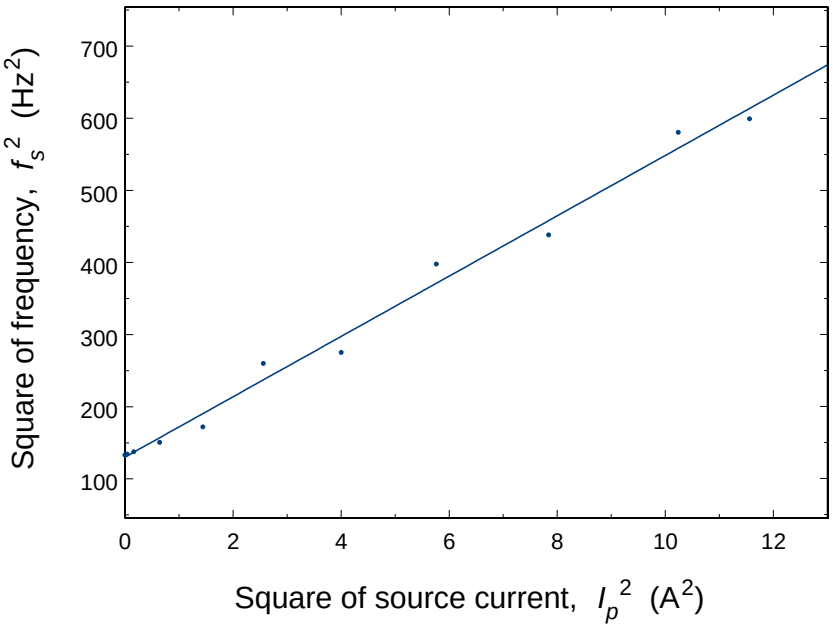

Figure 5.4: Source mass frequency as a function of the stored parallel current.

5.6 Frequency as a function of the current

In each circuit, it is possible to store parallel and series currents, and from the dependence, determine the inductance coefficients λ and γ. Figures 5.3 and 5.4 are plots of the resonance frequency of the source mass squared as a function of the series and parallel current in the source circuit squared, respectively, as described by Eqs. (3.55) and (3.54):

$$\omega_S^2 = \omega_s^2 + \frac{2I_{S10}I_{S20}\lambda_{S1}\lambda_{S2}L_{S3}}{m_s L_{S\text{tot}}^2} + \frac{1}{m_s}\sum_{i=1}^{2}\left[I_{Si0}^2\left(\frac{\lambda_{Si}^2(L_{Si0}+L_{S3})}{L_{S\text{tot}}^2} - \gamma_{Si}\right)\right] \quad (5.18)$$

The intercepts are in close agreement with the resonance frequency with no current in the circuit, 11.549 and 11.385 Hz for the series and parallel circuits, respectively. The slopes, on the other hand, give 47.57 Hz^2/A^2 for the series and 41.89 Hz^2/A^2 for the parallel.

Figures 5.5 and 5.6 are plots of the measured frequency squared as a function of the series and parallel current in circuit 2 squared, respectively. Note that for small currents, these correspond to the test mass frequencies, as described by Eqs. (3.43)

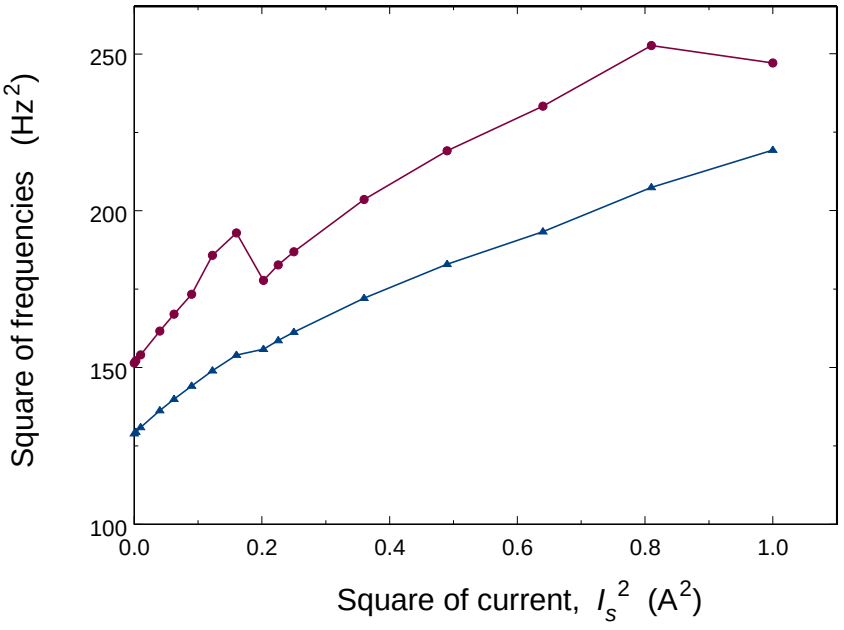

Figure 5.5: Measured frequencies as a function of the stored series current in circuit 2.

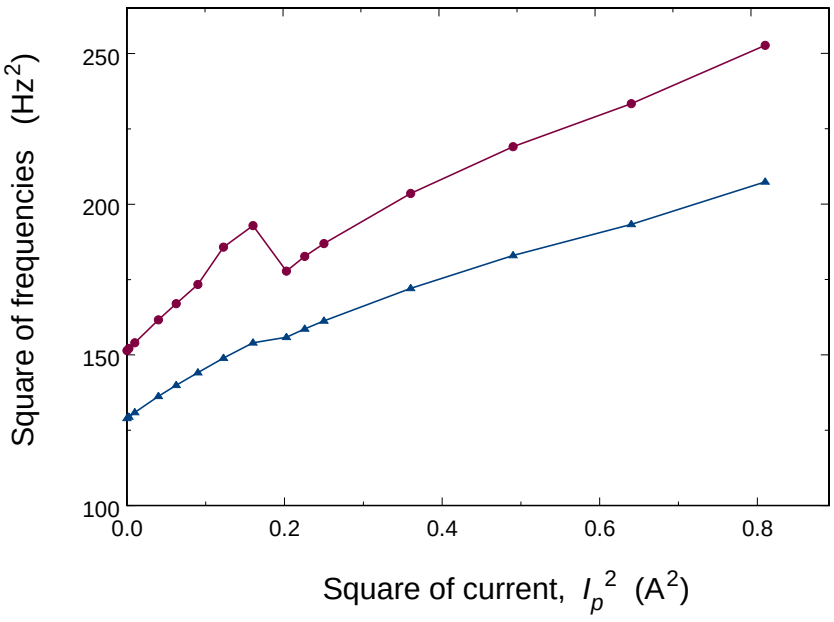

Figure 5.6: Measured frequencies as a function of the stored parallel current in circuit 2.

and (3.42):

$$\omega_{i0}^2 = \omega_{mi}^2 + \frac{1}{m_i}\left[\frac{(L_{j0}+L_e)\lambda_i^2}{L_{\rm tot}^2} - \gamma_i\right] I_{i0}^2. \tag{5.19}$$

For larger currents, we actually observe the CM and DM frequencies.

The intercepts correspond to no current in the circuits and are in close agreement with the resonance frequencies of both test masses. However, storing both series and parallel currents in the circuit causes the sudden jump in the frequency of the test mass 2. This may be due to an "oil can effect" on the named test mass, which would add to the nonlinearities of the circuit. The "oil can effect" represents the snap-displacement of a metal when subjected to a force. We did not expect to see this effect in the test masses, but it could be produced due to differential contraction between the Nb and the Ta. Note that there is a small flat in the frequency of test mass 1 where the jump in the frequency of test mass 2 occurs. Since the sudden jump in test mass 2 changes its spacing to the sensing coil, we would expect a redistribution in the currents, which is consistent with the small flat observed.

An additional peculiar behavior occurs around 1.8 A in parallel and 900 mA in series. According to our numerical model, for 1.8 A in parallel, test mass 1 moves by 199 μm and test mass 2 by 164 μm, while for 900 mA in series, test mass 1 moves by 186 μm and test mass 2 by 176 μm. The spacings to the shields are estimated at (183 ± 10) μm for side 1 and (254 ± 10) μm for side 2, according to our measurements in Section 5.3. This is consistent with test mass 1 touching the shield.

5.7 CM balance

5.7.1 Achievable balance

A CM balance of the differential accelerometer is achieved when the accelerometer response to acceleration is nulled. In the case of perfectly matched accelerometers, a current stored in the loop comprised of the transformer primary and the parallel combination of the sensing coils would achieve a CM balance (see Section 2.3.1, Figure 2.13). However, even if the masses and resonance frequencies were identical,

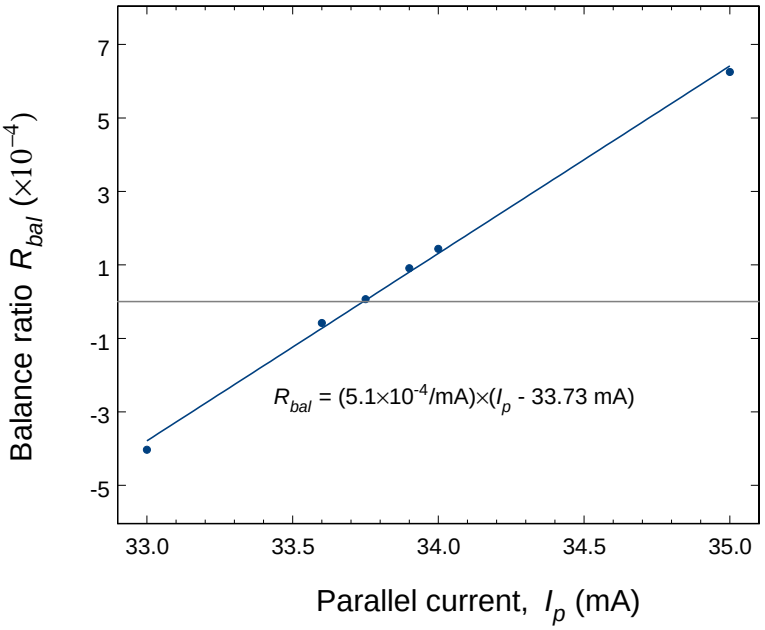

Figure 5.7: CM balance as a function of the parallel current.

it would be nearly impossible to match the coil parameters and spacings precisely. For this reason, a small current needs to be added in the series combination of the sensing coils.

A persistent current is stored in the series combination of the sensing coils. The balance is obtained by tilting the experiment about the y axis and adjusting the current through the transformer primary and the parallel combination of the sensing coils I_p, until the DM output is minimized. The balance is measured from the ratio between the DM output acceleration and the CM output acceleration:

$$R_{bal} = \frac{a_d(f)}{a_c(f)}. \tag{5.20}$$

Figure 5.7 shows the balance achieved as a function of the parallel current I_p. We were able to achieve a CM rejection ratio (CMRR) of 1.5×10^5.

5.7.2 CM balance drift

In order to obtain meaningful results for the CM balance, the balance had to be achieved over a very short period of time. The experiment appeared to have a drift

in orientation that could be read out of the tilt sensors. There are various possible sources for this drift. For instance, the dewar is not very stable by construction due to its inner and outer walls with pressure pads sandwiched between them. In addition, the level of LHe appeared to contribute to the drift.

If the tilt of the experiment is modified, the CM balance is modified as well. We found that the CM balance changed as a function of time at up to 2×10^4/day. Since the balance changed so significantly, after the initial balance:

- CM balances were made and checked frequently.
- Since the drift was somewhat predictable, I took that into account when making the balance.
- The goal was to have a CMRR of at least 5×10^4 through the experiment. I did not attempt to achieve optimal balance as long as this was satisfied.

5.7.3 Achieved balance and wide-band balance

Since the experiment is performed at low frequency, the CM balance was achieved for low frequencies. The general CM balance condition, given by Eq. (3.87), takes the low-frequency form given by Eq. (3.91):

$$\frac{1}{\omega_{1c}^2}\frac{I_{10}\lambda_1}{L_{10}} = \frac{1}{\omega_{2c}^2}\frac{I_{20}\lambda_2}{L_{20}}. \tag{5.21}$$

The resonance frequencies of the test masses were measured to be

$$f_{10} = 12.53\,\mathrm{Hz} \tag{5.22}$$

and

$$f_{20} = 11.50\,\mathrm{Hz}. \tag{5.23}$$

The inductance of the two sensing coils was calculated from the inductance measurements and the inductance coefficients were determined by fitting the current dependence of the frequency, obtaining

$$L_{10} = 12.75\,\mu\mathrm{H} \tag{5.24}$$

and

$$L_{20} = 17.11\,\mu\mathrm{H}, \tag{5.25}$$

$$\lambda_1 = 0.0537\,\mathrm{H/m} \tag{5.26}$$

and

$$\lambda_2 = 0.0495\,\mathrm{H/m}. \tag{5.27}$$

Most of the data was taken using a series current of 10 mA and a parallel current of 90 mA in the DM circuit. Using a numerical model, this leads to current distributions $I_{10} = 41.59\,\mathrm{mA}$ and $I_{20} = 48.41\,\mathrm{mA}$. The equivalent frequencies of the test masses, given by Eq. (3.88), are

$$f_{1c} = \frac{\omega_{1c}}{2\pi} = 12.545\,\mathrm{Hz} \tag{5.28}$$

and

$$f_{2c} = \frac{\omega_{2c}}{2\pi} = 11.516\,\mathrm{Hz}, \tag{5.29}$$

which yield

$$\frac{1}{\omega_{1c}^2}\frac{I_{10}\lambda_1}{L_{10}} = 0.0271\,\mathrm{A/(m/s^2)} \tag{5.30}$$

and

$$\frac{1}{\omega_{2c}^2}\frac{I_{20}\lambda_2}{L_{20}} = 0.0268\,\mathrm{A/(m/s^2)}. \tag{5.31}$$

The balance calculated using this model is one part in 100, which should allow a close guess for the wide-band balance (as defined and discussed in in Chapter 3) as well.

The wide-band balance is necessary, because even for small sensing currents, the resonance frequencies of the two test masses were excited at all times, due to the ground noise and the SQUIDs were overloading. In order for the CM balance to be frequency-independent, it is required that both Eqs. (3.89) and (3.90)

$$\omega_{1c}^2 = \omega_{2c}^2 \tag{5.32}$$

and

$$\frac{I_{10}\lambda_1}{L_{10}} = \frac{I_{20}\lambda_2}{L_{20}} \tag{5.33}$$

are simultaneously satisfied. Numerically, this leads to currents $I_{10} = 0.479\,\mathrm{A}$ and $I_{20} = 0.697\,\mathrm{mA}$, or approximately $110\,\mathrm{mA}$ in series and $1.18\,\mathrm{A}$ in parallel. This leads to equivalent frequencies of the test masses $f_c = 14.401\,\mathrm{Hz}$, and CM and DM observable frequencies of

$$f_c = 15.153\,\mathrm{Hz} \tag{5.34}$$

and

$$f_d = 13.608\,\mathrm{Hz}. \tag{5.35}$$

I attempted achieving the wide-band balance, but due to the nonlinearity in one of the test mass frequencies, seen in Section 5.6, this was not possible. The CM balance was achieved for $200\,\mathrm{mA}$ in series and $1.05\,\mathrm{A}$ in parallel with resonance frequencies of 14.292 and $13.204\,\mathrm{Hz}$.

A second way of achieving the wide-band balance is by satisfying the low-frequency CM balance with the DM circuit while matching the equivalent frequencies of the test masses with the CM circuit. This usually requires large currents in the CM circuit that may impede the operation of the CM SQUID. In addition, matching the equivalent frequencies of the test masses is a difficult task, since the equivalent frequencies are not actually observable. Unfortunately, one of the sensing coils in the CM circuit was disconnected and it was possible to store only very small currents, making this alternative wide-band balance procedure not possible.

5.8 Misalignment and CM misbalance

The misalignment and CM balance errors depend on the sensitive axis misalignment $\delta\hat{n}$, the misalignment between the baseline axis and the sensitive axis $\delta\hat{l}$, and the CM balance δh^c. Combining Eqs. (4.61) and (4.62),

$$\delta a_d = -l(\vec{\Omega}\cdot\hat{n})(\vec{\Omega}\cdot\delta\hat{l}) - l\hat{n}\cdot(\dot{\vec{\Omega}}\times\delta\hat{l}) + (\delta\hat{n}+\delta h^c\hat{n})\cdot(-\ddot{\vec{r}}_{pl}+\vec{g}). \tag{5.36}$$

The coordinate system is chosen so that

$$\hat{n} = \hat{x}, \tag{5.37}$$

$$\delta\hat{n} = \delta n_j \hat{y} + \delta n_k \hat{z}, \tag{5.38}$$

and

$$\delta\hat{l} = \delta l_j \hat{y} + \delta l_k \hat{z}. \tag{5.39}$$

In this case, for pure rotation about $\hat{x}$ or $\hat{y}$, the first term in Eq. (5.36) will not contribute, so it will be omitted. The actual motion of the experiment in the case when only tilt about the x or y axis is applied is much more complicated due to the nonlinearities in the shaker motion and will limit the accuracy of the calibration (included as uncertainties in the measurements). Moving the experiment in a known way, either by tilting it about different axes, or providing a known linear acceleration will make the different terms from Eq. (5.36) contribute. In this section, I will analyze the response of the differential accelerometer to tilt about the x or y axis, or to vertical acceleration.

5.8.1 Tilt about $\hat{y}$

For a tilt at frequency f and angle

$$\theta(f) = \theta_0 \sin(2\pi f t), \tag{5.40}$$

the angular velocity is

$$\Omega(f) = \dot{\theta}(f) = 2\pi f\, \theta_0 \cos(2\pi f t), \tag{5.41}$$

and the resulting acceleration is

$$\dot{\Omega}(f) = \ddot{\theta}(f) = -(2\pi f)^2\, \theta_0 \sin(2\pi f t). \tag{5.42}$$

For tilts about the y axis, the acceleration of the test masses is

$$\ddot{\vec{r}}_{pl} = -\vec{\theta} \times \vec{g} = g\, \theta_0 \sin(2\pi f t)\, \hat{x}. \tag{5.43}$$

Both linear and angular acceleration will couple to the differential output. Substituting Eqs. (5.41), (5.42), and (5.43) into Eq. (5.36), the residual DM acceleration is

$$\delta a_d = [l(2\pi f)^2\, \delta l_k - g\delta h^c]\theta_0 \sin(2\pi f t). \tag{5.44}$$

Frequency (Hz)	δa_d peak (m/s^2)	a_c peak (m/s^2)	$\delta a_d/a_c$
0.01	8.18×10^{-8}	4.65×10^{-4}	1.76×10^{-4}
0.02	1.04×10^{-7}	4.61×10^{-4}	2.25×10^{-4}
0.05	4.54×10^{-8}	4.54×10^{-4}	1.00×10^{-4}
0.1	1.53×10^{-8}	4.48×10^{-4}	3.41×10^{-5}

Table 5.9: Outputs of both sensing circuits for tilts about the y axis for a fixed driving amplitude of 0.125 V at various frequencies. The currents in the circuits are 10 mA series current in the CM sensing, and 20 mA series and 175.7 mA parallel current in the DM sensing circuit.

This acceleration, however, is a function of the applied acceleration

$$a_c = -\hat{n} \cdot \ddot{\vec{r}}_{pl} = -g\,\theta_0 \sin(2\pi f t), \tag{5.45}$$

measured directly by the CM circuit. Dividing the residual DM acceleration by the applied CM acceleration, I obtain

$$\frac{\delta a_d}{a_c} = \delta h^c - \frac{(2\pi f)^2}{g} l\,\delta l_k. \tag{5.46}$$

Periodically tilting the experiment by the same angle about the y axis at four separate frequencies produces the results in Table 5.9. On the other hand, Table 5.10 contains the results from periodically tilting the experiment about the y axis at 0.1 Hz with four different amplitudes. A fit of the data from both tables gives

$$\delta h^c = (1.6 \pm 0.2) \times 10^{-4} \tag{5.47}$$

and

$$l\,\delta l_k = (3.8 \pm 0.3) \times 10^{-3}\,\mathrm{m}. \tag{5.48}$$

5.8.2 Tilt about $\hat{x}$

The rotation angle, angular velocity, and angular acceleration are given by Eqs. (5.40), (5.41), and (5.42), respectively. For a tilt about the x axis, the angular acceleration

Tilt angle (rad)	δa_d peak (m/s^2)	a_c peak (m/s^2)	$\delta a_d/a_c$
5.70×10^{-6}	8.10×10^{-9}	5.59×10^{-5}	1.45×10^{-4}
1.13×10^{-5}	1.36×10^{-8}	1.12×10^{-4}	1.22×10^{-4}
2.28×10^{-5}	2.56×10^{-8}	2.24×10^{-4}	1.14×10^{-4}
4.59×10^{-5}	1.53×10^{-8}	4.48×10^{-4}	3.41×10^{-5}

Table 5.10: Outputs of both sensing circuits for tilts for different tilt angles about the y axis at a fixed driving frequency of 0.1 Hz. The currents in the circuits are 10 mA series current in the CM sensing, and 20 mA series and 175.7 mA parallel current in the DM sensing circuit.

will not couple to the differential output. In this case, the platform acceleration is

$$\ddot{\vec{r}}_{pl} = -\ddot{\vec{\theta}} \times \vec{g} = -g\,\theta_{i0} \sin(2\pi f t)\,\hat{y}. \tag{5.49}$$

Substituting the rotation angle, angular velocity, angular acceleration, and platform acceleration into Eq. (5.36), the residual DM acceleration is

$$\delta a_d = g \delta n_j \theta_0 \sin(2\pi f t). \tag{5.50}$$

This acceleration, like before, is a function of the applied acceleration. In this case, however, the CM circuit does not measure it, since it is perpendicular to its sensitive axis. In fact, one of the tests performed to align the drive of the shaker is to make sure that a rotation about the x axis has a minimum in the CM output, while a rotation about the y axis has a maximum. For this reason, the applied acceleration is taken as the one corresponding to a rotation about the y axis, given in Eq. (5.45). Dividing the residual DM acceleration by the effective applied CM acceleration, we obtain

$$\frac{\delta a_d}{a_c} = \delta n_j. \tag{5.51}$$

Periodically tilting the experiment about the x axis at 0.1 Hz with four different amplitudes produces the results in Table 5.11. A fit of the data from the table gives

$$\delta n_j = (1.1 \pm 0.4) \times 10^{-4}. \tag{5.52}$$

Tilt angle (rad)	δa_d peak (m/s^2)	a_c peak (m/s^2)	$\delta a_d/a_c$
5.70×10^{-6}	4.41×10^{-9}	5.59×10^{-5}	7.9×10^{-5}
1.13×10^{-5}	1.68×10^{-8}	1.12×10^{-4}	1.5×10^{-4}
2.28×10^{-5}	2.20×10^{-8}	2.24×10^{-4}	9.8×10^{-5}
4.59×10^{-5}	3.85×10^{-8}	4.48×10^{-4}	8.6×10^{-5}

Table 5.11: Outputs of both sensing circuits for tilts for different tilt angles about the x axis at a fixed driving frequency of 0.1 Hz. The currents in the circuits are 10 mA series current in the CM sensing, and 20 mA series and 175.7 mA parallel current in the DM sensing circuit.

5.8.3 Rotation about $\hat{z}$

For a rotation about the z axis, the angle, angular velocity, and angular acceleration are again given by Eqs. (5.40), (5.41), and (5.42), but in this case, this rotation will not be detected by the tilt sensor, since it occurs in the x-y plane and

$$\ddot{\vec{r}}_{pl} = -\vec{\theta} \times \vec{g} = 0. \tag{5.53}$$

The amplitude of the DM acceleration is then

$$\delta a_d = -l(2\pi f)^2 \, \delta l_j \theta_0 \sin(2\pi f t). \tag{5.54}$$

There is no way to quantify the corresponding acceleration using the CM output. It is, however, possible to achieve this with the second harmonic of the differential output, which measures the centrifugal acceleration given by

$$a_d(2f) = l(2\pi f \theta_0)^2 \frac{1 + \cos(4\pi f t)}{2}. \tag{5.55}$$

Note that its amplitude is

$$|a_d(2f)| = \frac{1}{2} l(2\pi f \theta_0)^2. \tag{5.56}$$

Dividing δa_d by the square root of $2l|a_d(2f)|$ and $2\pi f$,

$$\frac{|\delta a_d|}{2\pi f \sqrt{2l|\, a_d(2\omega)|}} = \delta l_j, \tag{5.57}$$

we obtain the misalignment between the sensitive and the baseline axes. A way of measuring this would be exciting the torsional mode of the suspension, but since the centrifugal acceleration is a very small portion of the actual second harmonic (as it will be seen in Section 5.9), I have not measured δl_j and assumed that the two components of the misalignment between the baseline axis and the sensitive axis are comparable to each other.

5.8.4 Vertical acceleration

The shakers are calibrated such that it is possible to tilt the experiment by the same amount about the x axis and the y axis. With the shakers calibrated, it is also possible to drive the experiment vertically, providing a periodic acceleration with a known amplitude

$$\ddot{\vec{r}} = a \sin(2\pi f t)\, \hat{z}. \tag{5.58}$$

There is no measurable angular acceleration, and the differential output will couple only to the vertical acceleration. Then the residual DM acceleration given by Eq. (5.36) is

$$\delta a_d = a \delta n_k \sin(2\pi f t). \tag{5.59}$$

Dividing this by the applied CM acceleration $a = a_c$,

$$\frac{\delta a_d}{a_c} = \delta n_k. \tag{5.60}$$

Periodically moving the experiment in the $\hat{z}$ direction by a known amount gives

$$\delta n_k = (1.3 \pm 0.4) \times 10^{-3}. \tag{5.61}$$

Note that δn_k is about one order of magnitude larger than δn_j. This was very puzzling during the experiment, but is in agreement with the findings after opening the experiment up (see Section C.10).

5.9 Baseline and nonlinearities

As explained in Section 4.3.2, the centrifugal acceleration error is used to calibrate the DM accelerometer. By tilting the experiment by a known amount about an axis

chosen *a priori*, the DM acceleration is given by Eq. (4.48):

$$\delta a_d = l\Omega^2 - l(\vec{\Omega} \cdot \hat{n})^2, \tag{5.62}$$

where $\vec{\Omega} = \Omega\hat{\alpha}$, is the angular velocity due to the tilt about the axis of rotation $\hat{\alpha}$. Note that δa_d is maximum when $\hat{\alpha}$ is perpendicular to $\hat{n}$. The centrifugal acceleration calibration is performed for rotation about the y axis, since the shaker cannot be driven about the z axis. For a tilt of an angle $\theta(f)$ given by Eq. (5.40), the angular velocity is given by Eq. (5.41). For a tilt about the y axis, the resulting acceleration is then given by Eq. (5.55) and is at $2f$. However, due to the sensing circuits nonlinearities, the signal is not just due to the centrifugal acceleration. It will also contain a term proportional to the CM acceleration squared, as discussed in Section 4.2.

Dividing δa_d by the applied CM acceleration given by Eq. (5.45) produces an equation of the form

$$\frac{\delta a_d(2\,f)}{a_c^2(f)} = \delta\epsilon_{nl} + l\,\frac{\omega^2}{2\,g^2}, \tag{5.63}$$

where a_c is given by Eq. (5.45) and $\delta\epsilon_{nl} = H_{cc}/H_d$ is the error due to the circuit nonlinearities.

Driving the shaker at several different frequencies gives the data summarized in Table 5.12. A fit of these data points gives

$$\delta\epsilon_{nl} = (0.075 \pm 0.008)\,(\mathrm{m/s^2})^{-1} \tag{5.64}$$

and

$$l = (3.1 \pm 0.8) \times 10^{-3}\,\mathrm{m}. \tag{5.65}$$

Note that this is the nonlinearity coefficient and baseline measured for 10 mA series current in the CM sensing and 10 mA series and 90.4 mA parallel current in the DM sensing circuit.

Frequency (Hz)	$\delta a_d(2\,f)$ peak (m/s^2)	$a_c(f)$ peak (m/s^2)	$\delta a_d(2\,f)/a_c^2(f)$
0.01	1.81×10^{-6}	4.90×10^{-3}	7.51×10^{-2}
0.02	1.76×10^{-6}	4.85×10^{-3}	7.49×10^{-2}
0.05	1.71×10^{-6}	4.79×10^{-3}	7.48×10^{-2}
0.1	1.68×10^{-6}	4.75×10^{-3}	7.46×10^{-2}
0.2	1.65×10^{-6}	4.69×10^{-3}	7.49×10^{-2}
0.25	1.63×10^{-6}	4.66×10^{-3}	7.49×10^{-2}
0.4	1.58×10^{-6}	4.60×10^{-3}	7.52×10^{-2}
0.5	1.53×10^{-6}	4.56×10^{-3}	7.38×10^{-2}

Table 5.12: Outputs of both sensing circuits with 10 mA series current in the CM sensing, and 10 mA series and 90.4 mA parallel current in the DM sensing circuit, and a fixed driving amplitude of 0.125 V at various frequencies.

Chapter 6

Experimental Procedure and Data Analysis

6.1 Determination of the source position and spacings

To determine to what amplitude the source mass can be driven, we first need to determine the spacing between the source mass and the shields. We can do this by several methods:

- Tilting the experiment. This will displace the source. The maximum spacing corresponds to the position when a capacitor plate on the side towards which we are tilting shorts. Note that the source displaces, but the center parts of the housings, which contain the test masses, shields, and capacitor plates, displace as well and this motion has to be taken into account to calculate the effective displacement of the source with respect to the housings.

- Storing current in the source circuit and moving the source until it touches the capacitor plates.

- Driving the source mass with increasing amplitudes until it touches.

The tilt test was the first performed. In all cool-downs in which the capacitor plates were already installed, except the last, at least one capacitor plate was shorted after cooling down. To determine the total space available for the source motion, the experiment was tilted until no capacitor plate was shorted and then tilted farther

until a capacitor plate on the other side became shorted. In the last cool-down, however, the source mass was not shorted to any of the capacitor plates. The tilt was limited by the available spacing, which we identified from the pendulum frequency. We tilted the experiment to both sides until the pendulum frequency of the platform changed, indicating that the suspension was not free any more. This gave us a lower bound for the spacing. From the tilt test, I determined a lower bound for the spacing of at least (22 ± 8) μm to side 1 and at least (33 ± 8) μm to side 2. This means that the sum of the spacings on both sides is at least (55 ± 11) μm.

The source position can be changed by storing different combinations of parallel and series DC currents in the source circuit, as described in Section 3.2.2. We stored 500 mA in the series combination of the two source coils and then varied the current passing through the shunt inductor and the parallel combination of the two source coils. This modified the ratio of the currents in the two source coils, exerting a net force to one side. By varying that force, I moved the source by a predictable amount. I was monitoring the capacitor plates and looking for shorts, corresponding to the source touching them. The capacitor plates were never shorted in this instance, either. Instead, I looked for changes in the source resonance. Using this method, I determined that the source spacing is (34 ± 6) μm from housing 1 and (21 ± 6) μm from housing 2.

This represents the spacing where the source appears to be free, but not necessarily the spacing to the shields. In order to calculate the spacing to the shields, recall that the capacitor plates were designed to stick out of the plane of the shield. In addition, after opening the experiment, we found that the center part of housing 1 was rotated (see Section C.10). According to this, we estimate the spacing to the shields to be $38 \pm^{77}_{4}$ μm to shield 1 and $24 \pm^{13}_{4}$ μm to shield 2.

The last determination of the source mass spacing was performed during the actual experiment and will be described in the next section.

6.2 Data as a function of the source position

Both measurements from Section 6.1 are in agreement, and, with them, we should be able to drive the source mass at different amplitudes from different positions. In this section, I will discuss four positions for the source mass and analyze the motion of the source in each case.

The following data was taken with 3.6 mA in series in sensing circuit 1, measuring CM acceleration and 200 mA in series and 1.05 A in parallel in sensing circuit 2, measuring DM acceleration. The source circuit had 500 mA in series and the parallel current was varied for the different positions 0 mA for Position 1, 10 mA for Position 2, 20 mA for Position 3, and 25 mA for Position 4. The AC current was varied as well to achieve the different displacements. We sent AC currents of 6.8, 13.7, 20.5, and 27.3 mA to achieve displacements of 4.0, 8.0, 12.1, and 16.1 μm, respectively. Intermediate and larger AC currents were sent as well.

For the data presented in this section, there was no attempt to cancel the tilt, or to remove the nonlinearities, or magnetic cross-talk. Only the raw data is presented. The analysis and investigation of errors will follow in a Section 6.3.

6.2.1 Position 1

Position 1 is the initial position of the source mass. Figure 6.1 represents the averaged signal of the CM and DM time trace for three different amplitudes of motion for the source (8.0, 16.1, and 24.2 μm). The first half period corresponds to the source mass moving towards side 1 and back to its initial position, while the second half corresponds to the motion towards side 2 and back.

There are a few noticeable features:

- The CM output is dominated by the tilt.
- The DM output is not symmetric.
- The asymmetry in the DM output comes from a strange structure of a sine wave only over half the cycle. The amplitude of the structure grows with the

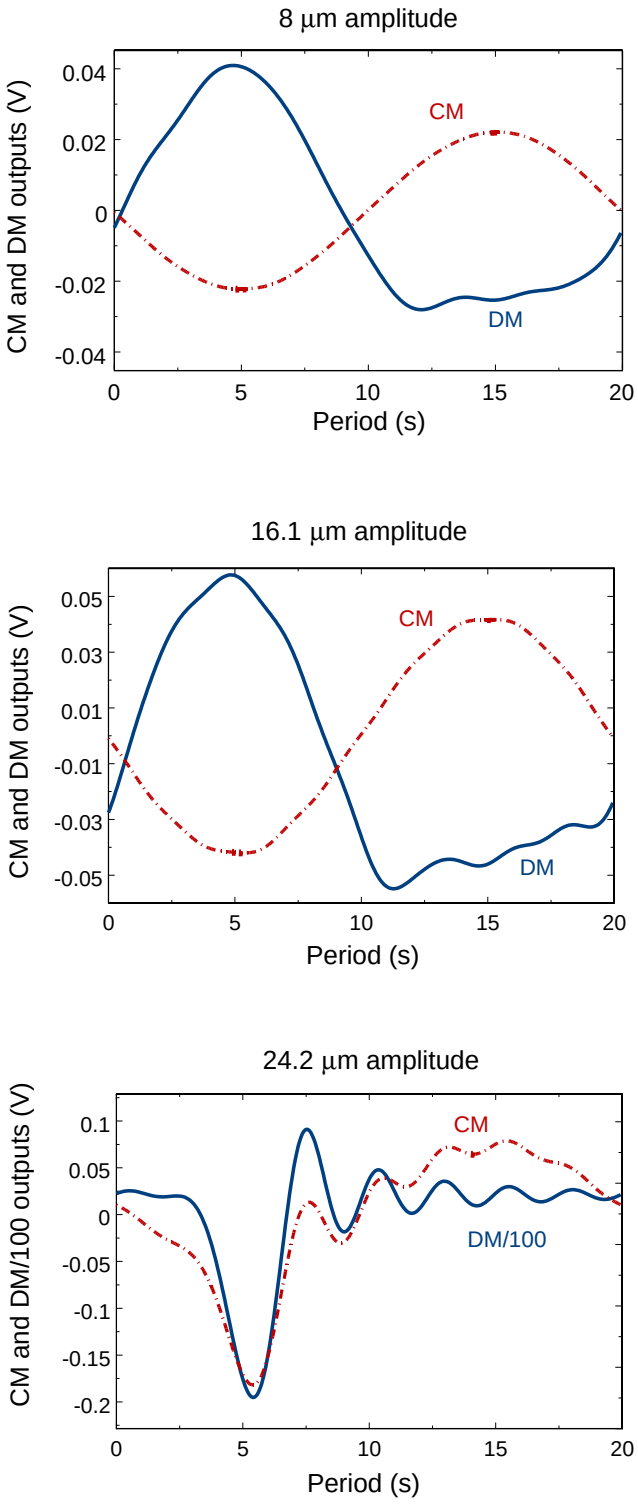

Figure 6.1: Averaged signal of the CM and DM time trace in the initial position of the source mass with amplitudes of the drive of 8.0, 16.1, and 24.2 μm.

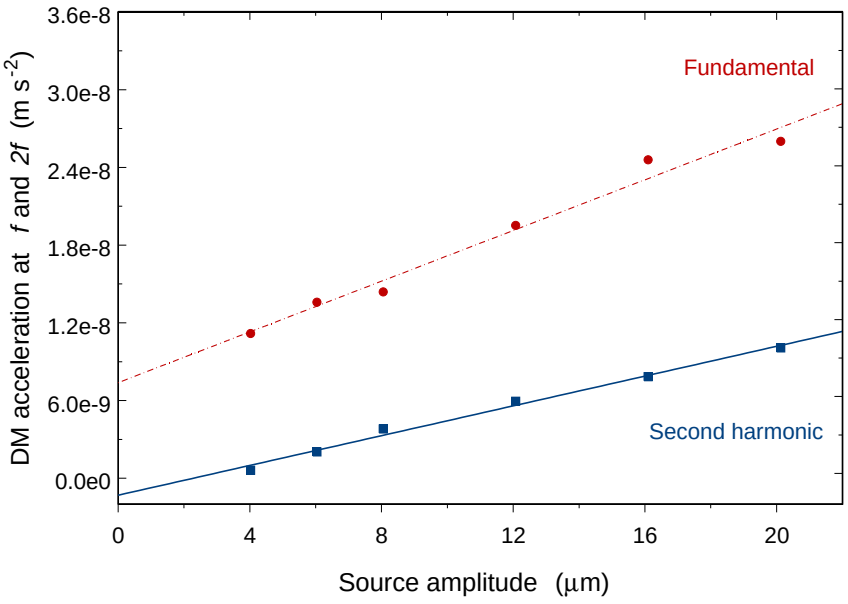

Figure 6.2: DM acceleration at f and $2f$ as a function of the source amplitude when the source mass is in its initial position. The point at which the source clearly touches has been excluded.

source driving amplitude.

- The strange structure of the DM output corresponds to when the source moves towards side 1.

- For a source driving amplitude of 24.2 μm, when moving towards side 1, both outputs overload. The DM output is 100 times larger than the CM output.

As a further test, the source was driven at smaller amplitudes of 4 μm (not shown in the figure). In this case, the DM output is almost symmetric, but with an amplitude larger than the CM output, which appears very puzzling.

Figure 6.2 represents the fundamental and second harmonic outputs in the DM circuit for different amplitudes of motion of the source, where the accelerations have been calculated using the DM calibration given in Section 5.5.2, adjusted for the corresponding currents. The point corresponding to a source driving amplitude of 24.2 μm at which the source touches has been excluded. We do not identify the DM

output at $2f$ with a Yukawa-type signal.

6.2.2 Position 2

In Position 2, the source mass is displaced by 6.75 μm from its initial position. We expect this to be very close to the optimal position, since this should nearly center the source and allow for the maximum displacement. Figures 6.3 and 6.4 represent the averaged signal of the CM and DM time trace for several amplitudes of motion for the source.

Similar to Position 1:

- The CM output is again dominated by the tilt.
- The DM output is not symmetric and becomes less symmetric as the source amplitude is increased.
- The strange structure of the DM output corresponds to when the source moves towards side 1, as before.

There are a few additional noticeable features:

- The CM amplitude is the same as before, but the DM amplitude is smaller.
- For a source driving amplitude of 28.3 μm, a new structure appears, this time when the source is moving towards side 2 and only in the DM output. In the graph, the DM output had to be divided by 3 to be comparable to the CM output. Since one of the sensing coils of the CM circuit, the one corresponding to side 2, is disconnected, we interpret this as the source touching side 2. Note that the distance is in agreement with the values from Section 6.1.
- For a source driving amplitude of 32.2 μm, both outputs overload when the source moves toward side 1. The DM output is 100 times larger than the CM output. We identify this with the source touching side 1.

Figure 6.5 represents the fundamental and second harmonic outputs in the DM circuit for different amplitudes of motion of the source. The points corresponding

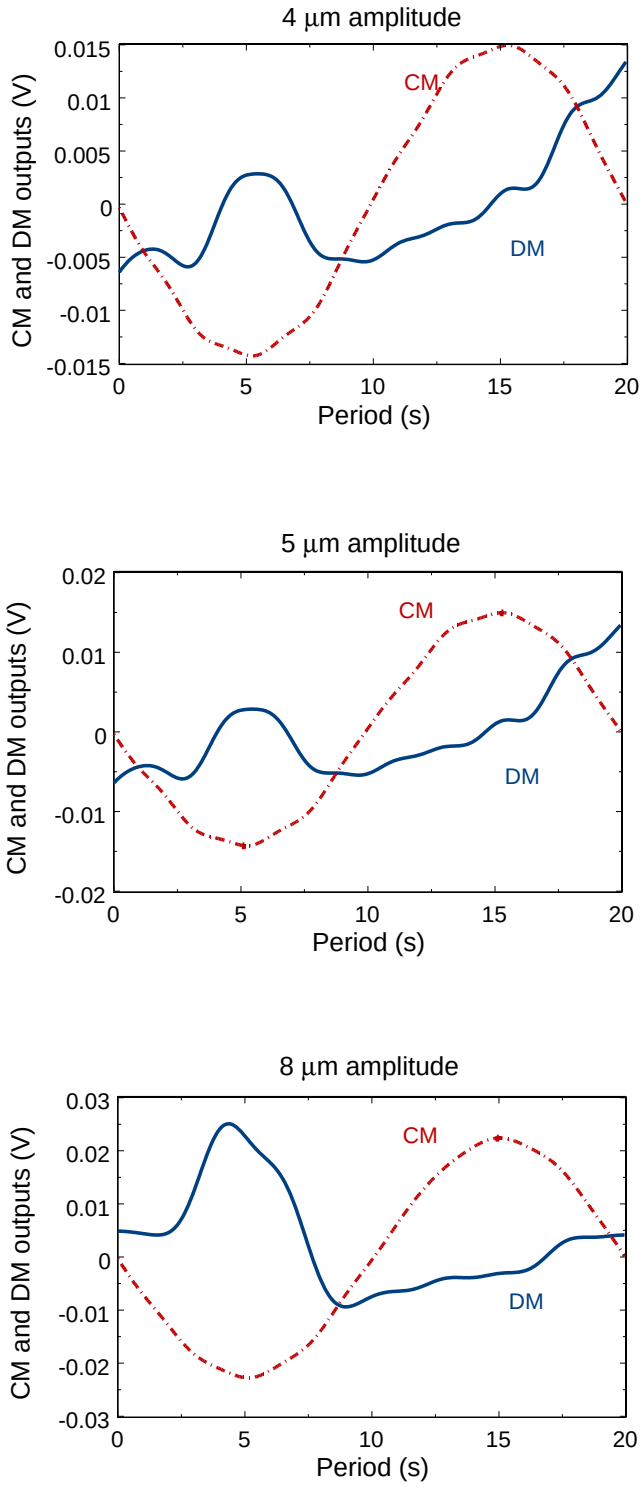

Figure 6.3: Averaged signal of the CM and DM time trace when the source mass is moved by 6.75 μm from its initial position. The driving amplitudes are 4.0, 5.0, and 8.0 μm.

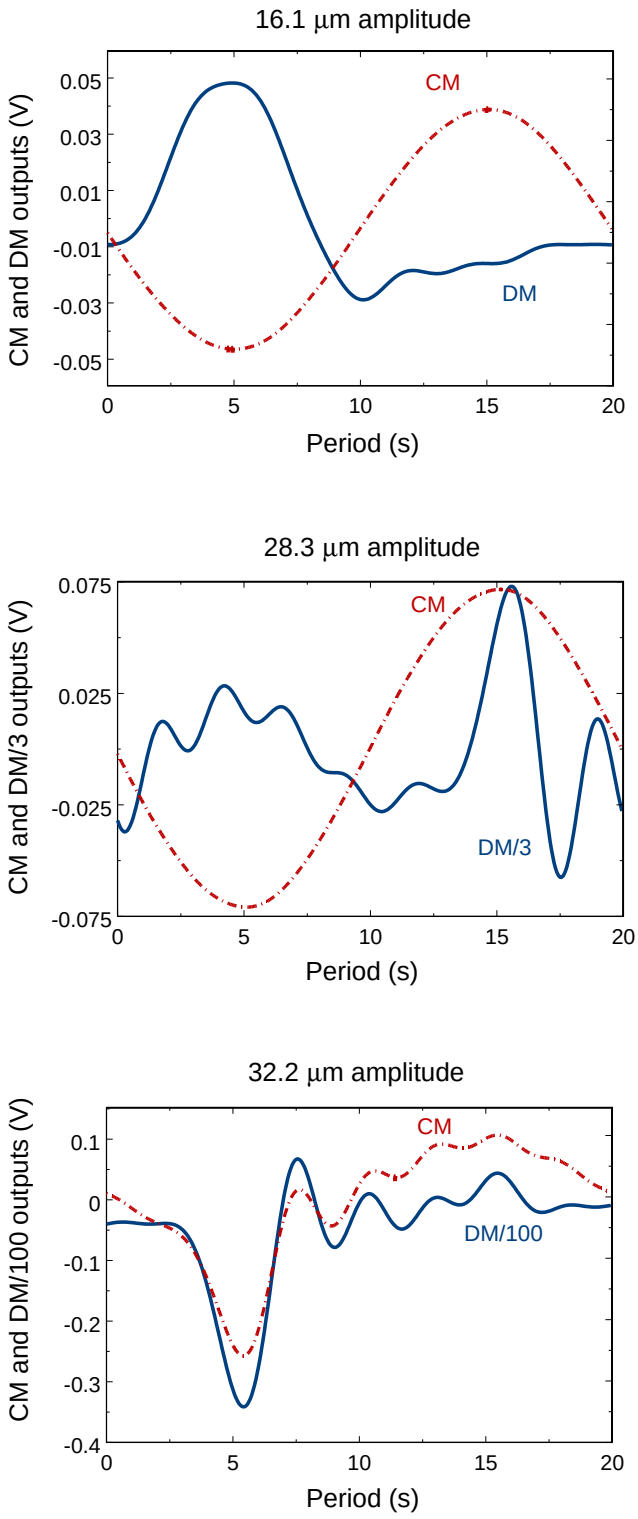

Figure 6.4: Averaged signal of the CM and DM time trace when the source mass is moved by 6.75 μm from its initial position. The driving amplitudes are 16.1, 28.3, and 32.2 μm.

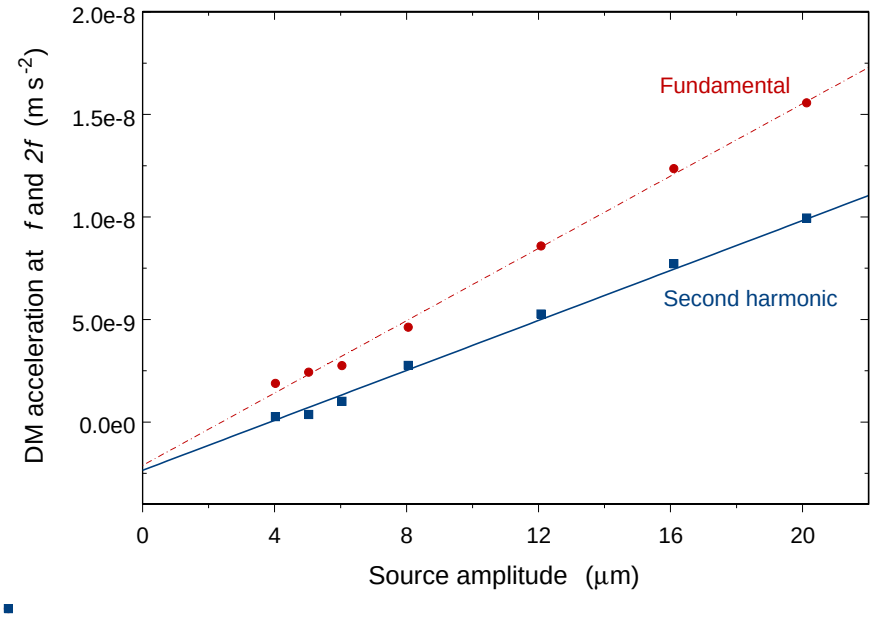

Figure 6.5: DM acceleration at f and $2f$ as a function of the source amplitude when the source mass is displaced by 6.75 μm from its initial position. The points at which the source clearly touches have been excluded.

to a source driving amplitude of 28.3 and 32.2 μm at which the source touches each side have been excluded.

The points have been fit to a line. The fit, however, does not pass through zero. It looks like the behavior changes near zero, in correspondence with the start of the strange structure. It would be interesting to know the signal output for amplitudes smaller than 4 μm. However, it was not possible to obtain that data due to the very small signal-to-noise ratio. We do not identify the DM output at $2f$ with a Yukawa-type signal.

6.2.3 Position 3

In Position 3, the source mass is displaced by 13.5 μm from its initial position. This should place the source closer to side 2. We would expected the data from this position to be a reflection of the data from position 1, since the separations between

the source and the two shields have been reversed. Figure 6.6 represents the averaged signal of the CM and DM time trace for several amplitudes of motion for the source.

From the graphs, we conclude the following:

- The CM output is again dominated by the tilt and unchanged when compared with the ones from Position 1 and 2.
- The DM output is not symmetric and becomes less symmetric as the source amplitude is increased.
- The strange structure of the DM output corresponds to when the source moves towards side 1.
- The DM amplitude appears to be further reduced.
- The strange structure is not apparent for source amplitudes of 14 μm or less.
- For a source driving amplitude of 24.2 μm, the source appears to be touching side 2 again. In the graph, the DM output was divided by 100 to be comparable to the CM output.

Figure 6.7 represents the fundamental and second harmonic outputs in the DM circuit for different amplitudes of motion of the source. The point corresponding to a source driving amplitude of 24.2 μm at which the source touches side 2 has been excluded.

A few interesting features are seen:

- The points have been fit to a line again.
- It does not look like a good fit. The plot may be separated into two parts: one corresponding to points for source driving amplitudes smaller than the ones for which the strange behavior starts appearing and the other for amplitudes at which the strange behavior is present.
- The output for both the fundamental and the second harmonic is reduced at the last point before the strange structure starts appearing.

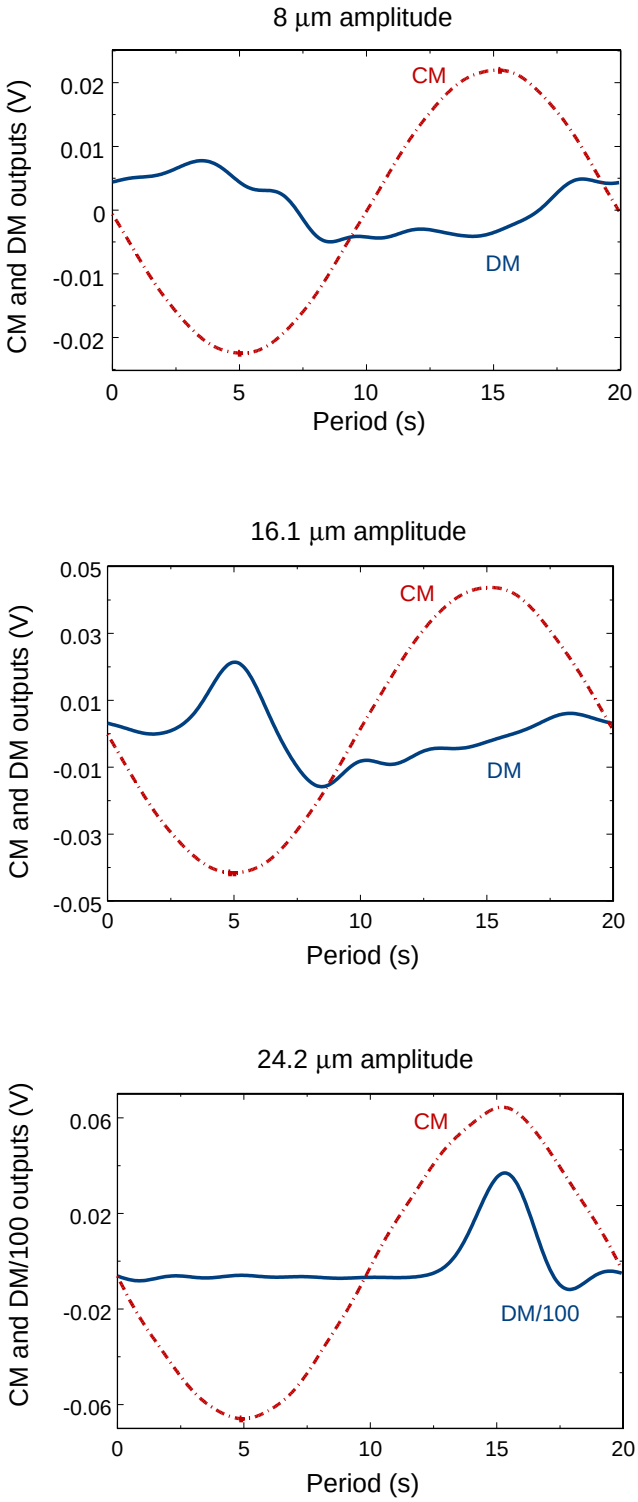

Figure 6.6: Averaged signal of the CM and DM time trace when the source mass is moved by 13.5 μm from its initial position. The driving amplitudes are 8.0, 16.1, and 24.2 μm.

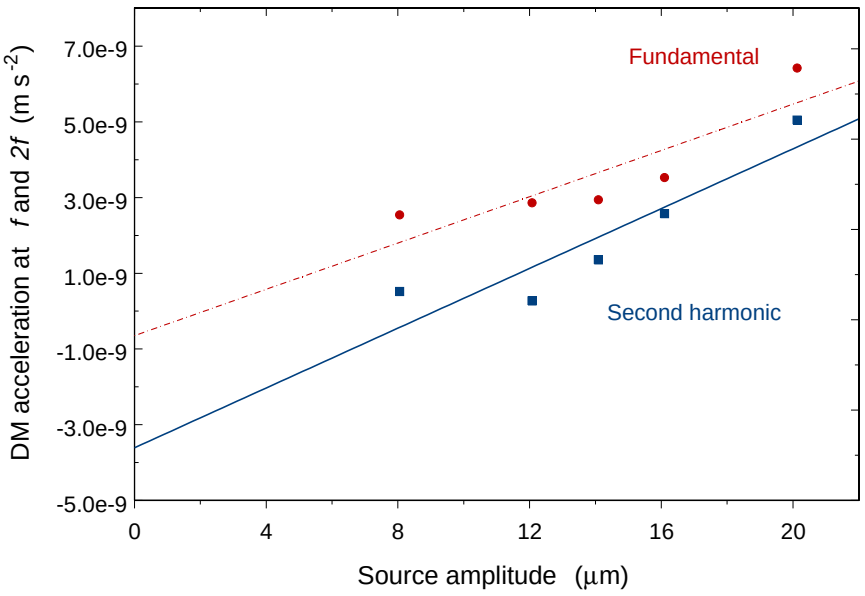

Figure 6.7: DM acceleration at f and $2f$ as a function of the source amplitude when the source mass is displaced by 13.5 μm from its initial position. The point at which the source touches has been excluded.

6.2.4 Position 4

In Position 4, the source mass is displaced by 16.9 μm from its initial position. The motivation for seeking this position was that the data from Position 3 allowed for a larger amplitude of motion for the source before running into the strange behavior than the data from Positions 1 and 2.

Figure 6.8 represents the averaged signal of the CM and DM time trace for several amplitudes of motion for the source.

The following is concluded from the graphs:

- The CM output is again dominated by the tilt and unchanged when compared the ones from Positions 1, 2 and 3.
- Before the source touches side 2, the DM output is *symmetric*.
- The strange structure *has disappeared*.

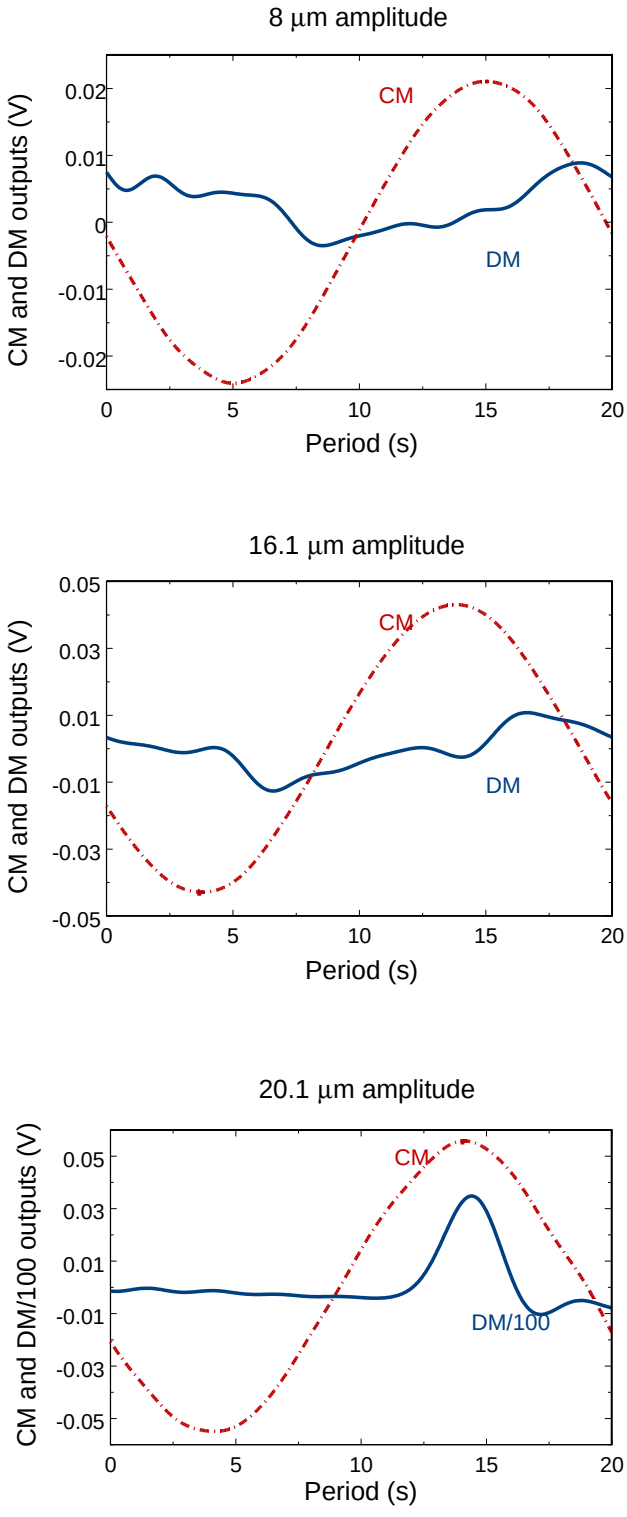

Figure 6.8: Averaged signal of the CM and DM time trace when the source mass is moved by 16.9 μm from its initial position. The driving amplitudes are 8.0, 16.1, and 20.1 μm.

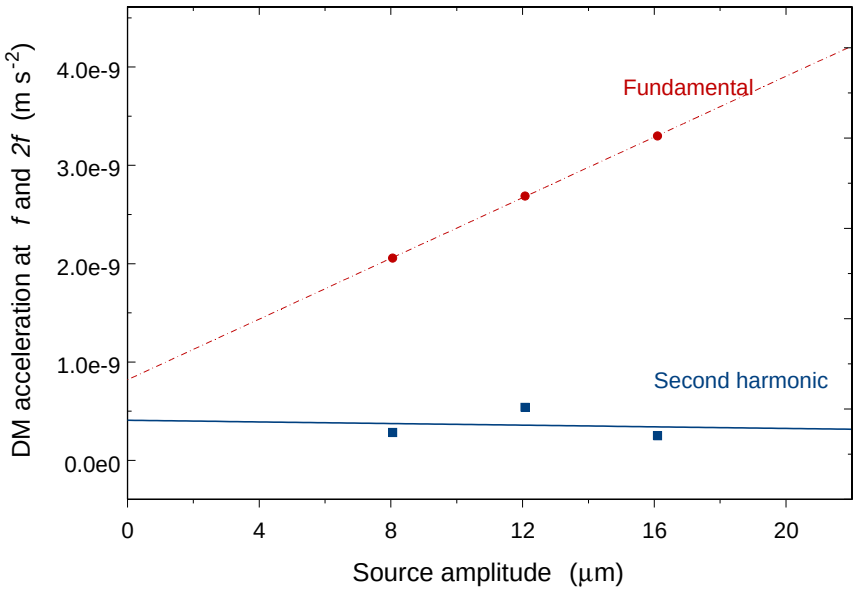

Figure 6.9: DM acceleration at f and $2f$ as a function of the source amplitude when the source mass is displaced by 16.9 μm from its initial position. The point at which the source touches has been excluded.

- For a source driving amplitude of 20.1 μm, the source appears to be touching side 2 again. In the graph, the DM output was divided by 100 to be comparable to the CM output.

Figure 6.9 represents the fundamental and second harmonic outputs in the DM circuit for different amplitudes of motion of the source.

From the graph:

- The points have been fit to a line again.
- Note that the DM acceleration at the fundamental appears to depend linearly with the source drive.
- The output for the second harmonic is reduced at the last point before the source touches side 2.

- The amplitude for the second harmonic is much smaller than for any of the other positions.

6.2.5 Summary

Combining the data from Positions 1 to 4, we find that the initial spacing for the source mass is (25±4) μm to side 1 and (37±3) μm to side 2, or a total of (62±5) μm, while its spacing to the shields is $41\pm^{77}_{4}$ μm to shield 1 and $20\pm^{13}_{4}$ μm to shield 2.

After reviewing all data, the best position for the source appears to be Position 4, because it allows a displacement of the source mass with the largest amplitude before running into the strange structure. This is unfortunate and disappointing since even though we had more spacing between the source and the shields, the source can be driven at amplitudes of only up to 16.1 μm (instead of 30 μm).

We believe that the strange behavior corresponds to some kind of soft touching. We expect it to be soft because it does not modify the source mass resonance frequency, but we think it is actually touching because of the output dependence on the source displacement. During the experiment, we thought it could be due to some kind of bump, imperfection, or some dust particles on shield 1, or due to a capacitor plate wire becoming loose. After opening the experiment, we did find a bump on the shield and there were visible dust particles. We did not find any evidence of loose wires.

6.3 Investigation of errors

We will use the data from Position 4 to determine a limit for α. Figure 6.10 shows the CM and DM accelerations for a source amplitude of 16.1 μm in Position 4, driven at a frequency of 0.05 Hz. This is the last data point plotted in Figure 6.9. To investigate errors, we have performed the experiments reported in this section.

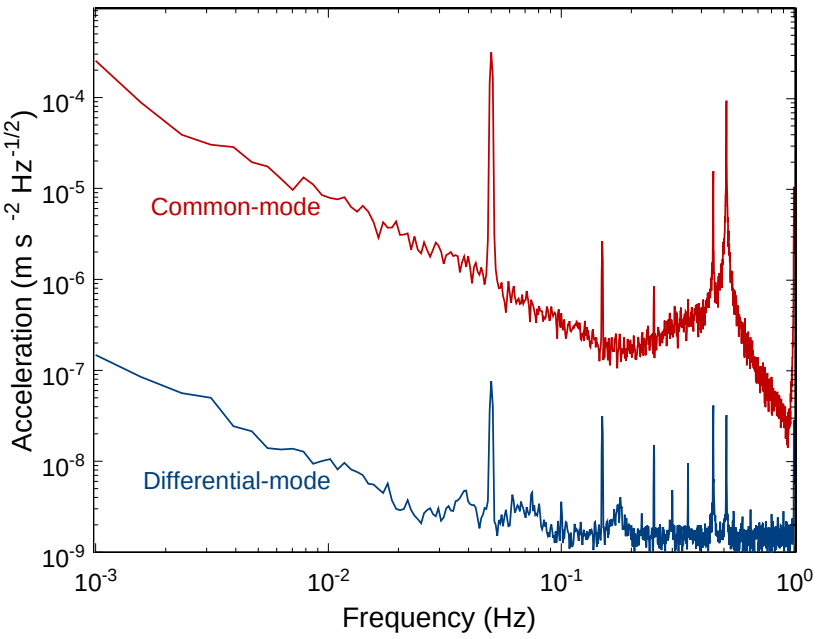

Figure 6.10: CM and DM acceleration for a source displaced from its initial position by 16.9 μm and being driven with an amplitude of 16.1 μm at 0.05 Hz.

6.3.1 Nonlinearities

The detector nonlinearities can be measured and, if needed, removed. The nonlinearities come from the square of the CM and DM outputs, as described in Section 4.2 and later estimated using Eq. (5.63). We can obtain the nonlinearity error by squaring the CM and DM accelerations and consequently, we can subtract it from our data. Figure 6.11 shows the same data as Figure 6.10, but with the nonlinear terms removed. The nonlinearity coefficient calculated by this means is $\delta\epsilon_{nl} = 1.8 \times 10^{-2}$ $(\mathrm{m/s^2})^{-1}$. This value is for 10 mA series current in the CM sensing, and 10 mA series and 90.4 mA parallel current in the DM sensing circuit. Note that removing the nonlinear terms flattens the spectrum above 0.1 Hz, but it does not eliminate the peak at 0.1 Hz. In agreement with the estimate of its magnitude from Table 6.2, the nonlinearities are not the limiting factor in the experiment.

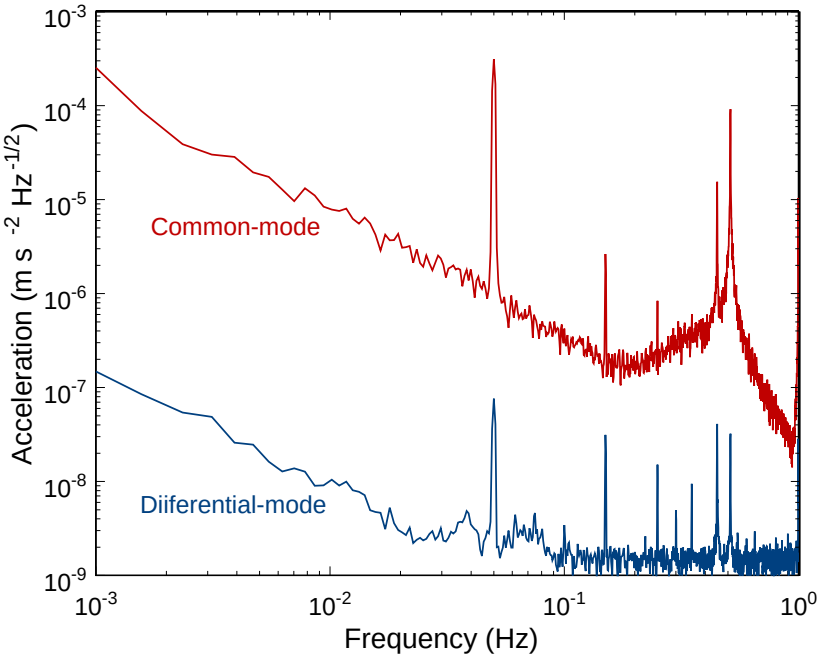

Figure 6.11: CM and DM acceleration for a source displaced from its initial position by 16.9 μm and being driven with an amplitude of 16.1 μm at 0.05 Hz. The nonlinearities have been removed in the DM output.

6.3.2 Tilt

The tilt is the dominant signal in the CM output. The procedure for removing the tilt is as follows:

- Measure the tilt using the tilt sensor. The tilt is either in phase or 180 degrees out of phase when compared to the driving signal.
- Apply an external compensation tilt using the voice-coil shakers.
- Adjust the amplitude of the compensation signal until the amplitude of the tilt sensor is nulled and the phase with respect to the drive is 90 degrees.

Figure 6.12 shows the CM and DM output with the tilt canceled to one part in 30. Even though we canceled the tilt by a factor of 30, the CM output at 0.05 Hz was reduced only by a factor of 4. This remaining signal comes from the magnetic

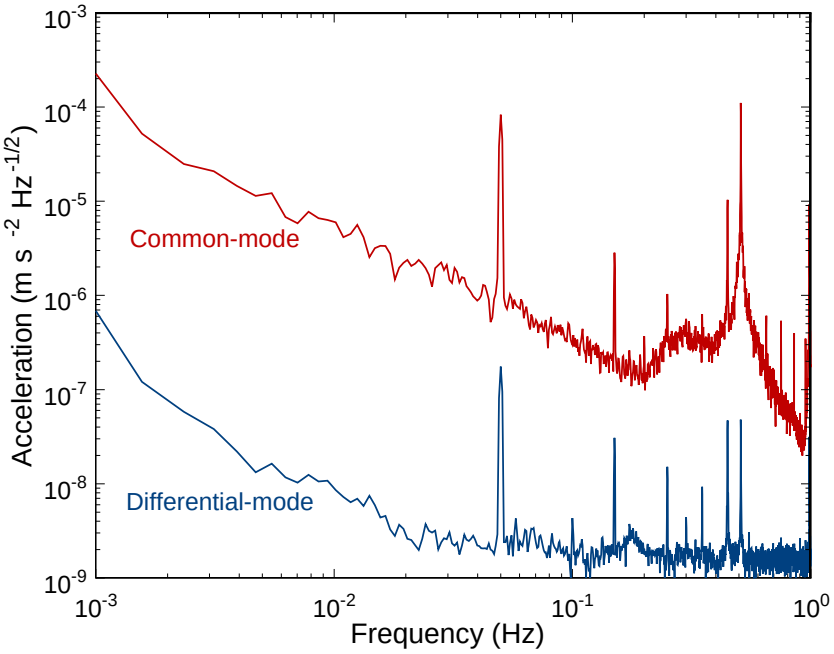

Figure 6.12: CM and DM acceleration for a source displaced from its initial position by 16.9 μm and being driven with an amplitude of 16.1 μm at 0.05 Hz. The tilt has been removed to one part in 30.

cross-talk. The DM output at 0.05 Hz is actually increased (by a factor of 2), but the output at 0.1 Hz appears unchanged.

6.3.3 Data as a function of the experiment orientation

When looking at the data taken at the same position with the same driving amplitude, but during different times, we found some deviations. We concluded that this error may be related to the experiment orientation.

The experiment was initially tilted during the cool-down to find the source-mass-to-shields spacing and look for changes in the resonance frequencies of the test masses, the source mass, and the suspension. In principle, we could center the source mass by tilting the experiment, drive it from this position, and look for additional information that helps us identify the strange behavior. In order to know that we are performing

the same measurement when tilted, our consistency check included:

- Check the suspension peaks to confirm we are still free.
- Calculate the source displacement from the tilt.
- Include the tilt-produced source displacement when computing the new source position.
- Monitor the tilt output to make sure we are driving the source in the same way.

A few things were found with the tilt experiment:

- The magnetic cross-talk has a significant dependence on the orientation of the experiment. We can interpret this as follows:
  - The cross-talk has two components, one corresponding to the AC current through the source coil and the other corresponding to the motion of the source.
  - As the source moves, the ratio between the AC currents on each side changes.
- Performing the experiment from various orientations is very time-consuming because we need to do the CM balance each time.
- Tilting the experiment increased the misalignment errors by two orders of magnitude and subsequently increased the noise floor of the DM SQUID.

The tilt increased the misalignment to one part in 80, while the effective balance was only one part in 300. This significantly increased noise floor, and the signal-to-noise ratio at Position 4 was too small for a conclusive analysis of the data.

6.3.4 Data as a function of the source current

It is possible to drive the source mass with the same amplitude but change the ratio between the DC and the AC currents. This would modify:

- The magnetic cross-talk, since it depends only on the AC current and not on the source amplitude of motion.
- The error due to nonlinearities in the source driving circuit.
- Other magnetic coupling mechanism.

As a consistency check:

- The displacement and new position of the source were calculated.
- The source was driven until it touched and then backed up for a maximum amplitude.
- The tilt was monitored to verify the same motion as before.

Three different ratios of DC to AC currents were stored in the source circuit, but no significant dependence was found in the DM output, indicating that the magnetic cross-talk was not the dominant source of error.

6.3.5 Data as a function of the sensing current

In order to look for other errors, we modified the sensing current in the DM circuit. By changing the sensing current, we will look for:

- Magnetic cross-talk. Since the magnetic cross-talk should be independent of the current in the sensing circuits, while the sensitivity of the circuits is proportional to it, the level of cross-talk is a smaller fraction of the total error as the sensing current is increased.
- Change of the error due to the nonlinearity of the sensing circuit.

The data corresponding to the smaller sensing current was heavily contaminated by the magnetic cross-talk, and the comparison to the larger sensing current was inconclusive.

6.3.6 Magnetic cross-talk

The magnetic cross-talk between the source mass and the detector is a very important source of error. Therefore, I have spent a considerable amount of time and effort to measure and possibly remove the magnetic cross-talk.

In order to measure the magnetic cross-talk, only AC current is sent through the source coils. This allows direct measurement of the magnetic cross-talk at frequency f. Since the violation signal occurs at the second harmonic, it is actually more important to measure the cross-talk at $2f$.

A potential problem comes from the fact that the AC current at f drives the source at $2f$. Since the two source driving coils are not perfectly matched, the AC current splits unevenly between them and consequently there is an effective force on the source mass at $2f$. It is, however, possible to discriminate between the motion and the cross-talk from the current dependence. The cross-talk will be proportional to the AC current, while the motion will be proportional to the AC current squared.

An additional check is performed by storing current in the sensing circuits. The magnetic cross-talk is independent of the sensing current. On the other hand, the sensitivity of the sensing circuit to motion is proportional to the sensing current when stored in the CM mode. By storing different sensing currents in the CM configuration in the sensing circuits, the term independent of the sensing current is identified as the magnetic cross-talk.

During the course of the experiment, I discovered that the magnetic cross-talk depends strongly on the exact position of the source. This was proven by tilting the whole experiment. We established that the magnetic cross-talk is due to the actual current passing through the source coils. We sent current through different leads in the source driving circuit so that the current would not go through the coils but still travel down the leads. We could not resolve any signal at f or $2f$.

The data for smaller sensing current was found to be strongly dependent on the magnetic cross-talk. When the magnetic cross-talk was removed, the result for the smaller sensing current was found to be consistent with the data for the higher current.

6.3.7 Pressure error

During the current run, we were not able to lower the pressure to below 1×10^{-5} due to the leak. However, we were able to raise it. The pressure was raised by a factor of three, but no significant change in the error was seen.

6.3.8 Electrostatic force from the capacitor plates

Since there are four capacitor plates on each side, the direction of the force can be changed by changing the capacitor plate being monitored. The magnitude of the force can be changed by changing the applied voltage. No significant change was seen when changing the sensing capacitor or voltage.

6.4 Error budget

In Chapter 4, I performed a detailed analysis of all the possible errors in the experiment and estimated their contributions. In this section, I describe the measurement of the actual errors for the experiment and determine the real error budget.

The section is organized as follows: First, I measure the SQUID noise and estimate the actual intrinsic noise of the detector. I follow with the measurement of the actual temperature noise at 1.7 K. Then, I determine the actual magnetic cross-talk between the source and the detector. Finally, I estimate the error due to the electrostatic coupling and residual gas pressure, and conclude with a summary of all contributing errors.

6.4.1 SQUID noise

Before storing any current in the sensing and temperature circuits, a trace of the SQUID noise with all cables disconnected was taken. Figure 6.13 shows the three outputs in one graph. From these, the voltage noise is measured to be $\nu_n \approx 4 \times 10^{-5}\,\mathrm{V\,Hz^{-1}}$. The equivalent current noise $I_{n,S}$ through the SQUID input coil is then found to be $1.0 \times 10^{-11}\,\mathrm{A\,Hz^{-1/2}}$. From this, the actual noise energy per bandwidth

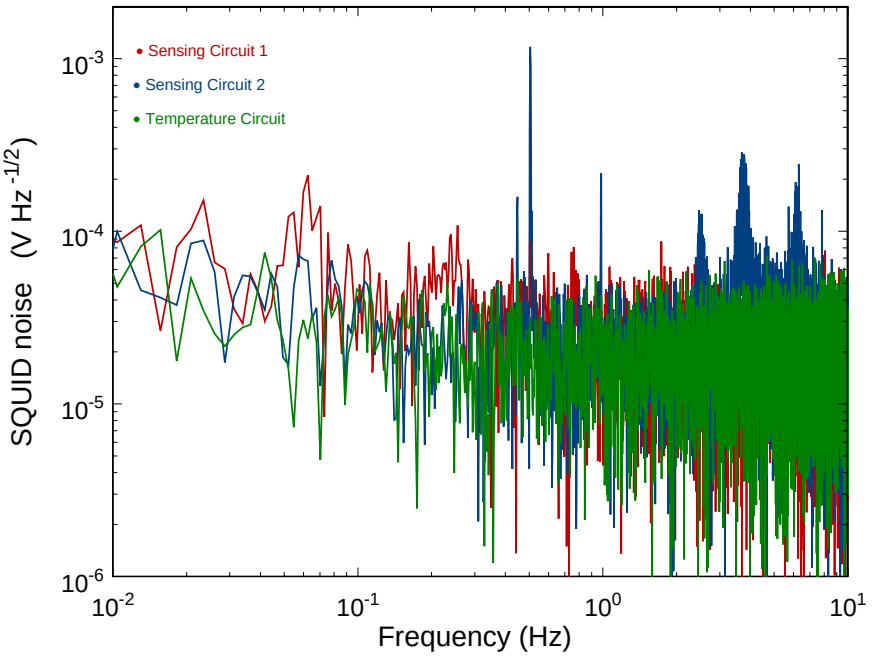

Figure 6.13: Noise level in the SQUIDs.

for 0.1 Hz is 9.0×10^{-29} J/Hz, about fifty times what we initially assumed and expected. We believe this was partially due to the electronics. Since we were not limited by the SQUID noise, we did not try to improve the SQUID performance further.

6.4.2 Intrinsic noise of the detector

In our experiment, we have $T = 1.7$ K, $Q = 10^5$, $m = 18.8$ g, and $l = 3.1$ mm. For the largest sensing currents of 200 mA in series and 1.05 A in parallel, $f_d = 13.1$ Hz, $\eta = 0.24$, and $\beta = 0.14$. Using these and the actual measured SQUID noise for the sensing circuit, the Brownian noise is calculated to be $S_T^{1/2}(0.1\,\mathrm{Hz}) = 2.68 \times 10^{-12}\,\mathrm{m\,s^{-2}\,Hz^{-1/2}}$, and the amplifier noise is $S_{SQ}^{1/2}(0.1\,\mathrm{Hz}) = 6.08 \times 10^{-11}\,\mathrm{m\,s^{-2}\,Hz^{-1/2}}$. Consequently, the total intrinsic noise of the detector is $S_\Gamma^{1/2}(0.1\,\mathrm{Hz}) = 6.09 \times 10^{-11}\,\mathrm{m\,s^{-2}\,Hz^{-1/2}}$. Assuming an integration time of 10^5 s (approximate amount of quiet data taken during the weekend), the error associated with the intrinsic noise

of the detector at 0.1 Hz is $1.9 \times 10^{-13}\,\mathrm{m\,s^{-2}}$. We did not integrate longer than 10^5 s, since the detector and other random noise were not a limiting factor in our experiment.

6.4.3 Temperature noise

In Section 4.5, we estimated the temperature noise using the data for the temperature noise of the SGG. In addition, we used the coefficients for the superconducting coils reported in [45]. These coefficients represent the effective mass displacement for a given temperature variation. It is expected that these coefficients arise from the penetration depth modulation with temperature, but Moody *et al.* [45] found the behavior unpredictable.

I measured the actual temperature noise spectrum for 1.7 K and computed the actual coefficient for the superconducting coils. The low-frequency behavior of the thermometer was reproduced by the temperature circuit. Figure 6.14 shows the direct correlation between the thermometer and the SQUID output of the temperature sensing circuit. At $f = 0.1$ Hz, the spectral density is $S_T^{1/2}(f) = 1.5 \times 10^{-7}\,\mathrm{K\,Hz^{-1/2}}$, lower than the one established in Section 4.5.

The figure also shows the sensitivity to motion of the temperature circuit. Although there was shielding between the temperature coil and the sensing coil, once current was stored in the sensing circuit, the temperature circuit became sensitive to motion. This behavior is still a puzzle and did not change with the current in the temperature coils. (The temperature sensitivity did depend on the current in the temperature coils.) The temperature coefficient of the superconducting coils was measured to be $(1.7 \pm 0.3) \times 10^{-8}\,\mathrm{m\,K^{-1}}$, in close agreement to the value measured at 4.3 K [45]. This measurement shows definitively that the temperature sensitivity is not due to a change in the penetration depth of the superconductor. This is because at 1.7 K, the modulation of penetration depth in Ta is 5.5 times smaller than observed, while in Nb it is about 200 times smaller.

The temperature-induced noise is $1.4 \times 10^{-11}\,\mathrm{m\,s^{-2}Hz^{-1/2}}$ at $f = 0.1$ Hz. As the temperature circuit was sensitive to motion, we could not use it for the purpose of

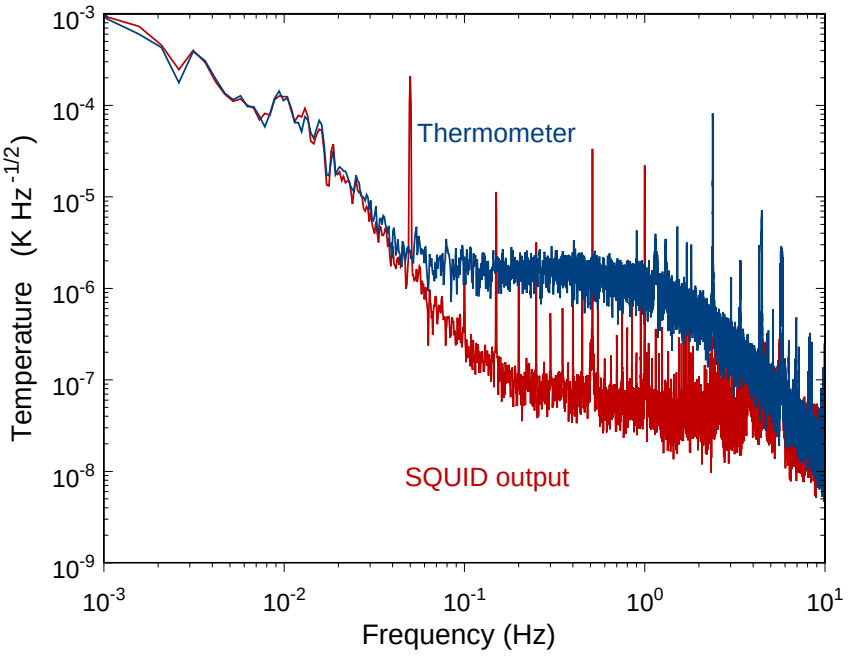

Figure 6.14: Correlation between the thermometer and the SQUID output of the temperature sensing circuit.

canceling the temperature sensitivity of the sensing circuits. For an integration time of 10^5 s, we obtain a noise of $4.2 \times 10^{-14}\,\mathrm{m\,s^{-2}}$ at $f = 0.1$ Hz.

6.4.4 Vibration noise

Seismic noise

The linear acceleration is rejected by a factor of CMRR=770 (see Section 5.8.4). The angular acceleration couples to the detector through misconcentricity between the two test masses, measured to be $\delta l = 3.8 \times 10^{-3}$ m. The accelerometer also has a residual sensitivity to centrifugal acceleration through its nonzero baseline, $l = 3.1$ mm.

Assuming an integration time of 10^5 s, Table 6.1 summarizes the residual seismic driven noise experienced by the detector.

Seismic noise (10^5 s averaging)	$a_d(2f)$ (m/s^2)
Linear acceleration	7.1×10^{-13}
Angular acceleration	9.5×10^{-14}
Centrifugal acceleration	9.8×10^{-16}
Total seismic noise	7.1×10^{-13}

Table 6.1: Seismic noise.

Source driven noise	$a_d(2f)$ (m/s^2) 8 μm	$a_d(2f)$ (m/s^2) 12.1 μm	$a_d(2f)$ (m/s^2) 16.1 μm
Linear acceleration	7.3×10^{-12}	1.1×10^{-11}	1.4×10^{-11}
Angular acceleration	1.4×10^{-12}	2.1×10^{-12}	2.8×10^{-12}
Nonlinear response	9.6×10^{-13}	2.2×10^{-12}	3.8×10^{-12}
Total source driven noise	7.5×10^{-12}	1.3×10^{-11}	1.5×10^{-11}

Table 6.2: Source-driven dynamic noise for three different source amplitudes.

Source-driven noise

In the actual experiment, the largest amplitude of source motion was 16.1 μm. This induces a platform displacement of 3.58×10^{-10} m and a tilt of 1.50×10^{-6} rad about the y axis at the driving frequency. With the measured nonlinearity $\delta\epsilon_{nl} = 1.8 \times 10^{-2}$ (m/s^2)$^{-1}$ and axis misalignment $\delta l = 3.8 \times 10^{-3}$ m (see Section 5.9), the errors due to the source motion are estimated in Table 6.2.

6.4.5 Magnetic cross-talk

Tables 6.3, 6.4, and 6.5 show the output from the three SQUIDs as a function of the AC current through the source driving coils with no DC currents stored in the circuits. The output at the fundamental is repeatable in amplitude and phase, but the output at the second harmonic is not. Storing current in the sensing circuits does not modify the output at f, but increases the noise level, so the signal at $2f$ is contaminated.

Driving current (mA)	Amplitude at f (V)	Phase at f (degrees)	Amplitude at $2f$ (V)	Phase at $2f$ (degrees)
6.825	3.05×10^{-3}	-167	1.65×10^{-5}	45.5
13.65	7.70×10^{-3}	-169	2.72×10^{-5}	-129
20.474	1.31×10^{-2}	-170	1.65×10^{-5}	26.7
27.299	1.88×10^{-2}	-171	2.27×10^{-5}	175

Table 6.3: Fundamental and second harmonic amplitude and phase of sensing circuit 1 SQUID output as a function of the source driving current.

Driving current (mA)	Amplitude at f (V)	Phase at f (degrees)	Amplitude at $2f$ (V)	Phase at $2f$ (degrees)
6.825	3.32×10^{-3}	30.1	6.29×10^{-5}	116
13.65	1.08×10^{-2}	21.2	4.78×10^{-5}	56.8
20.474	2.00×10^{-2}	17.3	4.86×10^{-5}	-75.1
27.299	2.83×10^{-2}	12.4	7.8×10^{-5}	61.2

Table 6.4: Fundamental and second harmonic amplitude and phase of sensing circuit 2 SQUID output as a function of the source driving current.

Driving current (mA)	Amplitude at f (V)	Phase at f (degrees)	Amplitude at $2f$ (V)	Phase at $2f$ (degrees)
6.825	1.03×10^{-3}	16.4	1.97×10^{-5}	-147
13.65	2.39×10^{-3}	3.7	8.62×10^{-6}	-158.8
20.474	3.40×10^{-3}	-38.5	1.04×10^{-5}	148.7
27.299	4.06×10^{-3}	-6.1	1.21×10^{-5}	75.5

Table 6.5: Fundamental and second harmonic amplitude and phase of the temperature circuit SQUID output as a function of the source driving current.

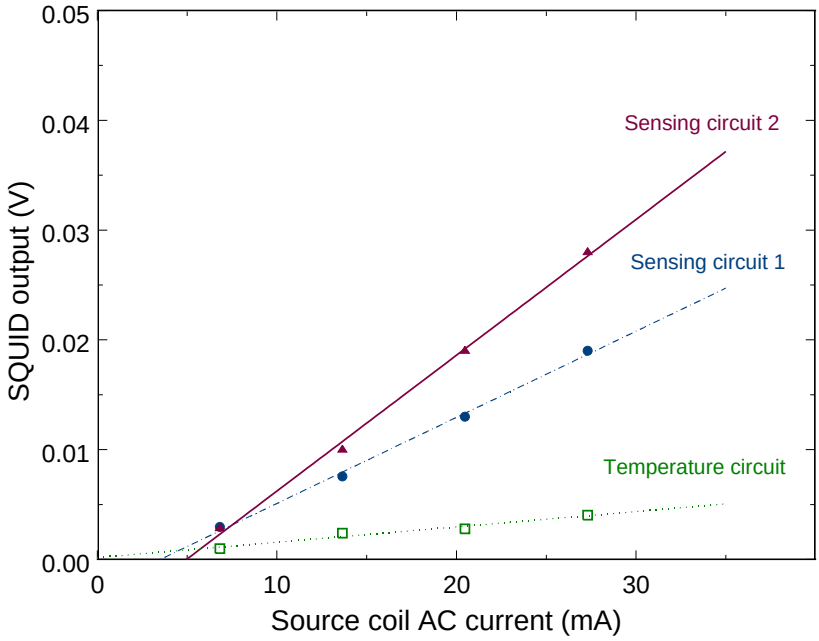

Figure 6.15: SQUID output component of the two sensing circuits and the temperature circuit in phase with the current through the source driving circuit at the driving frequency f.

The magnetic cross-talk is in phase with the drive. Figure 6.15 shows the components of the output at the fundamental frequency of all three circuits with no DC current in the circuits. The second harmonic outputs are plotted separately in Figure 6.16, with large error bars representing the variation of it. Note that for both the fundamental and the second harmonic, sensing circuit 2 has a larger cross-talk than sensing circuit 1, so it looks as if it would be better to use sensing circuit 1 to sense the DM output. Unfortunately, this was the circuit that had a disconnected coil.

Tables 6.6 and 6.7 give the corresponding equivalent accelerations in sensing circuit 1 and 2, respectively, for different currents in the two sensing circuits. Note that, after all we ended up using the better circuit (sensing circuit 2) in terms of the cross-talk as well.

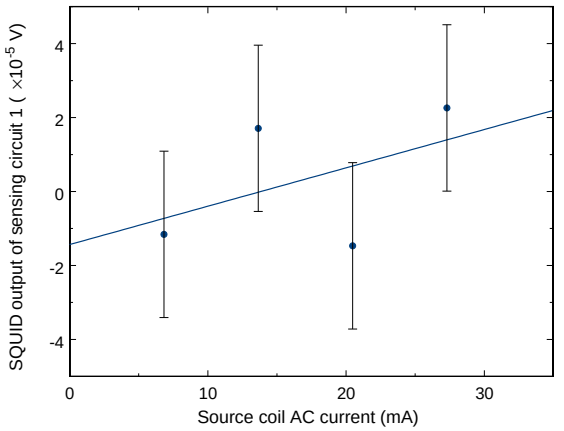

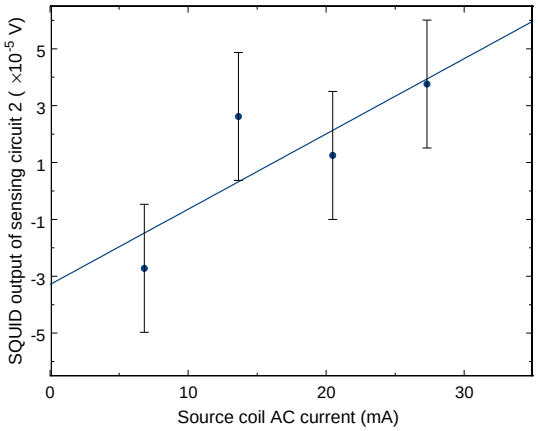

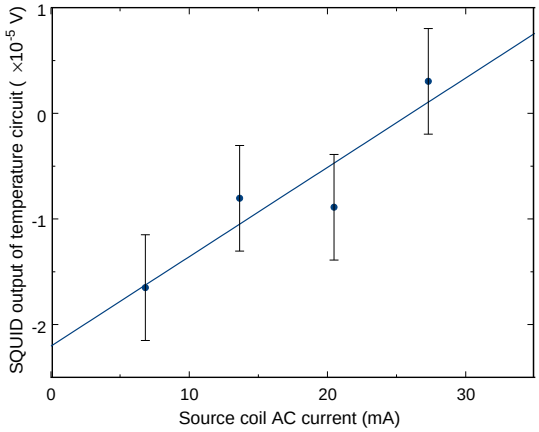

Figure 6.16: SQUID output of sensing circuit 1, sensing circuit 2, and the temperature circuit in phase with the current through the source driving circuit at $2f$.

Sensing current (mA)	Cross-talk level at f ($m/s^2/mA$)	Cross-talk level at $2f$ ($m/s^2/mA$)
50	1.63×10^{-8}	2.21×10^{-11}
100	8.30×10^{-9}	1.11×10^{-11}
200	4.27×10^{-9}	5.81×10^{-12}
1000	1.02×10^{-9}	1.38×10^{-12}

Table 6.6: Fundamental and second harmonic cross-talk level per source driving current in sensing circuit 1 as a function of the sensing current.

Sensing current (mA)	Cross-talk level at f ($m/s^2/mA$)	Cross-talk level at $2f$ ($m/s^2/mA$)
50	6.26×10^{-9}	1.35×10^{-11}
100	3.130×10^{-9}	6.80×10^{-12}
200	1.64×10^{-9}	3.57×10^{-12}
1000	3.91×10^{-10}	8.49×10^{-13}

Table 6.7: Fundamental and second harmonic cross-talk level per source driving current in sensing circuit 2 as a function of the sensing current.

The cross-talk is much larger than initially estimated. We do not understand the reason for this, but are addressing this issue in a second-generation experiment (see Section 7.1 for a detailed discussion).

6.4.6 Other errors

To compute other errors, we use the values for a source-to-shield spacing of 25 μm and a source modulation amplitude of 16.1 μm, as found in Section 6.2.5. The residual gas pressure and the magnetic pressure are discussed in Sections 4.8 and 4.9. We find that the errors at $2f$ are $1.3 \times 10^{-14}\,m/s^2$ for the gas pressure and $2.8 \times 10^{-13}\,m/s^2$ for the magnetic pressure.

The electrostatic coupling is a very important error. In Section 4.10, three major sources of the electrostatic force error were discussed, the force due to the capacitor

plates, the force due to the patch field, and the Casimir force. The estimated acceleration resulting from the force exerted by the capacitor plate on the center part of the housing is $1.3 \times 10^{-14}\,\mathrm{m/s^2}$. The estimated acceleration due to the Casimir force is $1.0 \times 10^{-16}\,\mathrm{m/s^2}$.

The estimated acceleration due to patch fields is $4.5 \times 10^{-10}\,\mathrm{m/s^2}$. This is an extremely large error that was not considered in detail when the experiment was first designed. The center part of the housings was made soft to minimize its distortion, as explained in Section 4.6.2. The soft suspension, however, made the experiment much more susceptible to the patch fields, since we have no way of performing a CM balance for it. This was a flaw in the original design.

There is ongoing research in the scientific community regarding the patch fields since they are found to be relevant for large scale experiments, such as LISA [70, 10] and GP-B [24]. Measuring the patch fields is beyond the scope of this thesis. Instead, we are designing a second-generation experiment, which is much less sensitive to the patch effect (see Section 7.1 for a detailed discussion).

6.4.7 Summary of errors

All the errors contributing to the experiment are summarized in Table 6.8. The source-to-shield spacing in Position 4 is $41\pm^{77}_{4}$ μm to shield 1 and $20\pm^{13}_{4}$ μm to shield 2, as obtained in Section 6.2.5. The source-to-test-mass spacing is calculated by adding the source-to-shield spacing to the shield-to-test-mass spacing. In Section 5.3, we obtained for the spacings between the test mass and the shields (183 ± 12) μm for side 1 and (254 ± 12) μm for side 2. However, since we stored a large current in the sensing circuit, the test masses are actually closer to the shields. Using the numerical model, I obtain that test masses 1 and 2 have moved by 53 and 86 μm, respectively. With this, I obtain that the shield-to-test-mass spacing is (130 ± 12) μm for side 1 and (168 ± 12) μm for side 2. This leads to the source-to-test-mass spacing $171\pm^{78}_{13}$ μm to test mass 1, and $188\pm^{18}_{13}$ μm to test mass 2.

The metrology errors have been calculated in Section 4.1. The source is displacing by 8.0, 12.1, and 16.1 μm. Since the spacing between the source and the test masses

Error source	$a_d(2f)$ (m/s^2) 8 μm	$a_d(2f)$ (m/s^2) 12.1 μm	$a_d(2f)$ (m/s^2) 16.1 μm
Metrology	$< 2.1 \times 10^{-15}$	$< 2.1 \times 10^{-15}$	$< 2.1 \times 10^{-15}$
Random errors	1.5×10^{-11}	9.3×10^{-11}	8.0×10^{-12}
Source dynamic	7.5×10^{-12}	1.3×10^{-11}	1.5×10^{-11}
Residual gas pressure	1.4×10^{-13}	2.1×10^{-13}	2.8×10^{-13}
Magnetic coupling	2.2×10^{-11}	3.3×10^{-11}	4.4×10^{-11}
Electrostatic coupling	1.5×10^{-10}	2.3×10^{-10}	3.0×10^{-10}
Total error	2.2×10^{-10}	3.4×10^{-10}	4.5×10^{-10}

Table 6.8: Estimated error budget for a source-to-shields spacing of 25 μm and a source modulation amplitude of 8.0, 12.1, and 16.1 μm.

is larger than previously assumed, the metrology errors in Table 6.8 are an upper bound on the actual errors.

The intrinsic noise of the detector, the temperature noise, and the seismic noise are all random errors. However, they may not include all the random errors. The data from one day to another, under the same conditions, had a significant fluctuation. This may be due to a drift in the tilt of the experiment, which changes the source mass position, the CM balance, and magnetic cross-talk. This is a random error, which is much bigger than the other random errors. For source amplitudes of 8.0, 12.1, and 16.1 μm, it is 1.5×10^{-11}, 9.3×10^{-11}, and 8.0×10^{-12} m/s^2, respectively. Table 6.8 summarizes all the errors for the 8.0, 12.1, and 16.1 μm displacement. The total random error in Table 6.8 has been estimated from the actual scatter of the data.

6.5 Experimental results

I analyze only the data from Position 4, because it allowed largest displacement of the source mass before running into the strange structure that we believe corresponds to some kind of soft touching. The soft touching was identified with a small bump

in the shields in addition to dust particles.

In Figure 6.9, we plotted the total DM acceleration at f and $2f$ as a function of the source amplitude. Here I take only the component in phase with the source drive since we expect the signal to be in phase with the displacement of the source. Figure 6.17 represents the fundamental and second harmonic outputs in the DM circuit for different amplitudes of motion of the source. The accelerations have been calculated using the DM calibration given in Section 5.5.2, adjusted for the corresponding currents.

The source-to-test-mass spacing are $171\pm^{78}_{13}$ μm for test mass 1 and $188\pm^{18}_{13}$ μm for test mass 2, as found in Section 6.4.7. I identify the DM output at $2f$ with a Yukawa-type signal and compute it as a function of the source amplitude. We obtain α equal to 475 ± 858, 905 ± 578, and -170 ± 425 at $\lambda = 180$ μm for driving amplitudes of 8.0, 12.1, and 16.1 μm, respectively. A weighted average of these three measurements gives

$$\alpha = 244 \pm 318. \tag{6.1}$$

This becomes ten times larger at $\lambda = 50$ μm. Our best sensitivity is $\alpha = 218 \pm 284$ at $\lambda = 282$ μm. We obtain a null result, but with a very large error that represents the uncertainty in the weighted average.

The error came mostly from the patch field effect. This effect was not considered in detail when the experiment was first designed and becomes important due to the soft suspension of the center blocks of the housings. This was an oversight in the original design since it allowed the parasitic forces from the source mass to drive each test mass block directly, increasing the effect from these forces several orders of magnitude. A solution to this problem is proposed in Section 7.1.

The magnetic cross-talk was found to be very important and much larger than initially estimated. I performed an in-depth study of this error and explain how to remove it in the next section.

In addition, the data appeared to have a large random fluctuation during the experiment. This made us believe that the output signal is affected by the bad housing. Tilting the experiment had a great effect on the alignment, determined

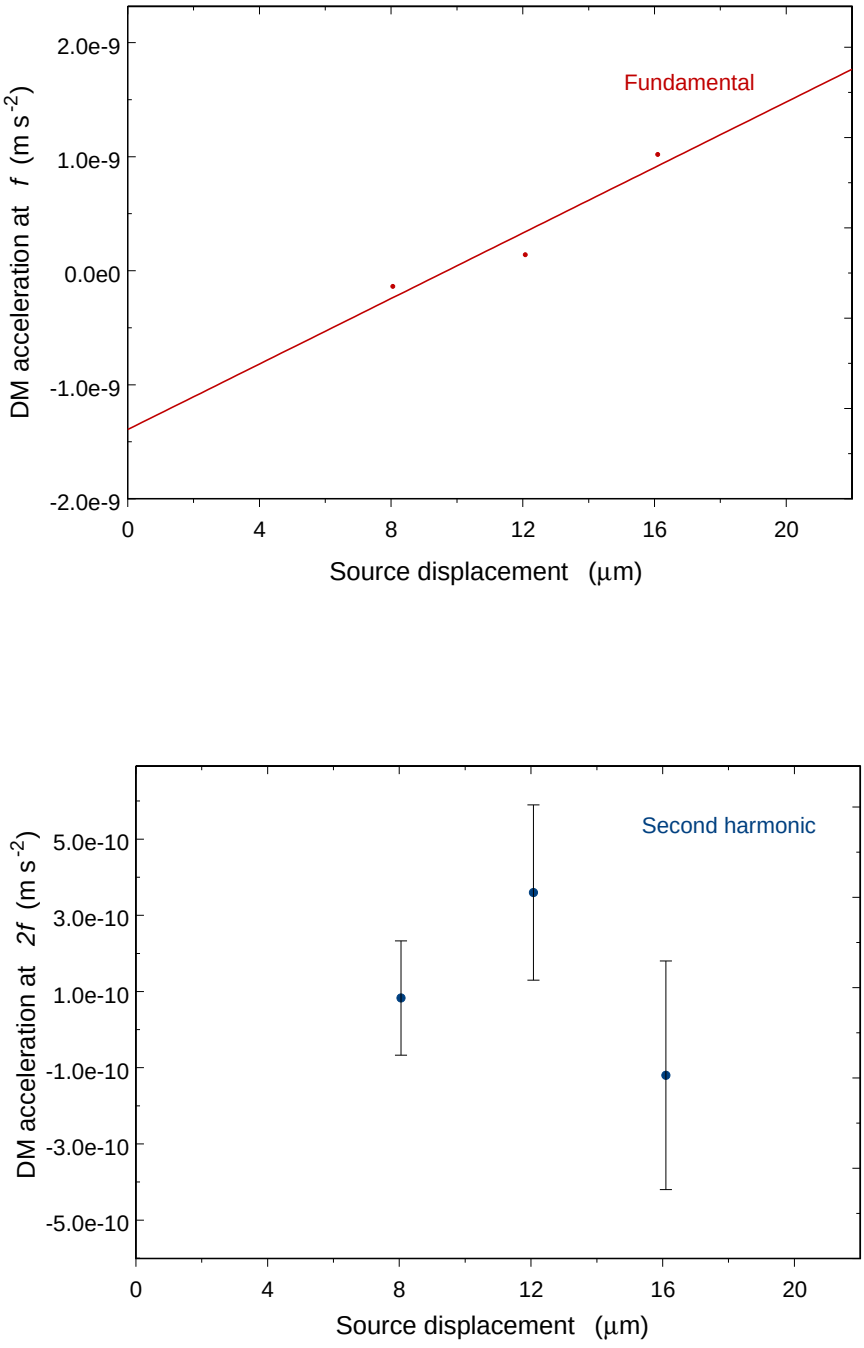

Figure 6.17: In-phase component of the DM acceleration at f and $2f$ as a function of the source amplitude for Position 4.

by the orientation of the center part of the housing. We conclude that the day-to-day drift fluctuations affected the housing orientation as well, leading to the large observed fluctuations.

Chapter 7

Improvements and Conclusions

7.1 Suggested improvements

In the current experiment, we obtained a result five orders of magnitude above the proposed sensitivity. Even though the result is inferior to our expectations, it helped us identify the problems and propose modifications and improvements to the design. In the current experiment, we found a random error due to the broken housing. We believe this was responsible for some of the problems we saw and limited our sensitivity. In addition, the largest estimated errors came from the patch fields, the magnetic cross-talk between the source and the detector, and the source-driven noise. In this section, I describe these problems and discuss how to address them and improve the assembly for a next-generation experiment.

7.1.1 The broken housing problem

The superconducting accelerometer technology used for this experiment was fully developed in our lab over the past two decades [13, 14, 45]. The mechanical design of the ISL experiment, however, was completely new. The main difference is that to achieve very small spacings, the source mass and the detector are suspended from the same platform. As the source mass moves, to prevent the reaction forces from distorting the detector, it was necessary to decouple the center parts of the housings containing the detector from the outer rim. This was achieved by inserting a mechanical weak link, a cantilever spring, between them. This soft suspension also

permitted the alignment of the test masses using the alignment coils.

In the initial design, the cantilever springs were 1.27 mm thick, but detailed calculations showed that to achieve the required alignment, we had to make them 0.635 mm, half of their initial thickness. Since the housings were already machined, a secondary machining had to be done. However, the spring on the first housing was machined badly, thinning it too much at some parts and making the spring weaker.

The spring started breaking in a corner. We foresaw this problem and ordered new housings. We believe that replacing the broken housing will resolve our largest error.

7.1.2 Patch fields

Replacing the housing, however, will not be enough to reach the desired sensitivity. Inserting the soft link in the housings made the experiment susceptible to the patch field effect as well as the force due to the residual gas pressure, increasing the error by several orders of magnitude. This was a very unfortunate oversight in the original design.

As suggested by Moody [42], a way to make these effects CM with the existing hardware is to connect the inner sections of the housings together with a bracket. The bracket would be external to the existing experiment and connect to the inner sections through holes drilled in the cover plates. The bracket would be symmetric relative to the horizontal plane passing through the center-of-mass and route over and below the outer housings. By placing a mirror on top of the bracket, we could cancel the tilt of the center part of the housing. This geometry retains the isolation of the center parts of the housings necessary to minimize distortion, but does not address the cross-talk issue.

A more drastic option is to make the center parts of the housings rigid. The mechanical cross coupling through either a source-driven distortion or motion of the detector is a large source of error. According to the performed FEA, driving the source mass by 87.5 μm at f produces a DM acceleration of $5.1 \times 10^{-12}\,\mathrm{m\,s^{-2}}$ at $2\,f$.

In order to use this modification, we need a different way to suspend and drive

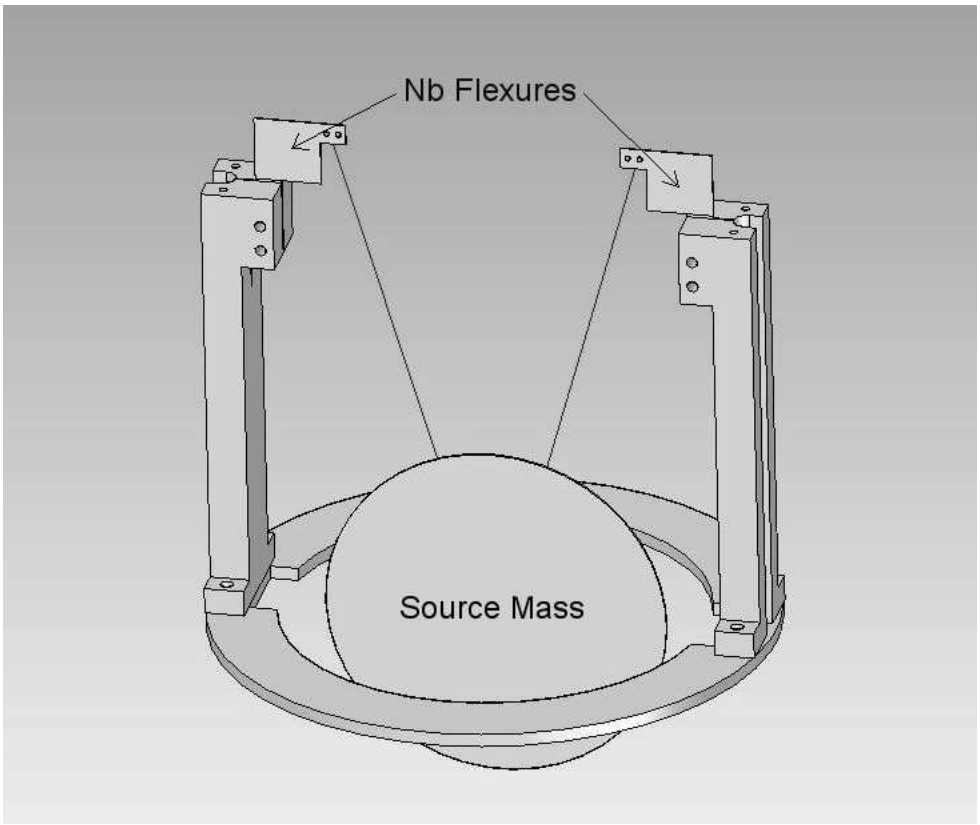

Figure 7.1: The new Source mass suspension.

the source mass. Paik [56] proposed completely decoupling the source by suspending it and driving it from the outside. The source driving coils will be placed inside separate Nb cavities, shielded from the rest of the assembly. Driving the source from outside will eliminate (or at least substantially reduce) the magnetic cross-talk and the distortion problem and allow making the center parts of the housings rigid. The idea is to suspend the source from two wires. The pendulum mode for the dimensions would be about 1 Hz.

If a mass is placed on the top of a piece of thin foil held from the bottom, the foil acts like a negative spring. By suspending the source from a thin foil, we would have a pendulum suspended from a negative spring. By adjusting the thickness of the foil, we could have a resonance frequency as low as 0.1 Hz. Venkateswara [83] is currently building a prototype to test the source mass suspension and resonance frequency. This is a very challenging design and we are still discussing the exact details of it.

Figure 7.1 shows the proposed suspension. The source would be driven at resonance by applying a force on the Nb flexures. By driving the source on resonance, we would also eliminate the effect of circuit nonlinearity. This experiment is currently being designed and is in preparation in our lab.

7.1.3 Magnetic cross-talk

If known precisely, the magnetic cross-talk can be taken into account and subtracted from the data. It can be removed by storing currents with opposite polarity in the source driving circuit and combining the data properly. The general idea is the following:

- Store DC current in the source circuit clockwise, as shown in Figure 7.2 and send AC current. For a periodic AC current $i_{\mathrm{AC}} = i_0 \cos 2\pi f t$, during the first half of the period, the current on side 1 is larger than the current on side 2, and consequently the source moves first to the right and then to the left, in phase with the driving current.

- Store DC current in the source circuit counterclockwise, as shown in Figure 7.3 and send AC current. For the same periodic AC current, during the first half of the period, the current on side 1 is smaller than the current on side 2, and consequently the source moves out of phase with the driving current.

- The CM and DM outputs are recorded in both cases as functions of the AC current, which can be used as a trigger to manipulate the data.

- The cross-talk depends only on the direction of the AC current, so it should be the same in both cases, while the motion-induced signals are opposite. Adding both signals with the AC current in phase and dividing by 2 gives a measure of the magnetic cross-talk.

- Phase-shifting the data from one case by 180 degrees with respect to the other, adding them, and dividing the sum by two, gives the pure motion.

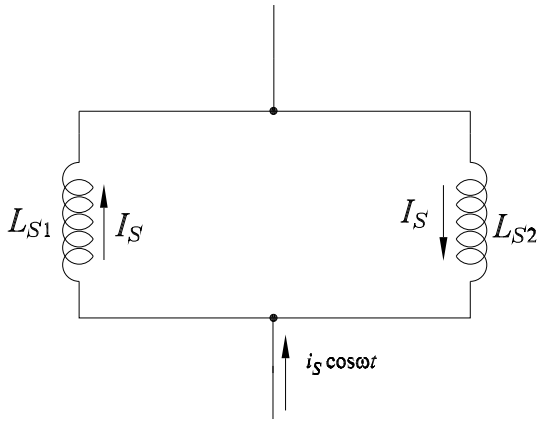

Figure 7.2: Source circuit configuration that allows motion in phase with the driving current.

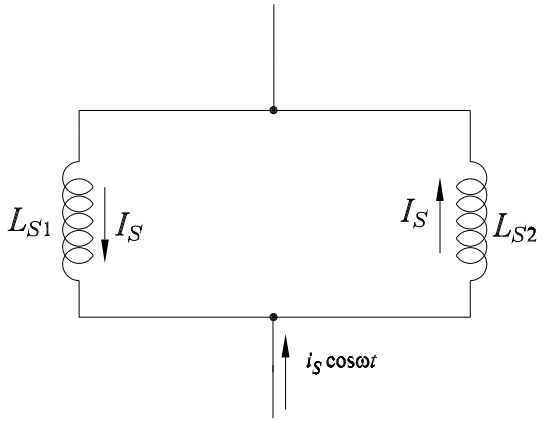

Figure 7.3: Source circuit configuration that allows motion out of phase with the driving current.

- As a consistency check, the same capacitor plate is monitored in both cases. As long as the capacitor signal at f and $2f$ are the same for both cases, the motion is considered the same.

Although the magnetic cross-talk can be removed in principle, removing it by manipulating the data is not the most desirable procedure in a null experiment. In addition, the magnetic cross-talk is currently four orders of magnitude above our

design sensitivity, making its removal extremely difficult.

A way to alleviate the magnetic cross-talk problem is by performing a resonance experiment in which the source driving current will be orders of magnitude smaller. During the course of this thesis, we have discussed the possibility of performing a resonance experiment many times, but this was not practical due to the high resonance frequency of the source mass. A resonance experiment at the current source mass frequency is not feasible since it would cause an uninhibitedly large linear acceleration error due to the platform recoil.

Achieving a low suspension frequency, as discussed in the previous section, would allow us to perform a resonance experiment.

7.1.4 Source-driven noise

The source-driven noise was a very large source of error as well. It can be reduced by improving the tilt control, the CM balance, the alignment, and the linearity of the source signal.

In the performed experiment, we were able to compensate for the tilt by up to a factor of 30. According to our error analysis, this improved both the linear and the angular acceleration noise by a factor of 30. The nonlinearity error, since it depends quadratically on the tilt, is reduced by three orders of magnitude. In our actual experiment, the error due to the tilt was smaller than our total error and we did not see an effect in our signal when compensating for the tilt.

To obtain a better tilt compensation, it is possible to take longer data sets. However, this is also limited. The sensitivity of the tilt sensor is a limiting factor for the accurate tilt compensation. There is an ongoing effort to improve the sensitivity of the tilt sensor. After a detailed inspection, Norton [48] found that the beam polarizers were peeling off, reducing the light intensity. The polarizers were replaced and the total signal was increased by a factor of 5. A room-temperature prototype is currently being tested.

7.1.5 Pressure

Although not the dominant source of error, the pressure becomes important quickly as we increase the ratio between the driving amplitude and the total spacing. Making the center part of the housings rigid will reduce this problem, but the shields will still be susceptible to it. A better pressure control is highly desirable. To reduce the pressure, we need to fix the cold leak.

Even if we eliminate the leak, the lowest pressure will be limited. The cryostat we are currently using was not designed to work in an extremely high vacuum since it contains several outgassing materials. As described in Section 5.1, the vacuum can is supported by four fiberglass tubes. The center tube opens up to the vacuum space for the laser beam. In addition, the suspension wires are connected to rubber tubes and are also inside the vacuum space. Finally, we attach and hold the wires with tape, sometimes masking tape.

We can eliminate the tape and use only GE-varnish, but modifying the cryostat is not feasible. Instead, we are investigating the possibility of adding a container with charcoal that will act as an absorption pump, just like in the space between the walls of the dewar, as described in Section 5.2. The major problem is that we need high pressure while storing persistent currents and want to be able to turn this pump on and off.

7.1.6 Capacitor plates

The capacitor plates turned out to be a very useful part of the experiment. We could monitor and verify the source position and motion with them. However, since the capacitor plates were so small, their capacitance was only a small fraction of the total capacitance including the leads. I believe that installing new larger capacitor plates will be an improvement with great benefits. Larger capacitor plates are being incorporated into the modified experiment.

7.1.7 Clean assembly

The experiment was assembled in a clean room. Even though extreme care was taken during the assembly process, after opening it, I found some dust particles. In the future, better care must be taken.

7.1.8 Source mass

The housings were made out of Nb, while the source and test masses were machined out of Ta, as described in Section 2.2. A finite element analysis showed that the bowing due to a differential contraction between Ta and Nb could cause no more than a 25-μm displacement. Inductance measurements of the source coils, however, indicated that the source bowed toward one side by an order of magnitude larger amplitude. This behavior is not understood and a Nb replacement source mass was ordered. In order to maintain a large signal, the new Nb source is thicker than the existing Ta one, making the baseline significantly larger. On the other hand, with a thicker plate, it is possible to grind and then lap the surface to 1 μm. The new Nb source will probably be used in the improved version of the existing experiment.

In addition, the experiment was designed to be compatible with some existing Nb test masses from the SGG project. If the source mass is replaced by a Nb one, it will be convenient to replace the test masses as well. This way, the experiment will not need to be cooled to below 4.2 K.

7.2 Conclusions

We performed the ISL experiment using a Newtonian null source and a superconducting differential accelerometer as the detector. Our initial plan was to use a nominal source-test mass spacing of 150 μm and a source drive amplitude of 87.5 μm. The potential sensitivity of this experiment was $|\alpha| = 2 \times 10^{-3}$ at $\lambda = 150$ μm.

Due to the difficulties in freeing the source mass, we increased the source-test mass spacing to $180 \pm^{80}_{13}$ μm. Presence of dust particles in the gaps limited the

source amplitude to 16.1 μm. In addition, the experiment suffered from a large error due to a mistake in the design (inserting the soft link in the housings), and residual gas pressure due to a He leak. A spring that supports the detector was partially broken and this yielded a random error, which is difficult to identify. These problems compromised our sensitivity by five orders of magnitude.

During the course of this thesis work, I performed a comprehensive analysis of the errors, identified the problems with the apparatus, and showed ways to improve the design of the experiment. A second-generation experiment, also using a Newtonian null source and a superconducting differential accelerometer as the detector is being currently designed and tested in our lab. In this experiment, all the problems found in the first experiment will be addressed.

The center parts of the housings will be hard-mounted to the rim. This will stiffen the structure and make the patch field and pressure forces CM, reducing their effect by five orders of magnitude. In addition, the source mass will be decoupled from the rest of the assembly and it will be driven from the outside with highly shielded superconducting coils. This will significantly reduce the magnetic cross-talk. The source mass will be driven at resonance, therefore, at a single frequency, and this would also alleviate the effects of nonlinearity in the driving circuit. The design and construction of the new experiment is beyond the scope of this thesis.

With this new experiment, we expect to achieve the design sensitivity of $|\alpha| = 2 \times 10^{-3}$ at $\lambda = 150$ μm, which will improve the current limits by one order of magnitude at 150 μm and by over two orders of magnitude at shorter distances.

Appendix A

Inductance Calculations

The resistance of a superconducting wire is zero. This implies that there is no power loss and the persistent current flowing through it is constant [49]. In addition, due to the Meissner effect, the magnetic field will not penetrate the superconductor. These two properties of superconductors modify the magnetic field close to a superconducting coil and modulate its inductance.

There are multiple coil geometries used in this experiment. In this appendix, I will calculate the magnetic field B corresponding to different geometries as a function of the current I, and find their respective inductances:

$$L = \frac{E_m}{2I^2} = \frac{1}{2I^2}\int_{Univ} \frac{B^2}{2\mu_0} dV, \tag{A.1}$$

where E_m is the magnetic field energy.

A.1 Pancake coil

A.1.1 Close to one superconducting surface

By placing a superconducting pancake coil close and parallel to the surface of a superconductor, the magnetic field will be parallel to the superconductor and the coil-form, and almost negligible everywhere else. Using Ampere's law, the magnetic field magnitude is

$$B = \mu_0 n I, \tag{A.2}$$

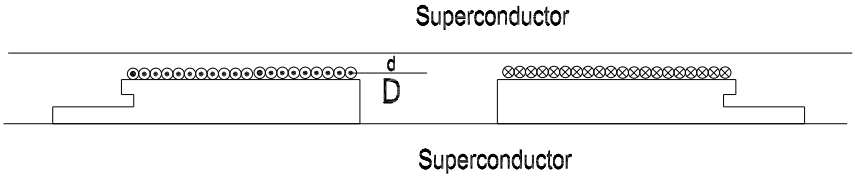

Figure A.1: Superconducting coil enclosed between two superconducting surfaces.

where μ_0 is the magnetic permeability of free space, $n = N/l$ is the coil turns density, the number of turns N per length l, and I is the current flowing through the wire of the coil. From Eq. (A.1), the inductance is

$$L = \mu_0 n^2 A d, \tag{A.3}$$

where A is the area on the pancake coil, and d is the distance of the coil to the superconducting surface.

A.1.2 Enclosed between two superconducting surfaces

In the experiment, the superconducting coils are usually enclosed inside the superconductor, so in addition to the superconducting plane in front of the coil, there will be a back superconducting plane. Keeping d as the distance between the pancake coil and the superconducting (front) surface, and adding another parallel superconducting surface on the other (back) side of it at a distance D (see Figure A.1), the magnetic field is enclosed on that side too, obtaining then two magnetic fields: B_1 over d and B_2 over D. Using the flux conservation, $B_1 d = B_2 D$. Using again Ampere's law, the magnetic field magnitude is given by

$$B_1 = \frac{D}{d+D}\ \mu_0 n I \tag{A.4}$$

and

$$B_2 = \frac{d}{d+D}\ \mu_0 n I. \tag{A.5}$$

The inductance is then

$$L = \mu_0 n^2 A \; d\frac{D}{d+D}. \tag{A.6}$$

If the front surface is displaced from its equilibrium position, $d = d_0 + x$, the inductance becomes

$$L(x) = \mu_0 n^2 A \; (d_0 + x)\frac{D}{d_0 + x + D}. \tag{A.7}$$

Expanding this in x to second order gives

$$L(x) = L_0 + \lambda x + \gamma x^2, \tag{A.8}$$

where

$$L_0 = \mu_0 n^2 A \; d_0\frac{D}{d_0 + D}, \tag{A.9}$$

$$\lambda = \mu_0 n^2 A \left(\frac{D}{d_0 + D}\right)^2, \tag{A.10}$$

and

$$\gamma = -\mu_0 n^2 A\frac{D^2}{(d_0 + D)^3}. \tag{A.11}$$

A.1.3 Inductance design

The design of the sensing, temperature, and alignment coils maximizes the number of turns that would fit on the coil-form using a single layer. A Nb wire with a 0.132-mm outer diameter was used for the sensing coils. Each sensing coil-form has three coils wound with approximately equal areas. The innermost coil has 90 turns and is used in one of the sensing circuits, the next has 50 turns and acts as a separation, and the final has 40 turn and is used in the other sensing circuit. The area of each winding is $A = 9.85 \pm 0.15\,\mathrm{cm}^2$, the turn density is given by

$$n = 1/d_w = 7.57 \times 10^3\,\mathrm{m}^{-1},$$

the initial distance to the test masses is

$$d_0 = d_w/2 + (160 \pm 33)\,\mu\mathrm{m} = (226 \pm 33)\,\mu\mathrm{m},$$

and the backplane spacing is $D = 4.6\,\mathrm{mm}$. The inductance, linear and quadratic coefficient of the sensing coils are calculated to be

$$L_0 = (14.8 \pm 2.1)\,\mu\mathrm{H}, \tag{A.12}$$

$$\lambda = (0.052 \pm 0.002)\,\mathrm{H/m}, \tag{A.13}$$

and

$$\gamma = (-29.7 \pm 1.7)\,\mathrm{H/m^2}. \tag{A.14}$$

Some pre-existing coils were used as temperature coils. They have a 0.152-mm diameter wire, with a winding area of $A = 25.6\,\mathrm{cm^2}$ and $N = 131$ turns. The turns density is $n = 1/d_w = 6.56 \times 10^3\,\mathrm{m^{-1}}$ and they are positioned touching the Nb housing, so $d_0 = d_w/2 + (13 \pm 13)\,\mu\mathrm{m} = (0.089 \pm 0.013)\,\mathrm{mm}$, while $D = 4.6\,\mathrm{mm}$. Their inductance and coefficients are then calculated:

$$L_T = (12.1 \pm 1.7)\,\mu\mathrm{H}, \tag{A.15}$$

$$\lambda_T = (0.124 \pm 0.002)\,\mathrm{H/m}, \tag{A.16}$$

and

$$\gamma_T = (-77.3 \pm 1.7)\,\mathrm{H/m^2}. \tag{A.17}$$

The alignment coils were wound with a Nb-clad Nb-Ti wire of 0.127-mm diameter. This wire is stronger than pure Nb wire, but the critical current is smaller. The area is $A = 4\,\mathrm{cm^2}$. The turns density is $n = 1/d_w = 7.87 \times 10^3\,\mathrm{m^{-1}}$ and they are positioned at 0.508 mm from the Nb cover, so $d_0 = d_w/2 + (0.55 \pm 0.05)\,\mathrm{mm} = (0.61 \pm 0.05)\,\mathrm{mm}$, while $D = 12\,\mathrm{mm}$. Their inductance and coefficients are then calculated:

$$L_{al} = (22.0 \pm 1.8)\,\mu\mathrm{H}, \tag{A.18}$$

$$\lambda_{al} = (0.029 \pm 0.001)\,\mathrm{H/m}, \tag{A.19}$$

and

$$\gamma_{al} = (-6.1 \pm 0.2)\,\mathrm{H/m^2}. \tag{A.20}$$

The source coils were wound using the new Nb wire of 0.133 mm. They are not single layer coils, but have effectively 2.75 layers of winding. This makes the turns

density $n = 2.75/d_w = 2.68 \times 10^4\,\mathrm{m}^{-1}$. Their area of winding is $A = 83.3\,\mathrm{cm}^2$, the distance from the center of the coil-winding to the source is in the range:

$$d_0 = 2.75\,d_{\mathrm{wire}}/2 + (1.29 \pm 0.07)\,\mathrm{mm} = (1.46 \pm 0.06)\,\mathrm{mm},$$

while $D = 9.65\,\mathrm{mm}$. This gives the predicted inductance, linear and quadratic coefficient of the source driving coils:

$$L_S = (13.2 \pm 0.5)\,\mathrm{mH}, \tag{A.21}$$

$$\lambda_S = (5.92 \pm 0.14)\,\mathrm{H/m}, \tag{A.22}$$

and

$$\gamma_S = (-1.06 \pm 0.05) \times 10^3\,\mathrm{H/m}^2. \tag{A.23}$$

A.2 Spool coil

The spool coil is probably of the most common geometry. It is used for single coils as well as for transformers. Figure 2.12 shows a spool coil next to the alignment coil.

In order to restrain the magnetic field in the spool and achieve high coupling, we use a field guide made out of a thin Nb foil. It wraps the coil-form but with a small spacing between the layers where the two ends overlap so the superconductor does not form a closed surface and the magnetic field can penetrate inside the spool. After winding the coil, the outer surface of the spool is wrapped with a second Nb foil, without a spacing so it does form a closed surface and does not let the magnetic field escape.

A.2.1 Single-layer coil

Let r be the inner and R the outer radius of the spool, d_w the diameter of the wire used, and l the length of the wound spool. Then, there will be two magnetic fields: B_1 inside r, and B_2 outside $r + d_w$ but inside R. Using the flux conservation, $B_1 r^2 = B_2[R^2 - (r + d_w)^2]$. Using again Ampere's law, the magnetic field magnitudes

are given by

$$B_1 = \mu_0 n I \frac{R^2 - (r + d_w)^2}{R^2 - 2 r d_w} \tag{A.24}$$

and

$$B_2 = \mu_0 n I \frac{r^2}{R^2 - 2 r d_w}. \tag{A.25}$$

The inductance,

$$L = \mu_0 n^2 \pi \; l \; \frac{r^2 [R^2 - (r + d_w)^2]}{R^2 - 2 r d_w} = \mu_0 n^2 l \; \frac{A_1 A_2}{A_1 + A_2 - A_w}, \tag{A.26}$$

is calculated from the magnetic field energy, where A_1 is the transversal area enclosed by the inner foil (B_1 is flowing through it), A_2 is the transversal area enclosed between the wire and the outer foil (B_2 is flowing through it), and A_w is the transversal area occupied by the wire at a fixed height in the spool.

A.2.2 Multi-layer coil

If there are N_l layers, the magnetic fields are modified to

$$B_1 = \mu_0 N_l n I \frac{R^2 - (r + N_l d_w)^2}{R^2 - 2 r N_l d_w} \tag{A.27}$$

and

$$B_2 = \mu_0 N_l n I \; \frac{r^2}{R^2 - 2 r N_l d_w}, \tag{A.28}$$

while the inductance becomes

$$L = \mu_0 N_l^2 n^2 \pi \; l \; \frac{r^2 [R^2 - (r + N_l d_w)^2]}{R^2 - 2 r N_l d_w} = \mu_0 N_l^2 n^2 l \; \frac{A_1 A_2}{A_1 + A_2 - N_l A_w}. \tag{A.29}$$

A.2.3 Transformer coil

For a transformer, there will be two windings with N_1 layers for the primary and N_2 for the secondary. In addition, there is the possibility that both windings do not have the same wire thickness. If d_{w1} is the thickness of the wire in the primary while d_{w2} in the secondary, this will give wire densities of $n_1 = 1/d_{w1}$ and $n_2 = 1/d_{w2}$ and transversal areas of wires A_{w1} and A_{w2}, respectively. From Eq. (A.29), the

inductances then are

$$L_i = \mu_0 N_i^2 n_i^2 \pi l \, \frac{r^2[R^2 - (r + N_1 d_{w1} + N_2 d_{w2})^2]}{R^2 - 2r(N_1 d_{w1} + N_2 d_{w2})}$$
$$= \mu_0 N_i^2 n_i^2 l \, \frac{A_1 A_2}{A_1 + A_2 - (N_1 A_{w1} + N_2 A_{w2})}, \tag{A.30}$$

where $i = 1, 2$.

A.2.4 Inductance design

Section 4.4.2 has a detailed analysis of the sensing circuit parameters which minimize the amplifier noise and optimize the coupling to the amplifier. According to Eqs. (4.77) and (4.78), the transformer optimum inductances will depend on the inductance in the circuit they couple to by

$$L_{t1,opt} = \frac{[L(-L\gamma + \lambda^2)]^{1/2}}{2(1 - \kappa_t^2)^{1/2}(-\gamma)^{1/2}} \tag{A.31}$$

and

$$L_{t2,opt} = \frac{L_s}{(1 - \kappa_t^2)^{1/2}}, \tag{A.32}$$

where κ_t is the coupling constant of the transformer, $L_s = 1.8\,\mu$H is the SQUID input inductance specified by the manufacturer, and L, λ, and γ correspond to the inductance and coefficients for the circuit. For the sensing circuits, according to Eq. (A.12), and assuming a coupling constant $\kappa_t = 0.97$ (consistent with my test windings), this leads to

$$L_{t1,opt} = (33.1 \pm 4.8)\,\mu\text{H} \tag{A.33}$$

and

$$L_{t2,opt} = (7.4 \pm 0.5)\,\mu\text{H}. \tag{A.34}$$

All the transformers are designed to fit inside the Nb housing and have inner radius of 5.0 mm, outer radius of 9.4 mm, length of 5.7 mm, and various wire thickness and number of layers.

Using the Nb wire with 0.132-mm diameter, 70 turns for the primary and 32 turns for the secondary, the actual inductances are calculated to be

$$L_{t1} = (35.5 \pm 0.5)\,\mu\text{H} \tag{A.35}$$

and

$$L_{t2} = (7.4 \pm 0.5)\,\mu\text{H}. \tag{A.36}$$

For the temperature coils, the optimization is not required, but nonetheless performed, obtaining the desired values as

$$L_{t1,opt} = (21.4 \pm 1.4)\,\mu\text{H} \tag{A.37}$$

and

$$L_{t2,opt} = (7.4 \pm 0.5)\,\mu\text{H}. \tag{A.38}$$

Choosing again the Nb wire, 58 turns for the primary and 32 turns for the secondary, the actual inductances are

$$L_{t1} = (25.1 \pm 0.5)\,\mu\text{H} \tag{A.39}$$

and

$$L_{t2} = (7.5 \pm 0.5)\,\mu\text{H}. \tag{A.40}$$

The supplementary shunt resistor has 2085 turns and was wound using a spool coil and a Nb-clad Nb-Ti wire of 0.103-mm diameter, the thinnest good wire available in the lab. The turns density is then $n = 1/d_w = 9.71 \times 10^3\,\text{m}^{-1}$, the inner radius is $r = 8.62\,\text{mm}$, the outer radius is $R = 1.22\,\text{cm}$, the wound length of spool is $l = 4.06\,\text{cm}$, and there are $N_l = 6$ layers. This gives a shunt inductance value of $L = 15.7\,\text{mH}$, significantly larger than those of the source driving coils.

Appendix B

The Source Mass Metrology Errors

A mass density distribution $\rho(\vec{x}')$ leads to a gravitational potential

$$\Phi(\vec{x}) = -G \int \frac{\rho(\vec{x}')}{|\vec{x} - \vec{x}'|} d^3x', \tag{B.1}$$

where $\vec{x} = (r, \phi, z)$ and $\vec{x}' = (r', \phi', z')$. Consider one source mass and two test masses. The potential is measured at $\vec{x}$, the position of a point of one of the test masses. The centers of the test masses are positioned symmetrically with respect to $z = 0$. Test mass 1 is centered at $z = d$, and test mass 2 at $z = -d$. On the other hand, $\vec{x}'$ is the position of one point of the source mass, whose density is responsible for the field. The source mass has a radius a and a thickness T. At an arbitrary instant, its center is located at $z = \delta z$, while its equilibrium position is $z = 0$ and is at a distance d from the center of each test mass. All masses are concentric. The potential can be rewritten explicitly as

$$\Phi(r, \phi, z) = -G \int_0^{2\pi} d\phi' \int_{\delta z - T/2}^{\delta z + T/2} dz' \int_0^a dr' \frac{\rho(r', \phi', z') r'}{\sqrt{r^2 + r'^2 - 2rr' \cos(\phi - \phi') + (z - z')^2}}. \tag{B.2}$$

If the density is constant and the source mass is a perfect cylinder of radius a and thickness T, the corresponding force will be explicitly calculable. This does not correspond to the real situation. The material has imperfections. There are several ways of including those imperfections and setting the maximum allowed deviations in the dimension so the deviation in the force is smaller than a certain value. In particular, I will consider two types of errors: (1) errors in the material, and (2) errors from the machining process. The first type of errors includes density errors

as well as bowing errors, while the second includes tolerance errors in the thickness and radius of the source mass, errors in the surface finish, represented as thickness variation errors, and radial taper errors.

I will start by discussing the ideal source situation, then compute the density fluctuation and the thickness variation errors as first-order corrections. Later, I will calculate the radial taper and bowing errors. In the constant density case, the potential $\Phi(\vec{x})$ and the force F_z will be numerically calculated. For the density fluctuation error, the density $\rho(\vec{x})$ will be expanded in a Fourier-Bessel series. This will modify the potential $\Phi(\vec{x})$. It will then be possible to find the error in the force for density fluctuations of a predetermined value. For simplicity, all calculations will be made first for the potential and then for the force components. The variable thickness error can be simulated as variable surface density; in this case, the extra mass due to thickness variations will be localized only at the surfaces of the source mass. This will closely approximate the real situation where the effect of the thickness variation modifies the mass distribution only near to the source mass.

B.1 Ideal source

The general Bessel expansion for the denominator of the potential can be written as

$$\frac{1}{|\vec{x}-\vec{x}'|} = \sum_{m=-\infty}^{+\infty} \int_0^\infty dk\ e^{im(\phi-\phi')} J_m(kr) J_m(kr') e^{-k(z_>-z_<)}, \tag{B.3}$$

where $z_>$ ($z_<$) is the larger (smaller) of z and z'. For test mass 1,

$$z_> = z, \quad z_< = z' \ \Rightarrow\ -k(z_>-z_<) = -k(z-z'), \tag{B.4}$$

while for test mass 2,

$$z_> = z', \quad z_< = z \ \Rightarrow\ -k(z_>-z_<) = k(z-z'). \tag{B.5}$$

If the density is constant, $\rho = \rho_0$, then all necessary expansions have already been performed. Substituting (B.3) into the potential (B.2) leads to

$$\Phi(r,\phi,z) = -G\rho_0 \int_0^{2\pi} d\phi' \int_{\delta z - T/2}^{\delta z + T/2} dz' \int_0^a dr' r' \sum_{m=-\infty}^{+\infty} \int_0^\infty dk e^{im(\phi-\phi')} \times J_m(kr) J_m(kr') e^{-k(z_>-z_<)}. \tag{B.6}$$

Note that the only dependence on ϕ and ϕ' comes from the $e^{im(\phi-\phi')}$ term. For $m \neq 0$,

$$\int_0^{2\pi} e^{im\phi'} d\phi' = \frac{e^{im\phi'}}{im}\bigg|_0^{2\pi} = 0.$$

I will therefore make the substitution

$$\sum_{m=-\infty}^{+\infty} e^{im(\phi-\phi')} J_m(kr) J_m(kr') \rightarrow J_0(kr) J_0(kr') \tag{B.7}$$

in all the future calculations. Then, (B.6) will look like

$$\Phi(r,\phi,z) = -2\pi G\rho_0 \int_{\delta z - T/2}^{\delta z + T/2} dz' \int_0^a dr' r' \int_0^\infty dk J_0(kr) J_0(kr') e^{-k(z_> - z_<)}. \tag{B.8}$$

Expressed in this form, (B.8) can be integrated with respect to r':

$$\Phi(r,\phi,z) = -2\pi G a \rho_0 \int_0^\infty dk \frac{J_0(kr) J_1(ka)}{k} \int_{\delta z - T/2}^{\delta z + T/2} dz' e^{-k(z_> - z_<)}, \tag{B.9}$$

where

$$\int_0^a dr\ r J_0(kr) = \frac{a}{k} J_1(ka) \tag{B.10}$$

has been used. In order to proceed with the z' integral, it is necessary to distinguish the test masses. For test mass 1,

$$\begin{aligned}
\Phi(r,\phi,z)\,|_{z>0} &= -2\pi G a \rho_0 \int_0^\infty dk \frac{J_0(kr) J_1(ka)}{k} \int_{\delta z - T/2}^{\delta z + T/2} dz' e^{-k(z - z')} \\
&= -4\pi G a \rho_0 \int_0^\infty dk \frac{J_0(kr) J_1(ka)}{k^2} e^{-k(z - \delta z)} \sinh(kT/2).
\end{aligned} \tag{B.11}$$

For test mass 2,

$$\begin{aligned}
\Phi(r,\phi,z)\,|_{z<0} &= -2\pi G a \rho_0 \int_0^\infty dk \frac{J_0(kr) J_1(ka)}{k} \int_{\delta z - T/2}^{\delta z + T/2} dz' e^{k(z - z')} \\
&= -4\pi G a \rho_0 \int_0^\infty dk \frac{J_0(kr) J_1(ka)}{k^2} e^{k(z - \delta z)} \sinh(kT/2).
\end{aligned} \tag{B.12}$$

Throughout this appendix, it is assumed that the test masses have constant density ρ_t. The z component of the force that each test mass would feel is computed by taking the derivative of (B.11) and (B.12) with respect to z, multiplying by ρ_t, and integrating over the test mass volume,

$$\begin{aligned}
F_z|_{z>0} &= -4\pi G \rho_0 \rho_t a \int_0^{2\pi} d\phi \int_{d_i}^{d_f} dz \int_0^b r dr \int_0^\infty dk \frac{J_0(kr) J_1(ka)}{k} e^{k(\delta z - z)} \sinh(kT/2) \\
&= -16\pi^2 G a b \rho_0 \rho_t \int_0^\infty dk \frac{J_1(ka) J_1(kb)}{k^3} e^{k(\delta z - d)} \sinh(kT/2) \sinh(kt/2)
\end{aligned} \tag{B.13}$$

and

$$F_z|_{z<0} = 4\pi G\rho_0\rho_t a\int_0^{2\pi}d\phi\int_{-d_f}^{-d_i}dz\int_0^b rdr\int_0^\infty dk\frac{J_0(kr)J_1(ka)}{k}e^{k(z-\delta z)}\sinh(kT/2)$$
$$= 16\pi^2 Gab\rho_0\rho_t\int_0^\infty dk\frac{J_1(ka)J_1(kb)}{k^3}e^{-k(\delta z+d)}\sinh(kT/2)\sinh(kt/2), \quad \text{(B.14)}$$

where b and t are the radius and thickness of each test mass.

From (B.13) and (B.14), the differential force $F_d = F_z|_{z>0} - F_z|_{z<0}$ is

$$F_d = -32\pi^2 Gab\rho_0\rho_t\int_0^\infty dk\frac{J_1(ka)J_1(kb)}{k^3}\cosh(k\delta z)e^{-kd}\sinh(kT/2)\sinh(kt/2). \quad \text{(B.15)}$$

Dividing this by the mass of each test mass $m_t = \pi b^2 t\rho_t$, the differential acceleration is

$$a_d = \frac{32\pi G a\rho_0}{bt}\int_0^\infty dk\frac{J_1(ka)J_1(kb)}{k^3}\cosh(k\delta z)e^{-kd}\sinh(kT/2)\sinh(kt/2). \quad \text{(B.16)}$$

The amplitude of the differential acceleration corresponding to the source displacement δz_{max} becomes

$$\Delta a_d = a_d(\delta z = \delta z_{max}) - a_d(\delta z = 0) \quad \text{(B.17)}$$
$$= \frac{32\pi G a\rho_0}{bt}\int_0^\infty dk\frac{J_1(ka)J_1(kb)}{k^3}\left[\cosh(k\delta z_{max})-1\right]e^{-kd}\sinh(kT/2)\sinh(kt/2).$$

This represents the Newtonian signal due to the finite diameter of the source mass. In the ideal case of an infinite source, this result would be zero.

On the other hand, the CM force $F_c = (1/2)(F_z|_{z>0} + F_z|_{z<0})$ is

$$F_c = -16\pi^2 Gab\rho_0\rho_t\int_0^\infty dk\frac{J_1(ka)J_1(kb)}{k^3}\sinh(k\delta z)e^{-kd}\sinh(kT/2)\sinh(kt/2). \quad \text{(B.18)}$$

Then the common acceleration is

$$a_c = \frac{16\pi G a\rho_0}{bt}\int_0^\infty dk\frac{J_1(ka)J_1(kb)}{k^3}\sinh(k\delta z)e^{-kd}\sinh(kT/2)\sinh(kt/2). \quad \text{(B.19)}$$

The amplitude of the common acceleration corresponding to the source displacement δz_{max} becomes

$$\Delta a_c = a_c(\delta z = \delta z_{max}) - a_c(\delta z = 0) \quad \text{(B.20)}$$
$$= \frac{16\pi G a\rho_0}{bt}\int_0^\infty dk\frac{J_1(ka)J_1(kb)}{k^3}\sinh(k\delta z_{max})e^{-kd}\sinh(kT/2)\sinh(kt/2).$$

This is an important value to be measured, since it needs to be rejected from the signal.

B.2 Density fluctuation

It is now necessary to find the right expansion for the density. The simplest case of nonconstant density is the one with radial dependence, in which $\rho = \rho(r')$, and this variation is taken over the whole source mass. Here the density is assumed to be independent of z' and ϕ'. Azimuthally dependent errors could be eliminated by repeating the experiment with the source mass rotated into various angular positions and averaging the result. Since the source mass also has a large diameter-to-thickness ratio, I ignore the effects of density variation along the z' axis.

The density

$$\rho(r') = \rho_0 + \Delta_\rho \rho(r'). \tag{B.21}$$

is expressed as a constant plus an error term. The error term $\Delta_\rho \rho$ can be expanded in Fourier-Bessel series

$$\Delta_\rho \rho(r') = \sum_{n=1}^{\infty} A_{0n} J_0 \left(\frac{x_{0n} r'}{a} \right), \tag{B.22}$$

where x_{0n} is the n-th root of the zeroth-order Bessel function J_0, in agreement with the boundary conditions: $\rho(a) = 0$, and the coefficients A_{0n} are given by

$$A_{0n} = \frac{2}{a^2 J_1^2(x_{0n})} \int_0^a dr' r' \Delta_\rho \rho(r') J_0 \left(\frac{x_{0n} r'}{a} \right). \tag{B.23}$$

Note that the zeroth-order Bessel function has been used for this expansion. Any order would give us an expansion, but the zeroth-order Bessel function is the only one that is nonzero at the origin (center of the disk). In addition, this leads to simplifications in the integration.

The total potential is expressed as $\Phi(r, \phi, z) = \Phi(r, \phi, z)|_{\rho=\text{const}} + \Delta_\rho \Phi(r, \phi, z)$. By substituting (B.22) and (B.3), and after making the simplification (B.7), the error

in the potential is

$$\begin{aligned}&\Delta_\rho\Phi(r,\phi,z) \qquad\qquad (B.24)\\ &= -2\pi G\sum_{n=1}^{\infty}A_{0n}\int_{\delta z-T/2}^{\delta z+T/2}dz'\int_0^a r'dr'J_0\left(\frac{x_{0n}r'}{a}\right)\int_0^\infty dkJ_0(kr)J_0(kr')e^{-k(z_>-z_<)}.\end{aligned}$$

In order to simplify (B.24), it is possible to use the orthonormality conditions of the Bessel functions

$$\int_0^a r'dr'J_0\left(\frac{x_{0n}r'}{a}\right)J_0(kr')=\frac{a^2x_{0n}}{x_{0n}^2-a^2k^2}J_0(ka)J_1(x_{0n}). \qquad (B.25)$$

With (B.25), (B.24) becomes

$$\begin{aligned}&\Delta_\rho\Phi(r,\phi,z) \qquad\qquad (B.26)\\ &= -2\pi Ga^2\sum_{n=1}^{\infty}A_{0n}x_{0n}J_1(x_{0n})\int_0^\infty dk\frac{J_0(kr)J_0(ka)}{x_{0n}^2-a^2k^2}\int_{\delta z-T/2}^{\delta z+T/2}dz'e^{-k(z_>-z_<)}.\end{aligned}$$

For test mass 1,

$$\begin{aligned}&\Delta_\rho\Phi(r,\phi,z)|_{z>0} \qquad\qquad (B.27)\\ &= -2\pi Ga^2\sum_{n=1}^{\infty}A_{0n}x_{0n}J_1(x_{0n})\int_0^\infty dk\frac{J_0(kr)J_0(ka)}{x_{0n}^2-a^2k^2}\int_{\delta z-T/2}^{\delta z+T/2}dz'e^{-k(z-z')}\\ &= -4\pi Ga^2\sum_{n=1}^{\infty}A_{0n}x_{0n}J_1(x_{0n})\int_0^\infty dk\frac{J_0(kr)J_0(ka)}{k(x_{0n}^2-a^2k^2)}e^{-k(z-\delta z)}\sinh(kT/2).\end{aligned}$$

For test mass 2,

$$\begin{aligned}&\Delta_\rho\Phi(r,\phi,z)|_{z<0} \qquad\qquad (B.28)\\ &= -2\pi Ga^2\sum_{n=1}^{\infty}A_{0n}x_{0n}J_1(x_{0n})\int_0^\infty dk\frac{J_0(kr)J_0(ka)}{x_{0n}^2-a^2k^2}\int_{\delta z-T/2}^{\delta z+T/2}dz'e^{k(z-z')}\\ &= -4\pi Ga^2\sum_{n=1}^{\infty}A_{0n}x_{0n}J_1(x_{0n})\int_0^\infty dk\frac{J_0(kr)J_0(ka)}{k(x_{0n}^2-a^2k^2)}e^{k(z-\delta z)}\sinh(kT/2).\end{aligned}$$

The z component of the force that each test mass would feel is found by taking the derivatives of (B.27) and (B.28) with respect to z, multiplying by ρ_t, and integrating

over the test mass volume:

$$\begin{aligned}\Delta_\rho F_z|_{z>0} &= -4\pi G a^2 \rho_t \int_0^{2\pi} d\phi \int_{d_i}^{d_f} dz \int_0^b r dr \sum_{n=1}^{\infty} A_{0n} x_{0n} J_1(x_{0n}) \\ &\quad \times \int_0^\infty dk \frac{J_0(kr) J_0(ka)}{x_{0n}^2 - a^2 k^2} \sinh(kT/2) e^{-k(z-\delta z)} \\ &= -16\pi^2 G a^2 \; b\rho_t \sum_{n=1}^{\infty} A_{0n} x_{0n} J_1(x_{0n}) \\ &\quad \times \int_0^\infty dk \frac{J_0(ka) J_1(kb)}{k^2(x_{0n}^2 - a^2 k^2)} e^{k(\delta z - d)} \sinh(kT/2) \sinh(kt/2) \quad \text{(B.29)}\end{aligned}$$

and

$$\begin{aligned}\Delta_\rho F_z|_{z<0} &= 4\pi G a^2 \rho_t \int_0^{2\pi} d\phi \int_{-d_f}^{-d_i} dz \int_0^b r dr \\ &\quad \times \sum_{n=1}^{\infty} A_{0n} x_{0n} J_1(x_{0n}) \int_0^\infty dk \frac{J_0(kr) J_0(ka)}{x_{0n}^2 - a^2 k^2} \sinh(kT/2) e^{k(z-\delta z)} \\ &= 16\pi^2 G a^2 b \rho_t \sum_{n=1}^{\infty} A_{0n} x_{0n} J_1(x_{0n}) \\ &\quad \times \int_0^\infty dk \frac{J_0(ka) J_1(kb)}{k^2(x_{0n}^2 - a^2 k^2)} e^{-k(\delta z + d)} \sinh(kT/2) \sinh(kt/2). \quad \text{(B.30)}\end{aligned}$$

From (B.29) and (B.30), it is possible to calculate the differential force

$$\begin{aligned}\Delta_\rho F_d &= \Delta_\rho F_z|_{z>0} - \Delta_\rho F_z|_{z<0} \quad \text{(B.31)} \\ &= -32\pi^2 \rho_t G a^2 b \sum_{n=1}^{\infty} A_{0n} x_{0n} J_1(x_{0n}) \int_0^\infty dk \frac{J_0(ka) J_1(kb)}{k^2(x_{0n}^2 - a^2 k^2)} e^{-kd} \\ &\quad \times \cosh(k\delta z) \sinh(kT/2) \sinh(kt/2). \quad \text{(B.32)}\end{aligned}$$

By dividing this by the mass of each test mass $m_t = \pi b^2 t \rho_t$, the differential acceleration is

$$\begin{aligned}\Delta_\rho a_d &= \frac{32\pi G a^2}{bt} \sum_{n=1}^{\infty} A_{0n} x_{0n} J_1(x_{0n}) \int_0^\infty dk \frac{J_0(ka) J_1(kb)}{k^2(x_{0n}^2 - a^2 k^2)} \\ &\quad \times \cosh(k\delta z) e^{-kd} \sinh(kT/2) \sinh(kt/2). \quad \text{(B.33)}\end{aligned}$$

The amplitude of the differential acceleration corresponding to the source displace-

ment δz_{max} becomes

$$\begin{aligned}\Delta_\rho \Delta a_d &= \Delta_\rho a_d(\delta z = \delta z_{max}) - \Delta_\rho a_d(\delta z = 0) \\ &= \frac{32\pi G a^2}{bt} \sum_{n=1}^{\infty} A_{0n} x_{0n} J_1(x_{0n}) \int_0^\infty dk \frac{J_0(ka)J_1(kb)}{k^2(x_{0n}^2 - a^2k^2)} \\ &\quad \times [\cosh(k\delta z) - 1] e^{-kd} \sinh(kT/2) \sinh(kt/2). \end{aligned} \tag{B.34}$$

On the other hand, the CM force $\Delta_\rho F_c = (1/2)(\Delta_\rho F_z|_{z>0} + \Delta_\rho F_z|_{z<0})$ is

$$\begin{aligned}\Delta_\rho F_c &= -16\pi^2 \rho_t \; G a^2 b \sum_{n=1}^{\infty} A_{0n} x_{0n} J_1(x_{0n}) \int_0^\infty dk \frac{J_0(ka)J_1(kb)}{k^2(x_{0n}^2 - a^2k^2)} e^{-kd} \\ &\quad \times \sinh(k\delta z) \sinh(kT/2) \sinh(kt/2), \end{aligned} \tag{B.35}$$

and the common acceleration is

$$\begin{aligned}\Delta_\rho a_c &= \frac{16\pi G a^2}{bt} \sum_{n=1}^{\infty} A_{0n} x_{0n} J_1(x_{0n}) \int_0^\infty dk \frac{J_0(ka)J_1(kb)}{k^2(x_{0n}^2 - a^2k^2)} \sinh(k\delta z) e^{-kd} \\ &\quad \times \sinh(kT/2) \sinh(kt/2). \end{aligned} \tag{B.36}$$

The amplitude of the common acceleration corresponding to the source displacement δz_{max} becomes

$$\begin{aligned}\Delta_\rho \Delta a_c &= \Delta_\rho a_c(\delta z = \delta z_{max}) - \Delta_\rho a_c(\delta z = 0) \\ &= \frac{16\pi G a^2}{bt} \sum_{n=1}^{\infty} A_{0n} x_{0n} J_1(x_{0n}) \\ &\quad \times \int_0^\infty dk \frac{J_0(ka)J_1(kb)}{k^2(x_{0n}^2 - a^2k^2)} \sinh(k\delta z_{max}) e^{-kd} \sinh(kT/2) \sinh(kt/2). \end{aligned} \tag{B.37}$$

B.3 Thickness variation

Directly expressing the thickness variation may lead to complications in the integration. Instead, the thickness variation can be modeled as surface density fluctuations of the source mass. The size of these fluctuations will be adjusted to match the mass errors due to the thickness variation. The surface fluctuations will have only radial dependence and will be independent of z' and ϕ' as before.

To accommodate the mass error due to the thickness variation, the density

$$\rho(r', z') = \rho_0 + \Delta_T \rho(r', z'). \tag{B.38}$$

is expressed as a constant plus an error term. For a source centered at $z = \delta z$,

$$\Delta_T \rho(r', z') = \rho_0[\Delta Z_+(r')\delta(z' - (\delta z + T/2)) + \Delta Z_-(r')\delta(z' - (\delta z - T/2))], \quad \text{(B.39)}$$

and the ΔZ's are just the sizes of the thickness fluctuations for each side of the source mass. Since the thickness depends on the position, it can be expanded in Fourier-Bessel series:

$$\Delta Z_\pm(r') = \sum_{n=1}^{\infty} B_{0n\pm} J_0\left(\frac{x_{0n} r'}{a}\right), \quad \text{(B.40)}$$

and the coefficients B_{0n} are given by

$$B_{0n\pm} = \frac{2}{a^2 J_1^2(x_{0n})} \int_0^a dr' r' \Delta Z_\pm(r') J_0\left(\frac{x_{0n} r'}{a}\right). \quad \text{(B.41)}$$

By substituting (B.40) in (B.39),

$$\begin{aligned} &\Delta_T \rho(r', z') \\ &= \rho_0 \sum_{n=1}^{\infty} [B_{0n+}\delta(z' - (\delta z + T/2)) + B_{0n-}\delta(z' - (\delta z - T/2))] J_0\left(\frac{x_{0n} r'}{a}\right) \end{aligned} \quad \text{(B.42)}$$

Again, expansion in the zeroth-order Bessel function has been taken for simplicity.

The potential is expressed as $\Phi(r, \phi, z) = \Phi(r, \phi, z)|_{\rho=\text{const}} + \Delta_T \Phi(r, \phi, z)$. By substituting (B.42) and (B.3), and after making the simplification (B.7),

$$\begin{aligned} \Delta_T \Phi(r, \phi, z) = -2\pi G \rho_0 \sum_{n=1}^{\infty} \int_{\delta z - T/2}^{\delta z + T/2} dz' \int_0^a r' dr' J_0\left(\frac{x_{0n} r'}{a}\right) \int_0^\infty dk J_0(kr) \\ \times J_0(kr') e^{-k(z_> - z_<)} \left[B_{0n+}\delta(z' - (\delta z + T/2)) + B_{0n-}\delta(z' - (\delta z - T/2))\right]. \end{aligned} \quad \text{(B.43)}$$

In order to simplify (B.43), it is possible to use the orthonormality condition of the Bessel functions (B.25). With this, (B.43) becomes

$$\begin{aligned} \Delta_T \Phi(r, \phi, z) = -2\pi \rho_0 G a^2 \sum_{n=1}^{\infty} x_{0n} J_1(x_{0n}) \int_0^\infty dk \frac{J_0(kr) J_0(ka)}{x_{0n}^2 - a^2 k^2} \int_{\delta z - T/2}^{\delta z + T/2} dz' \times \\ e^{-k(z_> - z_<)} \left[B_{0n+}\delta(z' - (\delta z + T/2)) + B_{0n-}\delta(z' - (\delta z - T/2))\right]. \end{aligned} \quad \text{(B.44)}$$

It is now necessary to distinguish the test masses. For test mass 1,

$$\begin{aligned}
&\Delta_T\Phi(r,\phi,z)|_{z>0} \\
&= -2\pi\rho_0 G a^2 \sum_{n=1}^{\infty} x_{0n} J_1(x_{0n}) \int_0^{\infty} dk \frac{J_0(kr)J_0(ka)}{x_{0n}^2 - a^2k^2} \\
&\quad \times \int_{\delta z - T/2}^{\delta z + T/2} dz' e^{-k(z-z')} [B_{0n+}\delta(z' - (\delta z + T/2)) + B_{0n-}\delta(z' - (\delta z - T/2))] \\
&= -2\pi\rho_0 G a^2 \sum_{n=1}^{\infty} x_{0n} J_1(x_{0n}) \int_0^{\infty} dk \frac{J_0(kr)J_0(ka)}{x_{0n}^2 - a^2k^2} e^{-k(z-\delta z)} \\
&\quad \times [B_{0n+}e^{(kT/2)} + B_{0n-}e^{(-kT/2)}]. \qquad \text{(B.45)}
\end{aligned}$$

For test mass 2,

$$\begin{aligned}
&\Delta_T\Phi(r,\phi,z)|_{z<0} \\
&= -2\pi\rho_0 G a^2 \sum_{n=1}^{\infty} x_{0n} J_1(x_{0n}) \int_0^{\infty} dk \frac{J_0(kr)J_0(ka)}{x_{0n}^2 - a^2k^2} \\
&\quad \times \int_{\delta z - T/2}^{\delta z + T/2} dz' e^{k(z-z')} [B_{0n+}\delta(z' - (\delta z + T/2)) + B_{0n-}\delta(z' - (\delta z - T/2))] \\
&= -2\pi\rho_0 G a^2 \sum_{n=1}^{\infty} x_{0n} J_1(x_{0n}) \int_0^{\infty} dk \frac{J_0(kr)J_0(ka)}{x_{0n}^2 - a^2k^2} e^{k(z-\delta z)} \\
&\quad \times [B_{0n+}e^{(-kT/2)} + B_{0n-}e^{(kT/2)}]. \qquad \text{(B.46)}
\end{aligned}$$

The z component of the force that each test mass would feel is found by taking the derivatives of the potential (B.45) and (B.46) with respect to z, multiplying by ρ_t, and integrating over the test mass volume,

$$\begin{aligned}
\Delta_T F(r,\phi,z)_z|_{z>0} &= -2\pi\rho_0 G a^2 \rho_t \int_0^{2\pi} d\phi \int_{d_i}^{d_f} dz \int_0^b r dr \sum_{n=1}^{\infty} x_{0n} J_1(x_{0n}) \\
&\quad \times \int_0^{\infty} dk \frac{k J_0(kr)J_0(ka)}{x_{0n}^2 - a^2k^2} e^{-k(z-\delta z)} [B_{0n+}e^{(kT/2)} + B_{0n-}e^{(-kT/2)}] \\
&= -8\pi^2\rho_0 G a^2 b \rho_t \sum_{n=1}^{\infty} x_{0n} J_1(x_{0n}) \int_0^{\infty} dk \frac{J_0(ka)\ J_1(kb)}{k(x_{0n}^2 - a^2k^2)} e^{k(\delta z - d)} \\
&\quad \times \sinh(kt/2) \left[B_{0n+}e^{(kT/2)} + B_{0n-}e^{(-kT/2)}\right] \qquad \text{(B.47)}
\end{aligned}$$

and

$$\begin{aligned}\Delta_T F(r,\phi,z)_z|_{z<0} &= 2\pi\rho_0 G a^2 \rho_t \int_0^{2\pi} d\phi \int_{-d_f}^{-d_i} dz \int_0^b r dr \sum_{n=1}^{\infty} x_{0n} J_1(x_{0n}) \\ &\quad \times \int_0^{\infty} dk \frac{k J_0(kr) J_0(ka)}{x_{0n}^2 - a^2 k^2} e^{k(z-\delta z)} [B_{0n+} e^{(-kT/2)} + B_{0n-} e^{(kT/2)}] \\ &= 8\pi^2 \rho_0 G a^2 \ b \ \rho_t \sum_{n=1}^{\infty} x_{0n} J_1(x_{0n}) \int_0^{\infty} dk \frac{J_0(ka) \ J_1(kb)}{k(x_{0n}^2 - a^2 k^2)} e^{-k(\delta z + d)} \\ &\quad \times \sinh(kt/2) \left[B_{0n+} e^{(-kT/2)} + B_{0n-} e^{(kT/2)} \right]. \end{aligned} \tag{B.48}$$

From (B.47) and (B.48), the differential force, $\Delta_T F_d = \Delta_T F_z|_{z>0} - \Delta_T F_z|_{z<0}$ is

$$\begin{aligned}\Delta_T F_d &= -16\pi^2 \rho_0 \rho_t G a^2 b \sum_{n=1}^{\infty} x_{0n} J_1(x_{0n}) \int_0^{\infty} dk \frac{J_0(ka) \ J_1(kb)}{k(x_{0n}^2 - a^2 k^2)} e^{-kd} \\ &\quad \times \sinh(kt/2) \left[B_{0n+} \cosh\left(k(\delta z + T/2)\right) + B_{0n-} \cosh\left(k(\delta z - T/2)\right) \right]. \end{aligned} \tag{B.49}$$

By dividing this by the mass of each test mass $m_t = \pi b^2 t \rho_t$, the differential acceleration is

$$\begin{aligned}\Delta_T a_d &= \frac{16\pi\rho_0 G a^2}{bt} \sum_{n=1}^{\infty} x_{0n} J_1(x_{0n}) \int_0^{\infty} dk \frac{J_0(ka) \ J_1(kb)}{k(x_{0n}^2 - a^2 k^2)} e^{-kd} \\ &\quad \times \sinh(kt/2) \left[B_{0n+} \cosh\left(k(\delta z + T/2)\right) + B_{0n-} \cosh\left(k(\delta z - T/2)\right) \right]. \end{aligned} \tag{B.50}$$

The amplitude of the differential acceleration corresponding to the source displacement δz_{max} becomes

$$\begin{aligned}\Delta_T \Delta a_d &= \Delta_T a_d(\delta z = \delta z_{max}) - \Delta_T a_d(\delta z = 0) \\ &= \frac{16\pi\rho_0 G a^2}{b \ t} \sum_{n=1}^{\infty} x_{0n} J_1(x_{0n}) \int_0^{\infty} dk \frac{J_0(ka) J_1(kb)}{k(x_{0n}^2 - a^2 k^2)} e^{-kd} \sinh(kt/2) \\ &\quad \times [B_{0n+} (\cosh\left(k(\delta z + T/2)\right) - \cosh\left(kT/2\right) \\ &\quad + B_{0n-} (\cosh\left(k(\delta z - T/2)\right) - \cosh\left(kT/2\right))]. \end{aligned} \tag{B.51}$$

On the other hand, the CM force $\Delta_\rho F_c = (1/2)(\Delta_\rho F_z|_{z>0} + \Delta_\rho F_z|_{z<0})$ is

$$\begin{aligned}\Delta_T F_c &= -8\pi^2 \rho_0 \rho_t G a^2 b \sum_{n=1}^{\infty} x_{0n} J_1(x_{0n}) \int_0^{\infty} dk \frac{J_0(ka) \ J_1(kb)}{k(x_{0n}^2 - a^2 k^2)} e^{-kd} \\ &\quad \times \sinh(kt/2) \left[B_{0n+} \sinh\left(k(\delta z + T/2)\right) + B_{0n-} \sinh\left(k(\delta z - T/2)\right) \right]. \end{aligned} \tag{B.52}$$

Then the common acceleration is

$$\begin{aligned}\Delta_T a_c &= \frac{8\pi\rho_0 G \ a^2}{b \ t} \sum_{n=1}^{\infty} x_{0n} J_1(x_{0n}) \int_0^{\infty} dk \frac{J_0(ka) \ J_1(kb)}{k(x_{0n}^2 - a^2 k^2)} e^{-kd} \\ &\quad \times \sinh(kt/2) \left[B_{0n+} \sinh\left(k(\delta z + T/2)\right) + B_{0n-} \sinh\left(k(\delta z - T/2)\right) \right]. \end{aligned} \tag{B.53}$$

Finally, the amplitude of the common acceleration corresponding to the source displacement δz_{max} becomes

$$\begin{aligned}\Delta_T \Delta a_c &= \Delta_T a_c(\delta z = \delta z_{max}) - \Delta_T a_c(\delta z = 0) \\ &= \frac{8\pi\rho_0 G a^2}{bt} \sum_{n=1}^{\infty} x_{0n} J_1(x_{0n}) \int_0^{\infty} dk \frac{J_0(ka) J_1(kb)}{k(x_{0n}^2 - a^2 k^2)}\ e^{-kd} \\ &\quad \times [B_{0n+}(\sinh(k(\delta z + T/2)) - \sinh(kT/2)) \\ &\quad + B_{0n-}(\sinh(k(\delta z - T/2)) + \sinh(kT/2))] \sinh(kt/2). \quad \text{(B.54)}\end{aligned}$$

B.4 Radial taper

When machining the source mass, a radial taper may occur. The radial taper will produce an error mainly at the source driving frequency f.

For simplicity, the taper is considered only on one surface of the test mass, the side located at $z_+ = \delta z + T/2$. The taper is assumed to have an angular size σ. This leaves an error for the potential (B.8):

$$\Phi(r, \phi, z) = -2\pi G \rho_0 \int_0^a r' dr' \int_{z_+}^{z_+ + \sigma r'} dz' \int_0^{\infty} dk J_0(kr) J_0(kr') e^{-k(z_> - z_<)}. \quad \text{(B.55)}$$

Unfortunately, now the integral over r' cannot be performed analytically. In order to proceed with the z' integral, it is necessary to distinguish the test masses. For test mass 1,

$$\begin{aligned}\Phi(r, \phi, z)|_{z>0} &= -2\pi G \rho_0 \int_0^a r' dr' \int_{z_+}^{z_+ + \sigma r'} dz' \int_0^{\infty} dk J_0(kr) J_0(kr') e^{-k(z - z')} \\ &= -2\pi G \rho_0 \int_0^{\infty} dk \frac{J_0(kr) \int_0^a dr' J_0(kr')(e^{k\sigma r'} - 1)}{k} e^{-k(z - z_+)}. \quad \text{(B.56)}\end{aligned}$$

For test mass 2,

$$\begin{aligned}\Phi(r, \phi, z)|_{z<0} &= -2\pi G \rho_0 \int_0^a r' dr' \int_{z_+}^{z_+ + \sigma r'} dz' \int_0^{\infty} dk J_0(kr) J_0(kr') e^{k(z - z')} \\ &= 2\pi G \rho_0 \int_0^{\infty} dk \frac{J_0(kr) \int_0^a r' dr' J_0(kr')(e^{-k\sigma r'} - 1)}{k} e^{k(z - z_+)}. \quad \text{(B.57)}\end{aligned}$$

The z component of the force that each test mass would feel is computed by taking the derivative of (B.56) and (B.57) with respect to z, multiplying by ρ_t, and

integrating over the test mass volume,

$$
\begin{aligned}
&F_z|_{z>0} \\
&= -2\pi G\rho_0\rho_t \int_0^{2\pi} d\phi \int_{d_i}^{d_f} dz \int_0^b r dr \int_0^\infty dk J_0(kr) \int_0^a r' dr' J_0(kr')(e^{k\sigma r'} - 1)e^{-k(z-z_+)} \\
&= -8\pi^2 G b \rho_0 \rho_t \sinh(kt/2) \qquad \text{(B.58)} \\
&\quad \times \left[\int_0^\infty dk \frac{J_1(kb) \int_0^a r' dr' J_0(kr') e^{k(z_+ + \sigma r')}\ e^{-kd}}{k^2} - \int_0^\infty dk \frac{a J_1(kb) J_1(ka) e^{k(z_+ - d)}}{k^3} \right]
\end{aligned}
$$

and

$$
\begin{aligned}
&F_z|_{z<0} \\
&= 2\pi G\rho_0\rho_t \int_0^{2\pi} d\phi \int_{-d_f}^{-d_i} dz \int_0^b r dr \int_0^\infty dk J_0(kr) \int_0^a r' dr' J_0(kr')(1 - e^{-k\sigma r'})e^{k(z-z_+)} \\
&= -8\pi^2 G b \rho_0 \rho_t \sinh(kt/2) \qquad \text{(B.59)} \\
&\quad \times \left[\int_0^\infty dk \frac{J_1(kb) \int_0^a r' dr' J_0(kr')\ e^{-k(z_+ + \sigma r')} e^{-kd}}{k^2} - \int_0^\infty dk \frac{a J_1(kb) J_1(ka) e^{-k(z_+ + d)}}{k^3} \right].
\end{aligned}
$$

From (B.58) and (B.59), the differential force $F_d = F_z|_{z>0} - F_z|_{z<0}$ is

$$
\begin{aligned}
F_d &= -16\pi^2 G b \rho_0 \rho_t e^{-kd} \sinh(kt/2) \\
&\quad \times \left[\int_0^\infty dk \frac{J_1(kb) \int_0^a r' dr' J_0(kr') \sinh(k(z_+ + \sigma r'))}{k^2} \right. \\
&\quad \left. - \int_0^\infty dk \frac{a J_1(kb) J_1(ka) \sinh(kz_+)}{k^3} \right]. \qquad \text{(B.60)}
\end{aligned}
$$

Dividing this by the mass of each test mass $m_t = \pi b^2 t \rho_t$, the differential acceleration is

$$
\begin{aligned}
a_d &= \frac{16\pi G\rho_0}{bt} e^{-kd} \sinh(kt/2) \left[\int_0^\infty dk \frac{J_1(kb) \int_0^a r' dr' J_0(kr') \sinh(k(z_+ + \sigma r'))}{k^2} \right. \\
&\quad \left. - \int_0^\infty dk \frac{a J_1(kb) J_1(ka) \sinh(kz_+)}{k^3} \right]. \qquad \text{(B.61)}
\end{aligned}
$$

The amplitude of the differential acceleration corresponding to the source displacement δz_{max} becomes

$$
\begin{aligned}
&\Delta a_d = a_d(\delta z = \delta z_{max}) - a_d(\delta z = 0) = \frac{16\pi G\rho_0}{bt} \int_0^\infty dk\ \frac{J_1(kb)}{k^2} \times \\
&\left\{ \int_0^a dr'\ r' J_0(kr') [\sinh(k(\delta z_{max} + T/2 + \sigma r')) - \sinh(k(T/2 + \sigma r'))] \ - \right. \\
&\left. (a/k) J_1(ka) [\sinh(k(\delta z_{max} + T/2)) - \sinh(kT/2)] \right\} e^{-kd} \sinh(kt/2). \qquad \text{(B.62)}
\end{aligned}
$$

On the other hand, the CM force $F_c = (1/2)(F_z|_{z>0} + F_z|_{z<0})$ is

$$\begin{aligned} F_c &= -8\pi^2 G b \rho_0 \rho_t e^{-kd} \sinh(kt/2) \\ &\left[\int_0^\infty dk \frac{J_1(kb) \int_0^a r' dr' J_0(kr') \cosh(k(z_+ + \sigma r'))}{k^2} \right. \\ &\left. - \int_0^\infty dk \frac{a J_1(kb) J_1(ka) \cosh(kz_+)}{k^3} \right]. \end{aligned} \tag{B.63}$$

Then the common acceleration is

$$\begin{aligned} a_c &= \frac{8\pi G \rho_0}{bt} e^{-kd} \sinh(kt/2) \\ &\left[\int_0^\infty dk \frac{J_1(kb) \int_0^a r' dr' J_0(kr') \cosh(k(z_+ + \sigma r'))}{k^2} \right. \\ &\left. - \int_0^\infty dk \frac{a J_1(kb) J_1(ka) \cosh(kz_+)}{k^3} \right]. \end{aligned} \tag{B.64}$$

The amplitude of the common acceleration corresponding to the source displacement δz_{max} becomes

$$\Delta a_c = a_c(\delta z = \delta z_{max}) - a_c(\delta z = 0) = \frac{8\pi G \rho_0}{bt} \int_0^\infty dk \ \frac{J_1(kb)}{k^2} \times$$
$$\left\{ \int_0^a dr' \ r' J_0(kr') [\cosh(k(\delta z_{max} + T/2 + \sigma r')) - \cosh(k(T/2 + \sigma r'))] \ - \right.$$
$$\left. (a/k) J_1(ka) [\cosh(k(\delta z_{max} + T/2)) - \cosh(kT/2)] \right\} e^{-kd} \sinh(kt/2). \tag{B.65}$$

B.5 Bowing

The source mass may bow due to residual stress in the material. It will also bow sinusoidally as it is driven. The static bowing will produce an error mainly at the source driving frequency f.

B.5.1 Static bowing

The static bowing is assumed to have a size ξ. For simplicity, the following abbreviations will be used $z_+ = \delta z + T/2$, $z_- = \delta z - T/2$, $z_{+\xi} = z_+ + \xi(r'^2 - a^2)$,

$z_{-\xi} = z_- + \xi(r'^2 - a^2)$. This leaves an error for the potential (B.8)

$$\begin{aligned}\Phi(r,\phi,z) &= -2\pi G\rho_0 \int_0^a r'dr' \left[\int_{z_+}^{z_{+\xi}} dz' \int_0^\infty dk J_0(kr)J_0(kr')e^{-k(z_>-z_<)} \right. \\ &\left. - \int_{z_{-\xi}}^{z_-} dz' \int_0^\infty dk J_0(kr)J_0(kr')e^{-k(z_>-z_<)}\right]. \end{aligned} \tag{B.66}$$

The integral over r' cannot be performed analytically. In order to proceed with the z' integral, it is necessary to distinguish the test masses. For test mass 1,

$$\begin{aligned}\Phi(r,\phi,z)|_{z>0} &= -2\pi G\rho_0 \int_0^a r'dr' \left[\int_{z_+}^{z_{+\xi}} dz' \int_0^\infty dk J_0(kr)J_0(kr')e^{-k(z-z')} \right. \\ &\left. - \int_{z_-}^{z_{-\xi}} dz' \int_0^\infty dk J_0(kr)J_0(kr')e^{-k(z-z')}\right] \\ &= -2\pi G\rho_0 e^{-kz}(e^{kz_+} - e^{kz_-}) \\ &\times \int_0^\infty dk \frac{J_0(kr)\int_0^a r'dr' J_0(kr')(e^{k\xi(r'^2-a^2)}-1)}{k}. \end{aligned} \tag{B.67}$$

For test mass 2,

$$\begin{aligned}\Phi(r,\phi,z)|_{z<0} &= -2\pi G\rho_0 \int_0^a r'dr' \left[\int_{z_+}^{z_{+\xi}} dz' \int_0^\infty dk J_0(kr)J_0(kr')e^{k(z-z')} \right. \\ &\left. - \int_{z^-}^{z_{-\xi}} dz' \int_0^\infty dk J_0(kr)J_0(kr')e^{k(z-z')}\right] \\ &= 2\pi G\rho_0 e^{kz}(e^{-kz_+} - e^{-kz_-}) \\ &\times \int_0^\infty dk \frac{J_0(kr)\int_0^a r'd' J_0(kr')(e^{-k\xi(r'^2-a^2)}-1)}{k}. \end{aligned} \tag{B.68}$$

The z component of the force that that each test mass would feel is computed by taking the derivative of (B.67) and (B.68) with respect to z, multiplying by ρ_t, and integrating over the test mass volume,

$$\begin{aligned}F_z|_{z>0} &= -2\pi G\rho_0\rho_t \int_0^{2\pi} d\phi \int_{d_i}^{d_f} dz \int_0^b rdr \int_0^\infty dk J_0(kr) \int_0^a r'dr' J_0(kr') \\ &\times (e^{k\xi(r'^2-a^2)}-1)e^{-kz}(e^{kz_+} - e^{kz_-}) \\ &= -8\pi^2 Gb\rho_0\rho_t \left[\int_0^\infty dk \frac{J_1(kb)\int_0^a r'dr' J_0(kr')e^{k\xi(r'^2-a^2)}}{k^2} e^{-kd} \right. \\ &\left. - \int_0^\infty dk \frac{aJ_1(kb)J_1(ka)}{k^2} e^{-kd}\right](e^{kz_+} - e^{kz_-})\sinh(kt/2) \end{aligned} \tag{B.69}$$

and

$$
\begin{aligned}
F_z|_{z<0} &= 2\pi G\rho_0\rho_t \int_0^{2\pi} d\phi \int_{-d_f}^{-d_i} dz \int_0^b rdr \int_0^\infty dk J_0(kr) \int_0^a r'dr' J_0(kr') \\
&\quad \times (1 - e^{-k\xi(r'^2-a^2)}) e^{kz} (e^{-kz_+} - e^{-kz_-}) \\
&= -8\pi^2 Gb\rho_0\rho_t \left[\int_0^\infty dk \frac{J_1(kb) \int_0^a r'dr' J_0(kr') e^{-k\xi(r'^2-a^2)}}{k^2} e^{-kd} \right. \\
&\quad \left. - \int_0^\infty dk \frac{aJ_1(kb)J_1(ka)}{k^2} e^{-kd} \right] (e^{-kz_+} - e^{-kz_-}) \sinh(kt/2). \qquad \text{(B.70)}
\end{aligned}
$$

From (B.69) and (B.70), the differential force $F_d = F_z|_{z>0} - F_z|_{z<0}$ is

$$
\begin{aligned}
F_d = 16\pi^2 Gb\rho_0\rho_t \int_0^\infty dk \frac{J_1(kb)}{k^2} \Big\{ (a/k) J_1(ka) \left[\sinh(kz_+) - \sinh(kz_-) \right] - \\
\int_0^a dr' \; r' J_0(kr') \left[\sinh(k(z_+ + \xi(r'^2 - a^2))) - \sinh(k(z_- + \xi(r'^2 - a^2))) \right] \Big\} \times \\
e^{-kd} \sinh(kt/2). \qquad \text{(B.71)}
\end{aligned}
$$

Dividing this by the mass of each test mass $m_t = \pi b^2 t \rho_t$, the differential acceleration is

$$
\begin{aligned}
a_d = \frac{16\pi G\rho_0}{bt} \int_0^\infty dk \frac{J_1(kb)}{k^2} \Big\{ (a/k) J_1(ka) \left[\sinh(kz_+) - \sinh(kz_-) \right] - \\
\int_0^a dr' \; r' J_0(kr') \left[\sinh(k(z_+ + \xi(r'^2 - a^2))) - \sinh(k(z_- + \xi(r'^2 - a^2))) \right] \Big\} \times \\
e^{-kd} \sinh(kt/2). \qquad \text{(B.72)}
\end{aligned}
$$

The amplitude of the differential acceleration corresponding to the source displacement δz_{max} becomes

$$
\begin{aligned}
\Delta a_d = a_d(\delta z = \delta z_{max}) - a_d(\delta z = 0) = \frac{16\pi G\rho_0}{bt} \int_0^\infty dk \frac{J_1(kb)}{k^2} \times \\
\Big\{ (a/k) J_1(ka) \left[\sinh(k(\delta z_{max} + T/2)) - \sinh(kT/2) \right] - \int_0^a dr' \; r' J_0(kr') \times \\
\left[\sinh(k(\delta z_{max} + T/2 + \xi(r'^2 - a^2))) - \sinh(k(T/2 + \xi(r'^2 - a^2))) \right] \Big\} \times \\
e^{-kd} \sinh(kt/2). \qquad \text{(B.73)}
\end{aligned}
$$

On the other hand, the CM force $F_c = (1/2)(F_z|_{z>0} + F_z|_{z<0})$ is

$$F_c = -8\pi^2 G b \rho_0 \rho_t \int_0^\infty dk \frac{J_1(kb)}{k^2} \Big\{ (a/k) J_1(ka) \left[\cosh(kz_+) - \cosh(kz_-)\right] - \int_0^a dr'\ r' J_0(kr') \left[\cosh\left(k(z_+ + \xi(r'^2 - a^2))\right) - \cosh\left(k(z_- + \xi(r'^2 - a^2))\right)\right] \Big\} \times e^{-kd} \sinh(kt/2). \quad \text{(B.74)}$$

Then the common acceleration is

$$a_c = \frac{8\pi G \rho_0}{bt} \int_0^\infty dk \frac{J_1(kb)}{k^2} \Big\{ (a/k) J_1(ka) \left[\cosh(kz_+) - \cosh(kz_-)\right] - \int_0^a dr'\ r' J_0(kr') \left[\cosh\left(k(z_+ + \xi(r'^2 - a^2))\right) - \cosh\left(k(z_- + \xi(r'^2 - a^2))\right)\right] \Big\} \times e^{-kd} \sinh(kt/2). \quad \text{(B.75)}$$

The amplitude of the common acceleration corresponding to the source displacement δz_{max} becomes

$$\Delta a_c = a_c(\delta z = \delta z_{max}) - a_c(\delta z = 0) = \frac{8\pi G \rho_0}{bt} \int_0^\infty dk \frac{J_1(kb)}{k^2} \times \Big\{ (a/k) J_1(ka) \left[\cosh(k(\delta z_{max} + T/2)) - \cosh(kT/2)\right] - \int_0^a dr'\ r' J_0(kr') \times \left[\cosh\left(k(\delta z_{max} + T/2 + \xi(r'^2 - a^2))\right) - \cosh\left(k(T/2 + \xi(r'^2 - a^2))\right)\right] \Big\} \times e^{-kd} \sinh(kt/2). \quad \text{(B.76)}$$

B.5.2 Dynamic bowing

The dynamic bowing is assumed to have a size $\varepsilon \delta z$. For simplicity, the following abbreviations will be used $z_+ = \delta z + T/2$, $z_- = \delta z - T/2$, $z_{+\varepsilon} = z_+ + \varepsilon \delta z (r'^2 - a^2)$, $z_{-\varepsilon} = z_- + \varepsilon \delta z (r'^2 - a^2)$. This leaves an error for the potential (B.8)

$$\Phi(r, \phi, z) = -2\pi G \rho_0 \int_0^a dr'\ r' \Big[\int_{z_+}^{z_{+\varepsilon\delta z}} dz' \int_0^\infty dk J_0(kr) J_0(kr') e^{-k(z_> - z_<)} - \int_{z_{-\varepsilon\delta z}}^{z_-} dz' \int_0^\infty dk J_0(kr) J_0(kr') e^{-k(z_> - z_<)} \Big]. \quad \text{(B.77)}$$

The integral over r' cannot be performed analytically. In order to proceed with the z' integral, it is necessary to distinguish the test masses. For test mass 1,

$$\Phi(r,\phi,z)|_{z>0} = -2\pi G\rho_0 \int_0^a dr' r' \Bigg[\int_{z_+}^{z_{+\varepsilon\delta z}} dz' \int_0^\infty dk J_0(kr) J_0(kr') e^{-k(z-z')} - \int_{z_-}^{z_{-\varepsilon\delta z}} dz' \int_0^\infty dk J_0(kr) J_0(kr') e^{-k(z-z')} \Bigg]$$
$$= -2\pi G\rho_0 \int_0^\infty dk \frac{J_0(kr) \int_0^a dr'\ r' J_0(kr') (e^{k\varepsilon\delta z(r'^2-a^2)} - 1)}{k} \times e^{-kz}(e^{kz_+} - e^{kz_-}). \quad \text{(B.78)}$$

For test mass 2,

$$\Phi(r,\phi,z)|_{z<0} = -2\pi G\rho_0 \int_0^a dr' r' \Bigg[\int_{z_+}^{z_{+\varepsilon\delta z}} dz' \int_0^\infty dk J_0(kr) J_0(kr') e^{k(z-z')} - \int_{z^-}^{z_{-\varepsilon\delta z}} dz' \int_0^\infty dk J_0(kr) J_0(kr') e^{k(z-z')} \Bigg]$$
$$= 2\pi G\rho_0 \int_0^\infty dk \frac{J_0(kr) \int_0^a dr'\ r' J_0(kr') (e^{-k\varepsilon\delta z(r'^2-a^2)} - 1)}{k} \times e^{kz}(e^{-kz_+} - e^{-kz_-}). \quad \text{(B.79)}$$

The z component of the force that each test mass would feel is computed by taking the derivative of (B.78) and (B.79) with respect to z, multiplying by ρ_t, and integrating over the test mass volume,

$$F_z|_{z>0} = -2\pi G\rho_0\rho_t \int_0^{2\pi} d\phi \int_{d_i}^{d_f} dz \int_0^b dr\ r \int_0^\infty dk J_0(kr) \int_0^a dr'\ r' J_0(kr') \times (e^{k\varepsilon\delta z(r'^2-a^2)} - 1) e^{-kz}(e^{kz_+} - e^{kz_-})$$
$$= -8\pi^2 G b\rho_0\rho_t \Bigg[\int_0^\infty dk\ \frac{J_1(kb) \int_0^a dr'\ r' J_0(kr')\ e^{k\varepsilon\delta z(r'^2-a^2)}}{k^2}\ e^{-kd} - \int_0^\infty dk \frac{a J_1(kb) J_1(ka)}{k^2}\ e^{-kd} \Bigg] (e^{kz_+} - e^{kz_-}) \sinh(kt/2) \quad \text{(B.80)}$$

and

$$F_z|_{z<0} = 2\pi G\rho_0\rho_t \int_0^{2\pi} d\phi \int_{-d_f}^{-d_i} dz \int_0^b dr\ r \int_0^\infty dk J_0(kr) \int_0^a dr'\ r' J_0(kr') \times (1 - e^{-k\varepsilon\delta z(r'^2-a^2)}) e^{kz}(e^{-kz_+} - e^{-kz_-})$$
$$= -8\pi^2 G b\rho_0\rho_t \Bigg[\int_0^\infty dk\ \frac{J_1(kb) \int_0^a dr'\ r' J_0(kr') e^{-k\varepsilon\delta z(r'^2-a^2)}}{k^2}\ e^{-kd} - \int_0^\infty dk \frac{a J_1(kb) J_1(ka)}{k^2}\ e^{-kd} \Bigg] (e^{-kz_+} - e^{-kz_-}) \sinh(kt/2). \quad \text{(B.81)}$$

From (B.80) and (B.81), the differential force $F_d = F_z|_{z>0} - F_z|_{z<0}$ is

$$F_d = 16\pi^2 Gb\rho_0\rho_t \int_0^\infty dk \frac{J_1(kb)}{k^2} \Big\{ (a/k)J_1(ka)\left[\sinh(kz_+) - \sinh(kz_-)\right] - \int_0^a dr' r' J_0(kr')[\sinh(k(z_+ + \varepsilon\delta z(r'^2 - a^2))) - \sinh(k(z_- + \varepsilon\delta z(r'^2 - a^2)))] \Big\} \times e^{-kd}\sinh(kt/2). \quad \text{(B.82)}$$

Dividing this by the mass of each test mass $m_t = \pi b^2 t\rho_t$, the differential acceleration is

$$a_d = \frac{16\pi G\rho_0}{bt} \int_0^\infty dk \frac{J_1(kb)}{k^2} \Big\{ (a/k)J_1(ka)\left[\sinh(kz_+) - \sinh(kz_-)\right] - \int_0^a dr' r' J_0(kr')[\sinh(k(z_+ + \varepsilon\delta z(r'^2 - a^2))) - \sinh(k(z_- + \varepsilon\delta z(r'^2 - a^2)))] \Big\} \times e^{-kd}\sinh(kt/2). \quad \text{(B.83)}$$

The amplitude of the differential acceleration corresponding to the source displacement δz_{max} becomes

$$\Delta a_d = a_d(\delta z = \delta z_{max}) - a_d(\delta z = 0) = \frac{16\pi G\rho_0}{bt} \int_0^\infty dk \frac{J_1(kb)}{k^2} \times \Big\{ (a/k)J_1(ka)\left[\sinh(k(\delta z_{max} + T/2)) - \sinh(kT/2)\right] - \int_0^a dr'\ r' J_0(kr') \times \left[\sinh(k(\delta z_{max} + T/2 + \varepsilon\delta z(r'^2 - a^2))) - \sinh(k(T/2 + \varepsilon\delta z(r'^2 - a^2)))\right] \Big\} \times e^{-kd}\sinh(kt/2). \quad \text{(B.84)}$$

On the other hand, the CM force $F_c = (1/2)(F_z|_{z>0} + F_z|_{z<0})$ is

$$F_c = -8\pi^2 Gb\rho_0\rho_t \int_0^\infty dk \frac{J_1(kb)}{k^2} \Big\{ (a/k)J_1(ka)\left[\cosh(kz_+) - \cosh(kz_-)\right] - \int_0^a dr' r' J_0(kr') \left[\cosh(k(z_+ + \varepsilon\delta z(r'^2 - a^2))) - \cosh(k(z_- + \varepsilon\delta z(r'^2 - a^2)))\right] \Big\} \times e^{-kd}\sinh(kt/2). \quad \text{(B.85)}$$

Then the common acceleration is

$$a_c = \frac{8\pi G\rho_0}{bt} \int_0^\infty dk \frac{J_1(kb)}{k^2} \Big\{ (a/k)J_1(ka)\left[\cosh(kz_+) - \cosh(kz_-)\right] - \int_0^a dr' r' J_0(kr')[\cosh(k(z_+ + \varepsilon\delta z(r'^2 - a^2))) - \cosh(k(z_- + \varepsilon\delta z(r'^2 - a^2)))] \Big\} \times e^{-kd}\sinh(kt/2). \quad \text{(B.86)}$$

The amplitude of the common acceleration corresponding to the source displacement δz_{max} becomes

$$\Delta a_c = a_c(\delta z = \delta z_{max}) - a_c(\delta z = 0) = \frac{8\pi G\rho_0}{bt}\int_0^\infty dk \frac{J_1(kb)}{k^2} \times$$
$$\Big\{(a/k)J_1(ka)\left[\cosh\left(k(\delta z_{max} + T/2)\right) - \cosh\left(kT/2\right)\right] - \int_0^a dr'\ r' J_0(kr') \times$$
$$\left[\cosh\left(k(\delta z_{max} + T/2 + \varepsilon\delta z(r'^2 - a^2))\right) - \cosh\left(k(T/2 + \varepsilon\delta z(r'^2 - a^2))\right)\right]\Big\} \times$$
$$e^{-kd}\sinh\left(kt/2\right). \quad \text{(B.87)}$$

Appendix C

Cool-down History

C.1 Pre-cool-down measurements

Room-temperature measurements in air indicated that the source mass has a resonance frequency of 10.375 Hz and a lateral rocking frequency of 16.625 Hz. The resonance frequencies of four test masses were measured to be 10.125, 10.187, 10.187, and 10.562 Hz, respectively. The transverse mode of the good housing was measured to be at 35.5 Hz and there were two identifiable rocking modes at 49.0 and 51.5 Hz, respectively. The resonance frequencies of the damaged housing were measured only before heat-treatment (as opposed to all the other measurements). For it, the following modes were seen: 32.9, 45.7, 47.3 Hz. These peaks were more difficult to observe and had significantly lower quality factors.

C.2 Cool-down I

The first cool-down was performed during the months of May and June of 2005. The resonance frequencies before the cool-down were measured in vacuum at 14.36 and 14.72 Hz for the test masses. No obvious resonance frequency was found for the source. No obvious, drivable resonance frequencies were found at cryogenic temperature for either the test masses or the source. Two circuits were disconnected: the source circuit and the circuit capable of fine-tuning the current in the DM circuit. From the inductance measurement of the remaining circuits, two additional

conclusions were made:

- The inductance measurement of the alignment coils revealed that the center blocks of the housings were farther away from the source than designed. Their displacements were 0.203 mm to 0.305 mm from their original position, which corresponds to an average displacement of 0.254 mm plus a rotation of about 1 mrad from the vertical.

- The test masses were made out of Ta, while the shields were made out of Nb. Since the critical temperature of Ta (4.3 K) is lower than that of Nb (9.26 K), it was possible to measure the spacing between the sensing coils and the test masses as well as the shields by raising the temperature of the apparatus to above 4.3 K. By performing these measurements, it was determined that the test masses were touching the shields.

After warming up the experiment, it was found additionally that one of the source coil-forms was cracked. A close examination of the housing confirmed that their center blocks were distorted. One of the housings (initially damaged by the machine shop) had very large distortions. A few repairs and small changes needed to be made. The most relevant were:

- Heat-treat the housings.

- Increase the initial spacing between the test masses and the shields to guarantee they will not touch each other. In order to maintain the nominal spacing between the source and the test masses, this implies

  - Machining additional spacers for the test masses as well as for the source mass, and

  - Modifying the circuit parameters, so that the test masses are pushed farther apart with the optimal currents.

- Wind a new source coil.

- Calculate maximum bowing of the source mass due to the differential contraction between Nb and Ta.
- Simplify the DM circuit by making it the same as the CM one in order to be able to exchange them.

If the source mass was initially responsible for the deformation of the center blocks of the housing, it would have needed to move by at least 0.203 mm. Using finite element analysis, it was estimated that the total displacement of the source due to the differential contraction between the Ta and Nb would be no more than 0.127 mm [9].

C.3 Cool-down II

In August 2005, while waiting for the machining of new spacers, a second cool-down was performed. The test masses were removed, keeping only the sensing coils and shields. The aim of this cool-down was to measure the resonance frequency of the shields and the source using two circuits, each one with a SQUID. It was found that:

- The resonance frequencies of the shields were identified as 625 and 1275 Hz, with quality factors of 1.9×10^5 and 1.5×10^5, respectively at 1.3×10^{-4} torr and were tunable with current.
- The source circuit did not function, so no source measurements were possible. After warming up the experiment, it was found that the wire of the source coil was broken.

A few repairs were made:

- The housings were heat-treated to recover flatness.
- New sensing coils were wound.
- New source coils were wound. The source coils had initially been wound using 5 layers of Nb-Ti wire of 0.076-mm diameter, to a total of 1225 turns. The

large amount of epoxy could have been causing the problem of the coil coming off the coil-form, or the wire breaking. We decided to modify them by using a thicker wire, this time made from Nb, fewer layers (2.7 on average), and 425 turns.

- New circuits were built such that CM and DM measurement could be made with either circuit.

C.4 Cool-down III

While assembling for a third cool-down, a new detail was found by making capacitance measurements during the assembly process. In the initial design, the shields held the test masses and spacers in place with vacuum grease, but with this attachment, the test masses displaced when the shields were tightened. An alternative method of attachment was used in which we glued the test masses to the housing using GE-varnish. In addition, the spacers were glued to the test masses. Tightening the shield after this had no effect on the test mass position.

The third cool-down was run during November-December 2005. The room-temperature vacuum measurements identified the test mass modes at 11.5 and 12.6 Hz and the source mode at 10.03 Hz. The source mode was very difficult to drive. After cooling down, it was found that:

- All circuits were continuous, except for one of the alignment coils.
- The refrigerator worked for extended periods of time at 2.37 K and was operational at 1.55 K.
- The resonance frequencies of the test masses were measured to be 12.23 and 14.96 Hz with quality factors of 2.2×10^3 and 3.8×10^4, respectively, at 6.1×10^{-6} torr.
- No source mode was found.
- Using inductance measurements, it was found that:

  - On housing 1, the alignment coil spacing was half of the expected value (reduced from 0.508 mm to 0.254 mm);
  - On housing 2, the alignment coil spacing was the expected value; and
  - The source was touching one of the source coils.

- It was possible to achieve CM balance of the DM circuit.

- Storing current in the parallel combination circuit (DM circuit) moved the frequencies (by an amount consistent with a model that ignores nonlinearity) as follows:
  - 1 A moved the peaks to 13.875 and 15.78 Hz,
  - 1.2 A moved them to 14.56 and 16.5 Hz,
  - 1.5 A made the 12.23 Hz peak disappear and moved the 14.96 Hz peak to 17.8 Hz,
  - 2 A moved the 14.96 Hz peak to 19.8 Hz, and
  - 2.5 A made the second peak disappear as well.

- Storing or pulsing current in all the alignment coils on side 1 excited the 14.96 Hz mode, in addition to some higher frequency modes at 63.2, 69.8, and 91.6 Hz.

- Storing or pulsing current in all the alignment coils on side 2 excited the 12.23 Hz peak, in addition to 29.85, 30.08, 57.5, 67.2, and 91.8 Hz.

After opening the experiment, a few additional issues were found:

- The source coil from side 1 was peeled off on one end and its coil-form was cracked. Note that the two coil-forms that had cracked were from the first batch of Macor material. The coil-forms made from the second batch (ordered later on) were intact.

- The sensing coil from side 1 had a little section of winding come off, unglued from the coil-form, but no damage to the coil-form was visible. This could explain the higher than expected frequency of the 14.96 Hz peak.
- The test mass on side 2 had a substantial quantity of GE-varnish on the springs. This can explain its lower quality factor.
- An approximate calculation that ignores nonlinearity suggests that for a system with two test masses of frequencies of 12.23 and 14.96 Hz, a current of 1.5 A in the DM circuit would move the mass with 12.23 Hz peak by 0.152 mm while moving the 14.96 Hz peak by only 0.0762 mm. In addition, storing 2.5 A would move the 14.96 Hz mass by 0.178 mm.
- In order to detach the test masses, it was necessary to soak the housing in solvent, ruining two of the alignment coils.
- The shields had been removed and replaced too many times and need to be remade.

Things to repair before the next cool-down:

- Wind a new source coil on the new Macor material.
- Wind a new sensing coil.
- Wind two new alignment coils.
- Heat-treat test masses and spacers.
- Diffusion-bond new shields.

C.5 Cool-down IV

The fourth cool-down started in April and lasted until the end of May of 2006. The room-temperature vacuum measurements of the frequencies gave 11.152 Hz for test mass 1, 11.191 Hz for test mass 2, and 10.166 Hz for the source. The source peak

was very difficult to excite. Since this measurement was not conclusive, a second, independent measurement was used. By tilting the experiment by a known angle and measuring the displacement of the source, the test masses, and center blocks of the housing, their respective frequencies were measured as a function of the tilt angle. The source frequency was calculated as (21.7±15.5) Hz, the frequency of test mass on side 1 as (11.57±0.59) Hz, the frequency of test mass on side 2 as (11.63±0.60) Hz, the frequency of the center block of the housing 1 as (14.5 ± 12.8) Hz, and the frequency of the center block of the housing 2 as (17.6 ± 8.8) Hz. The calculated frequencies of the test masses agree with the measured ones. The calculated frequencies of the center blocks had a huge error because of their large stray capacitance (about 75% of the total capacitance), making it worthless. The calculated frequency of the source mass was not very precise either due to a large stray capacitance, but it is possible to increase the capacitance significantly by adding spacers on the back of the source coils. The distance between the source coils and the source mass is decreased from 0.254 mm to 0.0763 mm. The tilt test was repeated, obtaining (9.6 ± 1.1) Hz.

In the fourth cool-down, it was found that:

- All circuits appeared to be working.
- Using inductance measurements, it was found that:
  - The alignment coils were closely matched, and
  - The source was touching one of the source coils.
- The resonance frequencies of the test masses were measured to be 11.304 and 11.359 Hz with quality factors of 2.5×10^5 and 8.2×10^4, respectively, at 2.5×10^{-5} torr and 2.5 K.
- The tilt sensor was DC calibrated. It was observed that the vertical springs had a substantial hysteretic behavior and allowed very small tilts.
- The vertical actuator was AC calibrated.
- The CM accelerometer was calibrated.

- The DM accelerometer was balanced. It was possible to achieve a CM balance of the DM circuit to one part in 1.5×10^5.
- It was observed that the balance had a strong dependence on the He level in the dewar.
- The balance was calibrated in terms of the tilt angle.
- The DM accelerometer was calibrated.
- One of the sensing coils from the CM circuit appeared to be disconnected. This still kept the circuit operational, but did not allow the flexibility to do a wide-band balance, making it impossible to store large currents in the DM circuit and be able to operate the SQUIDs.
- The misalignments δl and δn were measured.
- The shaker coil circuit stopped working.

After opening the experiment:

- The data from all cool-downs indicates that the source had consistently moved towards the same side. There was direct evidence (mark on the shields) that the source had been touching one of the shields.
- The source was attached to each housing independently and the capacitance of the alignment coils was measured, verifying that in fact the source does move when tightened.
- A room-temperature calibration of the tilt sensor showed that the hysteretic behavior of the vertical springs was present at room temperature as well.

We decided to make a few more modifications:

- Increase the source spacing until the source is obviously free.

- Machine capacitor plates to be attached to the rim of the shields that would allow room-temperature and cryogenic monitoring of the actual position of the source with respect to the shields. The capacitor plates would be slightly sticking out so that if the source moves too close it would first touch them and not the shields. The advantage of touching the capacitor plates is that they become shorted and there is direct evidence of touching.

- Add an extra coil in the source circuit that will allow us to center the source. The inductance of this coil needs to be very large so that the AC current that passes through it is much smaller than the one passing through the source coils.

- Remove the vertical springs in the cryogenic space.

C.6 Cool-down V

It was decided to perform a fifth cool-down containing the source and new source circuit only. The new hardware was prepared and tested during the months of June and July 2006 and the actual cool-down took place during August and the beginning of September 2006.

The following modifications were completed in preparation for the cool-down:

- The vertical springs were removed and a room-temperature calibration of the tilt sensor showed no hysteretic behavior. The suspension modes were identified at room temperature as:

  - Pendulum mode at 0.44 Hz,
  - Torsion mode at 0.92 Hz,
  - Rocking modes at 2.9 and 3.38 Hz.

- The extra coil was made using a Supermalloy core (in order to obtain large inductances) with Nb wire wound around it and had an inductance of about 30 mH.

- New spacers were machined in order to increase the source spacing.
- The capacitor plates were machined and installed.
- The capacitor plates were calibrated by using different spacers.
- Room-temperature measurements determined that, when tightened inside both housings, the source displaced 0.0763 mm towards side 1 and rotated 10^{-3} rad. The spacing was increased by 0.127 mm on each side leaving the final spacing to the shields to about 0.241 mm.
- The capacitance was measured using one of the spare SQUID leads. This increased the stray capacitance to about 82% of the total capacitance, making it difficult to identify the actual spacing, but still giving a good measure of the orientation of the source.
- A new procedure for making superconducting joints was developed. For a detailed description, see Section 2.2.10.

The room-temperature vacuum measurement of the frequencies were done using the capacitor plates. Two peaks were excited the most: 11.49 and 17.30 Hz. All eight capacitor plates detected those peaks.

The capacitor plates were monitored while cooling down. There was definite evidence that the source moved to one side: one of the capacitor plates was shorted near the beginning of the cool-down (at 93 K). The source moved in the same direction it moved at room temperature.

At 4.2 K, the following was found:

- The inductances of both source coils were closely matched (by about 95%), consequently, the source was very likely not touching the source coils.
- With no currents in the source circuit, the resonance frequencies were seen at 17.34 and 25.75 Hz with quality factors of order 100 at 10^{-5} torr.
- The resonance frequencies increased as a function of the stored current in the source coils.

- The source centering coil did not work properly. The inductance measurements were not consistent and their hysteretic behavior indicated that the saturation field of the metal was reached.
- One capacitor plate on side 1 was shorted, and consequently, we believe that the source mass was touching side 1.
- Knowing the side that the source was touching, it was possible to tilt the experiment towards the opposite side and try to free it. By tilting the assembly, we found that:
  - The capacitor plate measurements indicated that the source was moving away from the side it touched and toward the other side,
  - The tilt was not sufficient to remove the short, but
  - Tilting the experiment reduced the source mass main resonance peak from 17.34 Hz to 14.29 Hz and increased the quality factor to about 500.

A few more changes were necessary:

- A new supplementary source coil wound on a regular Macor coil-form.
- A test to determine if the source is bowing due to itself or due to some irregularity in the housing or spacers.

C.7 Cool-down VI

The sixth cool-down took place during the second part of the month of September 2006. A new supplementary coil was wound by using 2085 turns on a spool coil. The source mass was rotated by 180 degrees about the $\hat{z}$ axis along with the source coils. The spacers were kept unchanged. Before cooling down, the resonance frequency of the source was measured to be 11.30 Hz with a quality factor of 130 at 2.2×10^{-3} torr. During the cool-down, it was found that:

- One of the capacitor plates became shorted around 150 K and another around 120 K. Both of them were on side 2, consequently, the source appeared to be touching side 2.
- The resonance frequency of the source mass with no current in the source coils was 24.3 Hz.
- The inductance of both source coils were matched only to about 80%.
- By storing current in the supplementary source coil, it was possible to decrease the capacitances on side 2 while increasing them on side 1. With sufficient currents, it was possible to remove one of the shorts from side 2. For a larger current, however, a new short appeared, this time on side 1.

According to these results, it looks like the source supplementary circuit was working as expected. On the other hand, the source mass appeared to have less space than expected. This may be a consequence of it rotating and not being parallel to the housings, or it is still possible that the source coils are pushing it.

The motion and rotation of the source appears to be connected with the source coils. In order to fix this, we decided to:

- Move the source coils further back.
- Further increase the source-to-shields spacing.
- Attach the source coils to the housings instead of to the source directly.

C.8 Cool-downs VII-IX

Three more cool-downs including only the source circuit were performed between the months of October 2006 and January 2007 in an effort to free the source mass and get the source circuit working. The outcome of these was:

- The source mass was freed independently by two different methods: by tilting it and by storing current in the additional coil. Both methods were found to

be consistent and the range of motion for the source was 21 μm (before a short to the capacitor plates).

- The resonance frequency of the source mass at 2.3 K and 2.2×10^{-5} torr was measured to be 11.35 Hz with a quality factor of 4×10^4. A rocking mode was identified at 17.59 Hz with $Q = 5 \times 10^4$.

- Additional modes (maybe the housing modes) were found at 19.3 and 27.2 Hz, with quality factors of 500 and 3×10^3, respectively.

The source-mass-to-capacitor plate spacing was still much smaller than expected. A room-temperature inspection showed that the damaged housing was distorted. By measuring its displacement of the center part of the housing at different points with a depth gauge, we found that it was displaced by about 0.127 mm from its original position. The displacement appeared uniform within 10%. This explains the smaller spacing between the source and the capacitor plates. We identified the damaged housing with the 19.3-Hz peak, with a lower quality factor mode, and the good housing with the 27.2-Hz mode.

C.9 Cool-down X

A tenth cool-down was planned with all the circuits connected. The spacing to the source was additionally increased by 51 μm. This cool-down took place from February through the beginning of May 2007. During the cool-down:

- The source touched one of the capacitor plates but was freed by tilting the experiment.

- The source was moved by storing different currents in the supplementary source coil.

- The free range of the source motion was 58 μm.

- All circuits except for two of the alignment and the shaker circuits were operational. One of the sensing circuits was manifesting a strange behavior suggesting a bad joint.
- There was a leak and the experiment was continuously pumped in order to control it. The best stable pressure was about 9×10^{-6} torr.
- The refrigerator was operated at 1.65 K.
- The resonance frequency of the source mass was measured 13.28 Hz with a quality factor of 3×10^3 at the above pressure and temperature.
- The resonance frequencies of the two test masses were 11.52 and 12.30, with quality factors of 2×10^4 and 4×10^4, respectively, at the above pressure and temperature.
- The magnetic cross-talk of the source and shaker coils was measured.
- The experiment was taken to slightly above 4.5 K. This way the test masses and source mass were non-superconducting. At this temperature, the inductance of the sensing coils was measured, and the distance between the sensing coils and the shields was calculated. From this measurement, together with a measurement of the spacing between the sensing coils and the test masses, the actual distance between the test masses and the shields was calculated.
- The resonance peaks of the source and test masses were measured as a function of the experiment tilt. The suspension peaks were also measured as a function of the tilt, and were much higher than expected. This implies that the suspension was not completely free and the frequency measurements as a function of the tilt were not necessarily fully meaningful.
- The change in the resonance frequencies as a function of stored series and parallel currents in the sensing and source circuits were studied.
- The DM circuit was balanced. It was possible to achieve a CM balance of one part in 5×10^4 for extended periods of time.

- The tilt sensor was calibrated.
- The CM and DM circuits were calibrated.
- The misalignment and misbalance errors were measured.
- Actual experimental data was taken.

The noise level of the taken data was unacceptably high (by about three orders of magnitude). Since one of the sensing circuits was not working properly, the other circuit was chosen to be the DM circuit. However, it was not possible to achieve the wide-band balance (for a detailed discussion, see Section 5.7.3) and for this reason, the SQUID outputs had to be operated in their least sensitive range, contributing to the noise level. In addition, the pendulum frequency of the platform was about four times higher than expected. Reducing it would decrease the noise as well.

C.10 Cool-down XI

An eleventh cool-down was performed with the purpose of fixing the broken circuits and lowering the pendulum mode frequency. In order to lower the pendulum frequency, all leads connected to the experiment were loosened, in particular, special care was taken with the lead tubing current and SQUID probes. The same measurements of Cool-down X were repeated, with the following highlights:

- The source frequency was lower than before at 11.57 Hz.
- The test mass frequencies was higher than before at 11.495 Hz and 12.530 Hz.
- The source spacing is larger at at least 70 μm. The spacing could be larger, but it was not possible to estimate it since the capacitor plates were never shorted.
- The magnetic cross-talk was measured in more detail and was found that it depends on the source position.

- One of the sensing coils in one of the sensing circuits was disconnected. This did not allow the wide-band balance again, but gave crucial information about the different sides.

After opening the experiment, I found that the center part of the broken housing was not just translated, but it was rotated as well. The translation ranged between 25.4 and 177.8 μm, which corresponds to an average translation of 102.1 μm and a rotation of 10^{-3} rad.

The source could not touch the capacitor plates, since these were not sticking out of the plane of the shields anymore. Instead, one of the shield was starting to break and was sticking out.

Bibliography

[1] E. G. Adelberger, B. R. Heckel, and A. E. Nelson, *Tests of the gravitational inverse-square law*, Ann. Rev. Nucl. Part. Sci. **53** (2003), 77–121.

[2] I. Antoniadis, N. Arkani-Hammed, S. Dimopoulos, and G. R. Dvali, *New dimensions at a millimeter to a fermi and superstrings at a TeV*, Phys. Lett. B **436** (1998), 257–263.

[3] ———, *Phenomenology, astrophysics and cosmology of theories with sub-millimeter dimensions and TeV scale quantum gravity*, Phys. Rev. D **59** (1999), 086004.

[4] N. Arkani-Hammed, S. Dimopoulos, and G. R. Dvali, *The hierarchy problem and new dimensions at a millimeter*, Phys. Lett. B **429** (1998), 263–272.

[5] S. R. Beane, *On the importance of testing gravity at distances less than 1 cm*, General Relativity and Gravitation **29** (1997), 495–951.

[6] M. Bordag, B. Geyer, G. L. Klimchitskaya, and V. M. Mostepanenko, *New constraints for non-newtonian gravity in the nanometer range from the improved precision measurement of the Casimir force*, Phys. Rev. D **62** (2000), 011701.

[7] K. Burger and M. Ruhle, *Material transport mechanisms during the diffusion bonding of niobium to Al_2O_3*, Ultramicroscopy **29** (1989), 88–97.

[8] J. B. Camp, T. W. Darling, and R. E. Brown, *Macroscopic variations of surface potentials of conductors*, J. Appl. Phys. **69** (1991), 7126–7129.

[9] Y. Cao, Private communication, June 2005.

[10] L. Carbone, G. Ciani, R. Dolesi, M. Hueller, D. Tombolato, S. Vitale, W. J. Weber, and A. Cavalleri, *Upper limits to surface-force disturbances on LISA proof masses and the possibility of observing galactic binaries*, Phys. Rev. D **75** (2007), 042001.

[11] H. B. G. Casimir, *On the attraction between two perfectly conducting plates*, Proc. Kon. Nederland. Akad. Wetensch. **51** (1948), 793–795.

[12] H. A. Chan, *Null test of the gravitational inverse square law with a superconducting gravity gradiometer*, Ph.D. thesis, Univerity of Maryland, College Park, Maryland, 1982.

[13] H. A. Chan, M. V. Moody, and H. J. Paik, *Superconducting gravity gradiometer for sensitive gravity measurements. II. Experiment*, Phys. Rev. D **35** (1987), 3551–3571.

[14] H. A. Chan and H. J. Paik, *Superconducting gravity gradiometer for sensitive gravity measurements. I. Theory*, Phys. Rev. D **35** (1987), 3572–3597.

[15] F. Chen, G. L. Klimchitskaya, U. Mohideen, and V. M. Mostepanenko, *Theory confronts experiment in the Casimir force measurements: Quantification of errors and precision*, Phys. Rev. A **69** (2004), 022117.

[16] J. Chiaverini, S. J. Smullin, A. A. Geraci, D. M. Weld, and A. Kapitulnik, *New experimental constraints on non-Newtonian forces below 100 μm*, Phys. Rev. Lett. **90** (2003), 151101.

[17] R. S. Decca, E. Fischbach, G. L. Klimchitskaya, D. E. Krause, D. López, and V. M. Mostepanenko, *Improved tests of extra-dimensional physics and thermal quantum field theory from new Casimir force measurements*, Phys. Rev. D **68** (2003), 116003.

[18] R. S. Decca, D. López, E. Fischbach, G. L. Klimchitskaya, D. E. Krause, and V. M. Mostepanenko, *Tests of new physics from precise measurements of the Casimir pressure between two gold-coated plates*, Phys. Rev. D **75** (2007), 077101.

[19] M. Dine, *TASI lectures on the strong CP problem*, Unpublished lecture notes, 2000.

[20] G. Elssner and G. Petzow, *Metal ceramic joining*, ISIJ INTERNATIONAL **31** (1990), 1011–1032.

[21] D. K. Finnemor, T. F. Stromber, and C. A. Swenson, *Superconducting properties of high-purity niobium*, Phys. Rev. **149** (1966), 231.

[22] W. M. Folkner, M. V. Moody, and J.-P. Richards, *Very high-vacuum heat treatment facility*, Rev. Sci. Inst. **56** (1987), 2288–2291.

[23] H. Goldstein, *Classical mechanics*, second ed., Addison-Wesley, 1980.

[24] Online resource http://einstein.stanford.edu, September 2007.

[25] K. Hagiwara et al., *Review of particle properties*, Phys. Rev. D **66** (2002), 010001.

[26] C. Herring and M. H. Nichols, *Thermionic emission*, Rev. Mod. Phys. **21** (1949), 185–271.

[27] C. D. Hoyle, D. J. Kapner, B. R. Heckel, E. G. Adelberger, J. H. Gundlach, U. Schmidt, and H. E. Swanson, *Sub-millimeter tests of the gravitational inverse-square law*, Phys. Rev. D **70** (2004), 042004.

[28] C. D. Hoyle, U. Schmidt, B. R. Heckel, E. G. Adelberger, J. H. Gundlach, D. J. Kapner, and H. E. Swanson, *Sub-millimeter test of the gravitational inverse-square law: a search for "large" extra dimensions*, Phys. Rev. Lett. **86** (2001), 1418.

[29] S. Isagawa, *Fabrication of a superconducting niobium cavity by the diffusion-bonding method*, J. Appl. Phys. **49** (1978), 881–885.

[30] T. Kaluza, *On the problem of unity in physics*, Sitzungsber. Preuss. Akad. Wiss. Berlin. Math. Phys. Klasses (1921), 966–972.

[31] D. J. Kapner, T. S. Cook, E. G. Adelberger, J. H. Gundlach, B. R. Heckel, C. D. Hoyle, and H. E. Swanson, *Test of the gravitational inverse-square law below the dark-energy scale*, Phys. Rev. Lett. **98** (2007), 021101.

[32] O. Klein, *Quantum theory and five dimensional theory of relativity*, Z. F. Phys. **37** (1926), 895–906.

[33] S. K. Lamoreaux, *Demonstration of the Casimir force in the 0.6 to 6 mm range*, Phys. Rev. Lett. **78** (1997), 5–8.

[34] ———, *Calculation of the Casimir force between imperfectly conducting plates*, Phys. Rev. A **59** (1999), R3149–R3153.

[35] L. D. Landau and E. M. Lifshitz, *Mechanics*, third ed., Pergamon Press, New York, 1976.

[36] N. D. Lang and W. Kohn, *Theory of metals: Work function*, Phys. Rev. B **3** (1971), 1215–1223.

[37] E. M. Lifshitz, Zh. Eksp. Teor. Fiz. **29** (1955), 894.

[38] J. C. Long, H. W. Chan, A. B. Churnside, E. A. Gulibs, M. C. Varney, and J. C. Price, *Upper limits to submillimiter-range forces from extra space-time dimensions*, Nature **421** (2003), 922–925.

[39] J. C. Long and J. C. Price, *Current short-range tests of the gravitational inverse square law*, Comptes Rendus Physique **4** (2003), 337–346.

[40] E. R. Mapoles, *Development of a superconducting gravity gradioeter for a test of the inverse square law*, Ph.D. thesis, Stanford Univerity, Stanford, California, 1981.

[41] J. E. Moody and F. Wilczek, *New macroscopic forces?*, Phys. Rev. D **30** (1984), 130–138.

[42] M. V. Moody, Private communication, August 2007.

[43] M. V. Moody, H. A. Chan, C. Stephens, and H. J. Paik, *A superconducting penetration depth thermometer*, Proceedings of the 17th International Conference on Low Temperature Physics (Kahlsruhe, West Germany) (W. Weber B. Echern, A. Schmid and H. Wuhl, eds.), Elsevier, 1984.

[44] M. V. Moody and H. J. Paik, *Gauss's law test of gravity at short range*, Phys. Rev. Lett. **70** (1993), 1195–1198.

[45] M. V. Moody, H. J. Paik, and E. R. Canavan, *Three-axis superconducting gravity gradiometer for sensitive gravity experiments*, Rev. Sci. Inst. **73** (2002), 3957–3974.

[46] R. Newman, *Prospects for terrestrial equivalence principle tests with a cryogenic torsion pendulum*, Class. Quant. Grav. **18** (2001), 2407.

[47] M. Nonnenmacher, M. P. O. Boyle, and H. K. Wickramasinghe, *Kelvin probe force microscopy*, Appl. Phys. Lett. **58** (1991), 2921–2923.

[48] R. Norton, Private communication, October 2007.

[49] T. P. Orlando and K. A. Delin, *Foundations of applied superconductivity*, Addison-Wesley, 1991.

[50] H. J. Paik, *Analysis and development of a very sensitive low temperature gravitational radiation detector*, Ph.D. thesis, Stanford Univerity, Stanford, California, 1974.

[51] ———, *Superconducting tunable-diaphragm transducer for ensitive acceleration measurements*, J. Appl. Phys. **47** (1976), 1168–1178.

[52] ———, *New null experiment to test the inverse square law of gravitation*, Phys. Rev. D **19** (1979), 2320.

[53] ———, *New null experiment to test the inverse square law of gravitation*, Class. Quant. Grav. **11** (1994), A133–A144.

[54] ———, SQUID Handbook (J. Clarke and A. Braginski, eds.), vol. 2, Wiley, New York, 2006, pp. 545–579.

[55] ———, Physics 798G, Lecture 6, Tests of the Equivalence Principle and the Inverse-Square Law, Feb 2007.

[56] ———, Private communication, August 2007.

[57] H. J. Paik, E. R. Mapoles, and K. Y. Wang, *Superconducting gravity gradiometers*, Proc. Conference on Future Trends in Superconductive Electronics (1978), 166.

[58] H. J. Paik and M. V. Moody, *Null test of the inverse-square law of gravity*, Class. Quant. Grav. **11** (1994), A145–A152.

[59] ———, *Null test of Newton's law of gravitation on a 100-micrometer scale*, Proposal to NSF, 2002.

[60] H. J. Paik, M. V. Moody, and D. Strayer, *Short-range inverse-square law experiment in space*, Proposal to NASA, 2002.

[61] J. W. Parke, *Null test of the gravitational inverse square law and the development of a superconducting six-axis accelerometer*, Ph.D. thesis, Univerity of Maryland, College Park, Maryland, 1990.

[62] J. H. Parker and R. W. Warren, *Kelvin device to scan large areas for variations in contact potential*, Rev. Sci. Inst. **33** (1962), 948–950.

[63] R. D. Peccei and H. R. Quinn, *Constraints imposed by CP conservation in the presence of pseudoparticles*, Phys. Rev. Lett. **38** (1977), 1440–1443.

[64] ———, *CP conservation in the presence of pseudoparticles*, Phys. Rev. D **16** (1977), 1791–1797.

[65] K. Penanen, Private communication, May 2006.

[66] M. Pospelov and A. Ritz, *New macroscopic forces?*, Phys. Rev. Lett. **83** (1999), 2526–2529.

[67] L. Randall and R. Sundrum, *An alternative to compactification*, Phys. Rev. Lett. **83** (1999), 4690–4693.

[68] K. W. Rigby, D. Marek, and T. C. P. Chui, *SQUID holder with high magnetic shielding*, Rev. Sci. Inst. **61** (1990), 834–838.

[69] M. S. Roberts and A. H. Rots, *Comparison of rotation curves of different galaxy types*, Astronomy and Astrophysics **26** (1973), 483–485.

[70] N. A. Robertson, J. R. Blackwood, S. Buchman, R. L. Byer, J. Camp, D. Gill, J. Hanson, S. Williams, and P. Zhou, *Kelvin probe measurements: investigations of the patch effect with applications to st-7 and LISA*, Class. Quant. Grav. **23** (2006), 2665–2680.

[71] M. V. Romalis, W. C. Griffith, J. P. Jacobs, and E. N. Fortson, *New limit on the permanent electric dipole moment of ^{199}Hg*, Phys. Rev. Lett. **86** (2001), 2505–2508.

[72] F. Rossi and G. I. Opat, *Observations of the effects of adsorbates on patch potentials*, J. Phys. D **25** (1992), 1349–1353.

[73] V. Rubin, W. K. Ford, Jr., and N. Thonnard, *Rotational properties of 21 Sc galaxies with a large range of luminosities and radii from NGC* 4605 *($r = 4$ kpc) to UGC 2885 ($r = 122$ kpc)*, Astrophys. J. **238** (1980), 471.

[74] V. C. Rubin and W. K. Ford, Jr., *Rotation of the andromeda nebula from a spectroscopic survey of emission regions*, Astrophys. J. **159** (1970), 379.

[75] S. Smith, *The mass of the Virgo Cluster*, Astrophys. J. **83** (1936), 23.

[76] S. J. Smullin, A. A. Geraci, D. M. Weld, J. Chiaverini, S. Holmes, and A. Kapitulnik, *Constraints on Yukawa-type deviations from Newtonian gravity at 20 microns*, Phys. Rev. D **72** (2005), 122001.

[77] C. C. Speake, *Interaction potential between extended bodies*, Phys. Rev. Lett. **60** (1996), 107501.

[78] C. C. Speake and C. Trenkel, *Forces between conducting surfaces due to spatial variations of surface potential*, Phys. Rev. Lett. **90** (2003), 160403.

[79] D. N. Spergel, R. Bean, O. Doré, M. R. Nolta, C. L. Bennett, J. Dunkley, G. Hinshaw, N. Jarosik, E. Komatsu, L. Page, H. V. Peiris, L. Verde, M. Halpern, R. S. Hill, A. Kogut, M. Limon, S. S. Meyer, N. Odegard, G. S. Tucker, J. L. Weiland, E. Wollack, and E. L. Wright, *Three-year wilkinson microwave anisotropy probe (WMAP) observations: Implications for cosmology*, Astrophys. J. Supplement Series **170** (2007), 370–408.

[80] R. Sundrum, *Fat gravitons, the cosmological constant and submillimeter tests*, Phys. Rev. D **69** (2004), 044014.

[81] L.-C. Tu, S.-G. Guan, J. Luo, C.-G. Shao, and L.-X. Liu, *Null test of newtonian-square law at submillimiter range with a dual-modulation torsion pendulum*, Phys. Rev. Lett. **98** (2007), 201101.

[82] M. S. Turner, *Windows on the axion*, Phys. Rep. **197** (1990), 67.

[83] K. Venkateswara, Private communication, September 2007.

[84] K. Y. Wang, *Modeling and error analisis for a superconducting gravity gradiometer*, Ph.D. thesis, Stanford Univerity, Stanford, California, 1979.

[85] S. Weinberg, *A new light boson?*, Phys. Rev. Lett. **40** (1978), 223–226.

[86] F. Wilczek, *Problem of strong P and T invariance in the presence of instantons*, Phys. Rev. Lett. **40** (1978), 279–282.

[87] F. Zwicky, *Die Rotverschiebung von extragalaktischen Nebeln*, Helv. Phys. Acta **6** (1933), 110–127.

[88] ———, *On the masses of nebulae and of clusters of nebulae*, Astrophys. J. **86** (1937), 217.